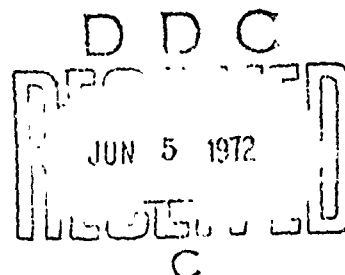AEDC-TR-72-46

AD742995

ABORT SEPARATION PRESSURE DISTRIBUTIONS
ON McDONNELL-DOUGLAS
SPACE SHUTTLE CONFIGURATIONS
AT MACH NUMBERS 2, 3, AND 5

W. T. Strike, Jr.

ARO, Inc.

May 1972

DDC

JUN 5 1972

C

Approved for public release; distribution unlimited.

VON KÁRMÁN GAS DYNAMICS FACILITY

ARNOLD ENGINEERING DEVELOPMENT CENTER

AIR FORCE SYSTEMS COMMAND

ARNOLD AIR FORCE STATION, TENNESSEE

NOTICES

DOCUMENT CONTROL DATA - R & D

(Security classification of title body of abstract and indexing annotation must be entered when the overall report is classified)

1 ORIGINATING ACTIVITY *(Corporate author)*	2a. REPORT SECURITY CLASSIFICATION
Arnold Engineering Development Center	UNCLASSIFIED
Arnold Air Force Station, Tennessee 37389	2b. GROUP N/A

3. REPORT TITLE

ABORT SEPARATION PRESSURE DISTRIBUTIONS ON McDONNELL-DOUGLAS
SPACE SHUTTLE CONFIGURATIONS AT MACH NUMBERS 2, 3, AND 5

4 DESCRIPTIVE NOTES *(Type of report and inclusive dates)*
July 22-27, 1971--Final Report

5. AUTHOR(S) *(First name, middle initial, last name)*

W. T. Strike, Jr., ARO, Inc.

6 REPORT DATE	7a. TOTAL NO. OF PAGES	7b. NO. OF REFS
May 1972	173	3
8a. CONTRACT OR GRANT NO.	9a. ORIGINATOR'S REPORT NUMBER(S)	
Program Element 921E	AEDC-TR-72-46	
	9b. OTHER REPORT NO(S) *(Any other numbers that may be assigned this report)*	
	ARO-VKF-TR-71-247	

10. DISTRIBUTION STATEMENT

Approved for public release; distribution unlimited.

11 SUPPLEMENTARY NOTES	12. SPONSORING MILITARY ACTIVITY
Available in DDC	NASA (Langley RC), Virginia 23365.

13 ABSTRACT The report summarized the pressure distributions obtained on the lower surface of the orbiter and upper surface of the booster (adjacent model surfaces) during possible staging and abort maneuvering positions and also for various proposed launch configurations, of the space shuttle vehicles. The results were obtained with and without booster and orbiter plume simulation at nominal free-stream Mach numbers of 2, 3, and 5. The report also contains a brief summary of the results obtained for the calibration of the nozzles used to generate the plumes for the power-on simulation. Results demonstrate the importance of plume simulation on the aerodynamic loading of a vehicle and, in particular, suggest that plume simulation is needed to evaluate properly the aerodynamic coefficients on the space shuttle vehicles during the staging and abort maneuvers of these vehicles. The Appendixes of this report contain additional comparisons of the pressure distributions obtained.

14. KEY WORDS	LINK A		LINK B		LINK C	
	ROLE	WT	ROLE	WT	ROLE	WT
supersonic flow						
space vehicle						
stage separation						
pressure distribution						
booster model						
orbiter model						
space stations						
aerodynamic characteristics						

AFSC
Arnold AFS Tenn

ABORT SEPARATION PRESSURE DISTRIBUTIONS
ON McDONNELL-DOUGLAS
SPACE SHUTTLE CONFIGURATIONS
AT MACH NUMBERS 2, 3, AND 5

W. T. Strike, Jr.

ARO, Inc.

Approved for public release; distribution unlimited.

FOREWORD

The work presented in this report was sponsored jointly by the Marshall Space Flight Center (MSFC) and the Langley Research Center (LaRC) of the National Aeronautics and Space Administration (NASA) under Program Element 921E.

The results of the test were obtained by ARO, Inc. (a subsidiary of Sverdrup & Parcel and Associates, Inc.), contract operator of the Arnold Engineering Development Center (AEDC), Air Force Systems Command (AFSC), Arnold Air Force Station, Tennessee, under Contract F40600-72-C-0003. This test program was conducted under ARO Project No. VA1163; the experimental data were obtained in the period from July 22 to July 27, 1971, and the final data package was completed on October 4, 1971. The manuscript was submitted for publication on December 30, 1971.

The test was conducted under the supervision of Mr. John Rampy and Mr. Ray Baker of the Lockheed Missiles Space Company Division (LMSC), Huntsville, Alabama, and Mr. Ken Blackwell and Mr. Dave Lane of the MSFC/NASA.

This technical report has been reviewed and is approved.

EMMETT A. NIBLACK, JR.
I t Colonel, USAF
Chief Air Force Test Director, VKF
Directorate of Test

FRANK J. PASSARELLO
Colonel, USAF
Acting Director of Test

ABSTRACT

The report summarizes the pressure distributions obtained on the lower surface of the orbiter and upper surface of the booster (adjacent model surfaces) during possible staging and abort maneuvering positions and also for various proposed launch configurations of the space shuttle vehicles. The results were obtained with and without booster and orbiter plume simulation at nominal free-stream Mach numbers of 2, 3, and 5. The report also contains a brief summary of the results obtained for the calibration of the nozzles used to generate the plumes for the power-on simulation. Results demonstrate the importance of plume simulation on the aerodynamic loading of a vehicle and, in particular, suggest that plume simulation is needed to evaluate properly the aerodynamic coefficients on the space shuttle vehicles during the staging and abort maneuvers of these vehicles. The Appendixes of this report contain additional comparisons of the pressure distributions.

CONTENTS

ILLUSTRATIONS

APPENDIXES

NOMENCLATURE

A/A^*	Nozzle area ratio with A^* the nozzle throat area
b	Span, in.
C_m	Pitching-moment coefficient (see Section 3.2)
C_N	Normal force coefficient (see Section 3.2)
C_p	Pressure coefficient, $(p-p_\infty)/q_\infty$
C_μ	Discharge coefficient, (actual/ideal) mass flow rate
c	Local chord (wing or chord length), in.
c_m	Local pitching moment coefficient per inch (see Section 3.2)
c_N	Local normal force coefficient per inch (see Section 3.2)
d_c	Sting (i.e., nozzle centerbody) diameter, in.
E_p	Nozzle gap setting, in. (see Section 2.3)
H, H_1, H_2	Dummy variables in Eq. (2)
i	Orbiter incidence angle relative to the booster, deg

L	Reference length, 16.14 in. (booster length)
ℓ	Local body length, in.
M	Mach number
$\dot{m}$	Mass flow rate, lbm/sec
p	Static pressure, psia
p_0	Stagnation pressure, psia
p_z	Measured local pitot pressure, psia
q_∞	Free-stream dynamic pressure, psia
Re_ℓ	Reynolds number based on the booster length
s	Reference area, in.
T_0	Tunnel stagnation temperature, °R
x, y	Either model surface coordinates relative to the model nose or coordinates relative to the center of the nozzle exit plane, in.
x_c	Displacement relative to the chord leading edge, in.
x_w	Displacement relative to the wing leading edge, in.
y_s	Internal plume shock location relative to the nozzle axis, in.
α	Angle of attack, deg
ΔC_m	Incremental change in pitching moment coefficient, change in pitching moment/$q_\infty Ls$
ΔC_N	Incremental change in normal force coefficient, change in normal force/$q_\infty s$
Δx	Axial displacement of orbiter moment reference from the booster moment of reference, in.
Δz	Vertical displacement between the orbiter and booster moment reference points, in.
δ_j	Initial turning angle of the plume boundary at the nozzle exit, deg
$\theta_{L.E.}$	Local model surface angle or wing leading edge angle of sweep, deg
θ_N	Nozzle exit angle, deg

SUBSCRIPTS

θ_w, θ	Local wing and local body angle, respectively, deg (see Fig. 1a)
b	Local environment or model base property
c	Local canard dimension or nozzle centerbody property
j	Local nozzle exit or chamber property
L.E.	Leading edge
ℓ	Local property or lower surface
N	Nose tap
T.E.	Trailing edge
u	Upper surface
w	Local wing dimension
x	Coefficient based on integration along an x coordinate
y	Coefficient based on integration along a y coordinate
∞	Free-stream property

SECTION I
INTRODUCTION

For the abort and normal staging of the space shuttle vehicles, the mutual aerodynamic interference and plume impingement loading must be evaluated so that an assessment of the separation of the vehicles can be made. The pressure tests described in this report were conducted to assess the nature of the interference loading on the upper surface of the booster and the lower surface of the orbiter; that is, on the adjacent surfaces of these two vehicles during a separation maneuver. The test objectives were to evaluate: (1) the aerodynamic interference between the two models with variations in the proximity and attitude of the two models, (2) the effects of booster and orbiter plume simulation on the interference loads, (3) the Mach number effects on the interference loading, and (4) the influence of an external stream on the simulated plume impingement loading. Also, possible launch configurations with the booster and orbiter mated were investigated at nominal Mach numbers 2 and 5 to examine the interference load distributions generated on the booster and orbiter.

Slightly modified 0.0055-scale models of the McDonnell Douglas (MDAC) booster and orbiter configurations were used in this investigation. The booster model was basically that designated by MDAC as the 19A configuration; however, the vertical tails were modified and resembled those of the Number 17 configuration. The high cross range orbiter configuration was used. The aft sections of both models were modified so that nozzles could be installed to generate a plume which simulated a particular thrust setting of the vehicle propulsion system. Booster and orbiter engine thrust levels of 0, 50, and 100 percent were simulated during the test program.

The plume simulation was generated with cold (about 560°R) airflow through an annular type of nozzle. The nozzles were designed with a variable-area-ratio capability so that the plume simulation of the full-scale vehicle could be varied, depending on the external stream conditions.

The tests were conducted in the 40-in., Supersonic Wind Tunnel (A) of the von Kármán Gas Dynamics Facility (VKF) at nominal Mach numbers 2, 3, and 5 and free-stream Reynolds numbers (Re_ℓ), based on the booster length, from 1.5 to 8.6 million. The angle-of-attack range was ±10 deg, and the relative angle between the orbiter and booster was zero, except for a few test points that were obtained at a relative angle of incidence of 5 deg. The relative position between the moment

1

reference points of the booster and orbiter was varied axially from
$\Delta x/L$ of -0.391 to 0.520 and vertically from a $\Delta z/L$ of 0.11 to 0.91.
For decreasing values of $\Delta x/L$, the orbiter moved downstream toward
the booster base region. The test results consisted of model surface
pressure measurements, nozzle chamber and exit pressure measure-
ments, and some holographic interferograms.

This report contains a brief summary of the power-on and power-
off interference effects on the orbiter and booster pressure distribu-
tions and also on the nozzle plume calibration results used to define
the proper plume simulation for each rocket thrust level and free-
stream Mach number condition.

A complete set of pressure data will be published under the
SADSAC Space Shuttle Aerothermodynamic Data Management System.

SECTION II
TEST EQUIPMENT

2.1 WIND TUNNEL

Tunnel A is a continuous, closed-circuit variable-density wind
tunnel which has an automatically positioned, flexible-plate-type nozzle
with a 40- by 40-in. test section and a model injection system. The
tunnel can be operated at Mach numbers from 1.5 to 6 at maximum
stagnation pressures from 29 to 200 psia, respectively, and stagnation
temperatures up to 750°R (M_∞ = 6). Minimum operating pressures
vary from about one-tenth to one-twentieth of the maximum at each
Mach number.

2.2 MODELS

The 1/180-scale models of the McDonnell Douglas (MDAC) booster
and orbiter configurations were specified for this investigation. The
booster model shown in Fig. 1a is basically the booster configuration
designated by MDAC as 19A. The vertical tails on this booster con-
figuration correspond to the tail designed for MDAC configuration 17.
The orbiter configuration is shown in Fig. 1b.
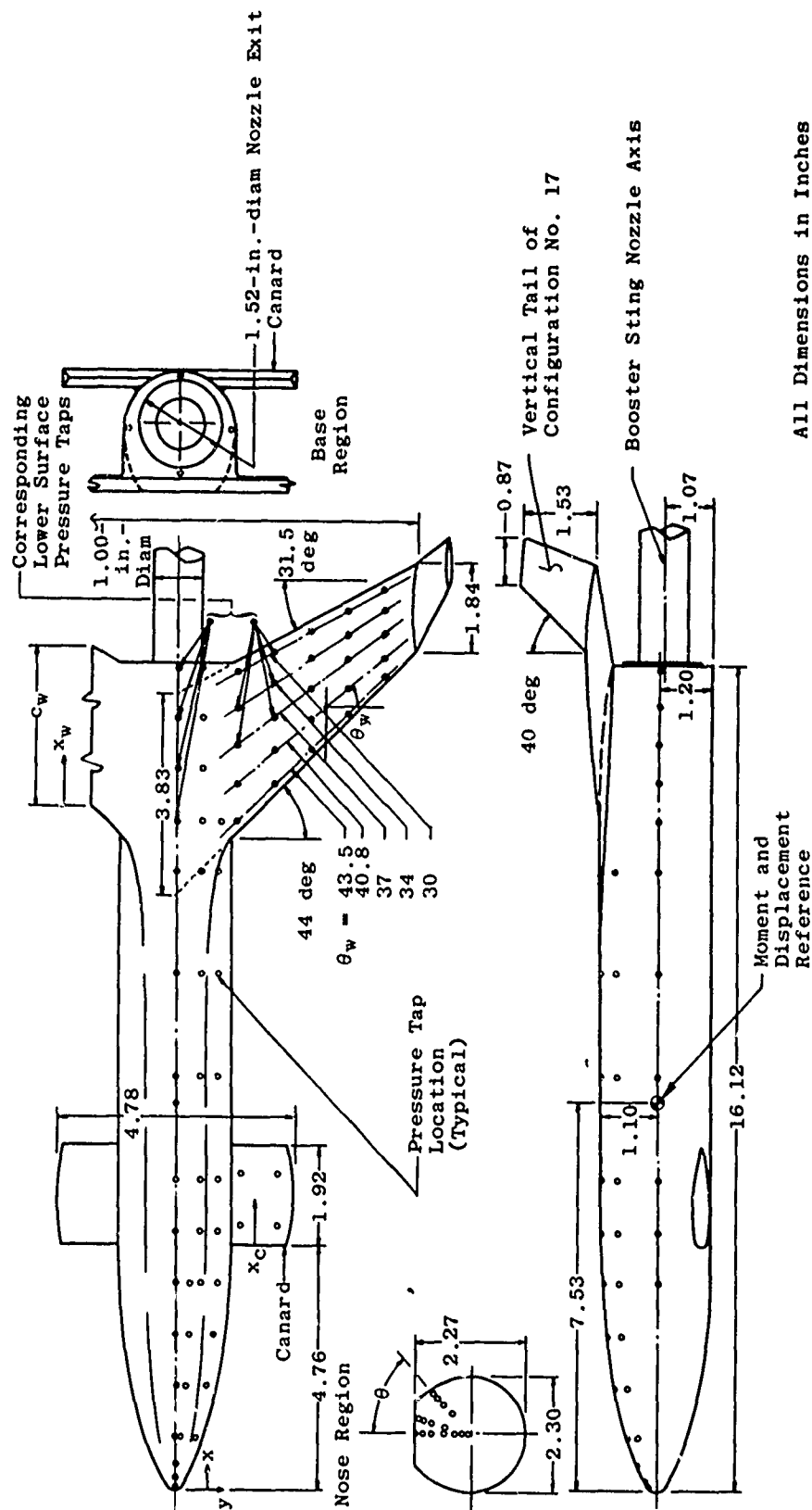
a. Booster Configuration (MDAC-19A Configuration)

Fig. 1 Model Configurations and Nominal Pressure Tap Locations

3
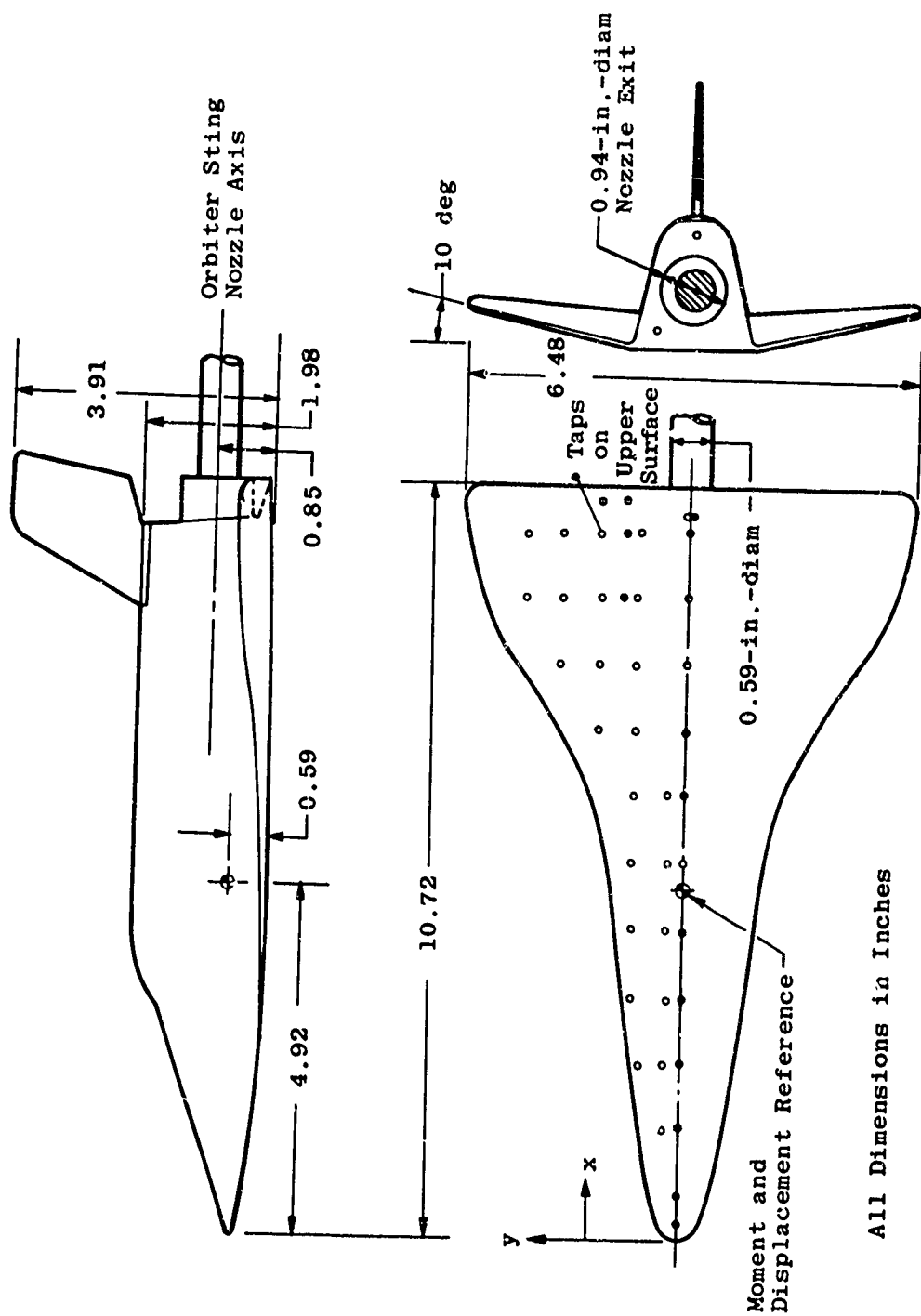
b. Orbiter Configuration (MDAC-Dwg. No. 255BJ0060)
Fig. 1 Concluded

All Dimensions in Inches

The pressure models were made of brass and fabricated by the investment casting technique employed by NASA at the Langley Research Center. The models were bored out and cut in sections so that three, 48-port S-type Scanivalves® could be installed inside. One Scanivalve was placed in the orbiter model, and two scanivalves were placed in the booster model. Most of the pressure taps were located on the adjacent surfaces of these bodies; that is, 38 pressure taps were located on the lower surface of the orbiter and 77 taps on the upper surfaces of the booster. Also, several additional taps were located in the base region and on the opposite surfaces near the model base of each model, as shown in Fig. 1. Boundary layer trips consisting of approximately 0.2-in.-wide strips of No. 28 Carborundum Grit for the $M_\infty = 5$ tests and No. 60 for the $M_\infty = 2$ and 3 tests were applied as shown in Fig. 2b.

2.3 NOZZLE AND MODEL SUPPORT SYSTEMS

The orbiter and booster models were supported on individual stings attached to a remotely controlled dual-sting support mechanism, as shown schematically in Fig. 2a and photographically in Fig. 2b. The model support mechanism provided movement of the orbiter relative to the booster, 17 in. in the axial direction and 15 in. in the vertical direction. An automatic control system allowed programming the orbiter mechanism to move to preselected axial and vertical positions relative to the booster during a test run. As indicated in Fig. 2, these displacements were referenced to the orbiter and booster moment reference point. The relative angle of incidence (i) between the two models was set manually. The entire dual-sting support mechanism was mounted on the tunnel sector to provide pitching the two models as a unit from -10 to +10 deg.

A concentric, annular, variable-area-ratio supersonic nozzle was furnished as an integral part of the upstream section of the model support strings, as shown in Fig. 3. High-pressure air flowed through the hollow sting into the nozzle chamber region and then expanded through the annular nozzle, generating a plume which enveloped the sting. The sting nozzle designs were similar in that the outer cylindrical sleeve (see Fig. 3) could be moved relative to the contoured nozzle centerbody section of the hollow string. The inner surface of this outer cylindrical sleeve was tapered so that the nozzle-to-exit area ratio of the orbiter nozzle could be varied from about 10 to 100, whereas the booster nozzle area ratio could be varied from about 3 to 20. The nozzles were designed to operate at a maximum chamber pressure of 1500 psia.

Dual Model Support

Orbiter Model Support
Remotely Controlled with
17.5-in. Axial Travel
and 14-in. Vertical Travel

Relative Angle
Position Preset

Orbiter Plume

Orbiter Gas Supply

Booster Gas Supply

Booster Plume

Plume Impingement
Loading on Booster

$+\Delta x$

$+\Delta z$

34.2

16.1

All Dimensions in Inches
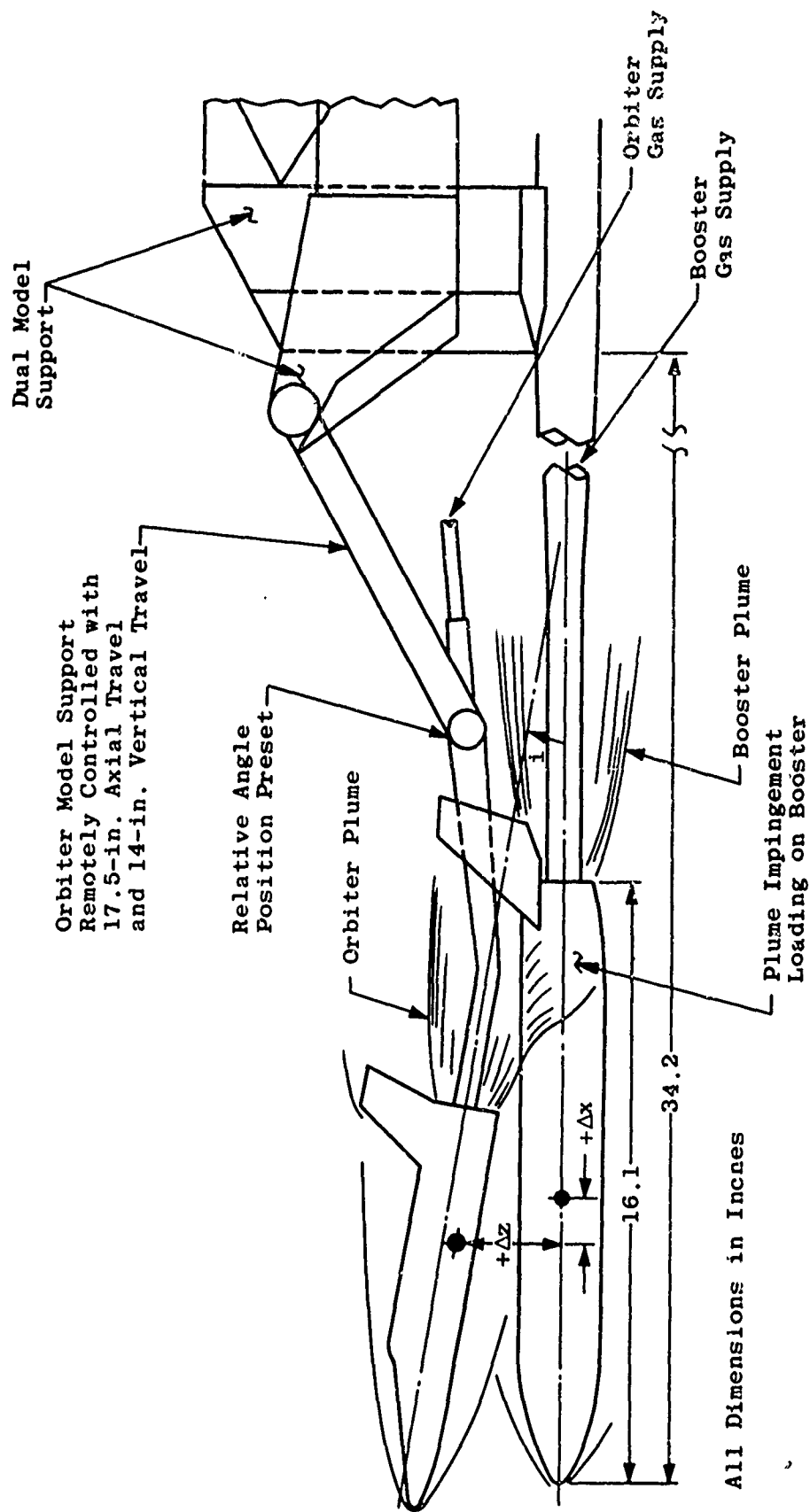
a. Model Support Components

Fig. 2 Test Installation on a Dual-Sting Sector Support System

6
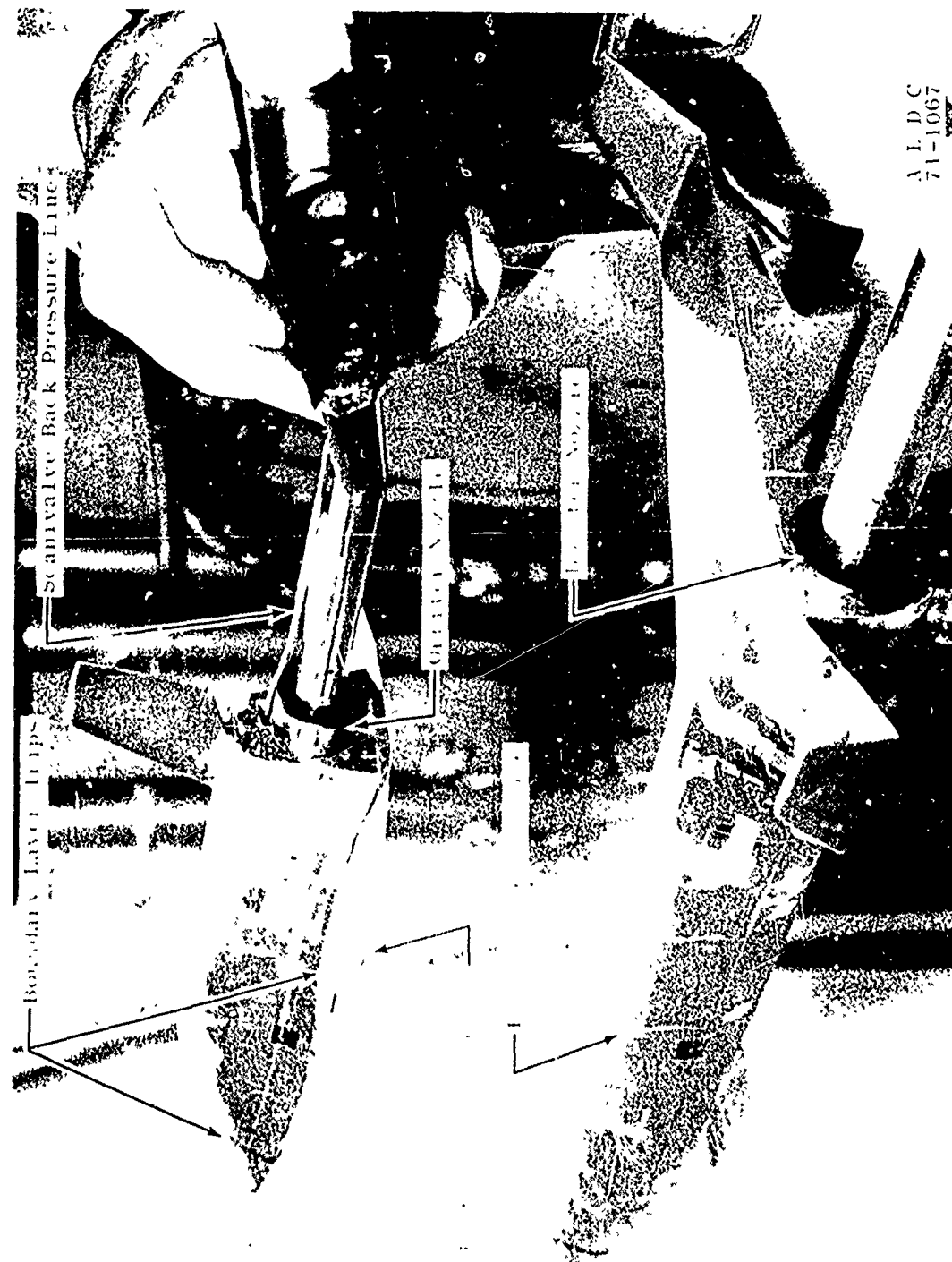
b. Installation Photograph of the Pressure Models
Fig. 2 Concluded
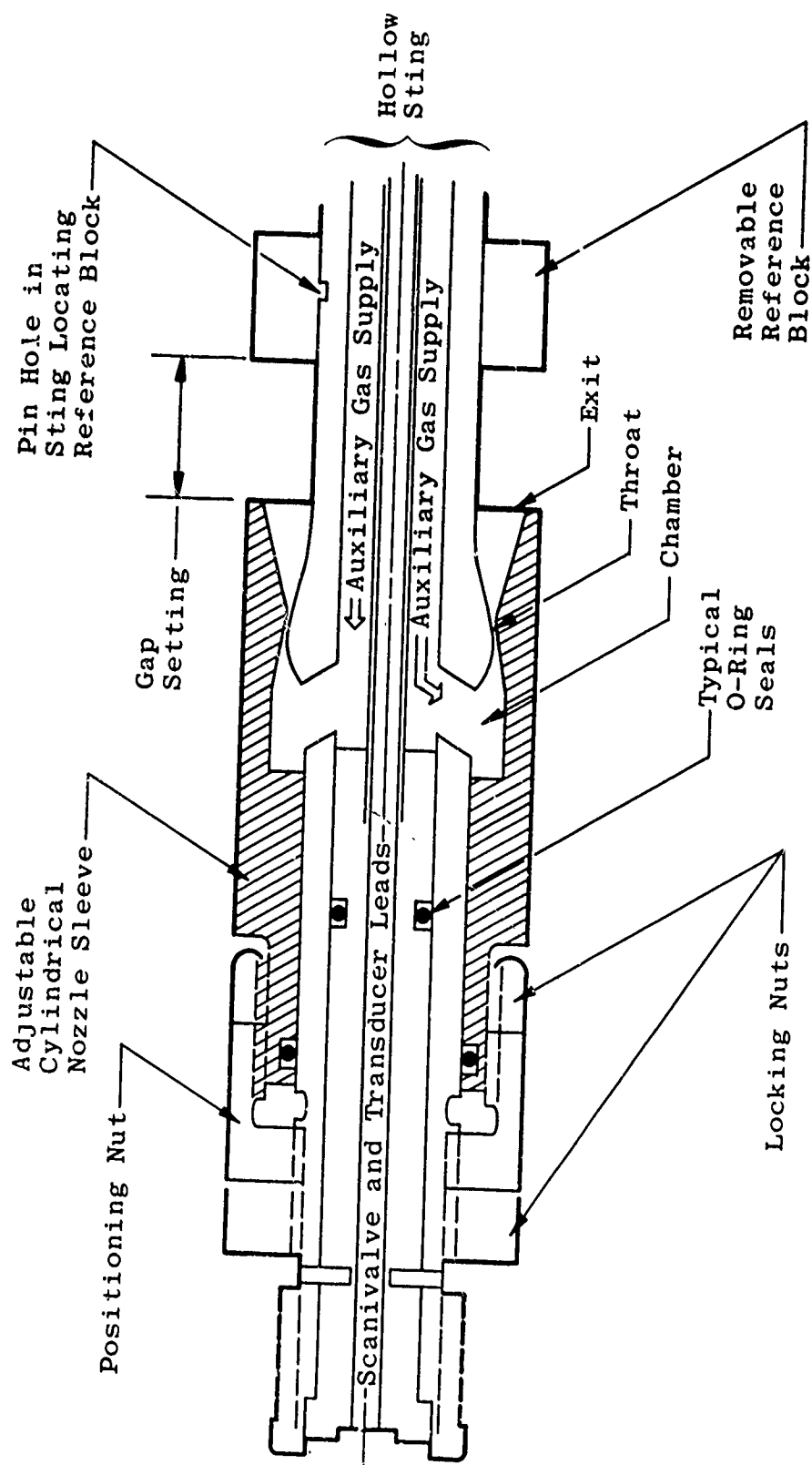
Fig. 3 Typical Components of the Orbiter and Booster Nozzle Stings

The nozzle area ratio was set by locating the outer cylindrical sleeve relative to a reference block positioned on the sting by a pin hole in the sting. This gap setting was positioned to within ± 0.0005 in., and the ratio of the nozzle exit static pressure to the nozzle chamber pressure was used to check experimentally the repeatability of the gap setting. The correlation between this pressure ratio and the gap setting was established during the calibration of the nozzles.

2.4 INSTRUMENTATION AND PRECISION

2.4.1 Orbiter and Booster Nozzle Plume Calibration

The model nozzles were calibrated at the VKF in the test section of Tunnel C (a 50-in. hypersonic tunnel) where a low ambient pressure could be maintained. The nozzle plume calibrations consisted of the following measurements: nozzle mass flow rate, plume flow field surveys with two 0.093-in. O.D. pitot probes and an unshielded 0.093-in. O.D. total temperature probe, nozzle chamber pressure, surface pressure at the nozzle exit, and finally, the Tunnel C test chamber pressure and temperature. The mass flow rate was obtained by using a standard ASME long radius venturi metering nozzle installed according to ASME specifications in the nozzle supply lines. The supply line pressure was recorded with a vacuum-referenced 2500-psid transducer calibrated full scale at 1500 psia. The differential pressure between the venturi throat tap and the supply line pressure was recorded with a 50-psid and a 200-psid transducer. Based on periodic comparisons with secondary standards, the precision of these transducers is estimated to be ± 0.2 percent based on the calibration range selected for the transducer. The jet gas temperature was recorded with a copper-constantan thermocouple located near the venturi mass-flow meter to an estimated precision of $\pm 2°F$. A summary of the estimated uncertainty of the mass flow results, assuming a Taylor series error propagation, is given in Table I.

TABLE I
UNCERTAINTY IN MASS FLOW MEASUREMENT PARAMETERS, PERCENT ($\pm$)

	p_o	T_o	$\dot{m}$	C_μ
Venturi Nozzle	0.33	0.36	0.55	---
Booster Nozzle	0.20	0.36	1.23	1.74
Orbiter Nozzle	0.20	0.36	9.39	9.41

The flow-field pitot pressure system used contained 500-, 100-, and 15- psid transducers, all referenced to a near vacuum of 15 to 25 μHg. The probe position was remotely controlled and digitized so that it was known to within ±0.001 in. in the coordinate normal to the plume axis and to within ±0.01 in. in displacement from the nozzle exit. The nozzle exit static pressure was recorded with a 50-psid transducer, and a 15-psid transducer calibrated full scale at 1 psid was used to record the test chamber pressure. The precision of these transducers is estimated to be ±0.2 percent of full scale of the range being used. The estimated uncertainty in the flow-field properties of the plume are summarized in Table II.

TABLE II
UNCERTAINTY OF PLUME FLOW-FIELD PROPERTIES

Probe Location	Nominal Ratio p_z/p_b	Percent (±) p_z/p_b	p_z/p_{o_j}	M
At Sting	300.0	1.2	0.6	0.6
At Plume Boundary	1.2	5.1	1.0	3.0

Near the stings, the Mach number calculations were based on p_z/p_{o_j} (normal shock Mach number), whereas, near the plume boundary where the local Mach number decays to zero, the Mach number was based on p_z/p_b (Rayleigh Mach number). For the uncertainties listed in Table II, the Taylor series propagation of individual uncertainties was used with the appropriate ideal gas Mach number relationships.

Single-plate, double-exposure holographic pictures were made of the plume flow field. These exposed holograms were later reconstructed to produce shadowgraphs, schlierens, conventional interferograms, and Hilbert transform pictures of the flow-field image. These photographs provide a simple method of defining the plume boundaries.

2.4.2 Model Surface Pressure Measurements

The Tunnel A stilling chamber conditions were recorded with a 150-psid transducer with an estimated uncertainty of ±0.2 percent of full scale of the calibrated range. For this test, these calibration ranges were 10, 50, and 150 psid. The tunnel total temperature was recorded with a copper-constantan thermocouple with an estimated uncertainty of ±1°F. By taking into account the repeatability and uniformity of the test section flow (M_∞ distribution) during tunnel calibrations,

the estimated uncertainty in the flow-field properties, using a Taylor series error propagation, is summarized in Table III.

TABLE III
UNCERTAINTY OF TUNNEL FLOW-FIELD PROPERTIES

Nominal Mach No.	$Re_\ell \times 10^6$	Percent ($\pm$)			
		M_∞	p_O	p_∞	Re_ℓ
2.0	2.3	0.5	0.27	1.58	0.57
3.0	2.2	0.4	0.88	1.83	1.05
5.0	1.5	0.3	0.45	1.76	0.87
5.0	8.6	0.3	0.20	1.77	0.77

The nozzle chamber pressures in the models were recorded with transducers calibrated full scale at 1500 psia. The estimated uncertainty of these pressure measurements was less than ± 3 psia. The nozzle exit pressure was measured with a 15-psid transducer having a variable reference pressure. This reference pressure was varied from a near vacuum (15 to 25 μHg) to atmospheric pressure, depending on the magnitude of the nozzle exit pressure.

Three Scanivalves, each with a 25-psia (absolute) transducer, were used to record the model surface pressures. In general, the precision of measurement of these transducers, based on VKF calibrations, was not expected to be any better than ± 0.3 percent of the full-scale range of the transducer; that is, no better than ± 0.07 psia (this is better than quoted by the manufacturer). Actually, the calibration of the transducer located in the orbiter appeared to be considerably better than this and better than the two transducers located in the booster.

This conclusion is based on the fact that the orbiter test data obtained at the maximum and minimum test Reynolds number (i.e., at 8.6×10^6 and 1.5×10^6) were in fairly good agreement (also indicating that the Reynolds number effects were negligible). In the case of the booster, this change in Reynolds number caused a change in the level of the pressure ratio distributions, although the change was within the quoted precision, the pressures recorded by the two transducers in the booster were consistently higher than the pressure sensed by the transducer in the orbiter when both models were exposed to the same subatmospheric pressure in the tunnel without tunnel flow.

If it is assumed that the orbiter transducer is more reliable, it is suggested that the booster pressure ratios should be adjusted as shown in Fig. 4. Note that, although these corrections are within the quoted
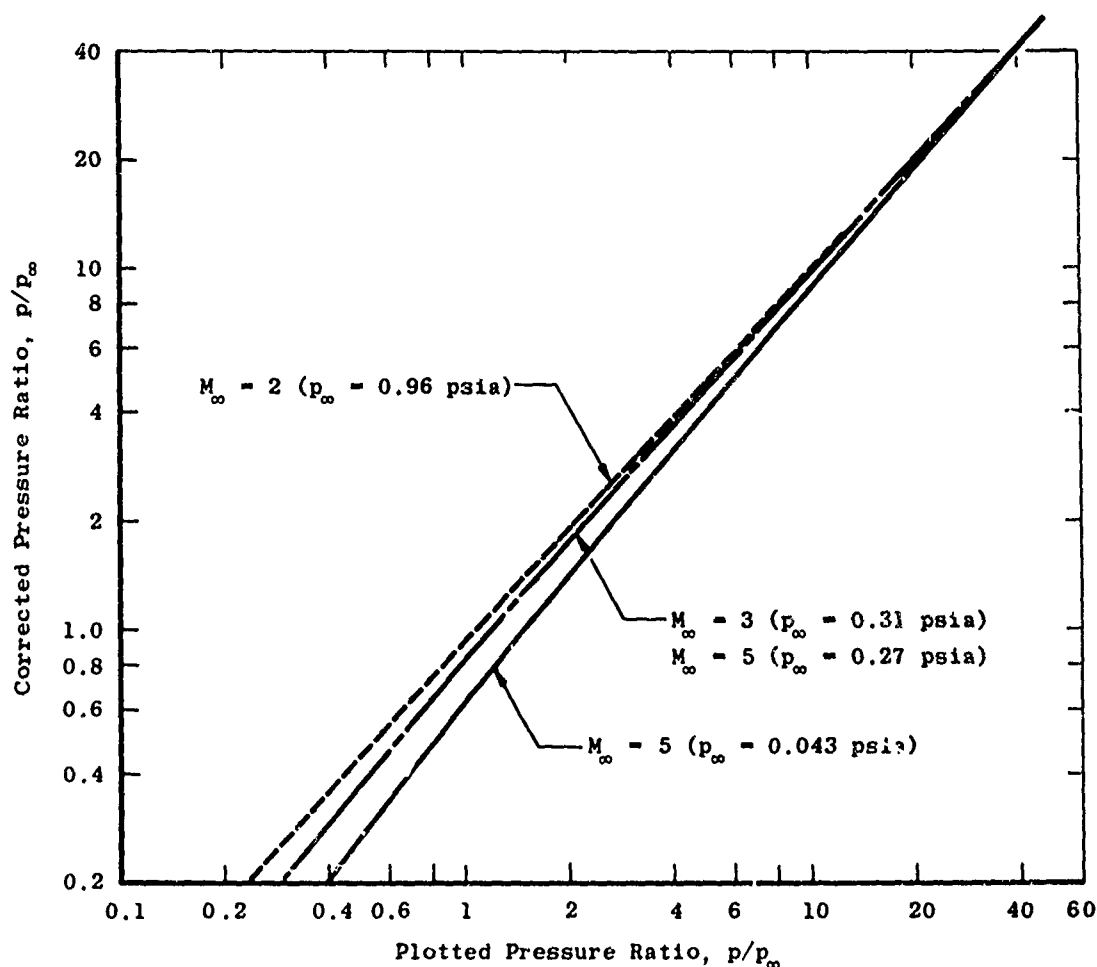
11

Fig. 4 The Estimated Correct Booster Pressure Ratios versus the Plotted Ratios in the Figures of Appendix II

uncertainty of the transducers, this adjustment in the booster pressure ratios makes the booster data slightly more consistent with the orbiter data. In this report, the figures in Appendix II are plotted in terms of the originally computed pressure ratios, but the booster pressure ratio data in the text of the report have been adjusted by the factors given in Fig. 4.

Based on the transducer precision determined by calibration, the estimated maximum uncertainty in the basic data is as follows:

Uncertainty in Pressure Ratio

M_∞	p_∞, psia	p/p_∞
2.0	0.96	±0.07
3.0	0.31	±0.22
5.0	0.27	±0.26
5.0	0.04	±1.60

Relative to the booster model, the orbiter model could be automatically driven from one position to the next in the horizontal and vertical directions with a repeatability of within ±0.006 in. of a desired location. Although attempts were made to attach strain gages to the orbiter and booster stings to monitor sting deflections due to aerodynamic loading, the installation of the high-pressure flexible gas supply line adversely influenced the strain-gage outputs. Therefore, the uncertainty in the vertical position of the orbiter was considerably larger than the uncertainty associated with its horizontal position. The vertical displacement factor ($\Delta z/L$) is therefore rounded off to the nearest hundredth, while the horizontal displacement factor ($\Delta x/L$) is rounded off to the nearest thousandth. The sector angle-of-attack repeatability is ±0.1 deg.

SECTION III
PROCEDURE

3.1 TEST PROCEDURE

The sector angle of attack, the vertical and horizontal travel of the orbiter relative to the booster, the operation of the model Scanivalves, and the recording of the model pressure transducers were all programmed electronically for automatic operation. Once the data taking sequence was initiated, the data were recorded in the following prescribed manner. At each angle of attack, all three Scanivalves, each containing 48 pressure ports, were simultaneously actuated, and the pressures were automatically recorded. Once the Scanivalves had completed scanning all 48 pressure ports, which took less than 30 sec, a signal from the Scanivalves was used to actuate the sector to move to the next angle-of-attack position. After the sector reached the next preselected position, the Scanivalves were again automatically actuated. This operation was continued until all preselected angle-of-attack positions were obtained. At this point, the orbiter support system was programmed to move automatically to the next preselected axial station. This sequence of operation continued until all angle-of-attack and orbiter axial stations were satisfied, and then the orbiter was programmed to move automatically in the vertical direction to the next preselected Δz location. At the new vertical position, all the axial and sector angle-of-attack positions were repeated with the pressures being recorded from all three Scanivalves at each new model position. The automatic sequence of operation continued until all preselected sector angles of attack were satisfied at all preselected orbiter axial and vertical positions.

13

A schematic of the control system used to record the data for this test matrix is shown in Fig. 5. As indicated in the figure, a "system control unit" coordinated the operation of the "scanner control," which was used to record the data, and the control panels were used to operate the mechanisms which pitched the models and moved the orbiter relative to the booster.
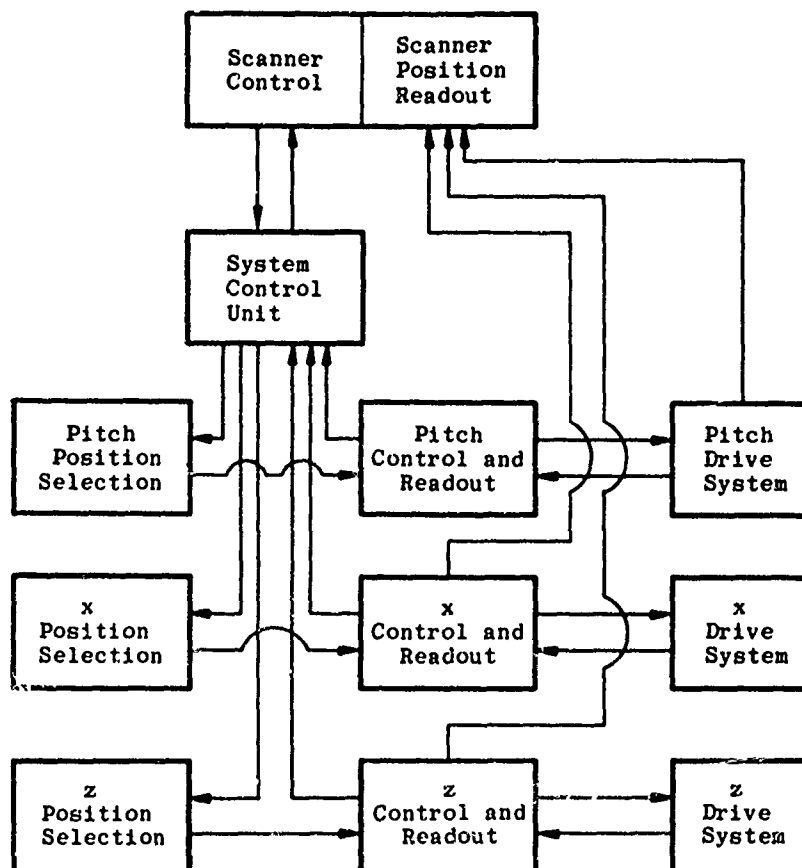

Fig. 5 The Automatic Data Recording and Model Positioning Control System

As the models moved automatically through the test matrix, holograms were made at selected points in the test matrix. By using a reference hologram of the tunnel flow with the model removed, these test holograms were used to reconstruct double-exposure, double-plate interferograms of the flow field. Most of the reconstructions were made with the models at zero angle of attack, and a few pictures were made at ±10 deg angle of attack.

3.2 NUMERICAL INTEGRATIONS

The primary purpose of the test program was to evaluate the pressure loading existing on the adjacent surfaces of the orbiter and booster configurations during the abort staging maneuvers. An attempt was

14

also made to integrate these limited pressure distributions and examine the distributions of the local normal force coefficients along the wings and body axes of the booster and orbiter. In addition, the net change in normal force and pitching moment coefficients produced by the interfering flow fields of the two bodies was evaluated from the pressure data and compared with the corresponding changes noted in the force measurements of Ref. 1.

The following numerical techniques were adopted and programmed to integrate the pressure distributions. In some cases, a pressure in a distribution was missing or known to be incorrect along a particular array of pressure taps involved in a particular line integral. A simple three-point Lagrange interpolation formula was used to estimate these missing pressures in a distribution. A three-point unequally spaced numerical integration subroutine was used to evaluate the integrals. This numerical scheme is based on an expression formulated from a Lagrange curve fit of three unequally spaced points. The integration is evaluated from the first point to the intermediate point of the group of three points. A next group of three points is selected, starting with the intermediate point and using the next two points, and the integration scheme is reapplied. This process is completed over the whole interval of the integration, and the last three points are simply evaluated over the entire three-point interval. This numerical scheme is outlined below:

$$\int_{y_o}^{y_{n+1}} x(dy) = \sum_{m=0}^{m=n} \int_{y_m}^{y_{m+1}} x(dy) \tag{1}$$

and

$$\int_{y_n}^{y_{n+1}} x(dy) = \frac{H_1}{6}\left[\left(\frac{2H_1 + 3H_2}{H}\right) x_n + \left(\frac{H_1 + 3H_2}{H_2}\right) x_{n+1} - \left(\frac{H_1^2}{H(H_2)}\right)x_{n+2}\right] \tag{2}$$

where

$$H = y_{n+2} - y_n$$
$$H_1 = y_{n+1} - y_n$$
$$H_2 = H - H_1 = y_{n+2} - y_{n+1}$$

3.2.1 Orbiter Integrations

At each pressure tap station along the centerline of the lower surface of the orbiter body, an integration of the pressure distributions

15

was made normal to the body axis in the spanwise direction; that is

$$c_{N_x} = \frac{1}{s} \int_0^{y_{L.E.}} C_p(dy) \tag{3}$$

where c_{N_x} is the local normal force coefficient per inch and $y_{L.E.}$ is the local span of the orbiter at any given model station. The pressure coefficient associated with the leading edge of the orbiter (i.e., at $y = y_{L.E.}$) was estimated as follows:

$$C_{p(y=y_{L.E.})} = C_{p_N} \cos^2 \theta_{L.E.} \tag{4}$$

where C_{p_N} is the pressure coefficient based on the measured orbiter nose tap pressure and $\theta_{L.E.}$ is the local sweep angle of the orbiter leading edge.

The normal force and pitching moment coefficients associated with the pressure distribution on the lower surface of the orbiter were then defined as follows:

$$C_{N_x} = 2\ell \int_0^1 c_{N_x}(d(x/\ell)) \tag{5}$$

where ℓ is the overall length of the orbiter, and

$$C_{m_x} = -2\ell \int_0^1 c_{N_x}[(x-4.92)/\ell]\, d(x/\ell) \tag{6}$$

A check on the uniqueness of these normal force and pitching moment coefficients was made by reversing the order of the numerical integration. At each of the six spanwise locations containing an array of pressure taps, the distributions were integrated in the axial direction:

$$c_{N_y} = \frac{1}{s} \int_{x_{L.E.}}^{x_{T.E.}} C_p(dx) \tag{7}$$

where $x_{L.E.}$ and $X_{T.E.}$ represent, respectively, the orbiter leading edge and trailing edge locations relative to the orbiter nose. This coefficient (c_{N_y}), when plotted as a function of the span coordinate (y), would represent the spanwise distribution of the local normal force

coefficient. The resultant normal force and pitching moment coefficients are defined by the following expressions:

$$C_{N_y} = 2b \int_0^1 c_{N_y} (d(y/b))$$ (8)

where b is the semi-span of the orbiter trailing edge wing surface.

$$C_{m_y} = 2b \int_0^1 c_{m_y} (d(y/b))$$ (9)

where

$$c_{m_y} = -\frac{1}{s} \int_{x_{L.E.}}^{x_{T.E.}} C_p [(x - 4.92)/\ell] \, dx$$

Theoretically, the coefficients C_{N_x} and C_{N_y} and similarly C_{m_x} and C_{m_y} should be equal. Actually, the difference in the normal force coefficients (C_{N_x}, C_{N_y}) was, in most cases, less than 0.01, as compared with an overall variation in this coefficient C_{N_x} of 0 to 0.8. The difference in the pitching moment coefficients (C_{m_x}, C_{m_y}) was about 0.005, as compared with an overall variation from -0.67 to 0.02.

3.2.2 Booster Integrations

The booster normal force and pitching moment coefficients were obtained by integrating separately the pressure distributions on the booster body, canard, and wing surfaces and then summing these results. All body and wing leading edge surfaces were evaluated in the same manner as adopted for the orbiter. In fact, the C_{p_N} value used for the booster was set equal to the value used for the orbiter, since the booster did not have a true nose pressure tap. The normal force and pitching moment coefficients associated with the booster body were evaluated as follows:

$$c_{N_x} = -\frac{1}{s} \int_0^{y_{L.E.}} C_p (dy)$$ (10)

$$C_{N_x} = 2\ell \int_0^{1.0} c_{N_x} (d(x/\ell))$$ (11)

17

$$C_{m_x} = -2\ell \int_0^{1.0} c_{N_x} \left[(x - 7.53)/\ell\right] d(x/\ell) \qquad (12)$$

The wing loading was obtained by integrating first in the axial direction at each of the five wing span stations and then integrating in the spanwise direction.

$$c_{N_y} = -\frac{1}{s} \int_{x_{L.E.}}^{x_{T.E.}} C_p(dx) \qquad (13)$$

$$c_{m_y} = -\frac{1}{s} \int_{x_{L.E.}}^{x_{T.E.}} C_p \left[(x - 7.53)/\ell\right] dx \qquad (14)$$

The spanwise integration covered the interval from the junction of the wing plan form and the booster body to the junction of the wing tip with the vertical tail section (see Fig. 1a).

$$C_{N_y} = 2 \int_{1.195}^{4.780} c_{N_y}(dy) \qquad (15)$$

$$C_{m_y} = 2 \int_{1.195}^{4.780} c_{m_y}(dy) \qquad (16)$$

A simple trapezoid approximation was used to estimate the loading on the canards, since the canard contained only four pressure taps. The resultant normal force and pitching moment coefficients on the upper surface of the booster were obtained by simply summing these results; namely,

$$C_N = C_{N_x}(\text{Body}) + C_N(\text{Canard}) + C_{N_y}(\text{Wing}) \qquad (17)$$

$$C_m = C_{m_x}(\text{Body}) + C_m(\text{Canard}) + C_{m_y}(\text{Wing}) \qquad (18)$$

Since these coefficients (C_N or C_m) only represent the loading on either the upper or lower surface of a body, these values cannot be compared directly with the force measurements. However, the incremental change in these coefficients between the interference-free results and the results obtained when the interference exists may be compared with

18

the corresponding change in the force measurements. Therefore, the following delta coefficients were also defined for use in this report:

$$\Delta C_N = C_N \text{ (Interference)} - C_N \text{ (Interference Free)} \qquad (19)$$

$$\Delta C_m = C_m \text{ (Interference)} - C_m \text{ (Interference Free)} \qquad (20)$$

3.3 TEST CONDITIONS

3.3.1 Plume Calibration

The variables in the plume calibration involved the nozzle gap setting which varied the nozzle area ratio, the nozzle chamber pressure, and the test cell pressure. The overall variation in the test parameters for this calibration is listed in Table IV.

TABLE IV
NOZZLE CALIBRATION

	E_p, in.	Nominal A/A^*	Nominal p_{o_j}/p_b	Survey Rake Location[1], in.
Booster	0.389	3.5	1400 to 1780	1.53, 2.24, and 3.06
	0.411	3.8	1390 to 1660	1.53 and 2.24
	0.426	4.1	760 to 2000	1.52, 2.28, and 3.03
	0.452	4.7	1390 to 1730	0.71 and 1.52
	0.504	6.5	1540 to 1730	0.71 and 1.52
	0.542	9.3	1560 to 1730	0.71, 1.72, and 2.28
	0.592	15.7	1430 to 5200	0.71
Orbiter	0.478	15	1590 to 4600	0.47 and 0.94
	0.495	20	1590 to 4600	0.47
	0.512	28	1590 to 4760	0.47 and 0.94
	0.545	63	1590 to 4600	---

[1]This location refers to the distance downstream of the nozzle exit plane. All plume flow-field surveys were made at a nominal pressure ratio (p_{o_j}/p_b) of about 1600 to 1780.

The nozzle area ratios were based on the nozzle exit area and the measured mass flow rate. The mass flow rate measurement was used to define a nozzle throat discharge coefficient which, in turn, could be used to define an effective nozzle area ratio listed in Table IV.

19

3.3.2 Model Test Program

A summary of the test conditions is given in Table V. At Mach number 5, one sequence of data not listed in the table was obtained without power simulation to evaluate the effects of the booster canard and the boundary layer trips on the booster and orbiter pressure distributions. The effects of the boundary layer trips were found to be negligible or fell within the repeatability of the pressure data. The test results obtained in the absence of an external stream ($M_\infty = 0$) were used to evaluate the orbiter plume impingement loading on the booster, and these results were obtained with the tunnel test section pressure at 0.48 psia and also at 0.86 psia, as shown in the table.

TABLE V
TEST SUMMARY

M_∞	$Re\ell \times 10^6$	T_o, °R	p_o, psia	p_∞, psia	ι, deg	Range of Variable			Plume Power Simulation, percent	
						α, deg	$\Delta x/L$	$\Delta z/L$	Booster	Orbiter
2.00	2.4	580	7.5	0.96	0	±10	-0.39 to 0.52	0.12 to 0.91	0	0
					0		-0.39 to 0.52	0.12 to 0.91	50	100
					5		-0.14 to 0.23	0.15 to 0.23	0	0
					5		-0.14 to 0.23	0.15 to 0.23	50	100
					0		0.04 to 0.17	Launch	0	0
							0.04 to 0.17	Launch	100	0
							-0.18	Launch	100	100
3.00	2.2		11.4	0.31			-0.39 to 0.51	0.12 to 0.91	0	0
3.00	2.2		11.4	0.31			-0.39 to 0.51	0.12 to 0.91	50	100
3.00	2.2		11.1	0.31			0.04 to 0.17	Launch	0	0
4.97	1.5	590	22.1	0.043			-0.39 to 0.52	0.11 to 0.91	0	0
							-0.39 to 0.52	0.11 to 0.91	50	100
					5	±5	-0.14 to 0.23	0.15 to 0.23	0	0
					5	±10	-0.14 to 0.23	0.15 to 0.23	50	100
					0	±10	-0.18 to 0.17	Launch	0	0
					0	±10	-0.18 to 0.17	Launch	100	100
5.04	8.6	640	149	0.27	0	0	-0.14 to 0.52	0.12 to 0.91	0	100
0	No Tunnel Flow			{0.48 and 0.86}	5	0	-0.14 to 0.35	0.15 to 0.23	0	100

The test matrix which covers all the positions of the orbiter relative to the booster are shown schematically in Fig. 6. At the maximum $\Delta z/L$ value of 0.91, the orbiter bow wave missed the booster with the orbiter located over the booster base; that is, the booster pressure distributions are interference free. Similarly, the forward orbiter position produced orbiter pressure distributions which are not influenced by the booster bow wave. Most of the interference data was obtained in a matrix area lying between $\Delta z/L$ values of 0.11 and 0.23 and $\Delta x/L$ values of -0.39 to 0.35.
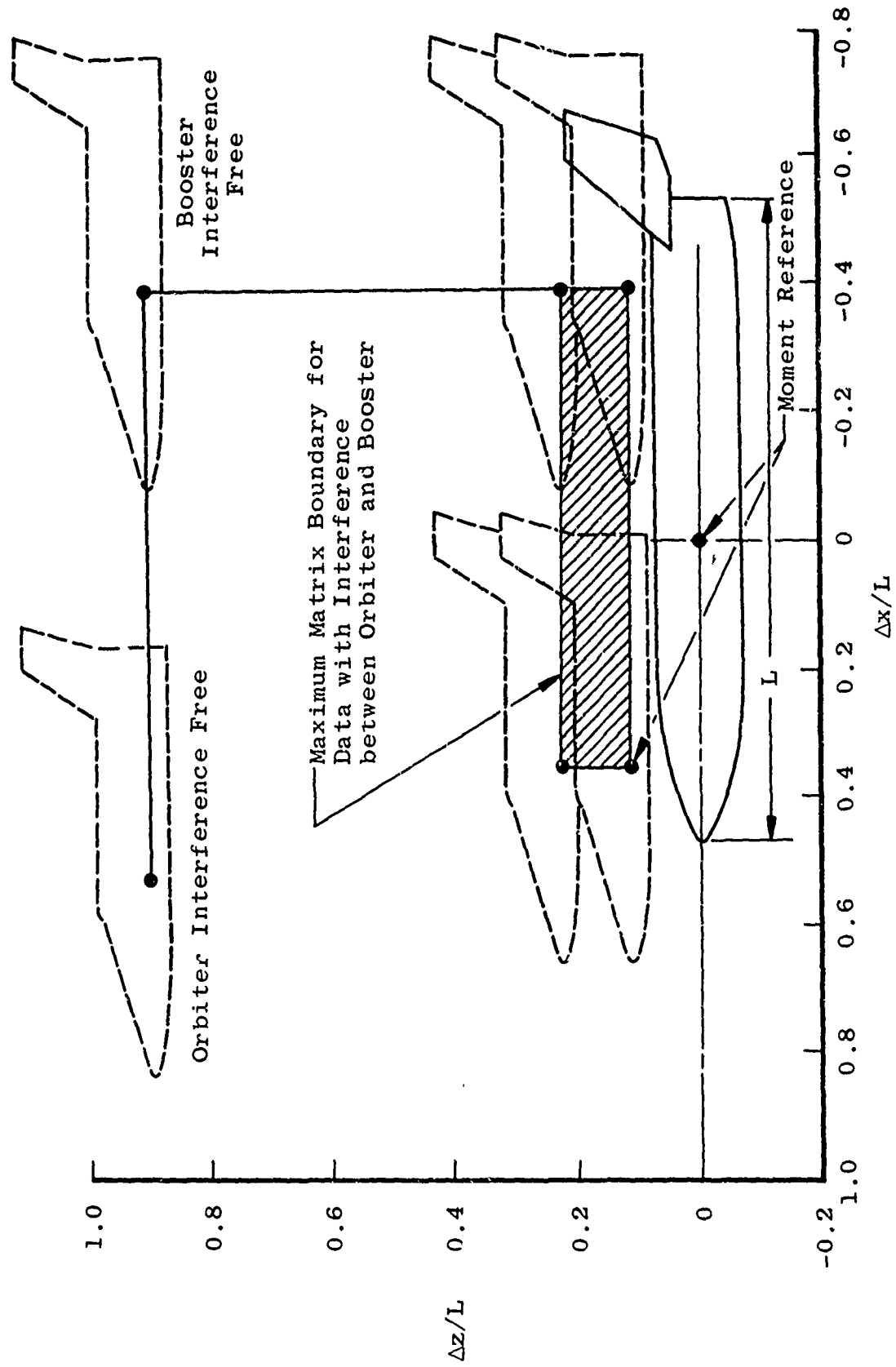
Fig. 6 The Test Program Matrix of the Relative Positions of the Orbiter to the Booster

The variations in the launch positions are shown in Fig. 7. Originally, the orbiter was supposed to be located on the forward section of the booster, but some consideration is also being given to the possibility of a dual burning base launch position where $\Delta x/L \approx -0.180$. At nominal Mach numbers 2 and 5, pressure distributions were obtained with the orbiter located in the dual base burning position.
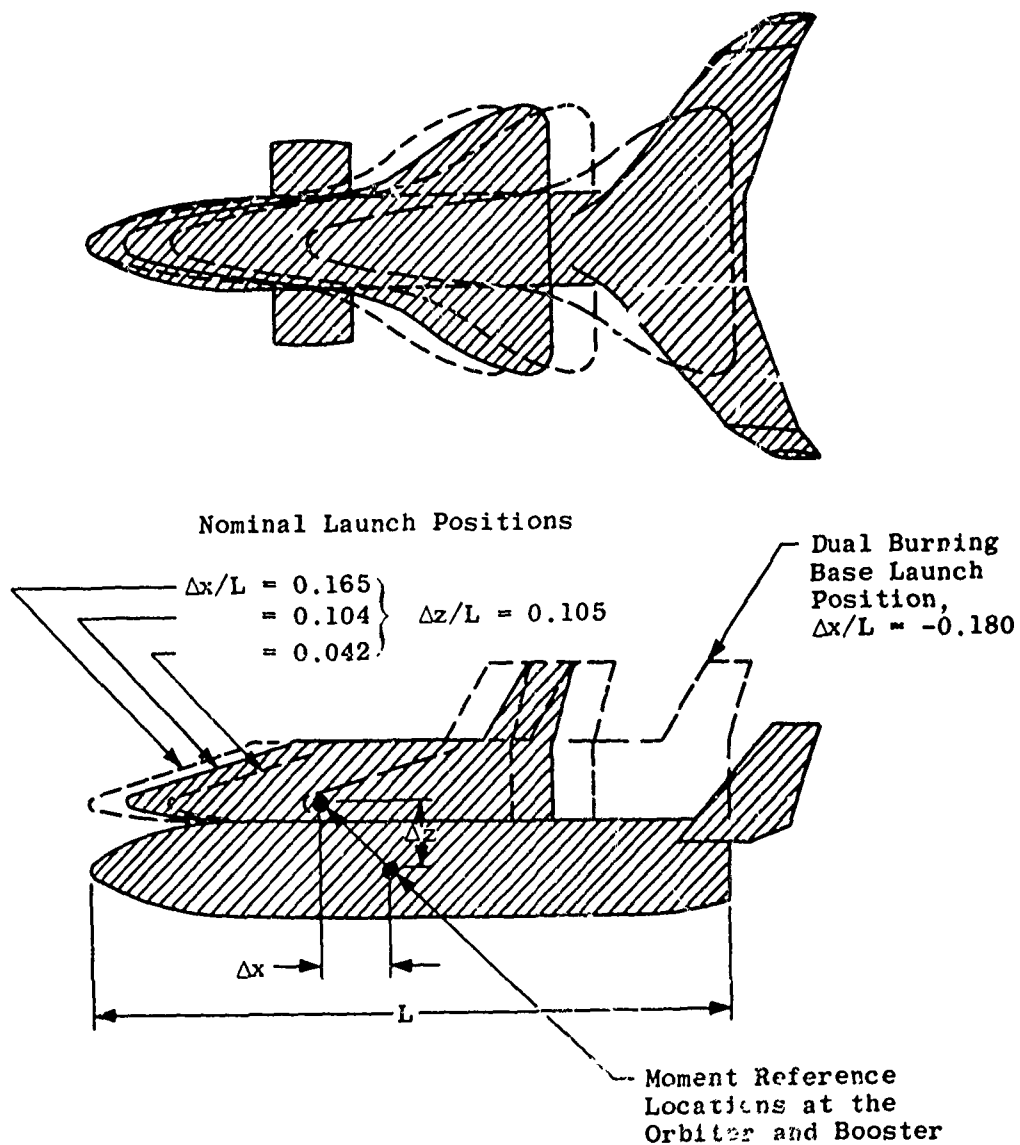
Fig. 7 The Variations in the Launch Positions

The plume power simulation was produced with the following booster and orbiter nozzle settings listed in Table VI. The basis for this plume power simulation is described in Refs. 2 and 3.

TABLE VI
PLUME POWER SIMULATION

a. Booster

M_∞ Nominal	Altitude, km	p_∞, psia	Percent of Power Simulation	Gap Setting, E_p, in.	p_{o_j}, psia
2.0	18.4	0.96	50	0.560	748
2.0	18.4	0.96	100	0.522	1200
3.0	28.5	0.31	50	0.519	694
5.0	46.4	0.043	50	0.491	648
5.0	46.4	0.043	100	0.473	1200

b. Orbiter

M_∞ Nominal	Altitude, km	p_∞, psia	Percent of Power Simulation	Gap Setting, E_p, in.	p_{o_j}, psia
2.0	18.4	0.9	100	0.502	1200
3.0	28.5	0.3	100	0.490	1200
5.0	46.4	0.043	100	0.471	1200

SECTION IV
RESULTS AND DISCUSSION

4.1 NOZZLE CALIBRATION RESULTS

The booster nozzle sting and later the orbiter nozzle sting were each mounted to the Tunnel C sector and injected into the 50-in.-diam test section where an ambient ($M_\infty = 0$) pressure of about 0.30 psia was maintained for nozzle plume calibration. During the calibration, most of the test results were obtained at a ratio of nozzle chamber pressure to test section pressure (p_{o_j}/p_b) of 1600 to 1700; some additional data were obtained at ratios up to 5200. The purpose of the calibration was to establish the sting nozzle operating conditions and the plume size generated in a quiescent environment. The assumption was made that if the nozzles generated a plume which properly simulated the full-scale

plume size in a quiescent environment, then the simulation would also hold in the presence of an external stream.

4.1.1 Booster Nozzle

Interferograms similar to the ones shown in Fig. 8 were used to evaluate the size and initial turning angle of the plume generated by the booster nozzle. These are single-plate, double-exposure holographic interferograms of the flow field. The figure also contains a Hilbert transform (Fig. 8b) of the holographic image which, in many respects, is similar to the interferogram in Fig. 8a. The Hilbert transform of the holograph represents changes in the density gradient through the flow field, whereas the conventional interferogram represents simple changes in the flow-field density. Both pictures clearly locate a nozzle shock generated by the booster nozzle at this particular gap setting. The presence of the internal shock located just inside the plume boundary causes a shift or blip in the interferogram fringes, as shown in Fig. 8a. Decreasing the gap setting (E_p) enlarged the nozzle throat area; that is, decreased the nozzle area ratio which caused the plume size and initial turning angle to increase as indicated by comparing Figs. 8a and c. Also, the internal nozzle shock disappeared as the nozzle area ratio decreased (Fig. 8c).
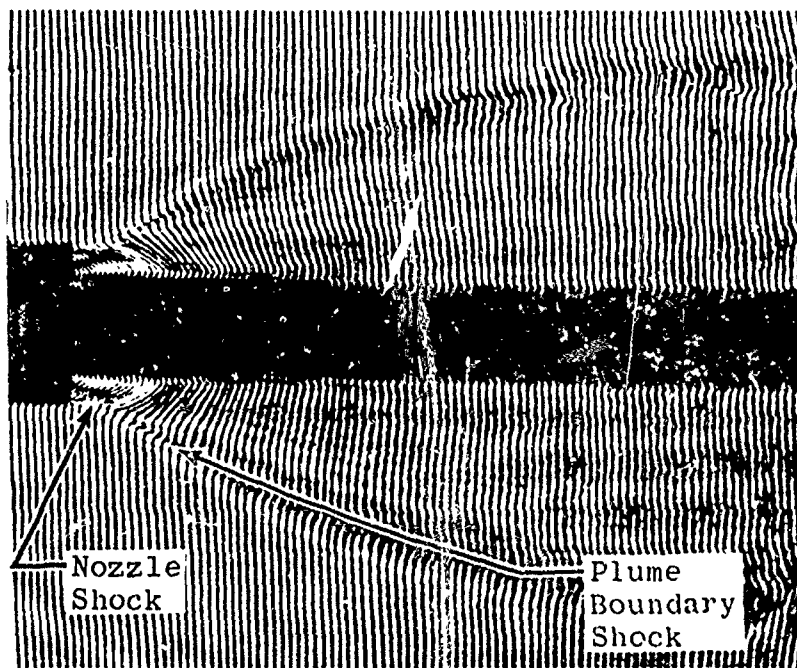
a. Interferogram, Nozzle Gap Setting 0.542 in., p_{o_j}/p_b = 1700

Fig. 8 Plume Generated by the Booster Model Nozzle in a
Quiescent Environment ($p_b \simeq$ 0.27 psia)

24
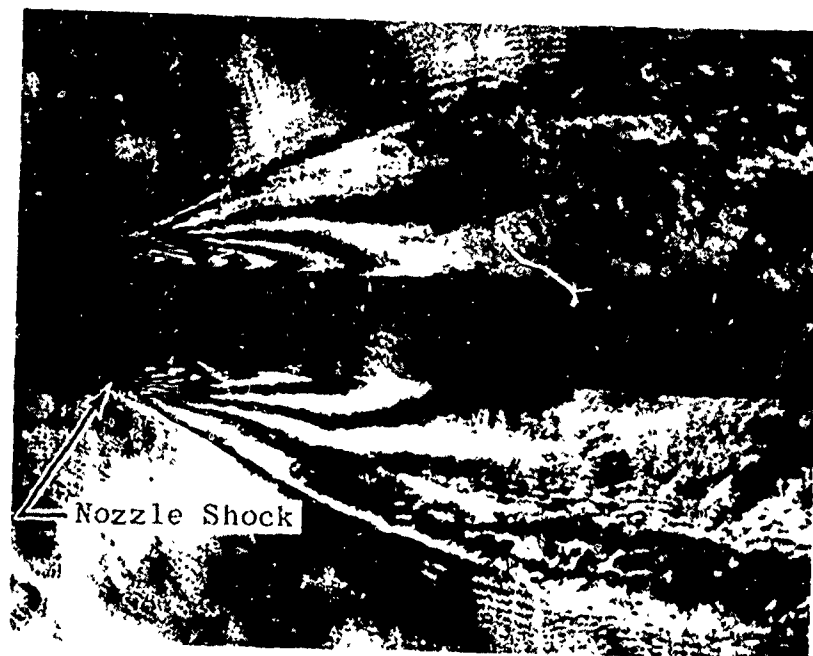
b. Hilbert Transform, Nozzle Gap Setting 0.542 in.,
$p_{o_j}/p_b = 1700$
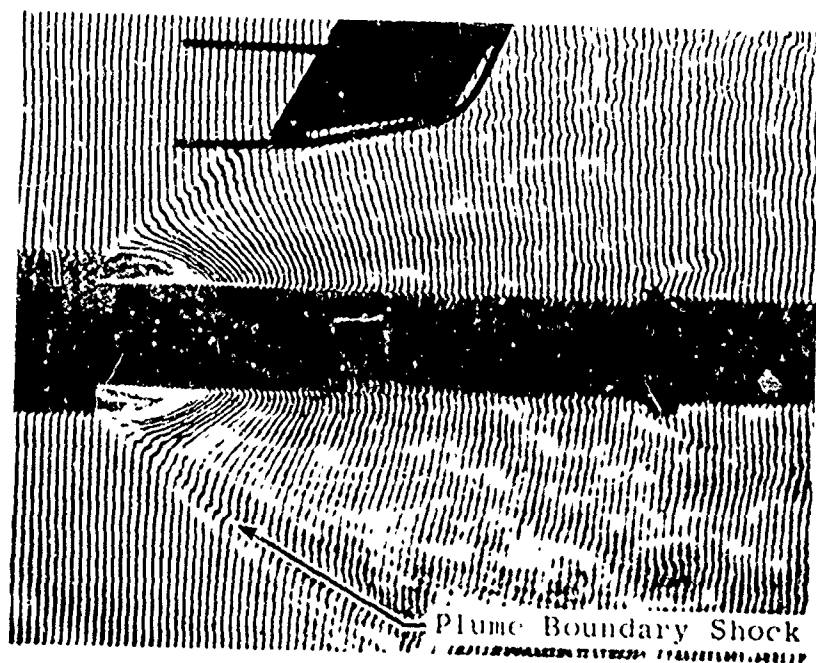
c. Interferogram, Nozzle Gap Setting 0.452 in.,
$p_{o_j}/p_b = 1780$

Fig. 8 Concluded

The computed mass flow through the nozzle was compared with the actual mass flow to determine the effective nozzle throat area. A comparison of the nozzle area ratio based on this effective throat area with the geometric nozzle area ratio (the theoretical value) is given in Fig. 9a. In general at a given gap setting, these results indicate that the actual or effective nozzle throat area (A^*) was significantly larger than the designed geometric nozzle throat area. This difference in nozzle area ratio for the worse case corresponds to 0.0017-in. error in nozzle throat gap or a shift in nozzle coordinates; that is, in the axial position of the inner sting nozzle contour relative to the outer nozzle sleeve contour of 0.050 in., or some combination of these two effects. When the complexity of the fabrication problem and the machining tolerances are considered, this calibration result was quite reasonable.

The initial turning angle computed on the basis of the experimentally defined nozzle area ratio and the ratio of the nozzle chamber pressure to the pressure in the test chamber compares favorably with the turning angle measurements obtained from the interferogram pictures as indicated in Fig. 9b. A simple isentropic perfect gas two-dimensional analysis was used in computing this turning angle. This two-dimensional analysis also provided an estimate of the nozzle exit to chamber pressure ratio which agreed reasonably well with the measured pressure ratio, as indicated in Fig. 9c. The measured nozzle exit to chamber pressure ratio was subsequently used to verify that the nozzle gap size was properly set during the test program.

Pitot pressure flow-field surveys were made at various stations aft of the nozzle exit to check the nature of the internal gas dynamic properties of the plume. An example of the results obtained from these surveys is shown in Appendix I, Fig. I-1, for two nozzle gap settings which correspond to the interferogram pictures shown in Fig. 8. The measured pitot pressure was normalized by the quiescent pressure existing in the test chamber and, therefore, as the probe approached the outer boundary of the plume, this ratio should approach unity as suggested in Figs. I-1a and c. The profiles are displaced along the x-axis of the plot to reflect the actual position of the flow-field survey relative to the nozzle exit plane. The x and y coordinates of the survey were normalized by the nozzle sting diameter, d_c (the nozzle centerbody diameter).

An estimate of the plume boundary location and shape and the location of the internal plume boundary shock are superimposed on these pitot pressure plume flow-field distributions.
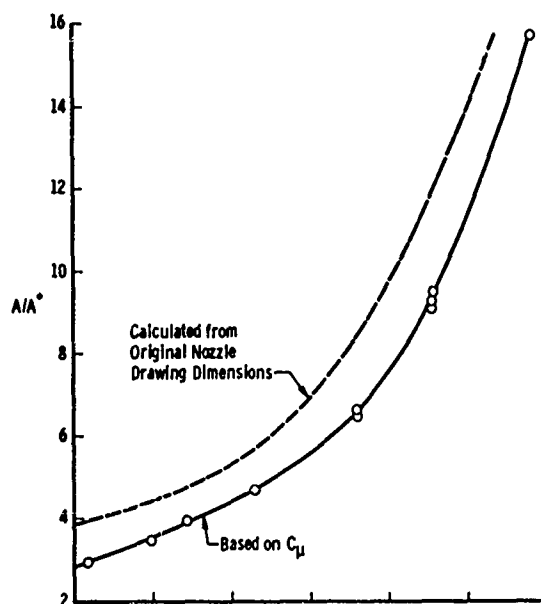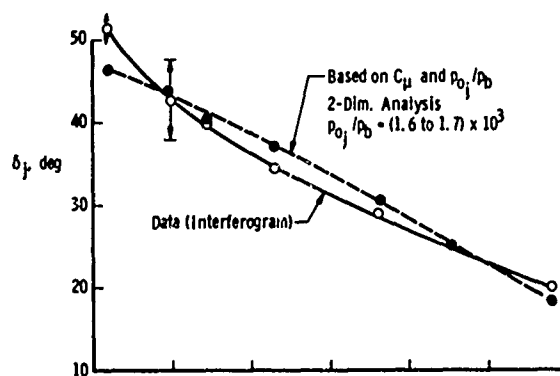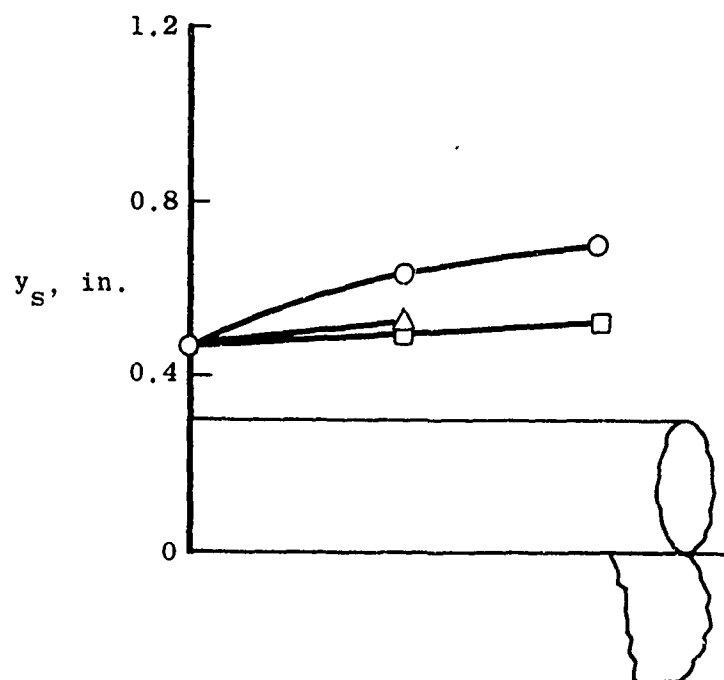
26

a. Nozzle Area Ratio

b. Initial Plume Boundary Turning Angle at the Nozzle Exit
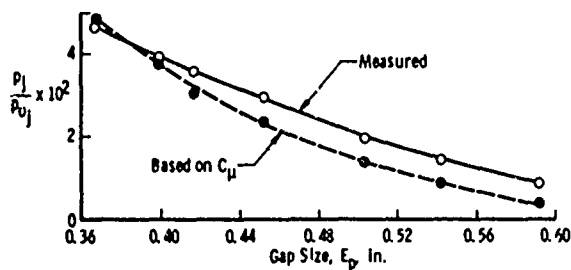
c. Nozzle Exit Static Pressure Ratio

Fig. 9 Booster Nozzle Plume Calibration Results

As indicated in Figs. I-1a and c, the internal plume shock produces a discontinuity in the pitot pressure distribution near the plume boundary. The abrupt reduction in the pitot pressure near the nozzle sting ($y/d_c \rightarrow 0.5$) reflects the presence of the boundary layer growth along the sting.

An estimate of the Mach number distribution through the plume flow field is given in Figs. I-1b and d. Between the internal plume boundary shock and the maximum pitot pressure measurement obtained above the nozzle sting, the Mach number is based on a ratio of the measured pitot pressure to the nozzle chamber pressure. The assumption is made that the total pressure of the plume flow field is equal to the nozzle chamber pressure (p_{o_j}). Above or beyond the internal plume boundary shock, the Mach number is based on a ratio of the pressure in the test section (p_b) to the local pitot pressure measurement (Rayleigh pitot pressure relationship). Within the boundary layer on the nozzle sting, the static pressure is assumed to be constant and equal to the static pressure existing where the measured pitot pressure reaches a maximum value. The ratio of the maximum pitot pressure to the nozzle chamber pressure defines not only the local stream Mach number, but also the local static pressure which is assumed to remain constant through the boundary layer. This procedure for experimentally estimating the local Mach number distribution through the plume flow field could be compromised by the presence of sting nozzle shocks which would significantly reduce the total pressure associated with the expanding plume flow field.

The effect of the gap setting (that is, the nozzle area ratio) on the location of the internal plume boundary shock and the Mach number distribution over the nozzle sting are summarized in Fig. 10. Increasing the nozzle gap setting (i.e., increasing the nozzle area ratio) reduced the plume size and shifted the internal plume boundary shock toward the sting. This variation in gap setting increased the Mach number along the sting in the immediate vicinity of the nozzle exit (i.e., for x values less than 3 in.). The shaded symbols in Fig. 10b denote the Mach number based on the local static pressure measurement made near the nozzle exit and the nozzle chamber total pressure.

4.1.2 Orbiter Nozzle

All the interferograms of the orbiter nozzle indicate that a nozzle shock exists in the plume flow field, as shown in Fig. 11. The presence of this nozzle shock indicates that the nozzle was not properly shaped to cancel the formation of these compression waves formed within the nozzle. These two interferograms also show the location of the pressure probe and the thermocouple used to monitor the quiescent conditions existing in the test chamber. Although not shown, a similar set of measurements was made during the booster nozzle calibration.

28

a. Internal Plume Boundary Shock Location

Sym	Gap Setting, in.	
○	0.366	Pitot Probe Survey
△	0.399	
□	0.417	
◇	0.452	
◁	0.504	
◁	0.542	

Solid Symbol: Static Tap
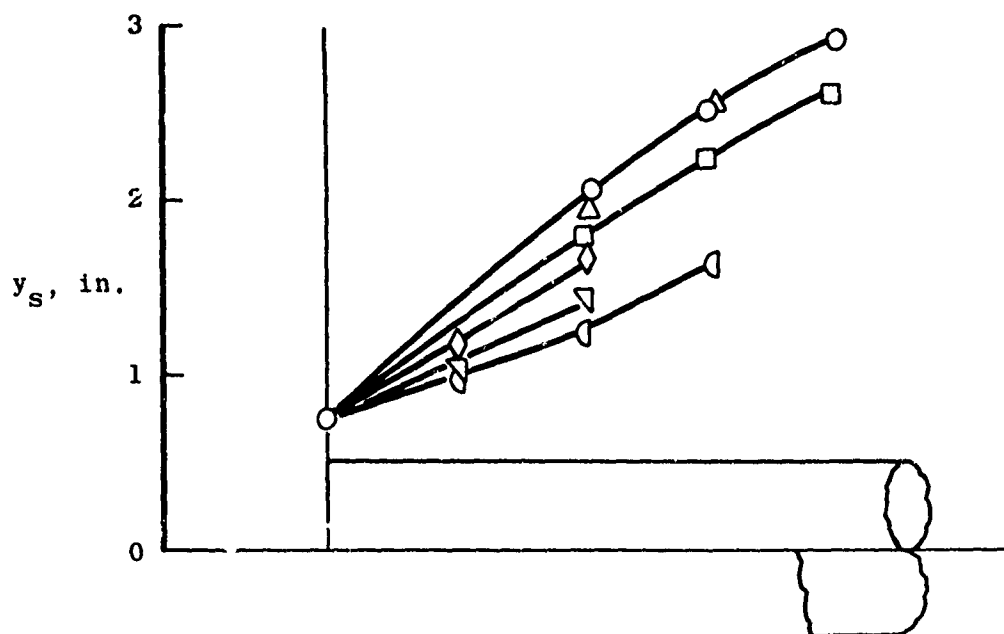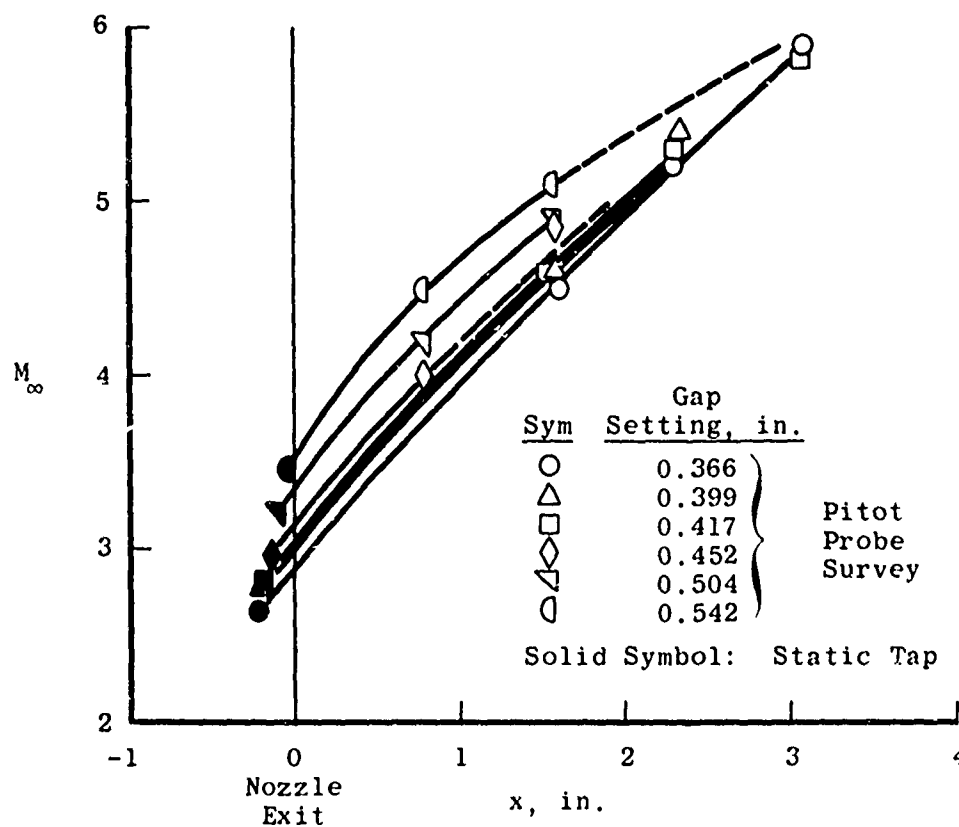
b. Mach Number Distribution

Fig. 10 Internal Plume Boundary Shock Location and the Mach Number Distribution along the Booster Sting
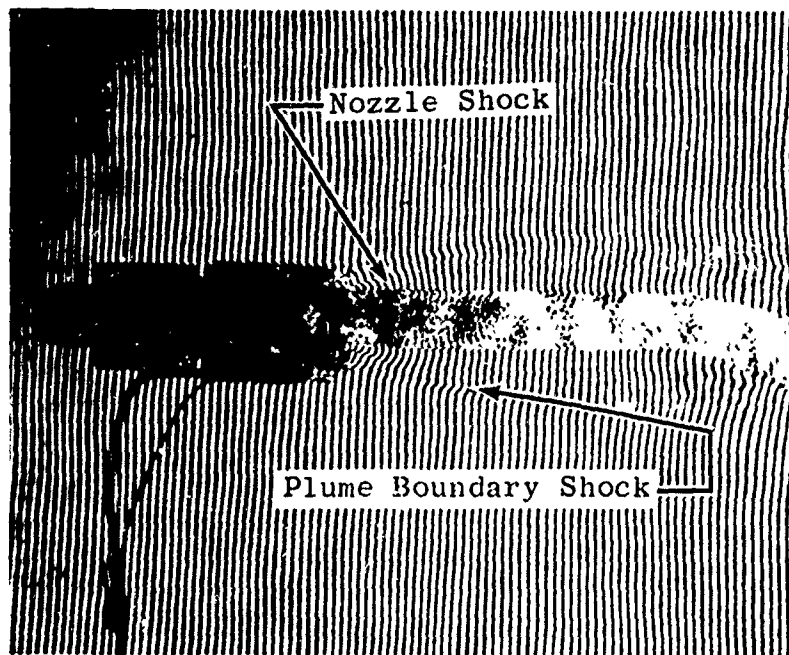
a. Interferogram, Nozzle Gap Setting 0.512 in.,
$p_{o_j}/p_\infty = 1600$
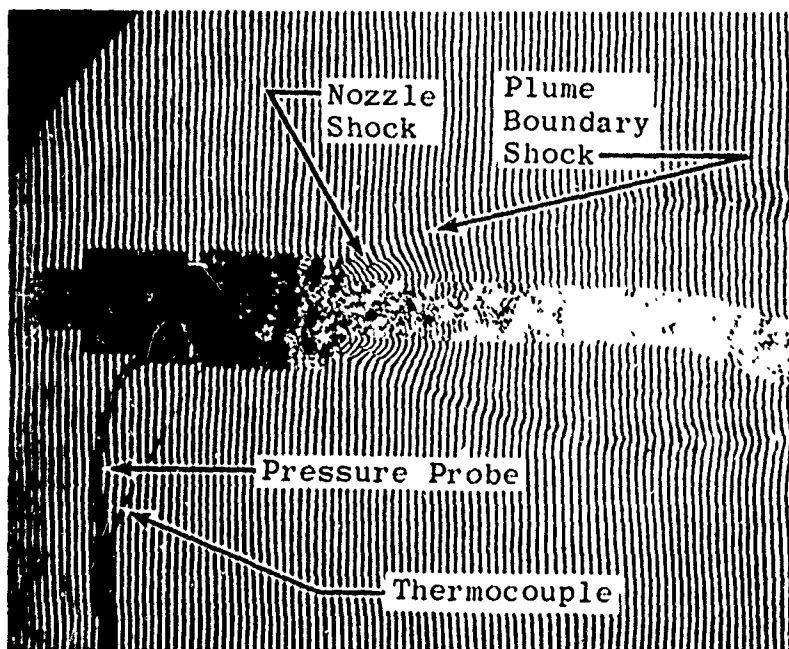
b. Interferogram, Nozzle Gap Setting 0.478 in.,
$p_{o_j}/p_\infty = 1620$

Fig. 11 Plume Generated by the Orbiter Model Nozzle in a
Quiescent Environment ($p_b \simeq 0.26$ psia)

30

In comparison with the booster nozzle, the agreement between the orbiter nozzle area ratio based on the measured discharge coefficient and the computed (theoretical) geometric nozzle area ratio is significantly better, as shown in Fig. 12a. Also, the designed orbiter nozzle area ratio variation with gap setting is significantly larger.

The initial turning angle of the plume boundary, as defined by the interferogram pictures, was evaluated for three nominal nozzle chamber to test chamber pressure ratios (p_{0_j}/p_b), and the results are given in Fig. 12b. As expected, increasing the nozzle to chamber pressure ratio (p_{0_j}/p_b) or decreasing the gap setting (i.e., decreasing the nozzle area ratio) increased the plume size, as reflected by the increase in the initial plume boundary turning angle. Superimposed on this figure is an estimate of the initial turning angle based on the nozzle discharge coefficient and nozzle to chamber pressure ratio (p_{0_j}/p_b) of 1600. In this case, the two-dimensional estimate of the initial turning angle is greater than the measured angle obtained from the interferograms. The nozzle shock which existed in the plume flow field was not taken into account when making these estimates of the initial turning angle and, therefore, is most likely responsible for the discrepancy shown in Fig. 12b. Similarly, the discrepancy in the measured versus computed nozzle exit to chamber pressure ratio (Fig. 12c) is attributed to the effects caused by this nozzle shock.

A sample of the pitot pressure surveys made through the plume flow field is shown in Fig. I-2a for two nozzle gap settings. Although the Mach number distributions based on these pitot pressure measurements are also presented in Figs. I-2b and d, these Mach number values may be too large in the region between the sting and the internal plume boundary shock wave location because the influence of the nozzle shock was not taken into account.

The variation with gap setting of the internal plume boundary shock location and the estimated local Mach number distribution along the nozzle sting is summarized in Fig. 13. As expected in comparison with the booster nozzle results, the orbiter plumes are significantly smaller, as reflected by the fact that the plume boundary shock is closer to the sting. As in the case of the booster, the Mach number tends to increase along the orbiter sting which simply reflects the effects of the expanding nozzle plume.
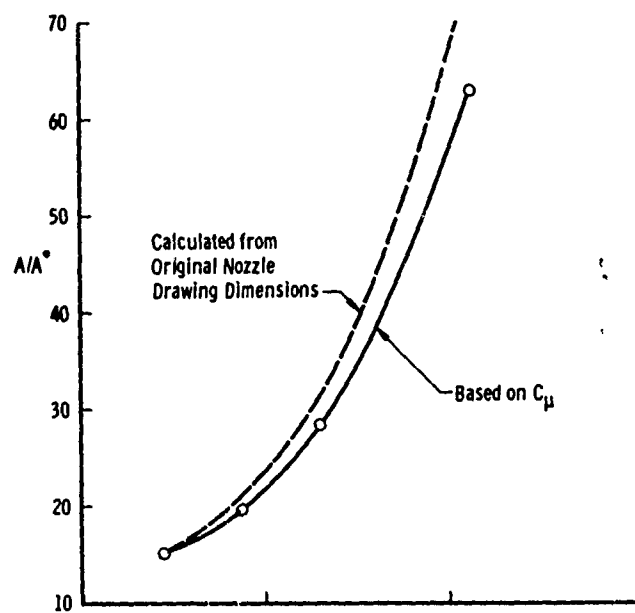
a. Nozzle Area Ratio
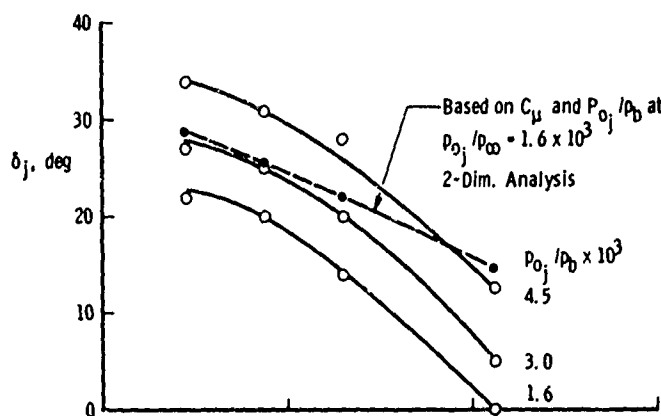
b. Initial Plume Boundary Turning Angle at the Nozzle Exit
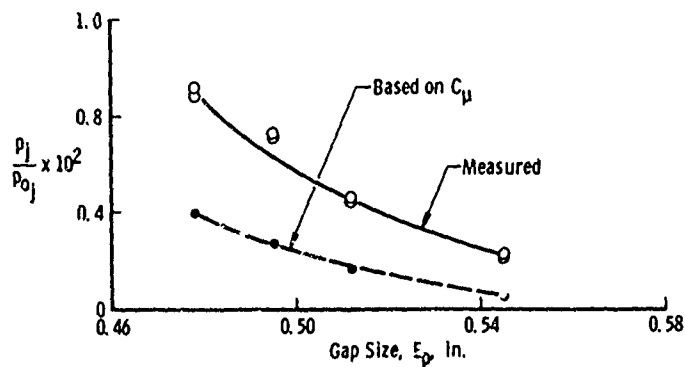
c. Nozzle Exit Static Pressure Ratio
Fig. 12 Orbiter Nozzle Plume Calibration Results

a. Internal Plume Boundary Shock Location

Sym	Gap Setting, in.	
○	0.478	Pitot
△	0.495	Probe
□	0.512	Survey
◇	0.545	

Solid Symbol: Static Tap
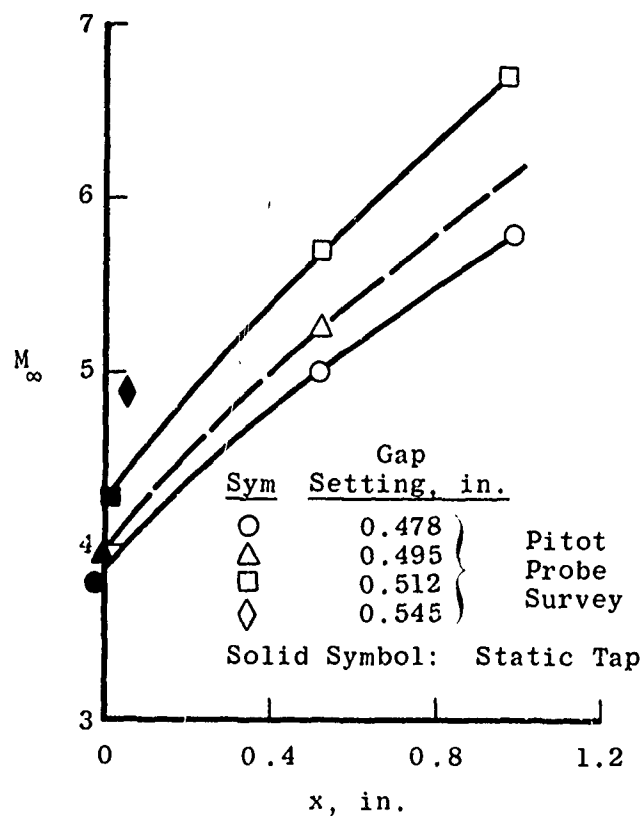
b. Mach Number Distribution

Fig. 13 Internal Plume Boundary Shock Location and the Mach Number Distributions along the Orbiter Sting

4.2 BOOSTER AND ORBITER PRESSURE DISTRIBUTIONS

Over 1450 pressure distributions were obtained during the test program, and these results have been condensed to 170 comparison plots presented in Appendix II. The booster pressure distributions presented consist of the data obtained from a row of taps lying along the centerline of the upper surface of the booster body, the inboard row of pressure taps on the upper wing surface, and the inboard row of two pressure taps on the canard. The orbiter distributions are represented by the pressures obtained from the row of taps laying along the centerline of the lower surface of the body and a row of taps running parallel with the wing trailing edge at an x/ℓ value of approximately 0.95. The purpose of these distributions is to show the effects of flow-field interference with and without power simulation on the pressure loading on the lower surface of the orbiter and the upper surface of the booster. The test variables include free-stream Mach number, angles of attack, the relative angle of incidence of the orbiter with respect to the booster, and the relative location of the orbiter and booster. The text of the report contains illustrations of the types of flow-field interference effects produced by the close proximity of the orbiter and booster on their pressure distributions.

4.2.1 Mach Number and Reynolds Number Effects

The interference-free distributions in Fig. 14 were obtained with the orbiter and booster displaced so that the flow-field disturbance produced by one model did not disturb the flow over the other model. The gradients in the pressure distributions are due to the bluntness of each of the bodies. For example, the orbiter which has a smaller blunt nose produced a more severe surface pressure gradient over the forward section of the body. Reducing the free-stream Mach number simply reduced the pressure gradient over both body nose sections.

The Reynolds number effects (which in most cases fall within the quoted repeatability of the data) are negligible on the orbiter and also on the booster body, but the booster wing data indicate a stronger Reynolds number effect. At the higher free-stream Reynolds number, the booster wing distributions indicate that the flow expands further over the aft section or trailing edge surfaces of the wing. This trend is also present to some degree over the aft portion of the booster body where there is an increase in the surface pressure ratio gradients at the higher Reynolds number. According to Fig. 14b, the increase in free-stream Reynolds number reduced the orbiter base pressure ratio, which suggests that the boundary layer in the base region of these models is becoming more transitional or turbulent at the higher free-stream Reynolds number.

34
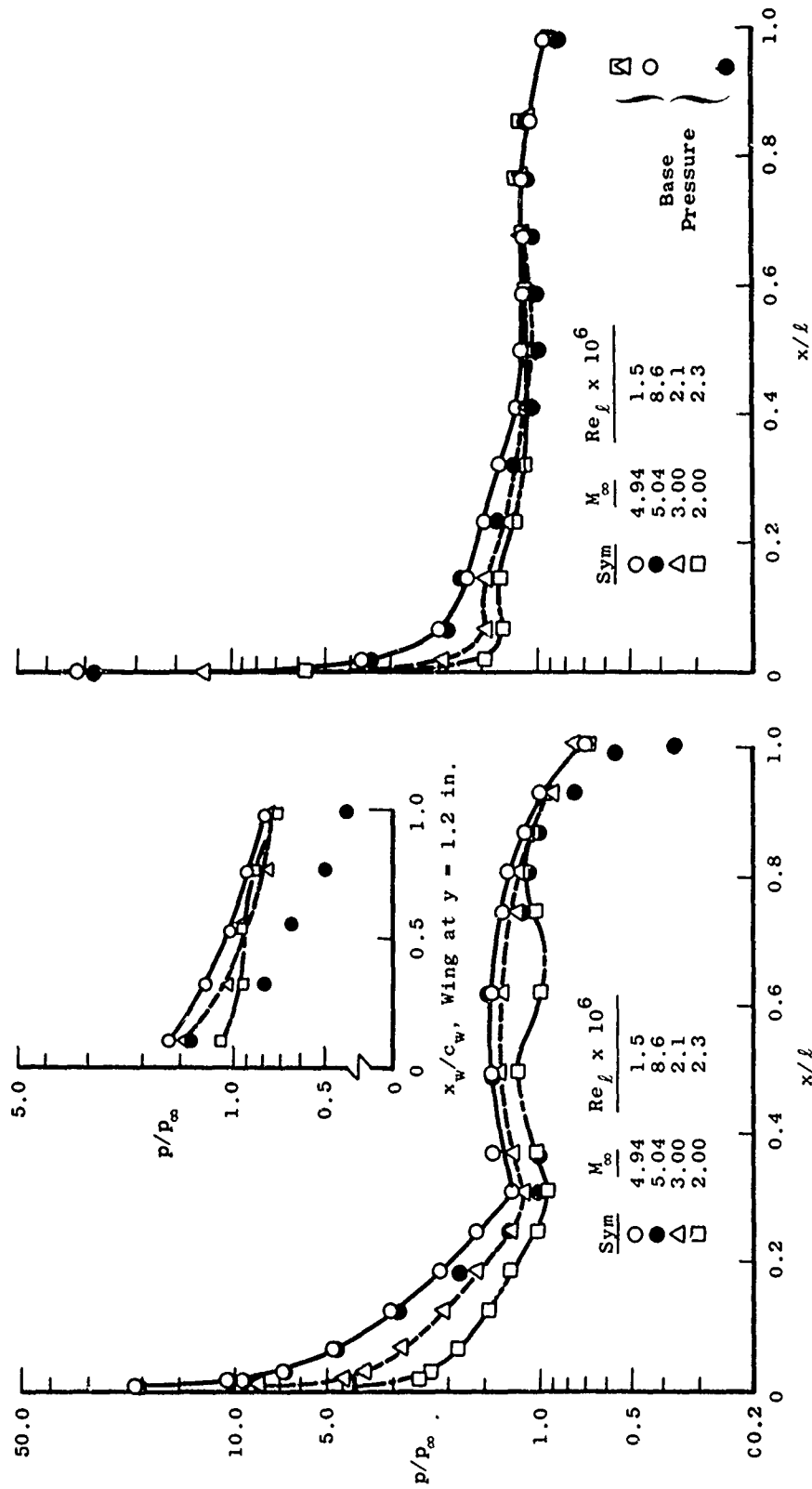
a. Upper Surface of the Booster

b. Lower Surface of the Orbiter

Fig. 14 Interference-Free Pressure Distributions along the Body Centerline of the Booster and Orbiter Configurations at Various Free-Stream Mach Numbers ($\alpha = 0$)

35

4.2.2 Flow-Field Interference Effects

Examples of the type of holographic reconstructed interferograms obtained in this test program are shown in Fig. 15. In both figures, the orbiter and booster are in close proximity to each other with plume simulation present for both models. Some of the more obvious features of the flow-field disturbance are pointed out in these two pictures. The plume-induced external stream shock wave, shown in Fig. 15a, simply denotes the presence of a compression wave generated by the interaction of the orbiter nozzle plume with the local external stream. The plume boundary is identified in Fig. 15b and corresponds to the location of the internal plume boundary compression wave described early in the plume calibration results (see either Fig. 8 or 11). The booster canard generates a strong bow wave and a fairly strong trailing edge shock which in these pictures intersects the lower surface of the orbiter. The impinging and reflecting bow waves of the booster are also fairly evident in these figures. The impinging orbiter bow wave is considerably weaker than the booster bow wave, as indicated by the magnitude of the shift in the fringe lines of the interferograms. In Fig. 15b, the orbiter plume has expanded enough to clearly impinge on the booster and form a compression wave or a plume-induced shock wave.
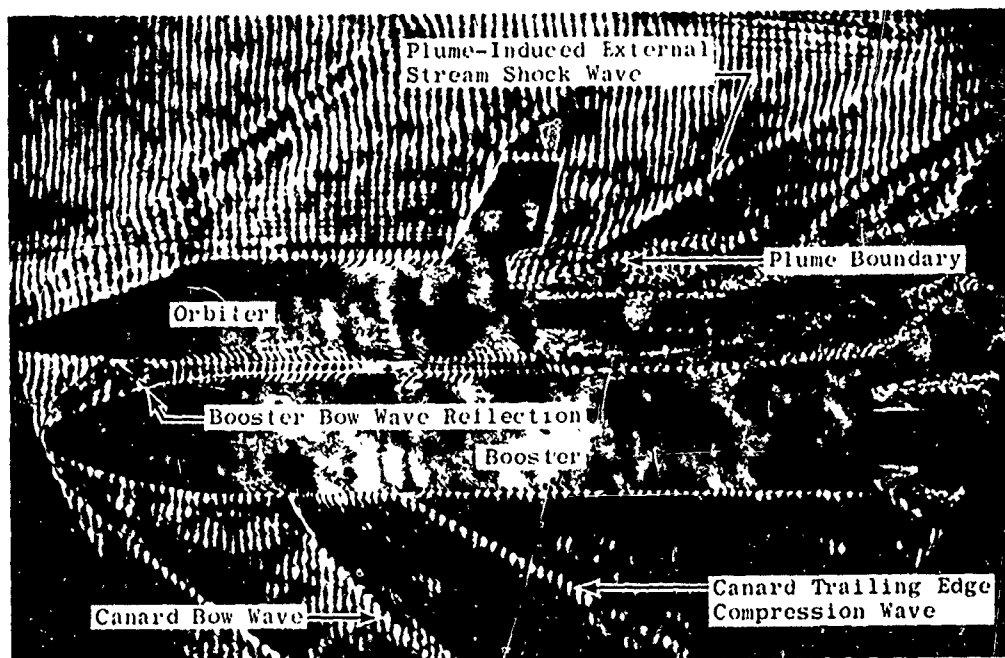
a. $M_\infty = 2.0$, $p_\infty = 0.96$ psia, and $Re_\ell = 2.3 \times 10^6$

Fig. 15 Interfering Flow Fields with 100-percent Orbiter Power Simulation and 50-percent Booster Power at Zero Angle of Attack, $\Delta x/L = 0.227$ and $\Delta z/L = 0.12$, $a = 0$, (Holographic Reconstructed Interferograms)
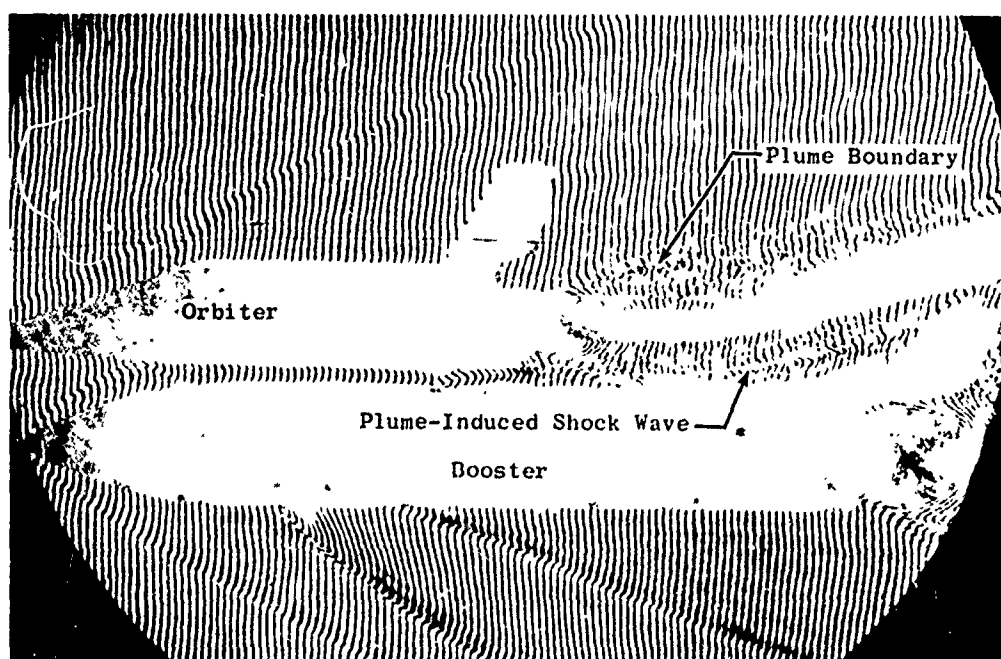
b. $M_\infty = 3.0$, $p_\infty = 0.31$ psia, and $Re_\ell = 2.1 \times 10^6$
Fig. 15 Concluded

The flow-field interference effects on the orbiter and booster pressure distributions shown in Fig. 16 correspond to the interferogram results in Fig. 15. In each case, the axial coordinates of these distributions were normalized by the model length (ℓ) which was 10.72 in. for the orbiter and 16.12 in. for the booster. The Reynolds number in the figures is always based on the booster length and not the orbiter length.

In the Mach number 2.0 results of Fig. 16a, the booster bow wave intersected the orbiter at an x/ℓ of ~0.20, causing an abrupt increase in the surface pressure, and then reflected back onto the booster at an x/ℓ of ~0.12. The reflected booster bow wave had a stronger effect on the booster pressure distribution than did the impinging orbiter bow wave which intersected the booster an an x/ℓ of about 0.03. The booster canard also generated a bow wave which would hypothetically intersect the orbiter at an x/ℓ of 0.73. Actually, the three-dimensional aspects of the expanding canard bow wave caused this bow wave to intersect the orbiter centerline row of pressure taps (the plotted values in Fig. 16) at a larger x/ℓ value of about 0.80. Similarly, the canard bow wave and trailing edge shock also wrapped around the booster and caused two additional pressure peaks in the booster distributions, as shown in Fig. 16a. Similar pressure peaks produced by the model bow waves and the booster canards are present in the pressure distributions obtained at Mach number 3.0 and shown in Fig. 16b. In Fig. 16c, the Mach number 5.0 distributions suggest that the canard influence on the pressure distributions were absent for this particular location of the orbiter relative to the booster.

37

The presence of the orbiter and booster power simulation does not noticeably alter the Mach number 2.0 orbiter pressure distributions, shown in Fig. 16a. The orbiter plume produced a small change in the pressure distribution over the aft section of the booster (i.e., for booster x/ℓ values greater than 0.80). At Mach numbers 3 and 5, the booster and orbiter power simulation influenced both the orbiter and booster pressure distributions. In the case of the orbiter, the plumes must influence the interfering flow fields between the two models because the pressure distribution still reflects the presence of the booster bow wave, but the distribution seems to be altered by the presence of the power simulation. In the case of the booster, the orbiter plume impinged on the booster, producing a typical plume impingement pressure distribution which at $M_\infty = 3$ (Fig. 16b) appeared to counteract the influence of the canard on the booster pressure distribution.
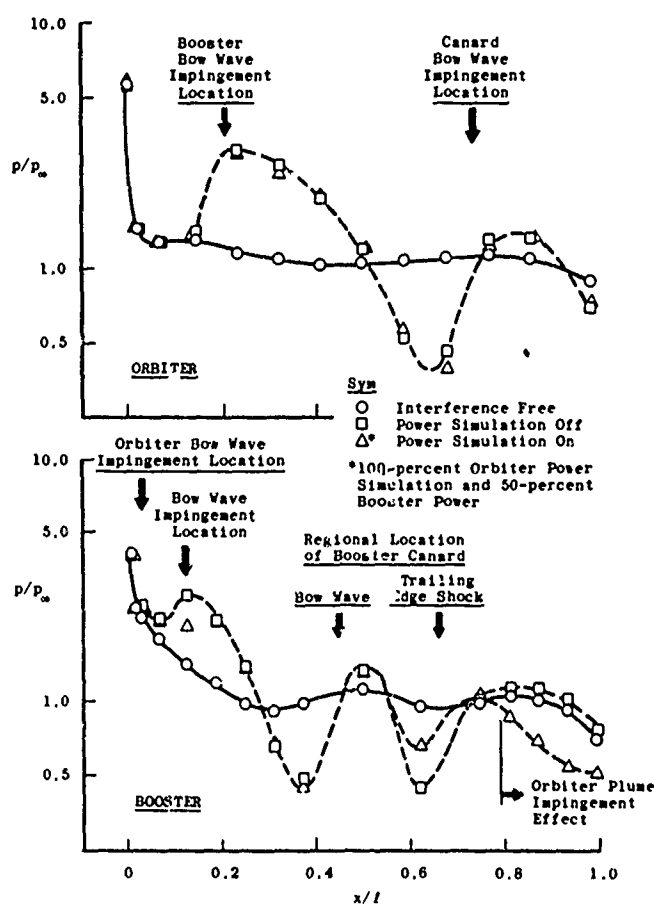
a. $M_\infty = 2.00$ and $Re_\ell = 2.3 \times 10^6$

Fig. 16 Interference Effects at $\Delta x/L = 0.227$ and $\Delta z/L = 0.12$ on the Centerline Booster and Orbiter Pressure Distributions with and without Plume Power Simulation Effects, $a = 0$

38
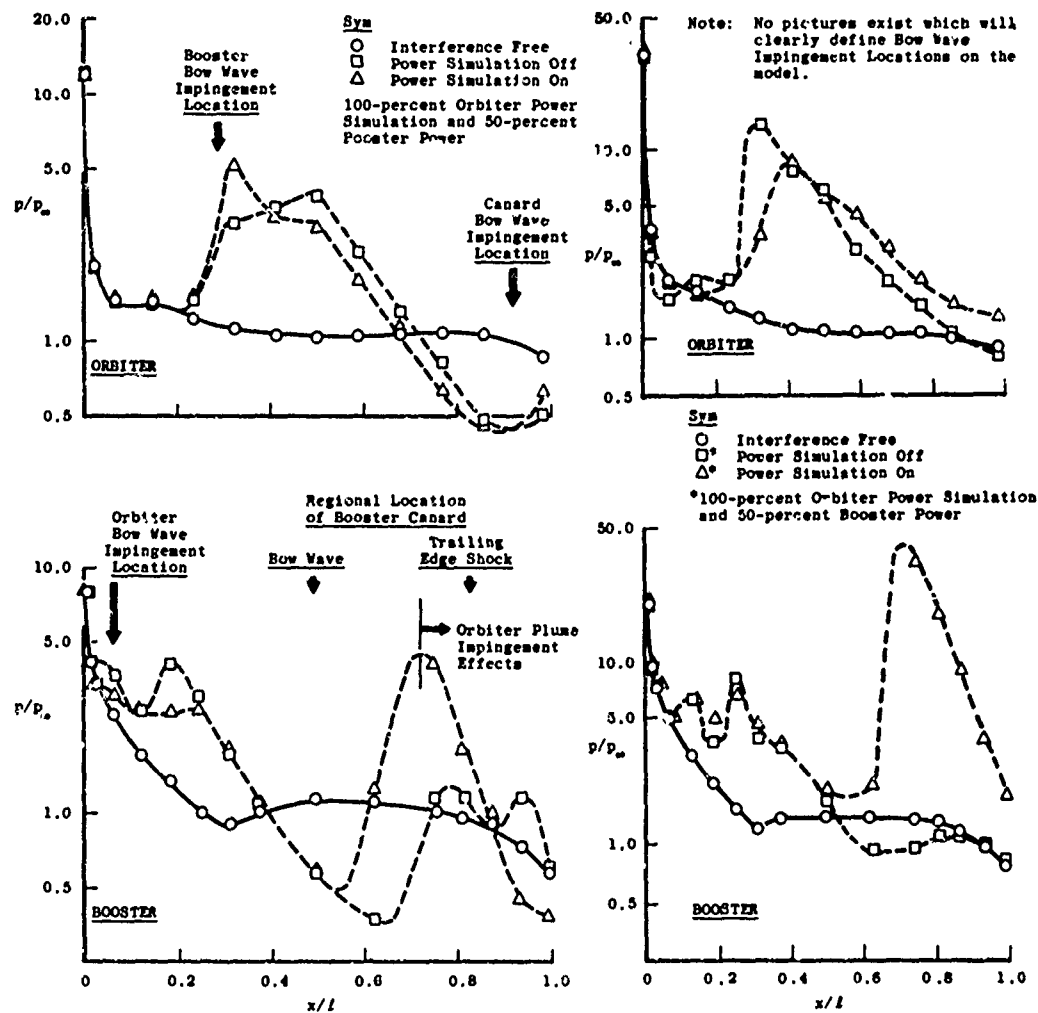
b. $M_\infty = 3.00$ and $Re_\ell = 2.1 \times 10^6$ c. $M_\infty = 4.97$ and $Re_\ell = 1.5 \times 10^6$

Fig. 16 Concluded

4.2.3 Mach Number 5.0 Power Simulation and Plume Impingement Effects

In general, the power simulation effects were stronger at the higher free-stream Mach number. The influence of the vertical displacement on the aerodynamic interference effects with and without power simulation on the booster and orbiter centerline pressure distributions at Mach number 5.0 is shown in Fig. 17. As expected, the interference effects on the pressure distributions diminished and moved downstream as the vertical separation between the two models increased.

A comparison of the orbiter pressure distributions obtained with and without power simulation (in Fig. 17a) clearly shows that the power simulation tends to reduce the interference loading on the orbiter. For example, in the launch configuration with the orbiter and booster touching, the power simulation reduced the peak pressure ratio from about 25 down to 11. In the launch configuration, without power simulation, the reflected booster bow wave intersected the booster at an x/ℓ of ~ 0.21, and actuating the power simulation reduced this peak pressure point. A possible explanation for this effect of the plume on the aerodynamic body interference loading is that the plumes probably act as an ejector when the two models are in close proximity to each other. This plume ejector effect would tend to accelerate the flow by scavenging flow from between the two bodies which would in turn reduce the angle of impingement and strength of the booster bow waves.

A close examination of the interference-free distributions obtained with and without plume simulation indicates that a little plume-induced separation was generated over the aft portion of these models. On the orbiter, the plume-induced separation apparently began at an x/ℓ of about 0.8 and on the booster at an x/ℓ of 0.95. The plume-induced separation refers to the condition when an expanding plume from the base of a vehicle acts as a blunt body trailing the vehicle and causes the boundary layer to separate from the vehicle surfaces.

The orbiter plume impingement loading on the booster is clearly evident in the booster pressure distributions shown in Fig. 17b. At this particular axial location of the orbiter relative to the booster, there is no booster plume impingement loading on the orbiter. In the launch configuration (the orbiter and booster touching), the peak plume impingement pressure ratio on the booster exceeds the free-stream Rayleigh pitot pressure ratio which corresponds to the maximum nose pressure ratio existing on the booster or orbiter models in a Mach number 5.0 free-stream flow. As the displacement between the two bodies increased, the plume impingement point on the booster moved downstream, and the peak pressure decreased because of the reduction in the plume boundary flow impingement angle on the booster surface.

40
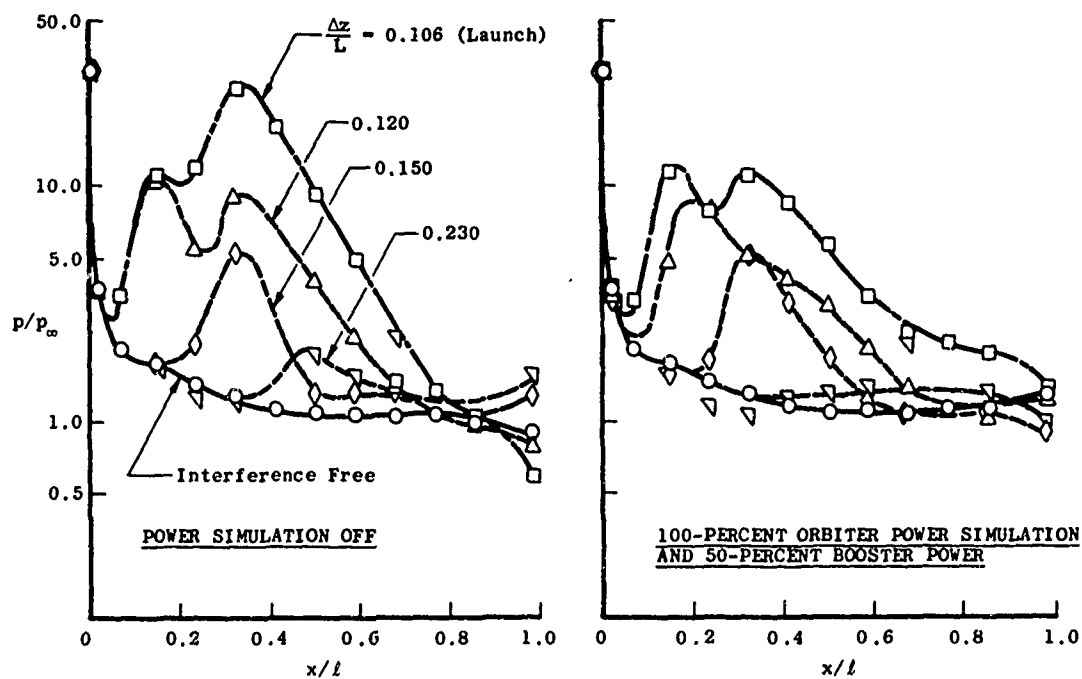
a. Orbiter
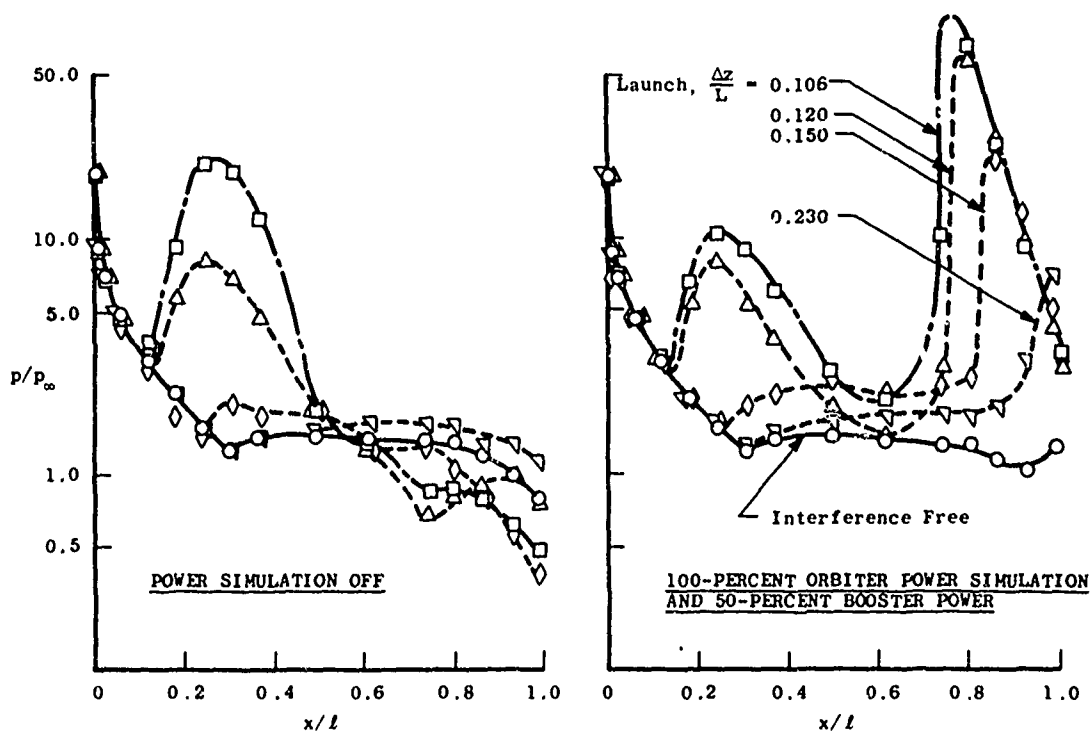
b. Booster

Fig. 17 The Effect of Vertical Displacement from a Launch Position on the Pressure Distributions with and without Plume Power Simulation at $\Delta x/L = 0.103$, $a = 0$, $M_\infty = 4.97$, and $Re_\varrho = 1.5 \times 10^6$

A comparison of the effect of an external Mach number 5.0 stream on the plume impingement flow field and loading is shown in Figs. 18, 19, and 20. Nozzle chamber pressure (p_{o_j}) is constant for this comparison. Superimposed on the orbiter plume generated in a chamber without external flow (Fig. 18a) are the boundaries of a plume produced in the presence of a Mach number 5.0 stream (Fig. 18b). The plume generated in the presence of the external stream is only slightly larger, and in fact, near the nozzle exit, the difference in the plume boundaries appears to be only 5 or 6 percent. Although the ambient pressure for the no-external-flow case is more than ten times larger than the ambient pressure in the Mach number 5.0 stream, the plumes are nearly equal in size. In both pictures, the orbiter angle of incidence (i) relative to the booster is 5 deg, and in both cases the orbiter plume corresponds to a 100-percent power simulation at $M_\infty = 5.0$.

The centerline pressure distributions on the booster for the conditions shown in Fig. 18 are given in Fig. 19. In the case when no external flow was present, the booster pressures were normalized by the test chamber pressure (p_b); whereas for the case of an external stream, the test section static pressure was used to normalize the pressure data. In both cases, a scale reflecting the absolute pressure distribution existing on the booster is included for each figure. Also, the pressure loading in the absence of the plume is superimposed on the figures in the form of a dashed line.

The plume impingement point on the booster moves upstream slightly with external flow, but the absolute peak pressure value in the distribution is only slightly affected by the presence of the external stream. The region of influence of the plume impingement (that is, the footprint of the orbiter plume on the booster) is considerably larger when the external stream is present. For example, the row of wing taps located 1.95 in. off the booster axis were not disturbed significantly when the external stream was absent; but when the external stream was present, these taps were strongly influenced by the plume.

The size and shape of the plume impingement loading was estimated from the pressure distributions and is presented schematically in Fig. 20 in the form of isobars. A comparison of Figs. 20a and b shows that the plume impingement loading extended out over the wing surfaces of the booster when the external stream was present. In the absence of the external stream, the plume impingement region is confined to the typical parabolically shaped load pattern. Apparently, the wake produced by the flow over the orbiter and booster interacted with the orbiter plume and expanded the plume boundaries laterally, that is in the yaw plane. The

42

movement of the plume impingement loading upstream on the booster when the orbiter was moved upstream (Figs. 20c and d) expanded the loading region on the booster. The shaded areas in these figures (Fig. 20) represent areas where the booster would probably sense a downward loading because of the plume impingement. For both orbiter locations shown, the external stream produces a condition in which the downward component of loading extends over a significantly larger region of the booster than for the case when no external stream is present.
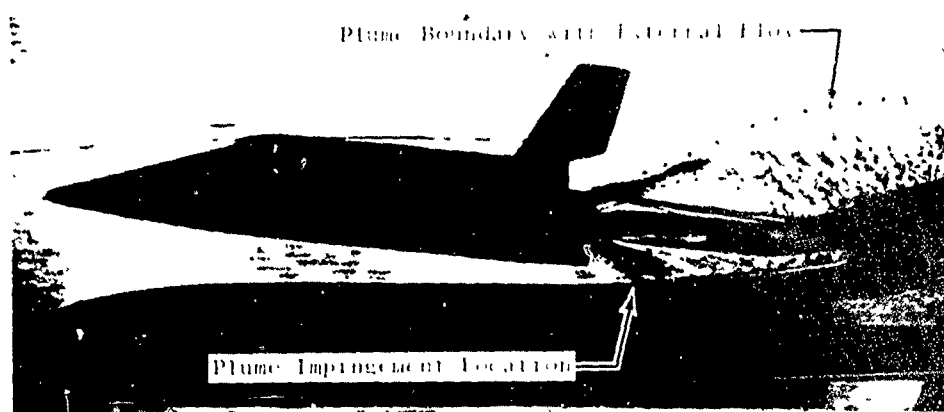
a. No External Flow, 100-percent Orbiter Power Simulation, $p_b \simeq 0.48$ psia (Schlieren)
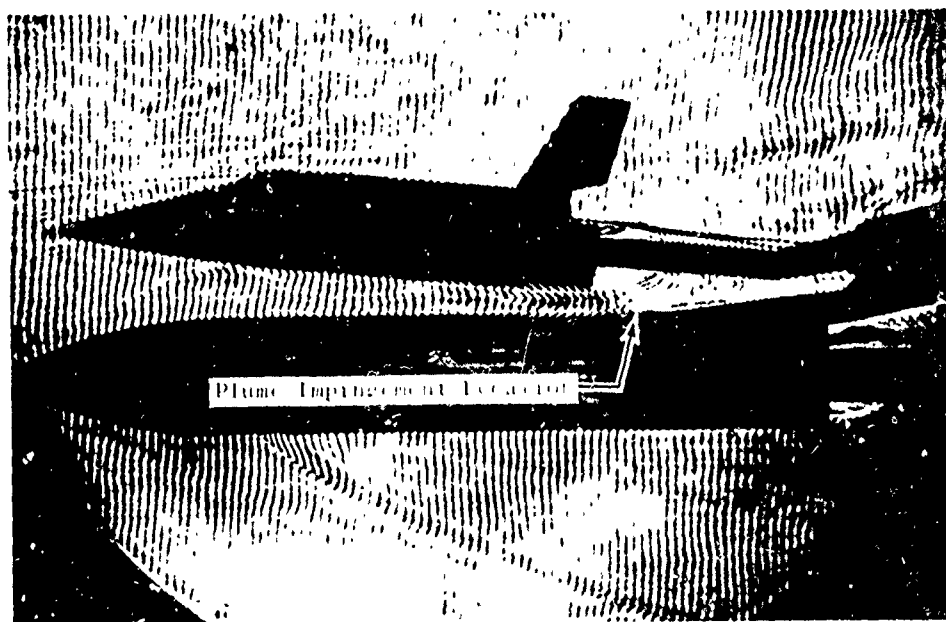
b. External Flow, $M_\infty = 4.97$ and $p_\infty = 0.043$ psia with 100-percent Orbiter Power Simulation and 50-percent Booster Power (Interferogram)

Fig. 18 Comparison of the External Flow Field Effects on the Plume Interference Flow Field Produced by the Orbiter with 100-percent Power Simulation, i = 5 deg, $a = 0$, $\Delta z/L = 0.15$, and $\Delta x/L = 0.103$
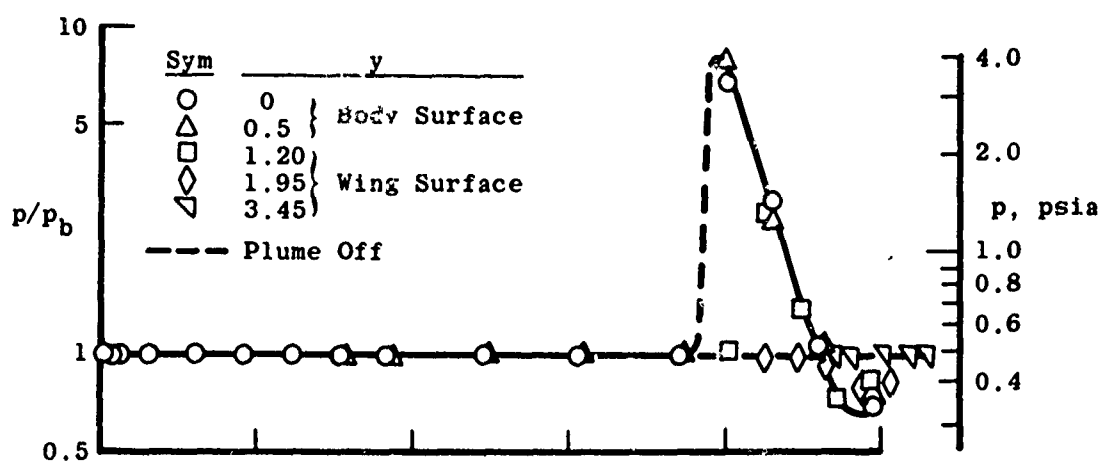
a. No External Flow, p_b = 0.48 psia
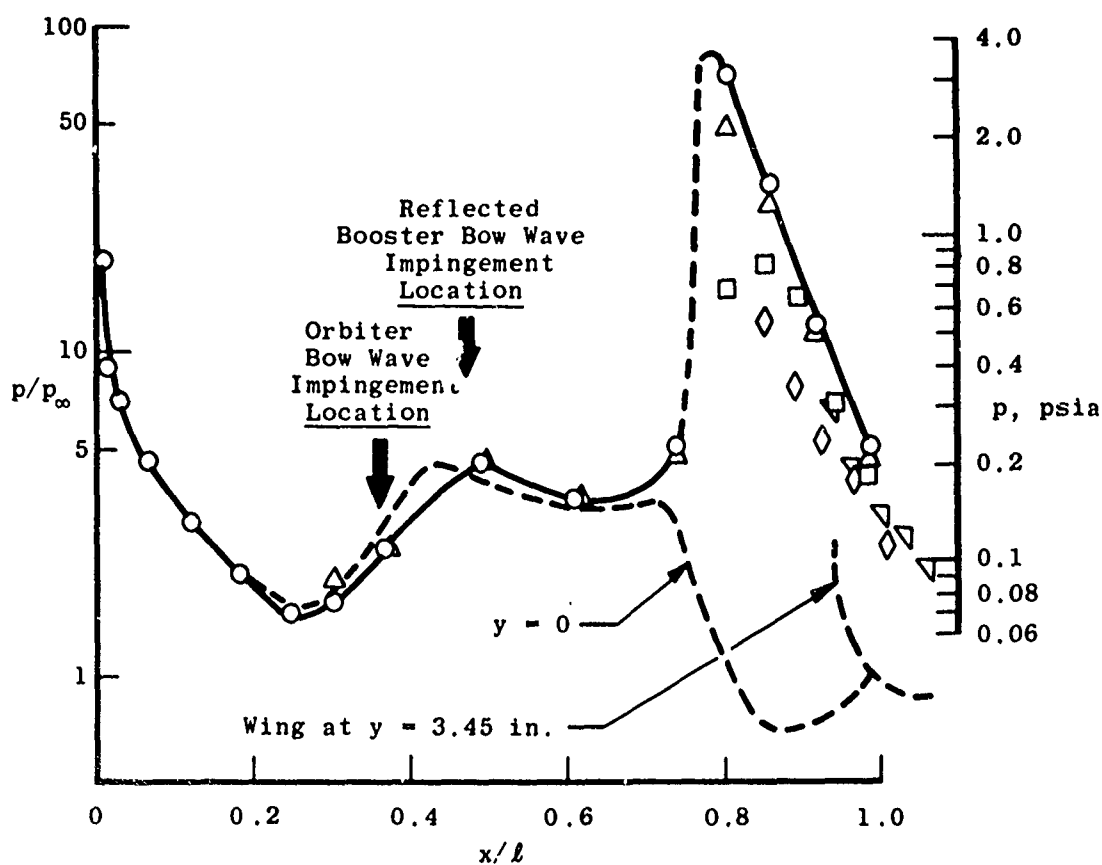
b. External Flow, M_∞ = 4.97, p_∞ = 0.043 psia, Re_ℓ = 1.5 x 10⁶

Fig. 19 Comparison of the External Flow Field Effects on the Plume-Induced Centerline Pressure Distributions on the Booster Produced by the Orbiter with 100-percent Power Simulation, i = 5 deg, a = 0, $\Delta z/L$ = 0.15, and $\Delta x/L$ = 0.103
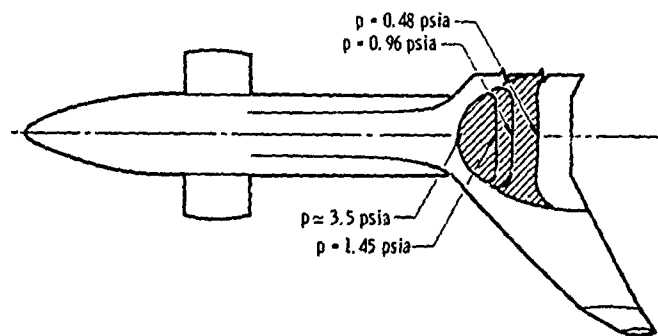
a. No External Flow, $p_b \simeq 0.48$ psia, $\Delta x/L = 0.103$
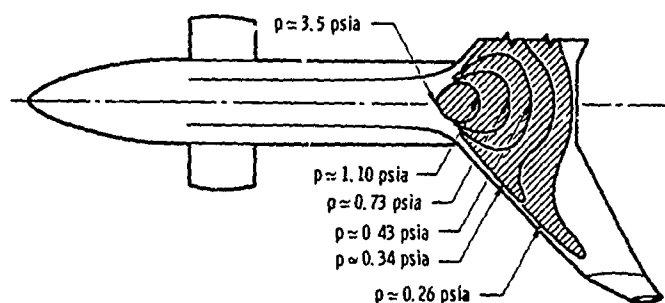
b. External Flow, $M_\infty = 0.97$, $p_\infty = 0.043$ psia, $\Delta x/L = 0.103$
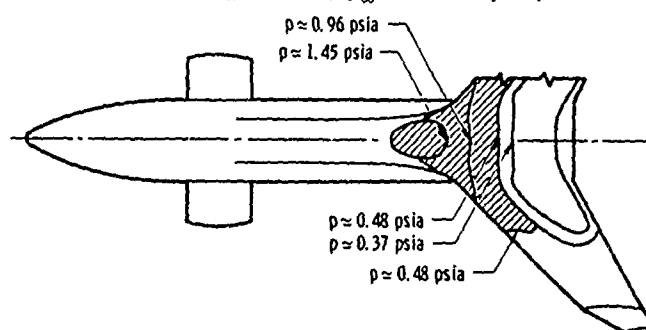
c. No External Flow, $p_b \simeq 0.48$ psia, $\Delta x/L = 0.228$
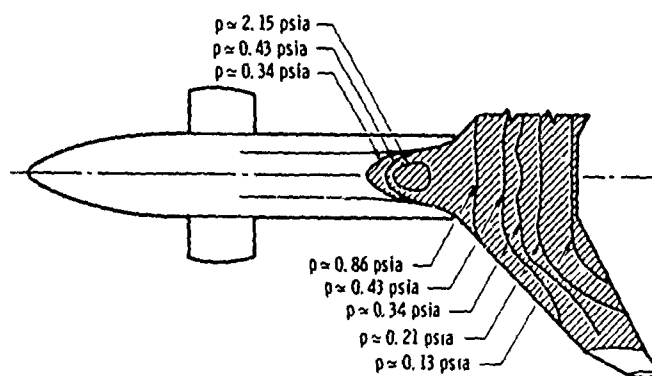
d. External Flow, $M_\infty = 4.97$, $p_\infty = 0.043$ psia, $\Delta x/L = 0.228$

Fig. 20 The Plume-Induced Impingement Pressure Distribution (Isobars) on the Upper Booster Surface with and without External Flow and the Orbiter at 100-percent Power Simulation, i = 5 deg, $a = 0$, and $\Delta z/L = 0.15$

4.2.4 Comparison of Force Data with Integrated Pressure Data

Although the integrated pressure data represents only the loading
on the lower surface of the orbiter and the upper surface of the booster,
a comparison of these normal force and pitching moment coefficients
with the force measurements of Ref. 1 is given in Figs. 21 and 22 for
the interference-free condition at M_∞ = 2 and 5, respectively. At posi-
tive angles of attack, the booster loading on the upper surface, as de-
fined by the integrated pressure data, contributes little to the positive
component of the booster normal force; whereas, at negative angles
of attack the upper surface loading is responsible for most of the nega-
tive component of the normal force, as shown in Figs. 21a and 22a.
Since the orbiter was instrumented on the lower surface, the integrated
pressure data should account for most of the positive component of
normal force at positive angles of attack, as shown in Figs. 21b and
22b. At Mach number 5.0 and 10-deg angle of attack, the integrated
orbiter pressure data produced a normal force coefficient equal to the
value obtained from the force measurements (see Fig. 22b).
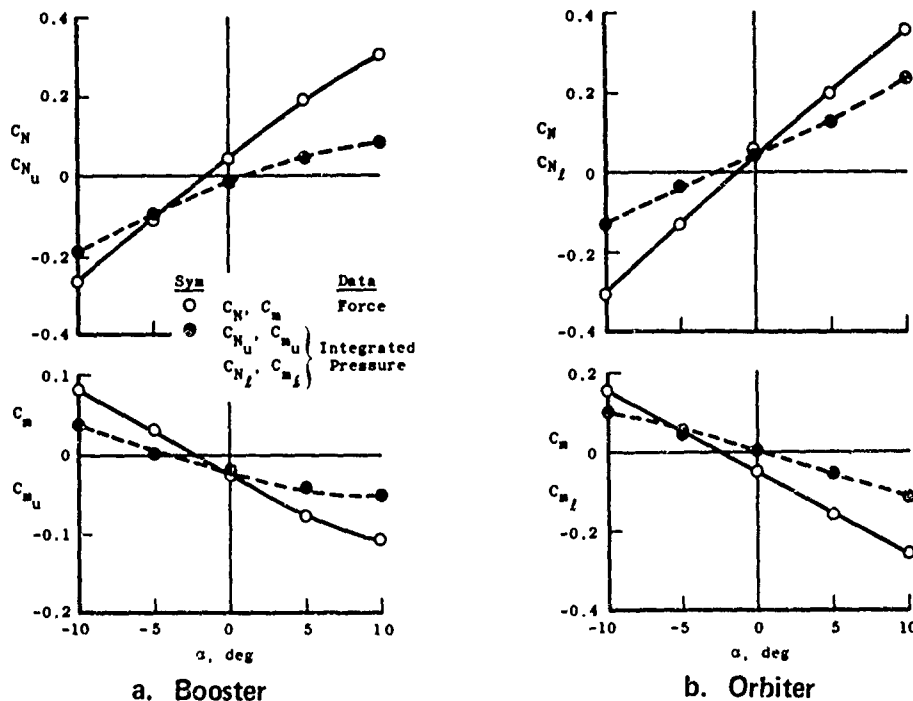
a. Booster   b. Orbiter

Fig. 21 Comparison of the Resultant Force and Moment Coefficients with
Those Associated with the Loadings on the Upper Surface of the
Booster and Lower Surface of the Orbiter, Zero Power,
Interference Free, M_∞ = 2.0, and Re_ℓ = 2.3 x 10^6

46
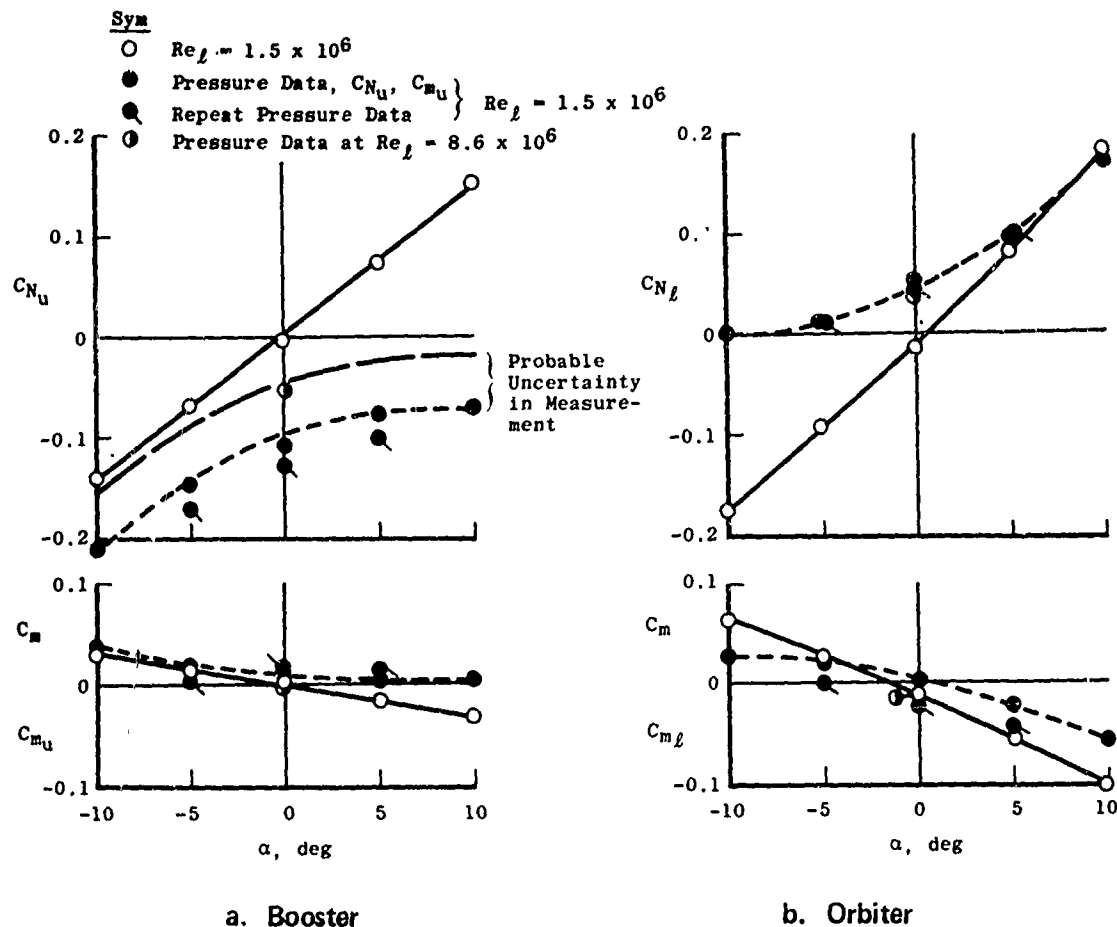
Fig. 22 Comparison of the Resultant Force and Moment Coefficients with Those Associated with the Loading on the Upper Surface of the Booster and Lower Surface of the Orbiter, Zero Power, Interference Free, $M_\infty = 4.97$, and $Re\ell = 1.5 \times 10^6$

As noted in Fig. 22a, the difference between the high and the low Reynolds numbers integrated estimate of the normal force on the booster can be associated with the probable uncertainty in measurement associated with the transducers used in the booster model. Although the calibration fell within the repeatability of the transducers, both of the booster transducers read consistently high, as noted previously in Section 2.4, and therefore, the magnitude of the normal force coefficient based on pressure data would tend to be higher by a fixed increment at all angles of attack; particularly, at the lower free-stream Reynolds number at a nominal Mach number of 5.0. Most of the integrated pressure data results to follow are presented as incremental changes between the interference and interference-free data, which compensate for this probable error in the integrated booster pressure data.

47

A comparison between force data and integrated pressure data of
the incremental changes in normal force and pitching moment produced
by the aerodynamic interference between the orbiter and booster models
is illustrated in Fig. 23 for Mach number 2 and in Figs. 24, 25, and 26
for a nominal Mach number of 5.0. At Mach number 2 (Fig. 23) and
except for the orbiter at a $\Delta x/L$ value of -0.14, the agreement between
the force and integrated pressure data is excellent. At Mach number
2.0 when the two models are in close proximity to each other, the
smaller changes in normal force and in pitching moment coefficients
(i.e., ΔC_N and ΔC_m values less than ±0.03) on both bodies occurs
between a $\Delta x/L$ value of about 0.1 and -0.05. At a $\Delta x/L$ value of zero,
the moment reference point of the booster and orbiter are in line, one
above the other. Between a $\Delta x/L$ value of 0.4 and -0.1, the orbiter
plume simulation had some influence on the booster normal force and
pitching moment coefficients, as shown by the force data in Fig. 23b
and suggested earlier in Fig. 16b. For the present range of relative
locations of the orbiter and booster, the plume simulation did not
significantly alter the interference loading on the orbiter at Mach num-
ber 2.0.
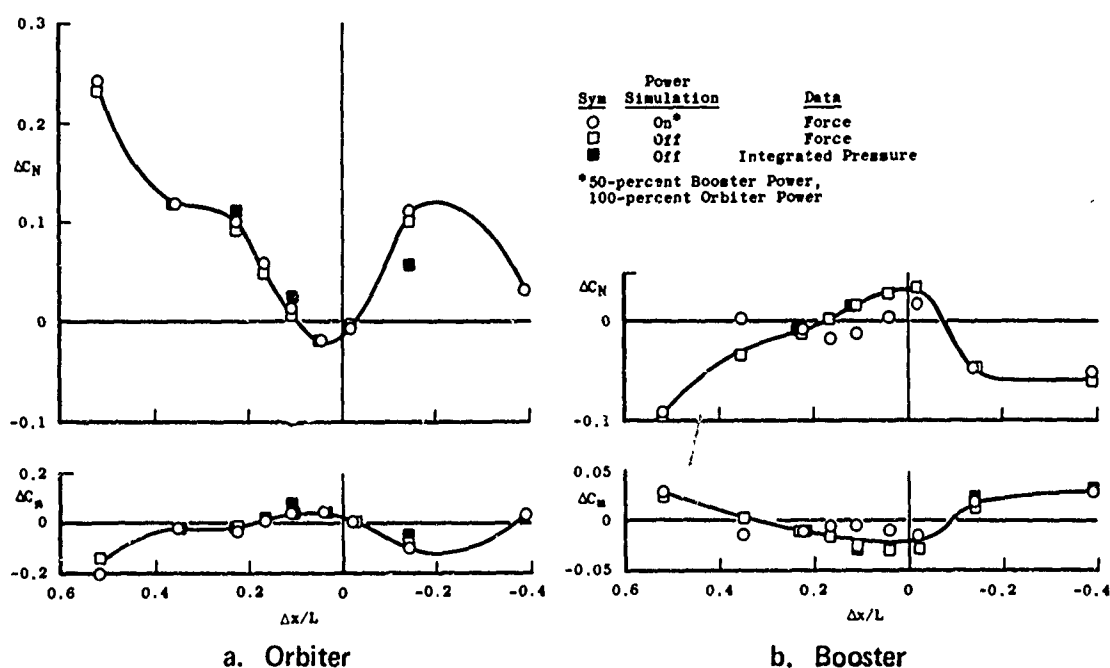
Fig. 23 The Variations with the Orbiter and Booster Interference
Loading with and without Power Simulation as Defined by
the Integrated Pressure Data and the Force Data, $a = 0$,
$\Delta z/L = 0.12$, $M_\infty = 2.00$, and $Re_\ell = 2.3 \times 10^6$

48

Increasing the displacement ($\Delta z/\ell$) between the orbiter and booster from 0.12 to 0.15 reduces the incremental change in loading on both vehicles, as shown by the nominal Mach number 5.0 results in Fig. 24. As shown in Fig. 25a, the power simulation tends to reduce the loading on the orbiter by about 20 percent except at the locations where the booster plume impinges directly on the orbiter which occurs when $\Delta x/L$ is less than -0.2 at $\Delta z/L$ of 0.12. For values of $\Delta x/L$ greater than -0.1, the orbiter plume impinges on the booster, increasing the negative component of normal force on the booster. In general, increasing the displacement between the models reduces the incremental changes in force and pitching moment coefficients and also shifts the location where the peak changes occur in these coefficients.

a. $\Delta z/L = 0.12$ b. $\Delta z/L = 0.15$
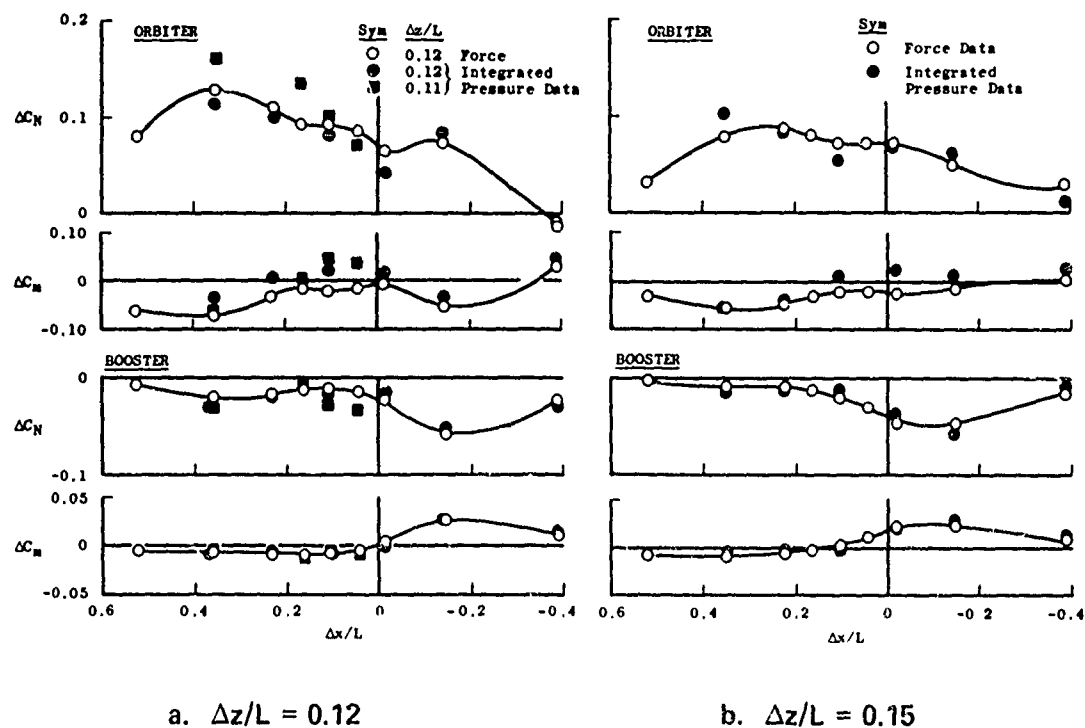
Fig. 24 The Variations in the Orbiter and Booster Interference Loading without Power Simulation as Defined / the Integrated Pressure Data and the Force Data, Power Simulation Off, $a = 0$, $M_\infty = 4.97$, and $Re_\ell = 1.5 \times 10^6$
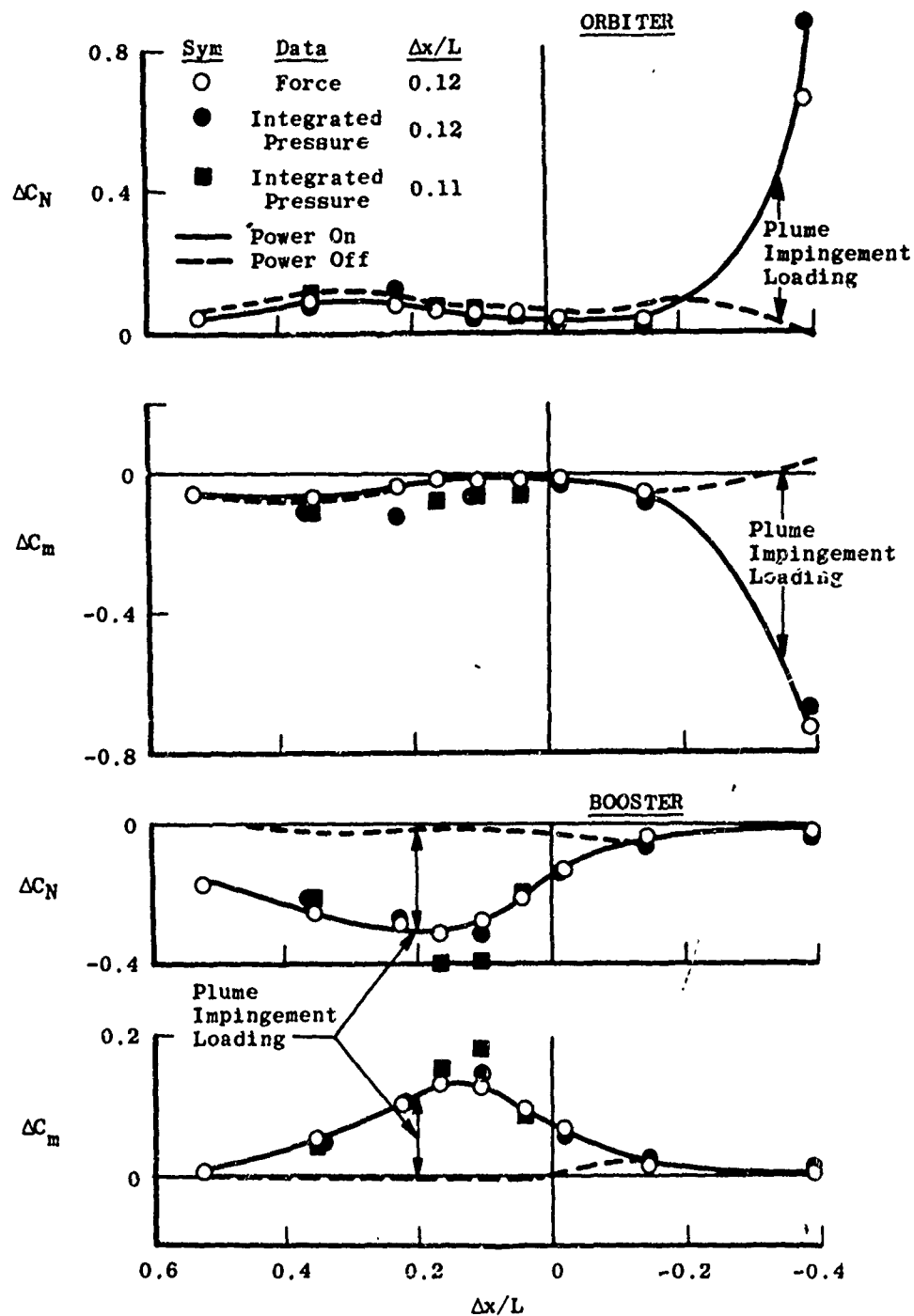
a. $\Delta z/L = 0.12$

Fig. 25 Comparison of the Integrated Pressure Data with the Force
Data, 50-percent Power Simulation on the Booster, 100-percent
Orbiter Power, $a = 0$, $M_\infty = 4.97$, and $Re_\ell = 1.5 \times 10^6$

50
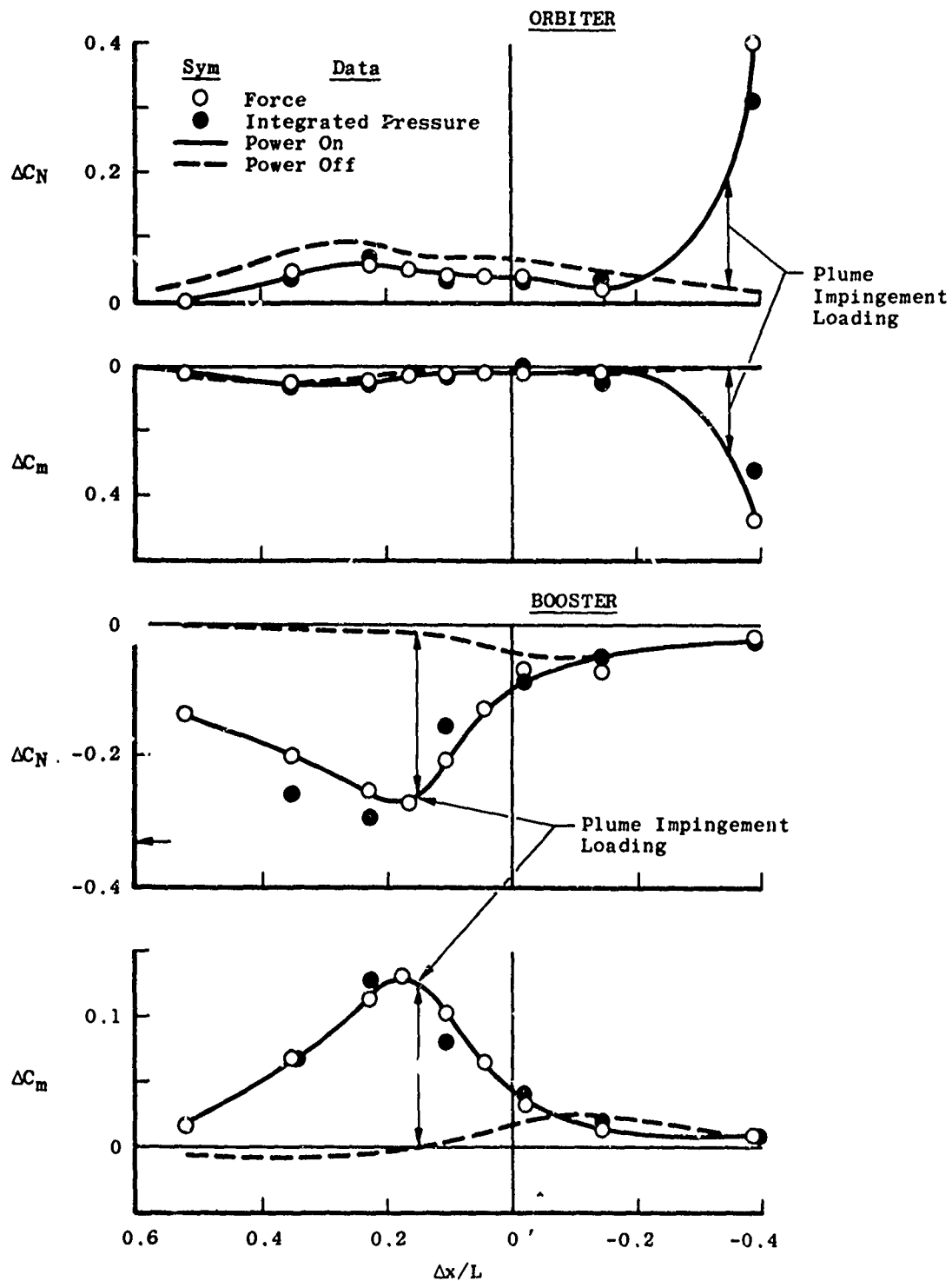
b. $\Delta z/L = 0.15$
Fig. 25 Concluded

51

A comparison of Fig. 24b with Fig. 26 shows that increasing the relative angle of incidence to 5 deg between the orbiter and booster increases the interference loading on these configurations. With power simulation, the interference on the booster reached a peak value when the orbiter was at a 5-deg angle of incidence and located upstream of the booster moment reference point at a $\Delta x/L$ value of about 0.15. As expected, increasing the orbiter angle of incidence also increases the orbiter plume impingement loading on the booster and the booster plume impingement loading on the orbiter (compare Fig. 25b with Fig. 26b, respectively). Increasing the relative angle of incidence between the two bodies increases the local angle of incidence of the plume streamlines on the adjacent body surface, which produces the increases in local impingement loading (see Fig. 26b).
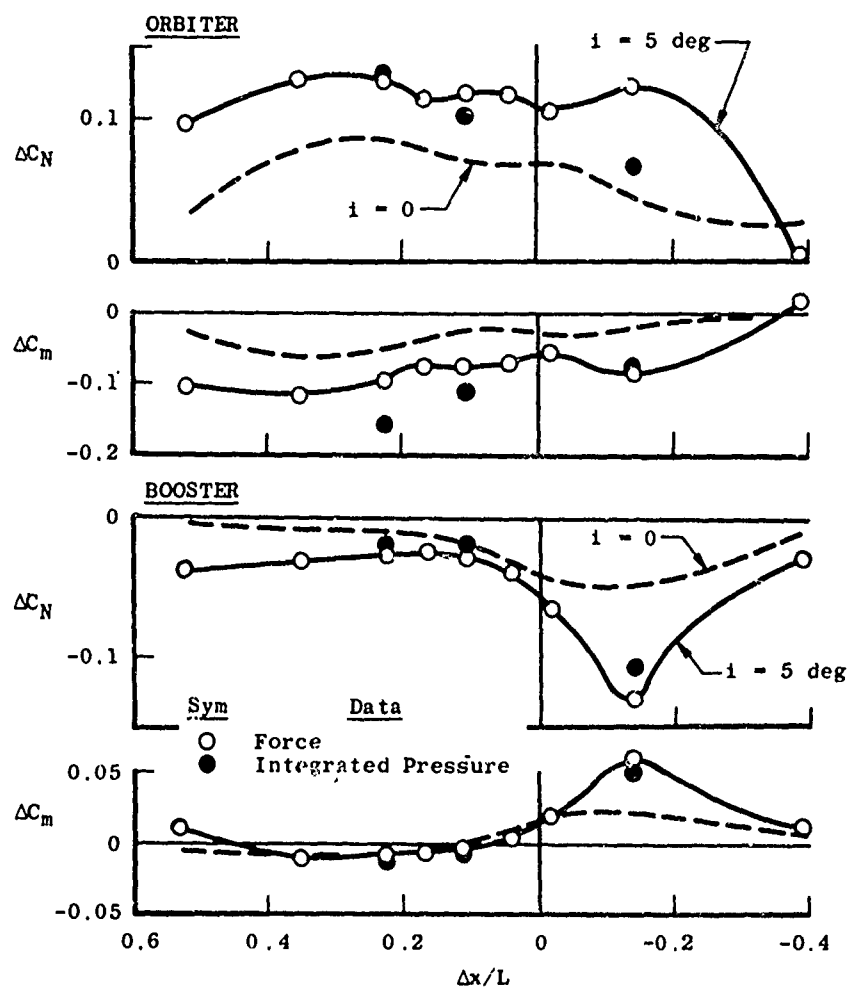
a. Power Simulation Off

Fig. 26 Comparison of the Integrated Pressure Data with the Force Data, i = 5 deg, $\Delta z/L$ = 0.15, M_∞ = 4.97, and Re_ℓ = 1.5 x 10^6

52
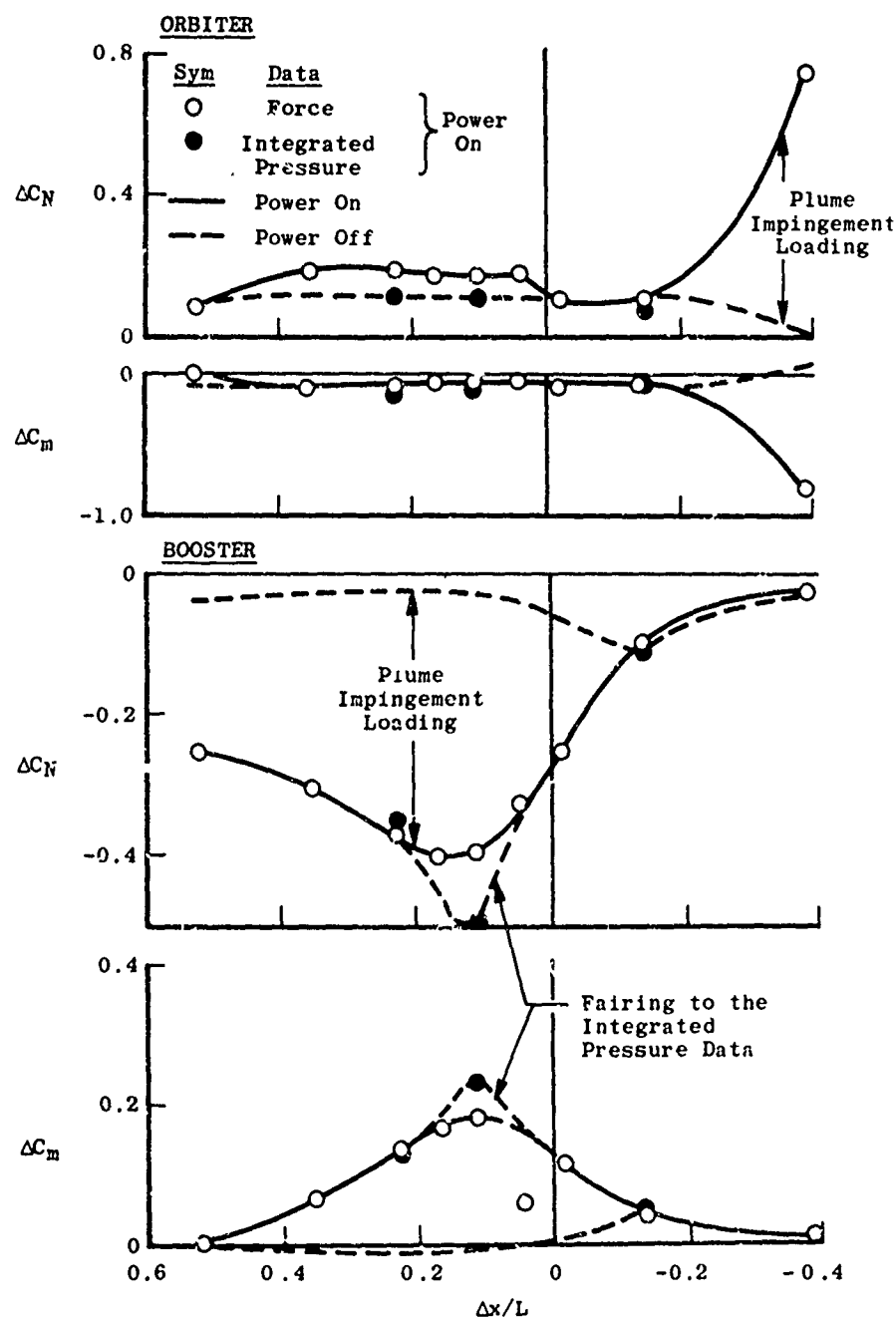
b. 100-percent Orbiter Power Simulation and 50-percent Booster Power

Fig. 26 Concluded

The integrated pressure data can also be used to estimate the local load distributions along the body axes or along the wing span. An example of the local loading coefficient distributions obtained from the Mach number 5.0 data is given in Fig. 27. The solid symbols represent the load distribution produced in the absence of power simulation, while the open symbols correspond to the distributions obtained with power simulation. The loading coefficient is simply the local normal force coefficient per inch existing at a particular model station. With the orbiter in the forward position ahead of the booster moment reference point ($\Delta x/L = 0.35$), most of the interference loading on the orbiter (Fig. 27a) occurs beyond a $\Delta x/\ell$ value of 0.5. As the orbiter moved aft, the peak interference loading moved forward on the orbiter, and the maximum local loading occurred on the orbiter at $\Delta x/L = -0.391$.
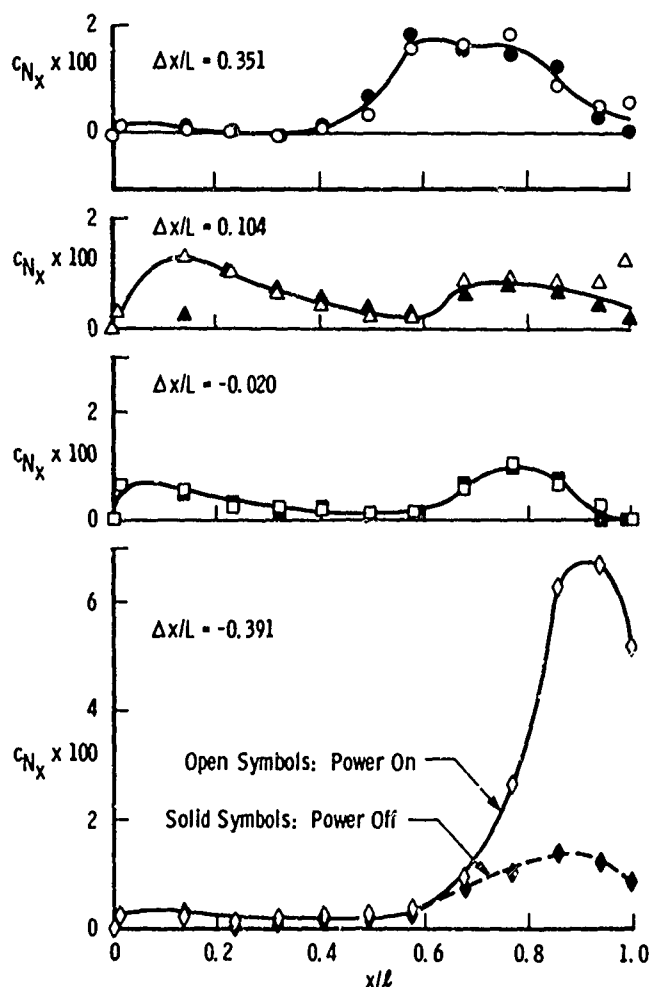
a. Orbiter Distributions

Fig. 27 Variation in the Local Normal Force Coefficient with the Axial Position ($\Delta x/L$) of the Orbiter Relative to the Booster with and without Power Simulation, $a = 0$, $\Delta z/L = 0.12$, $M_\infty = 4.97$, and $Re_\ell = 1.5 \times 10^6$

54

In the case of the booster loading (Fig. 27b), maximum loadings occurred when the orbiter was in the forward position ($\Delta x/L = 0.351$) and the orbiter plume impinged on the booster. The maximum booster wing loading occurred when the orbiter position was near a $\Delta x/L$ of 0.10 (Fig. 27c) and the orbiter plume impinged on the wing surfaces. In Fig. 27c, the force coefficient represents the local wing chord normal force coefficient per inch along the booster wing.
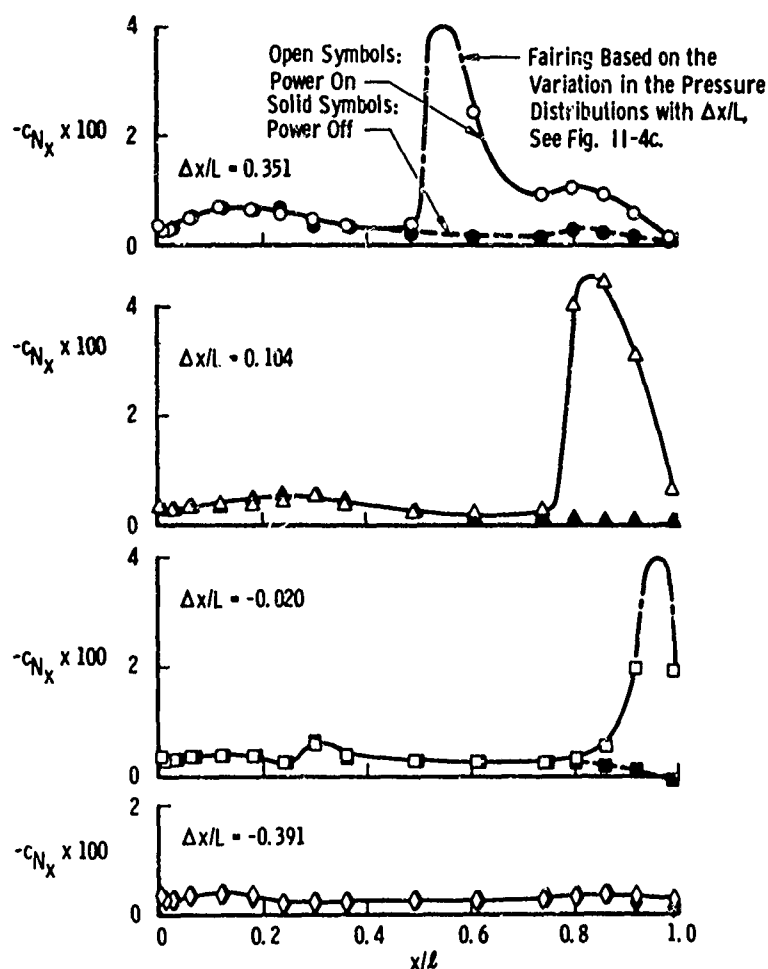
b. Booster Distributions
Fig. 27 Continued
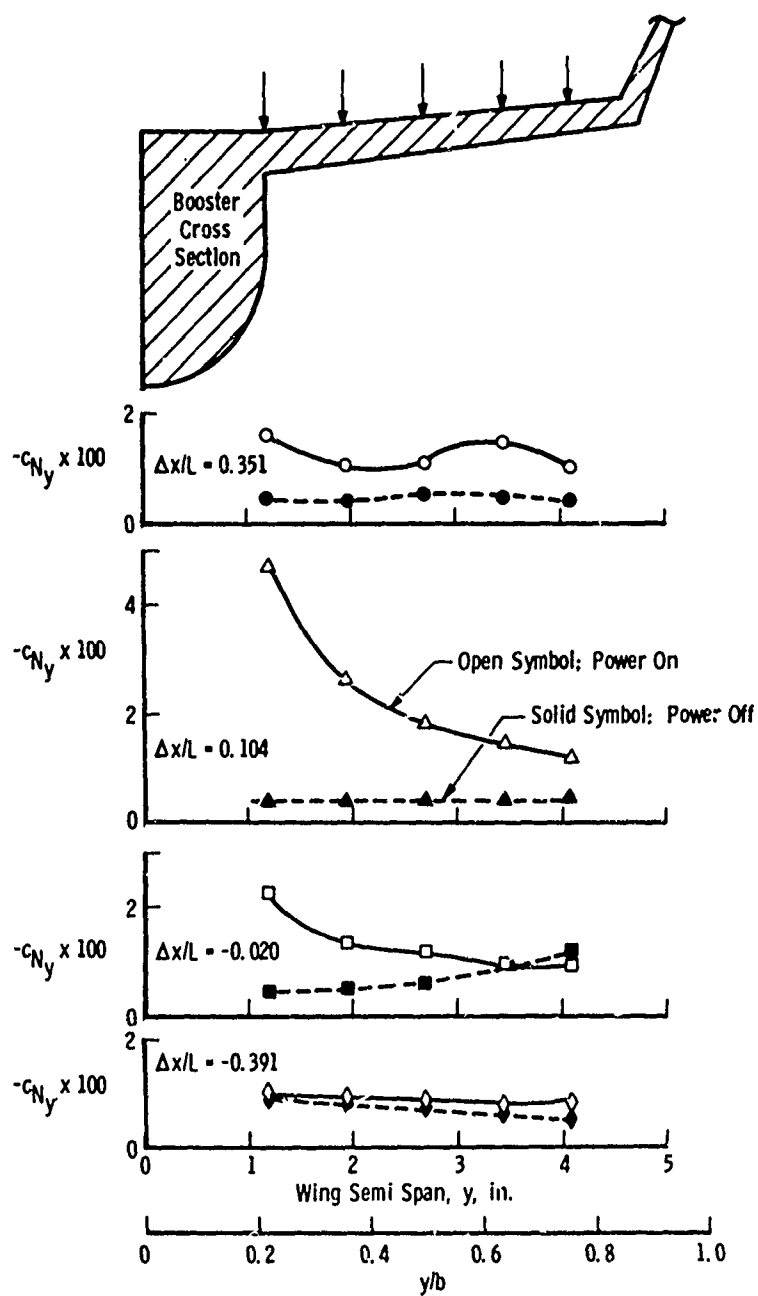
c. Booster Wing Distributions
Fig. 27 Concluded

56

4.2.5 Interference Effects on the Booster and Orbiter Base Pressures

The effect of angle of attack, orbiter position relative to the booster, and plume power simulation on the model base pressures are summarized in Figs. 28, 29, and 30, respectively, for nominal Mach numbers of 2, 3, and 5. In general, at Mach numbers 2 and 3 (Figs. 28 and 29), these factors had relatively small effects on the base pressure ratio (p/p_∞). At Mach number 2, one of the obvious effects occurred with the launch configuration, where the booster base pressure ratios increased from a nominal value of 0.65 to 1.00 when power simulation was applied. At Mach number 5.0 (Fig. 30), the power simulation had a more pronounced effect on the base pressures and, in general, increased the booster base pressure by at least a factor of two for most cases shown. In the launch configuration, power off, the yaw plane base pressures were much higher than when the two models were separated.

The effect of the relative position of the orbiter to the booster on the booster base pressures is summarized in Fig. 31. The open symbols represent the base pressure measured on the booster base, just below the upper surface of the booster. The solid symbols correspond to the average booster base pressure of the taps located in the yaw plane of the booster base. At Mach numbers 2 and 3, the variation in the orbiter position had little effect on the booster base pressure. At Mach number 5.0, there is a strong variation in the base pressure measurement obtained just below the upper surface of the booster (Fig. 31f) when the power simulation was on.

The variation in booster and orbiter base pressure at zero angle of attack with free-stream Mach number is shown in Fig. 32. This figure shows that the flow-field interference effects on the base pressures with and without plume simulation increased with increasing free-stream Mach number.
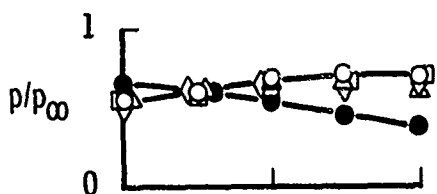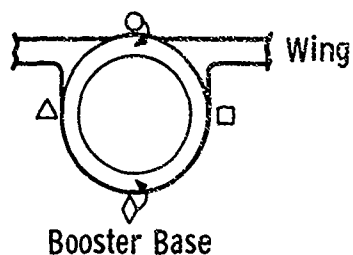
a. Interference Free and Power Off
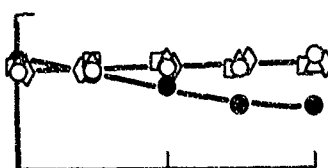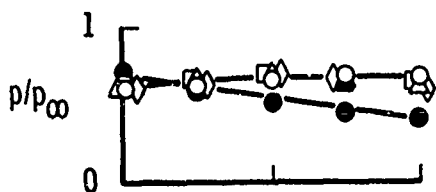
b. Launch $\Delta x/L = 0.10$, $\Delta z/L = 0.10$, and Power Off

c. $\Delta x/L = 0.23$, $\Delta z/L = 0.12$, and Power Off
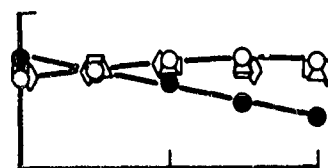
d. $\Delta x/L = 0.23$, $\Delta z/L = 0.23$, and Power Off
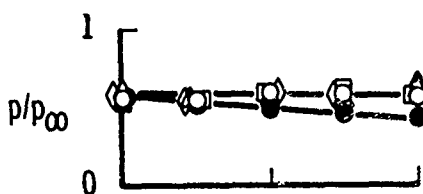
e. Interference Free and Power On
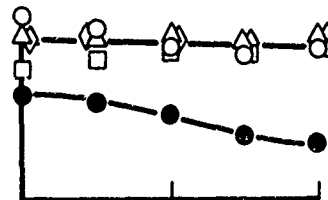
f. Launch, $\Delta x/L = 0.10$, $\Delta z/L = 0.10$, and Power On
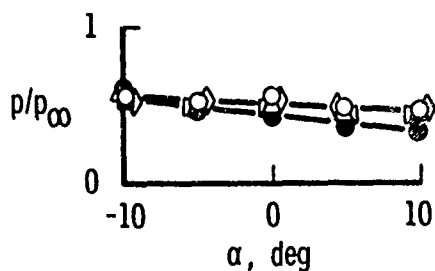
g. $\Delta x/L = 0.23$, $\Delta z/L = 0.12$, and Power On
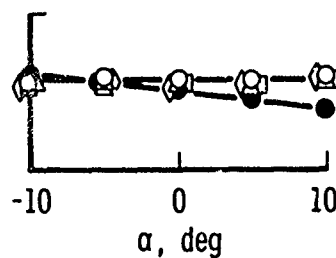
h. $\Delta x/L = 0.23$, $\Delta z/L = 0.23$, and Power On

Fig. 28 Angle-of-Attack and Power Simulation Effects on the Booster and Orbiter Base Pressures, $M_\infty = 2.00$ and $Re_\ell = 2.3 \times 10^6$ (Typically 50-percent Booster Power and 100-percent Orbiter Power Simulation)

58

Booster Base

Orbiter Base

a. Interference Free and
   Power Off

b. Launch, $\Delta x/L = 0.10$,
   $\Delta z/L = 0.10$, and Power Off

c. $\Delta x/L = 0.23$,
   $\Delta z/L = 0.12$, and Power Off

d. $\Delta x/L = 0.23$,
   $\Delta z/L = 0.23$, and Power Off

e. Interference Free and
   Power On

f. $\Delta x/L = 0.23$,
   $\Delta z/L = 0.12$, and Power On

g. $\Delta x/L = 0.23$,
   $\Delta z/L = 0.23$, and Power On
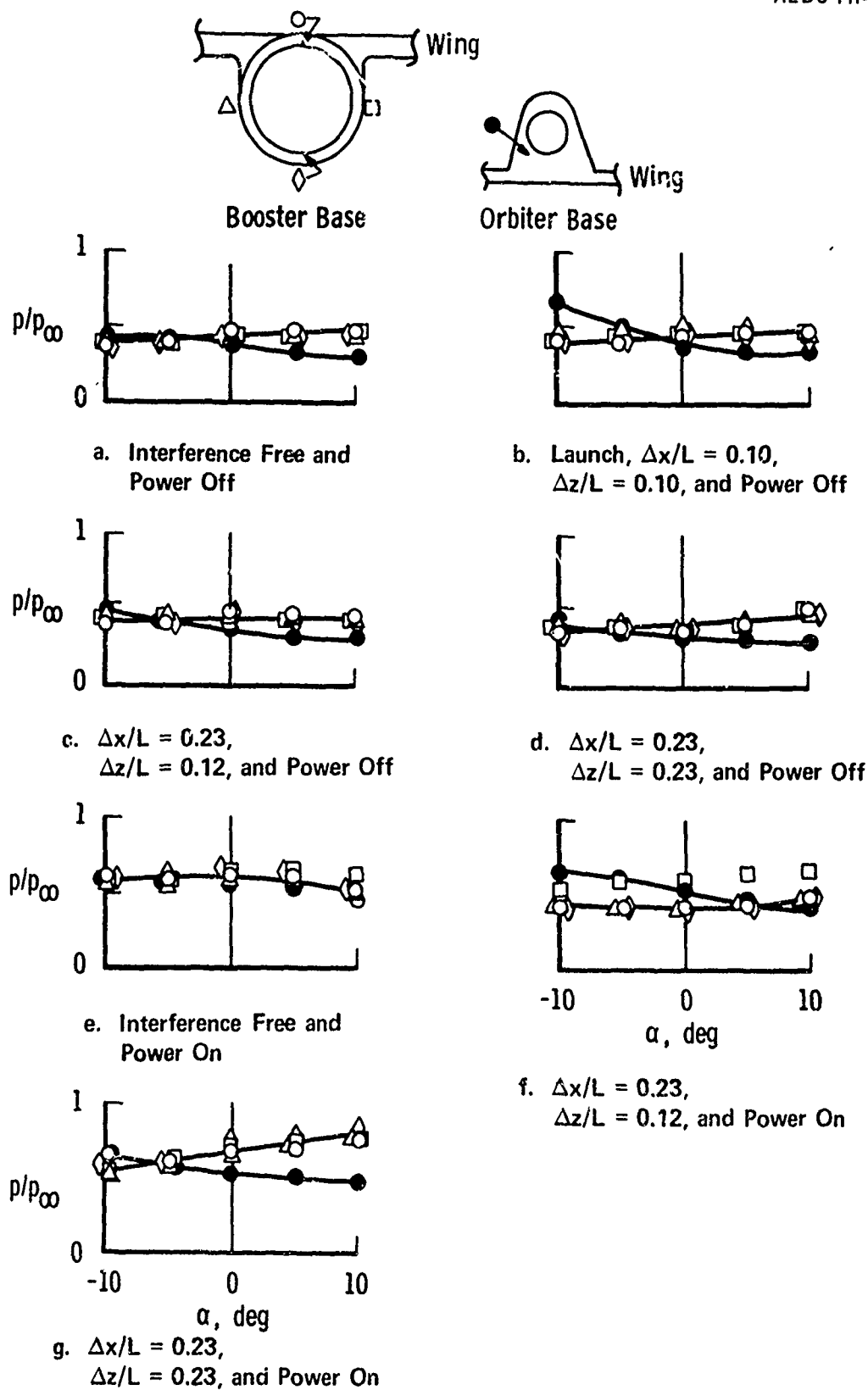
Fig. 29 Angle-of-Attack and Power Simulation Effects on the
        Booster and Orbiter Base Pressures, $M_\infty = 3.00$ and
        $Re_\ell = 2.1 \times 10^6$ (Typically, 50-percent Booster
        Power and 100-percent Orbiter Power Simulation)

a. Interference Free and Power Off

b. Launch, $\Delta x/L = 0.10$, $\Delta x/L = -0.10$ and Power Off

c. Forward, $\Delta x/L = 0.35$, $\Delta z/L = 0.12$ and Power Off

d. Forward, $\Delta x/L = 0.35$, $\Delta z/L = 0.23$ and Power Off

e. Interference Free and Power On

f. Launch, $\Delta x/L = 0.10$, $\Delta z/L = 0.10$ and Power On

g. Forward, $\Delta x/L = 0.35$, $\Delta z/L = 0.12$ and Power On

h. Forward, $\Delta x/L = 0.35$, $\Delta z/L = 0.23$ and Power On
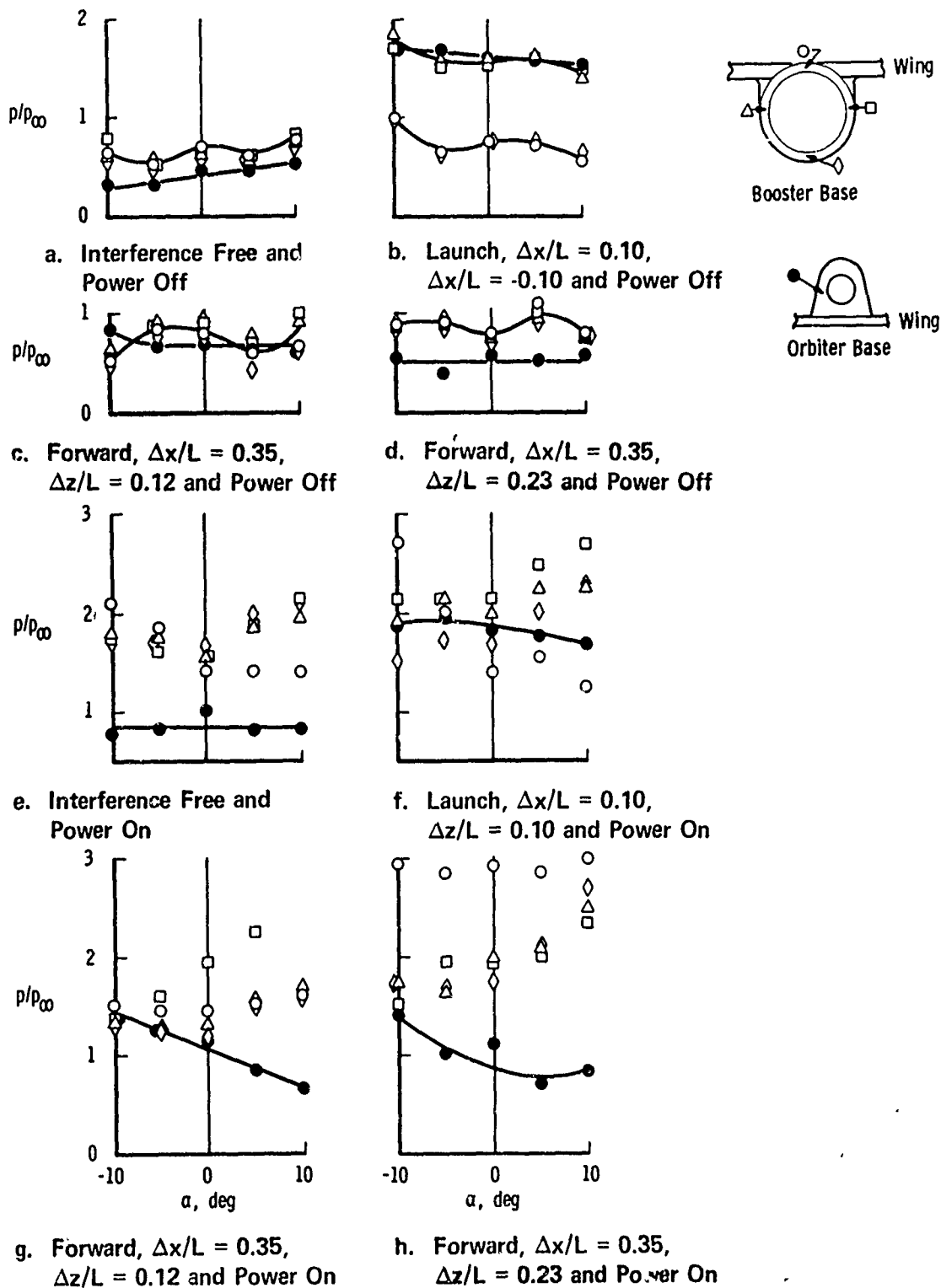
Fig. 30 Angle-of-Attack and Power Simulation Effects on the Booster and Orbiter Base Pressures, $M_\infty = 4.97$ and $Re_\ell = 1.5 \times 10^6$ (Typically, 50-percent Booster Power and 100-percent Orbiter Power Simulation)

60

Sym Δz/L
○   Launch⎫ Wing Trailing
△   0.120 ⎪ Edge - Body
□   0.151 ⎬ Base Pressure
◇   0.228 ⎭ Tap
⬤▲■◆ Average of the Base
      Pressure in Yaw
      Plane of the Booster

Open Symbols:
Base Pressure

Booster Base

Solid Symbols:
Average Base Pressure
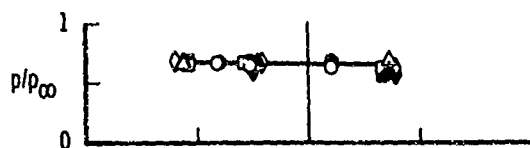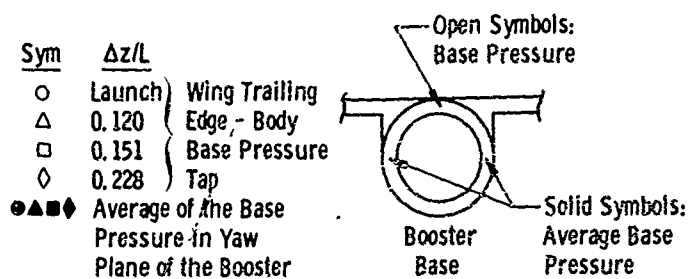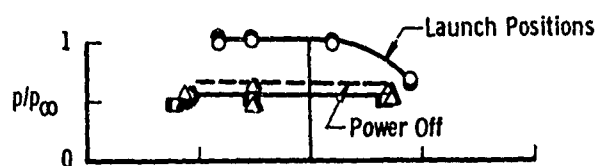
a. Power Off, M_∞ = 2.00

b. 100-percent Orbiter Power and 50-percent Booster
    Power, M_∞ = 2.00
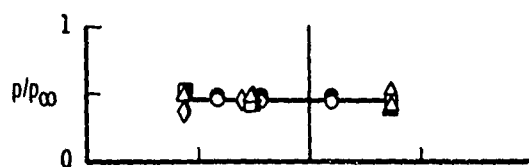
c. Power Off, M_∞ = 3.06
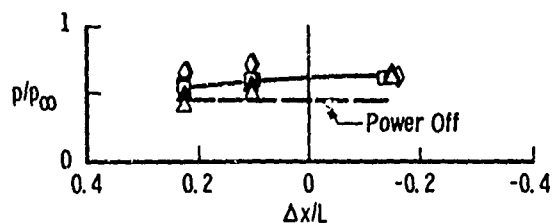
d. 100-percent Orbiter Power and 50-percent Booster
    Power, M_∞ = 3.00
    Fig. 31 Orbiter Positioning Effects on the Booster
             Base Pressure Distributions, a = 0

61
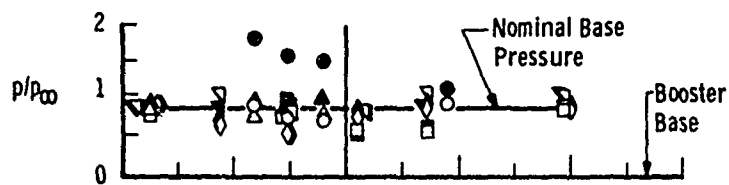
e. Power Off, $M_\infty = 4.97$

Sym	$\Delta z/L$
$\bigcirc$	Launch
$\triangle$	0.114
$\square$	0.120
$\Diamond$	0.151
$\triangledown$	0.228
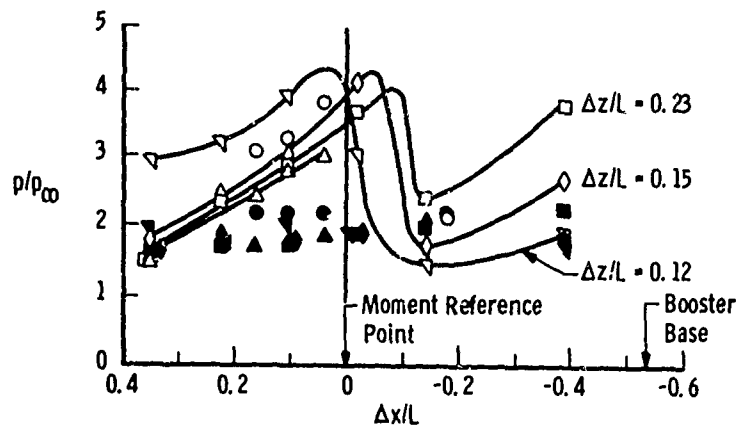
f. 100-percent Orbiter Power and 50-percent Booster Power, $M_\infty = 4.97$

Fig. 31 Concluded
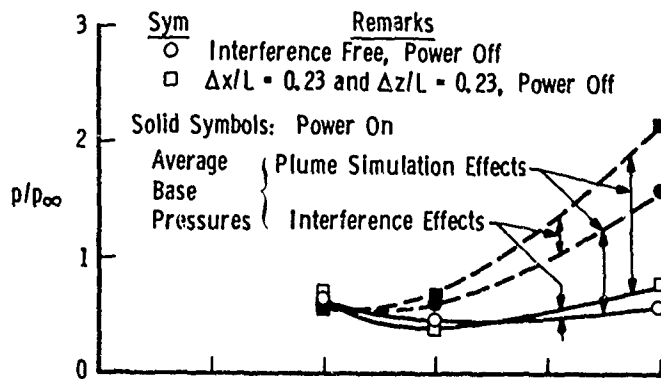
a. Booster
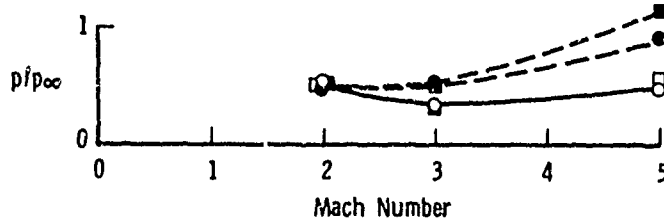
b. Orbiter

Fig. 32 Mach Number Effects on the Booster and Orbiter Base Pressure

SECTION V
SUMMARY

This test program has demonstrated that plume simulation can affect the aerodynamic interference on wind tunnel model configurations used to simulate the staging of the space shuttle vehicles in a supersonic stream. Several significant effects were observed during the test program:

1. When the models were in close proximity or in the launch position, the aerodynamic interference (other than the plume impingement loading) between the orbiter and booster was altered by the plume simulation, particularly at Mach numbers 3 and 5.

2. For altitude conditions simulated, plume impingement loading on the booster was present at all free-stream Mach numbers, but the maximum impingement loading occurred at the highest free-stream Mach number tested ($M_\infty = 5$) with the relative angle of incidence between the orbiter and booster equal to 5 deg. Also, as expected, the maximum impingement loading occurred when the models were in the launch position or in close proximity to each other.

3. The plume impingement effects tend to override or dominate any other aerodynamic flow field disturbance produced by one body on another. In many instances, the plume impingement loading remained unaffected by variations in the model angle of attack, whereas the interference data obtained without plume simulation or upstream of the plume impingement loading were strongly influenced by the angle of attack.

4. A comparison of plume impingement loading (with and without an external stream) indicated at Mach number 5, at least, that the lateral dimension of the plume impingement loading increased significantly when the external stream was present, even though the size of the plume in the pitch plane of the models was not significantly altered.

5. At Mach number 5, some plume-induced separation effects were observed on both models, but this separation was not observed at the lower free-stream Mach numbers.

63

The results obtained by integrating the pressure-distributions were quite useful in evaluating the variations in the local loading coefficient distributions on the space shuttle configurations produced by the aerodynamic interference between the two models and the plume impingement. In terms of the incremental changes in the resultant normal force and pitching moment coefficients produced by the aerodynamic interference and by the plume impingement, a fairly good comparison was obtained between the integrated pressure data and the force and moment data of Ref. 1.

REFERENCES

1. Burt, R. H. "Abort Separation, Longitudinal Force, and Moment Characteristics of McDonnell Douglas Booster and Orbiter Space Shuttle Vehicles at Mach Numbers 2.0 to 6.0." AEDC-TR-72-11

2. Sims, Joseph L. "Plume Simulation for Space Shuttle Abort Staging Aerodynamic Testing." NASA-MSFC-S&E-AERO-AF-70-6, December 1970.

3. Baker, L. Ray, Jr. "Calibration of Propulsion Simulation Nozzles for Space Shuttle Booster and Orbiter Models for Abort/Separation Staging Experimental Program." LMSC/HREC D225144, July 1971.

APPENDIX I
GRAPHICAL PRESENTATION OF PLUME FLOW-FIELD PITOT
PRESSURE AND CALIBRATION DATA
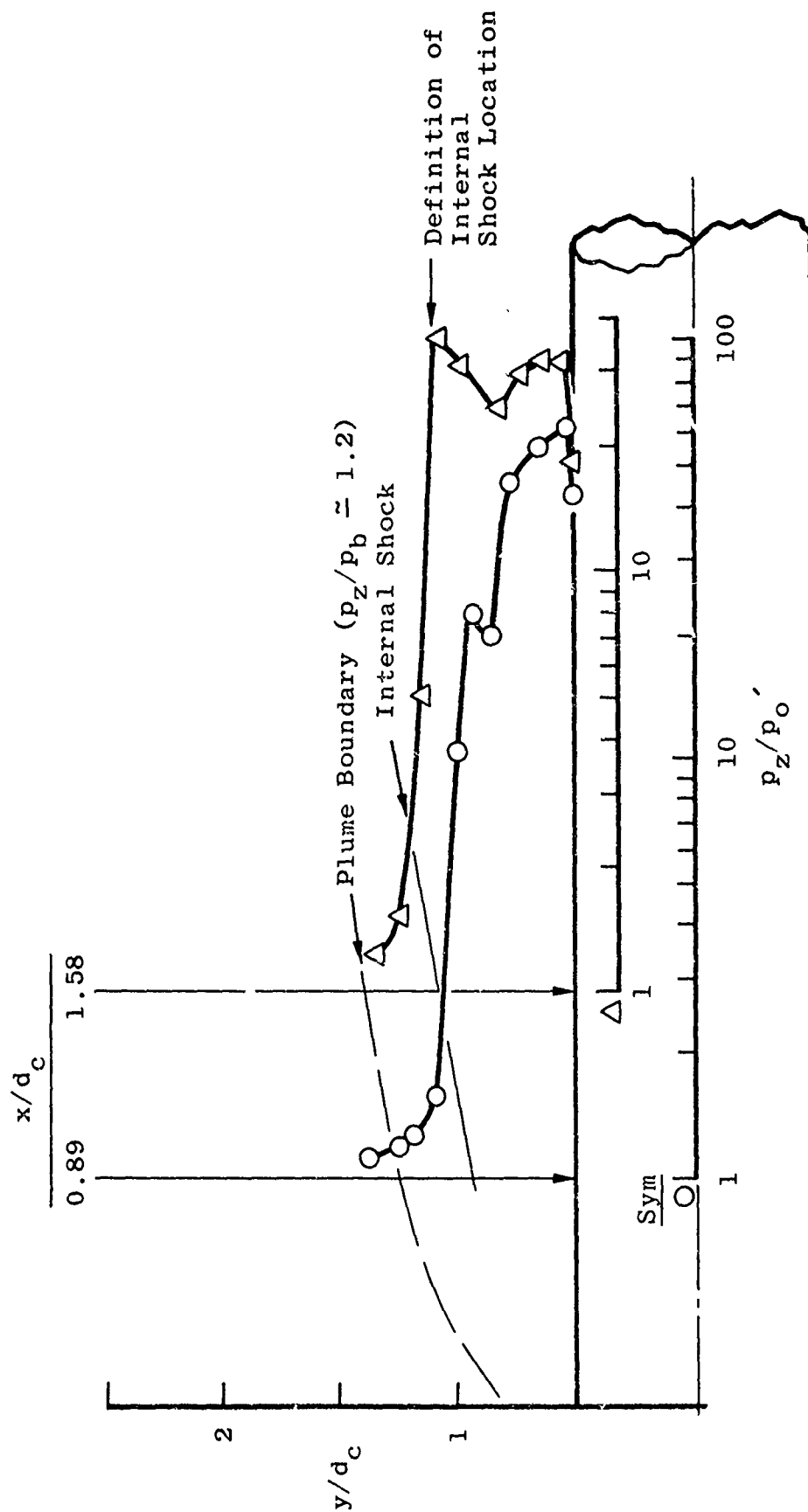
a. Pitot Pressure Surveys with a Gap Setting of 0.512 in.
Fig. I-1 Orbiter Nozzle Plume Flow Field Survey Results
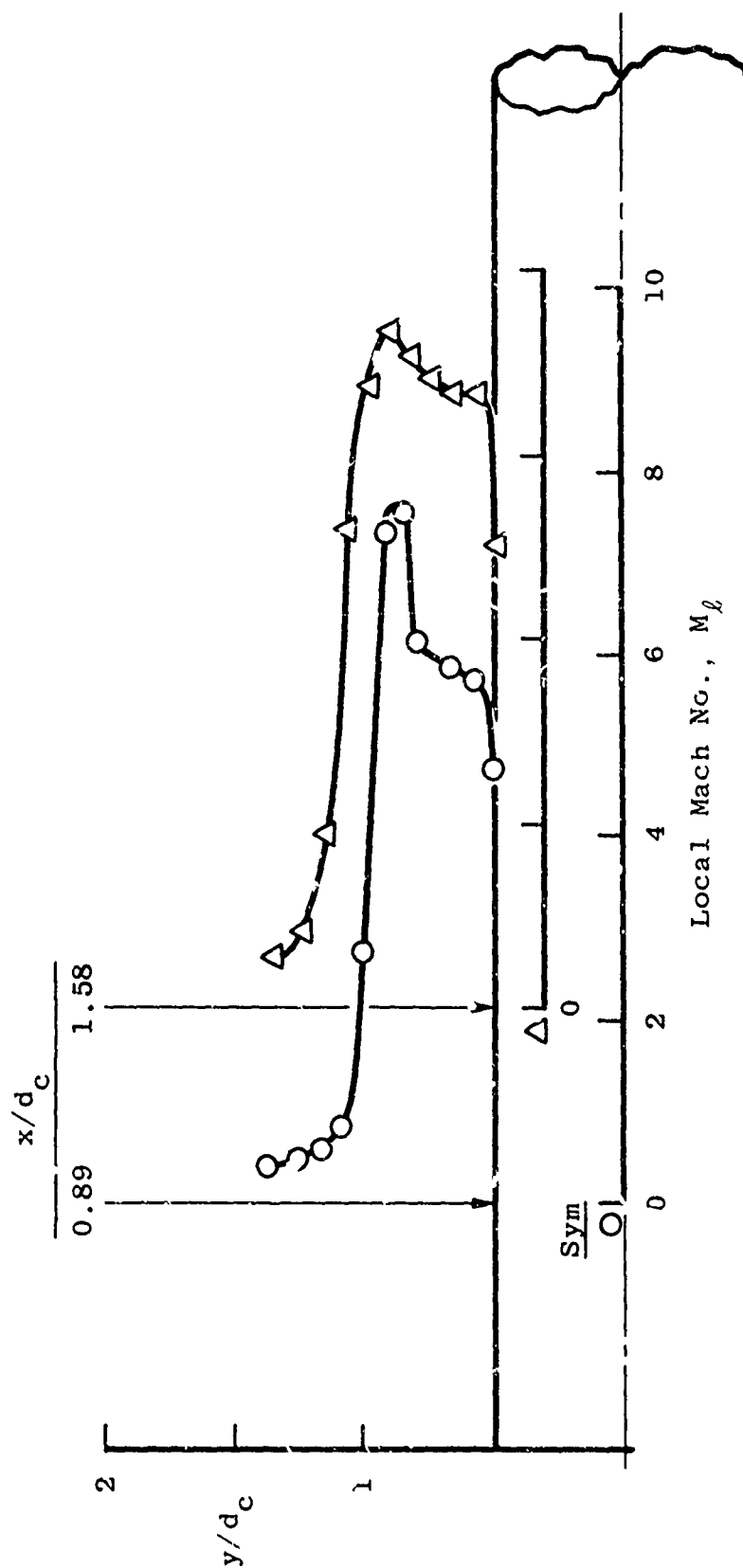
j. Mach Number Distributions with a Gap Setting of 0.512
Fig. I-1 Continued
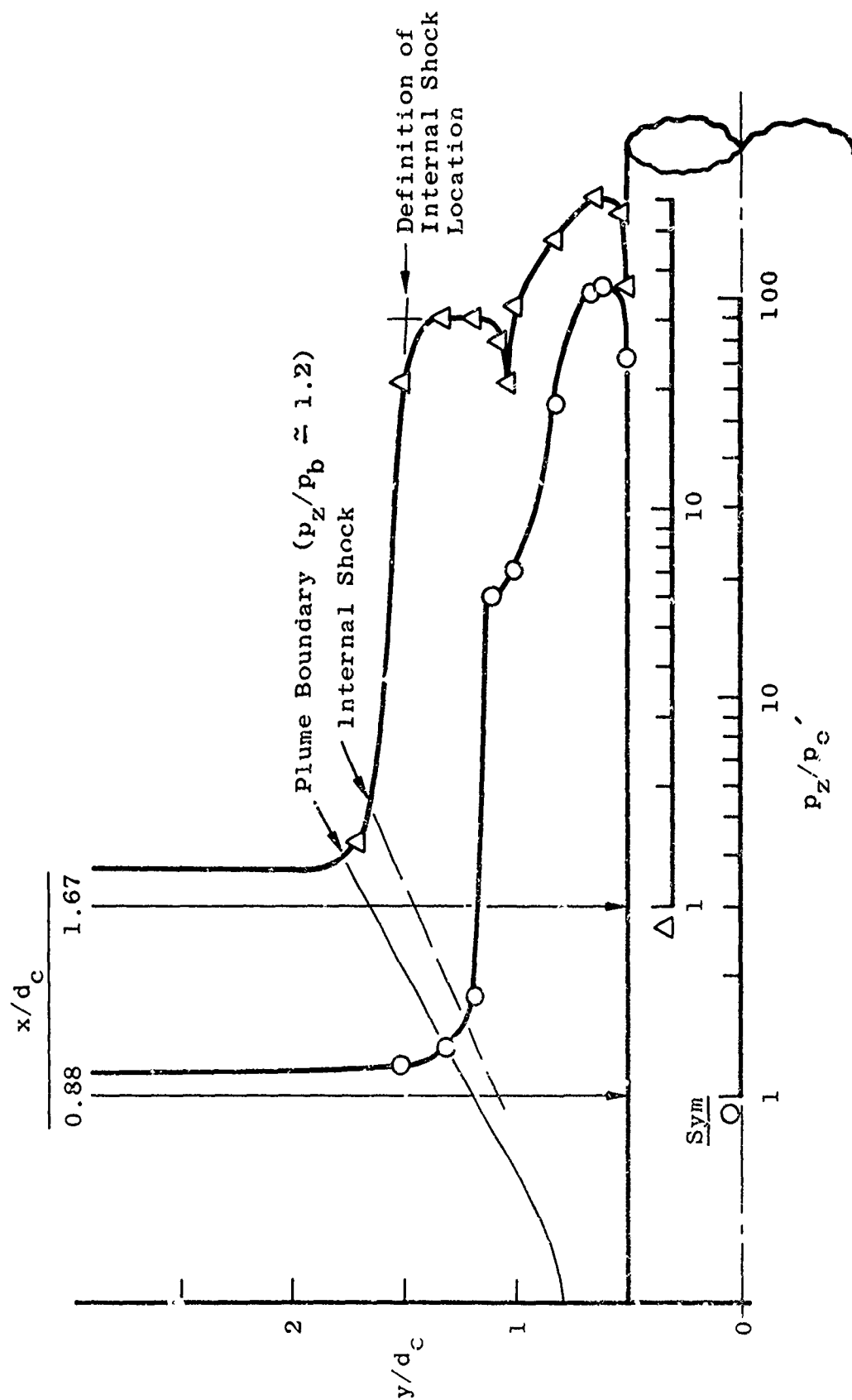
c. Pitot Pressure Surveys with a Gap Setting of 0.478 in.
Fig. I-1 Continued
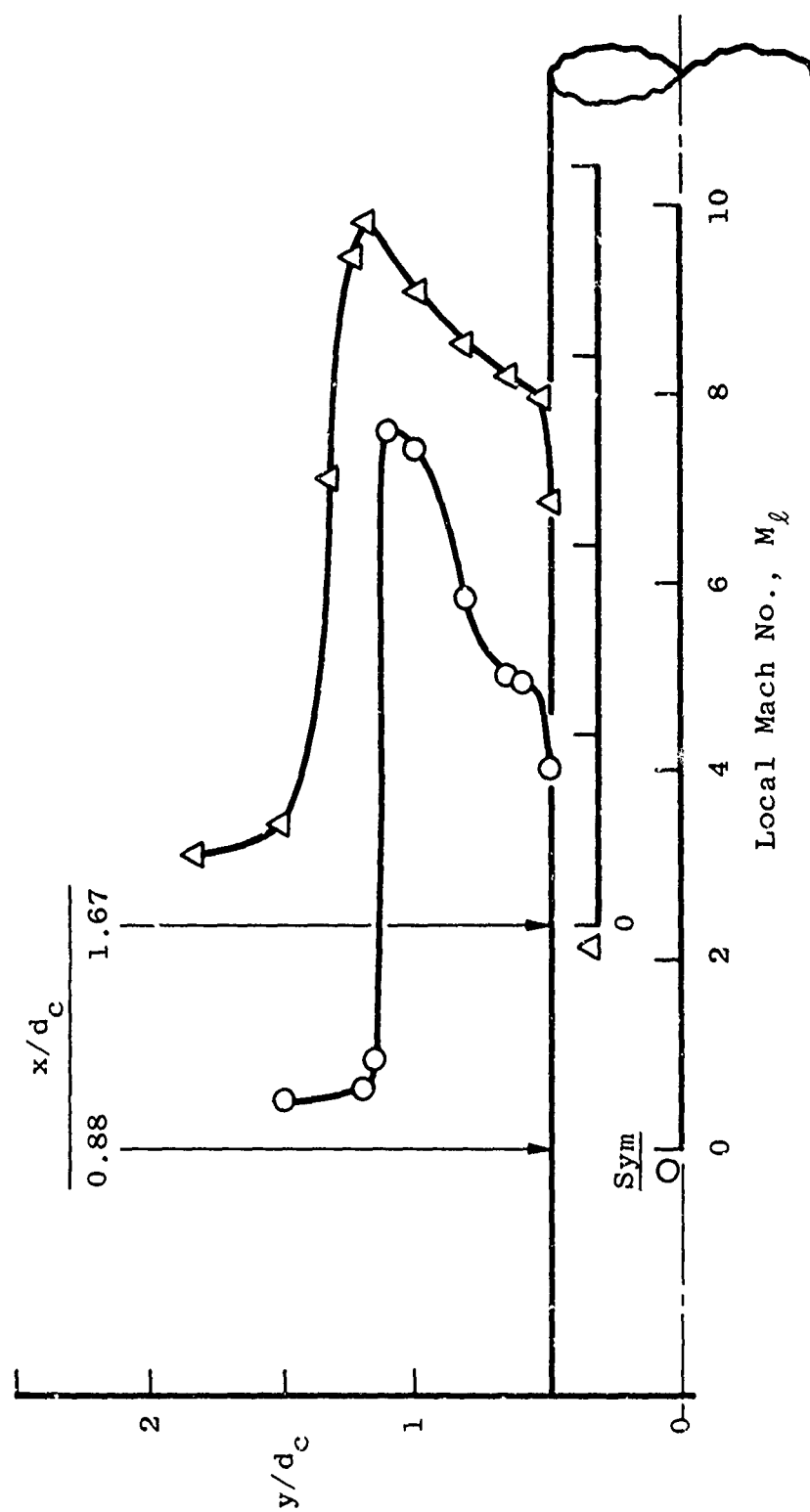
d. Mach Number Distribution with a Gap Setting of 0.478
Fig. l-1 Concluded
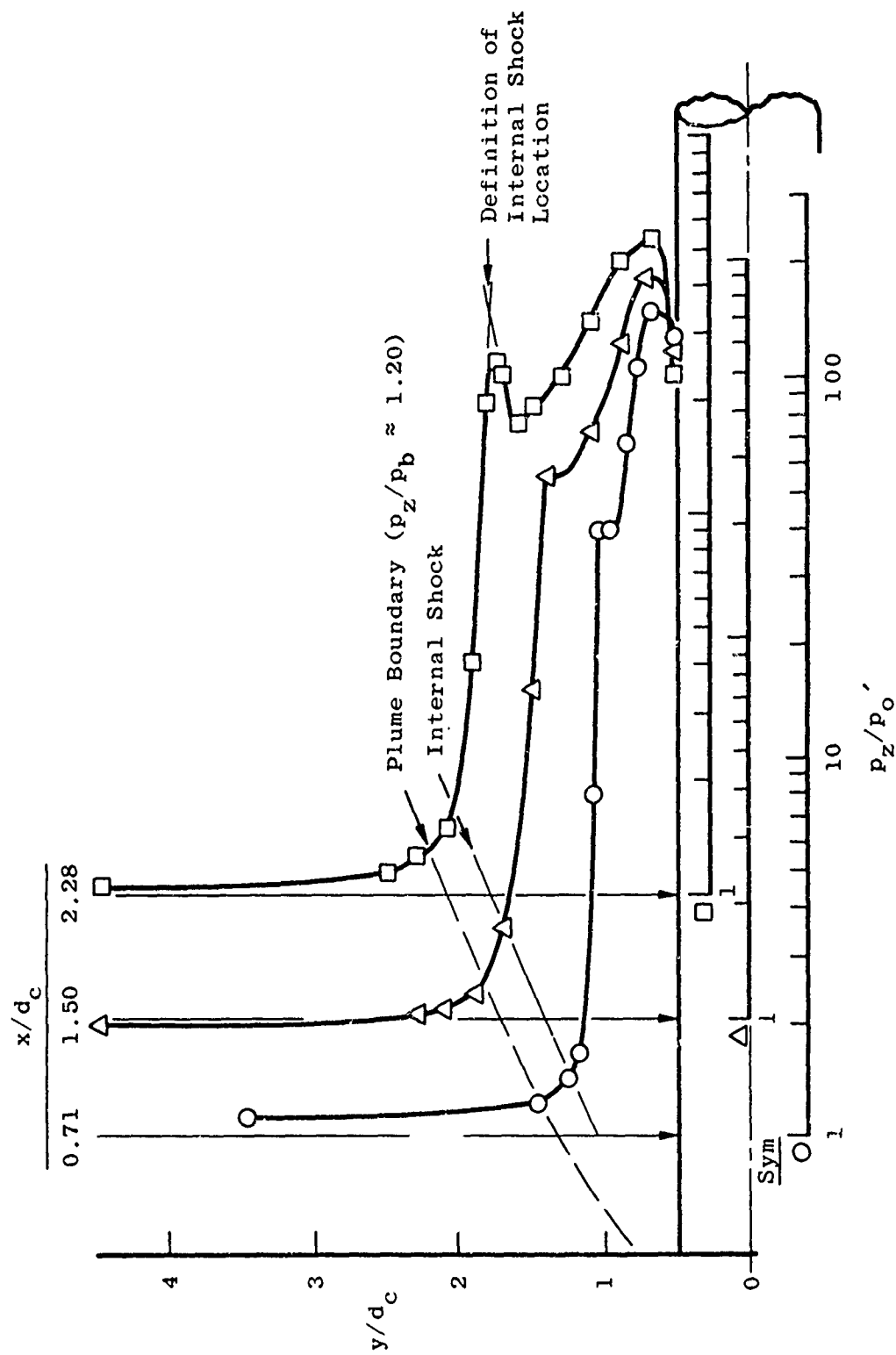
a. Pitot Pressure Surveys with a Gap Setting of 0.542 in.
Fig. I-2 Booster Nozzle Plume Flow Field Survey Results
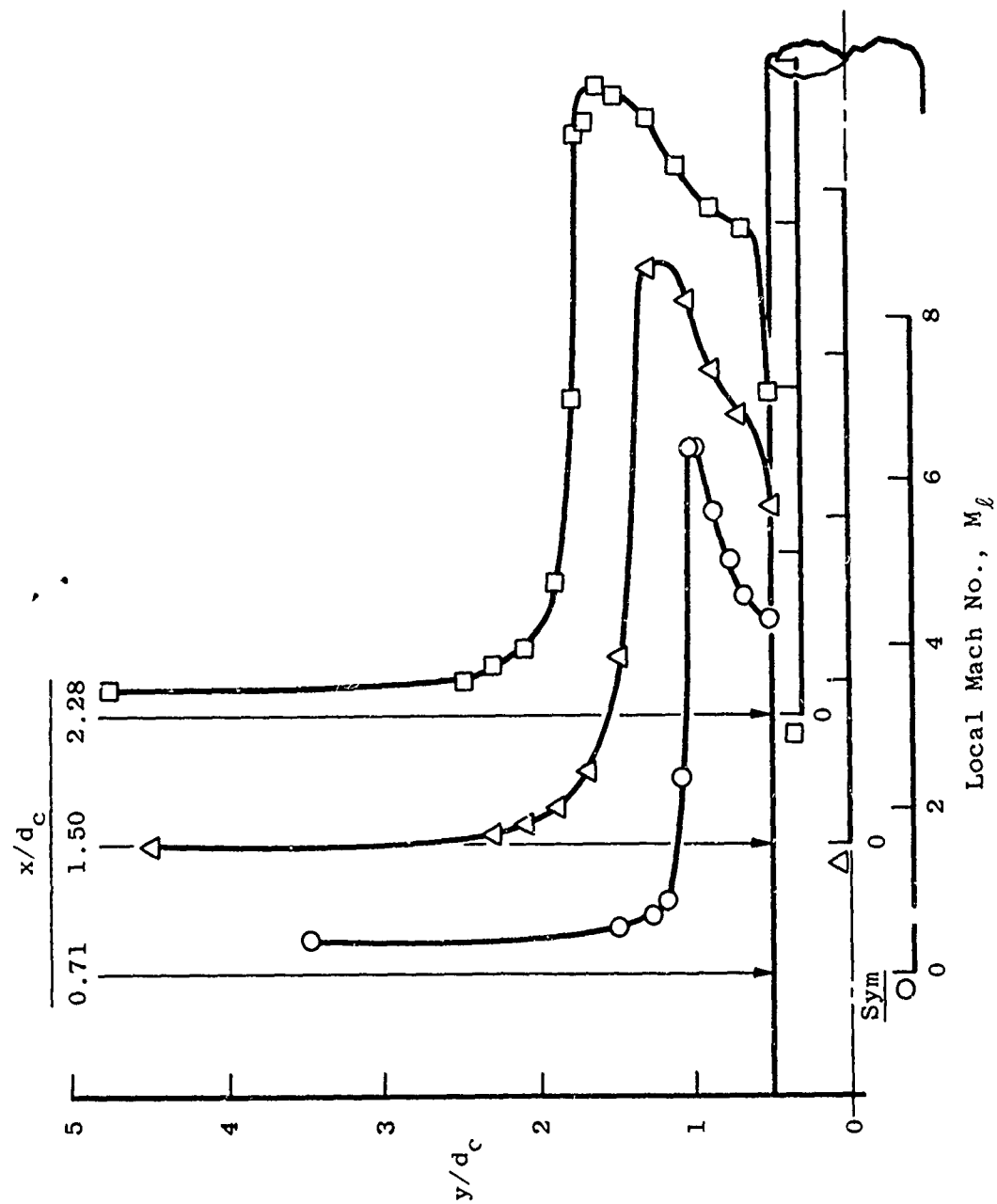
b. Mach Number Distributions with a Gap Setting of 0.542 in.
Fig. I-2 Continued
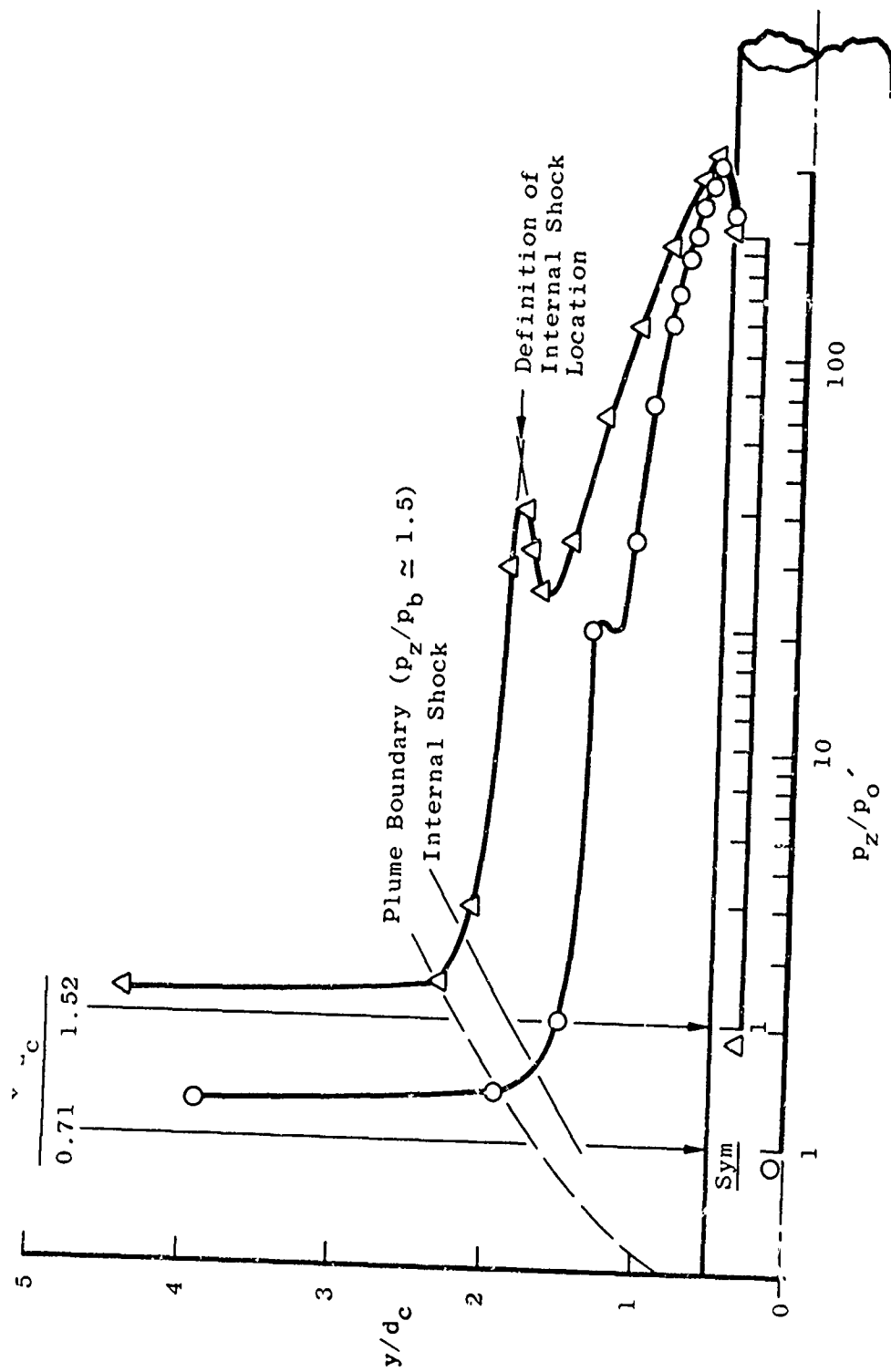
c. Pitot Pressure Surveys with a Gap Setting of 0.452 in.

Fig. I-2 Continued
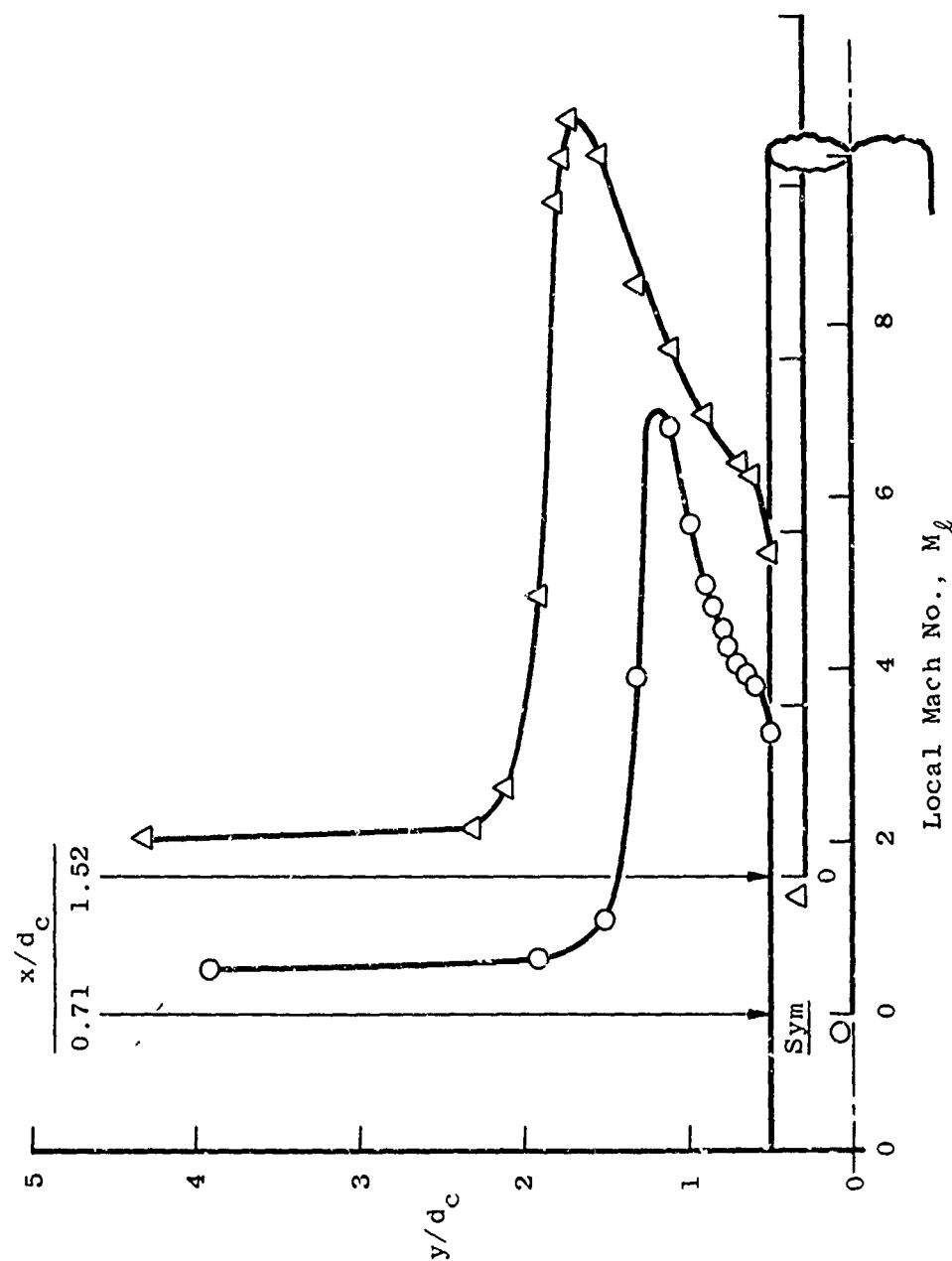
d. Mach Number Distribution with a Gap Setting of 0.452 in.
Fig. I-2 Concluded

APPENDIX II
GRAPHICAL COMPARISONS OF THE BOOSTER AND
ORBITER PRESSURE DISTRIBUTIONS

Preceding page blank
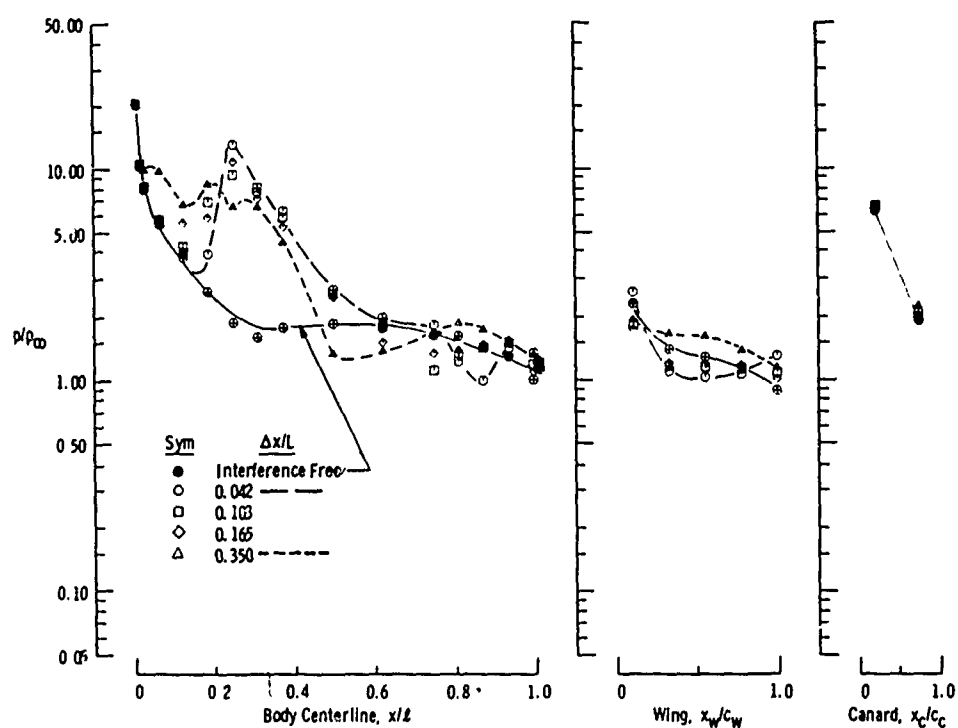
a. Booster, $\Delta z/L = 0.11$
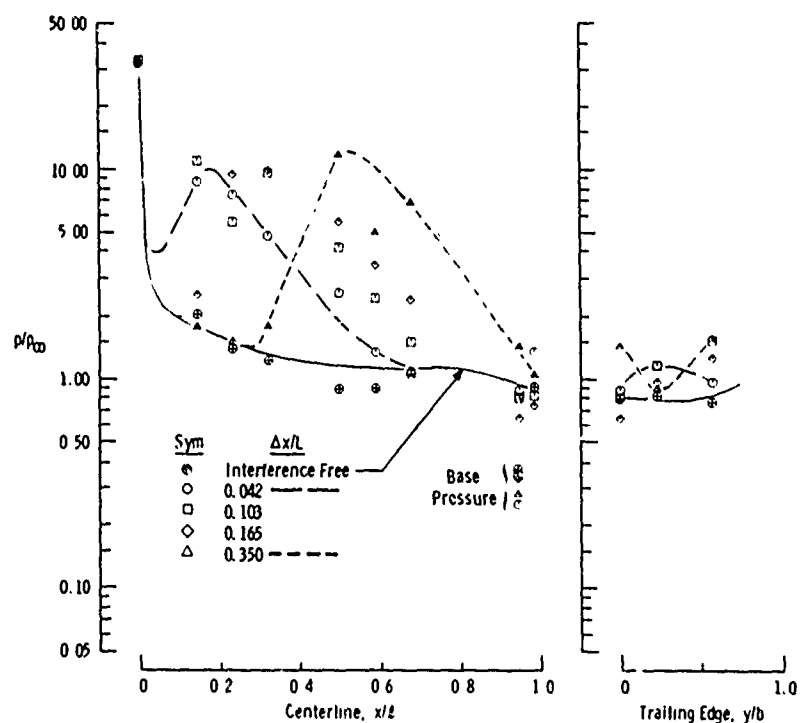
b. Orbiter, $\Delta z/L = 0.11$

Fig. II-1 Booster and Orbiter Pressure Distributions at Various Staging Positions without Plume Simulation at $a = 0$, $M_\infty = 4.97$, and $Re_\ell = 1.5 \times 10^6$ (Variables $\Delta x/L$ and $\Delta z/L$)
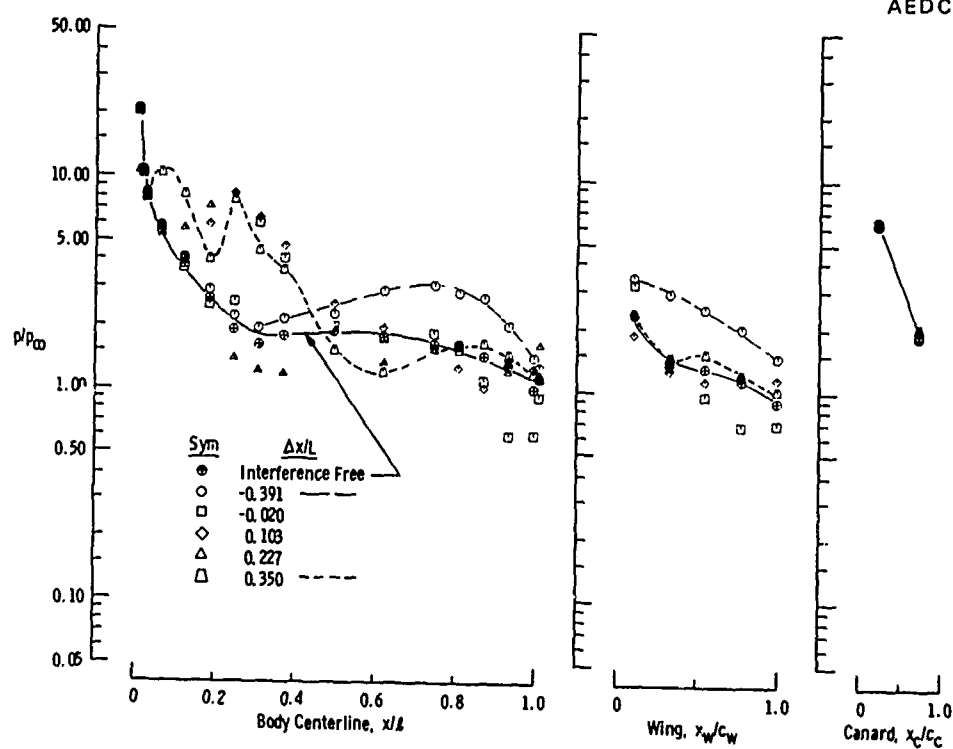
c. Booster, $\Delta z/L = 0.12$
Fig. II-1 Continued
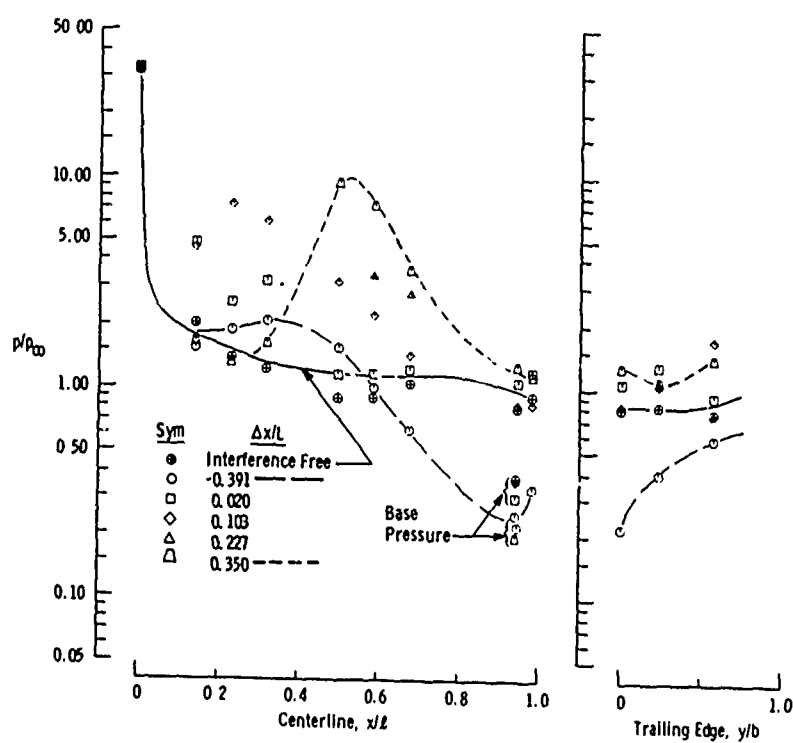
d. Orbiter, $\Delta z/L = 0.12$
Fig. II-1 Continued

77
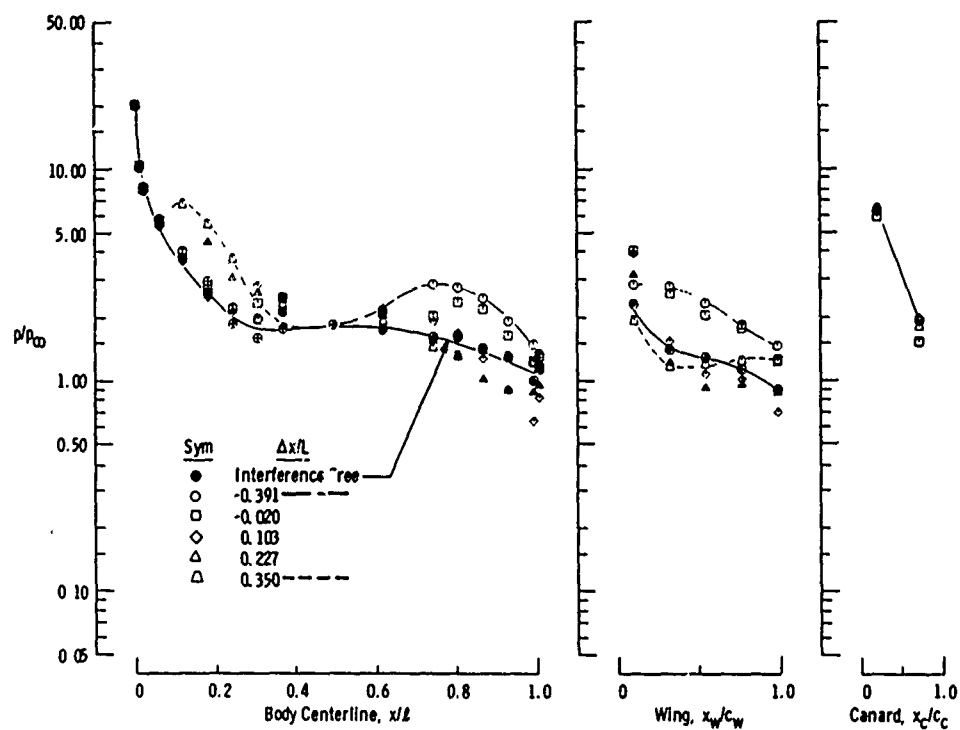
e. Booster, $\Delta z/L = 0.15$
Fig. II-1 Continued
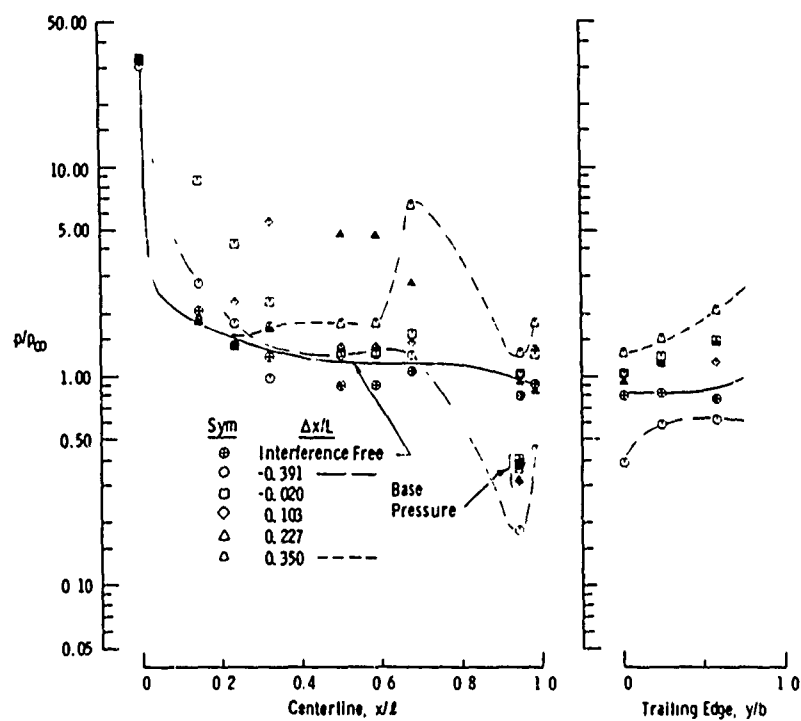
f. Orbiter, $\Delta z/L = 0.15$
Fig. II-1 Continued

78
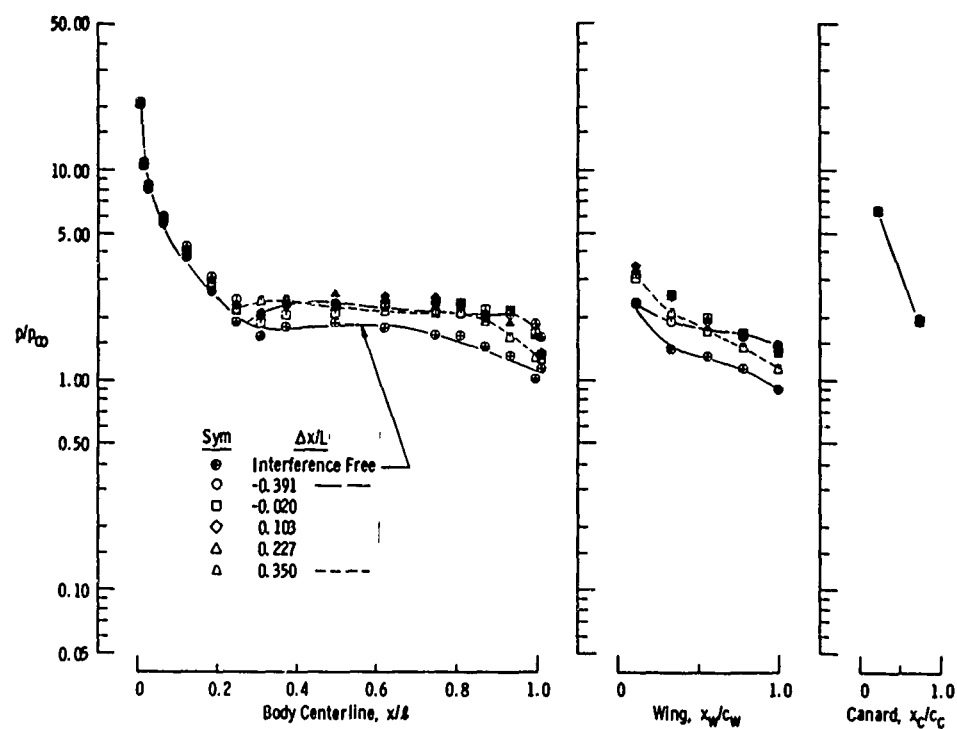
g. Booster, $\Delta z/L = 0.23$
Fig. II-1 Continued
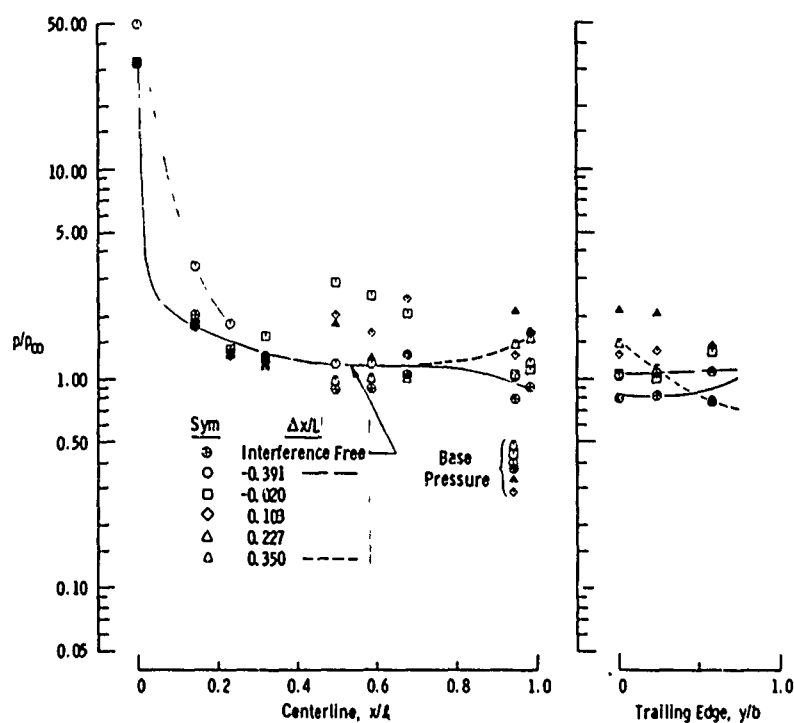
h. Orbiter, $\Delta z/L = 0.23$
Fig. II-1 Continued
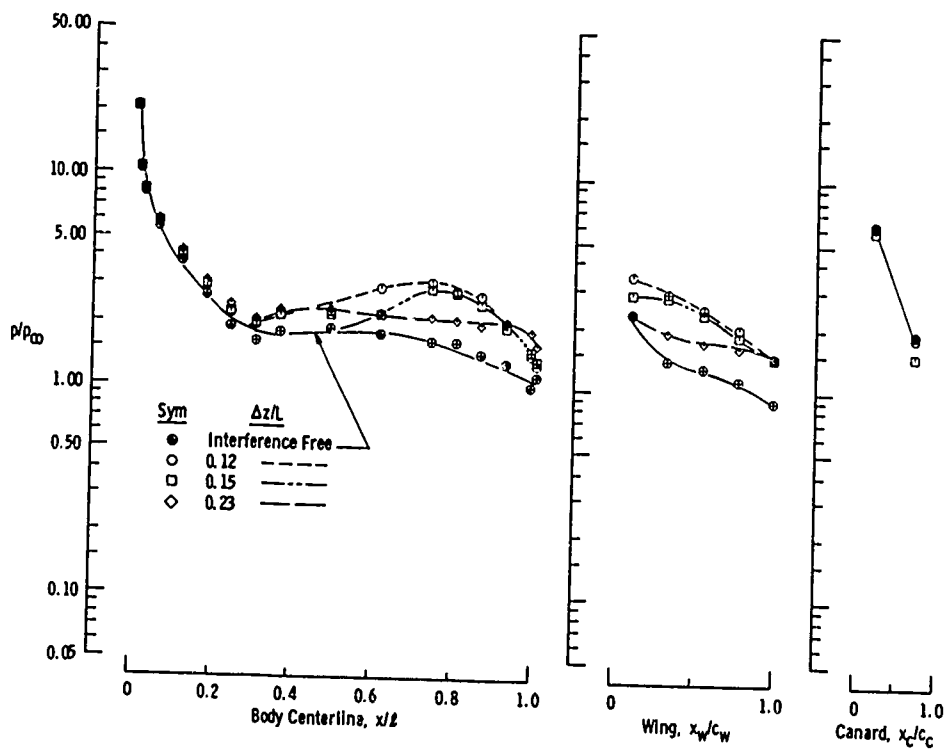
i. Booster, $\Delta x/L = -0.391$
Fig. II-1 Continued
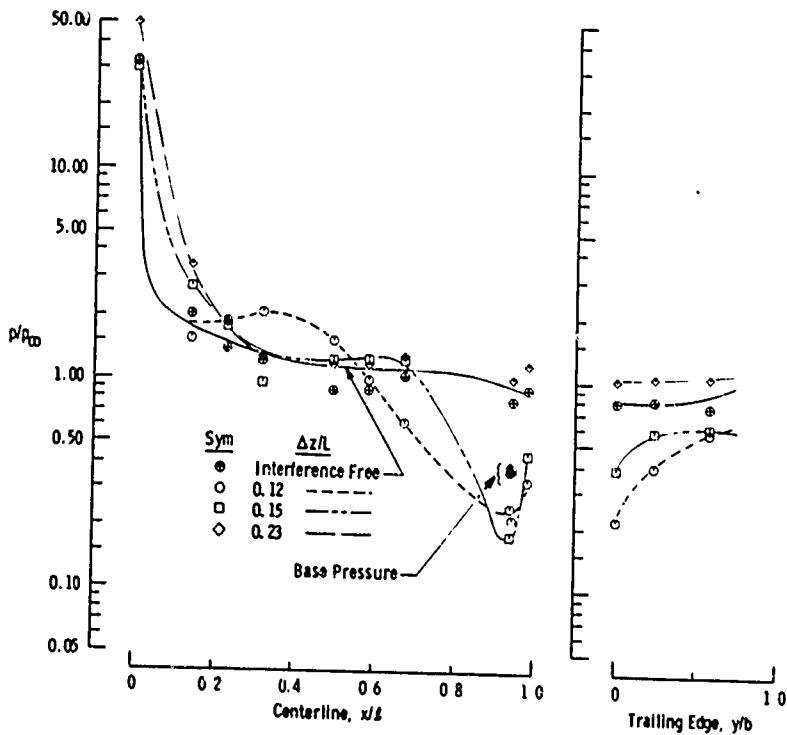
j. Orbiter, $\Delta x/L = -0.391$
Fig. II-1 Continued
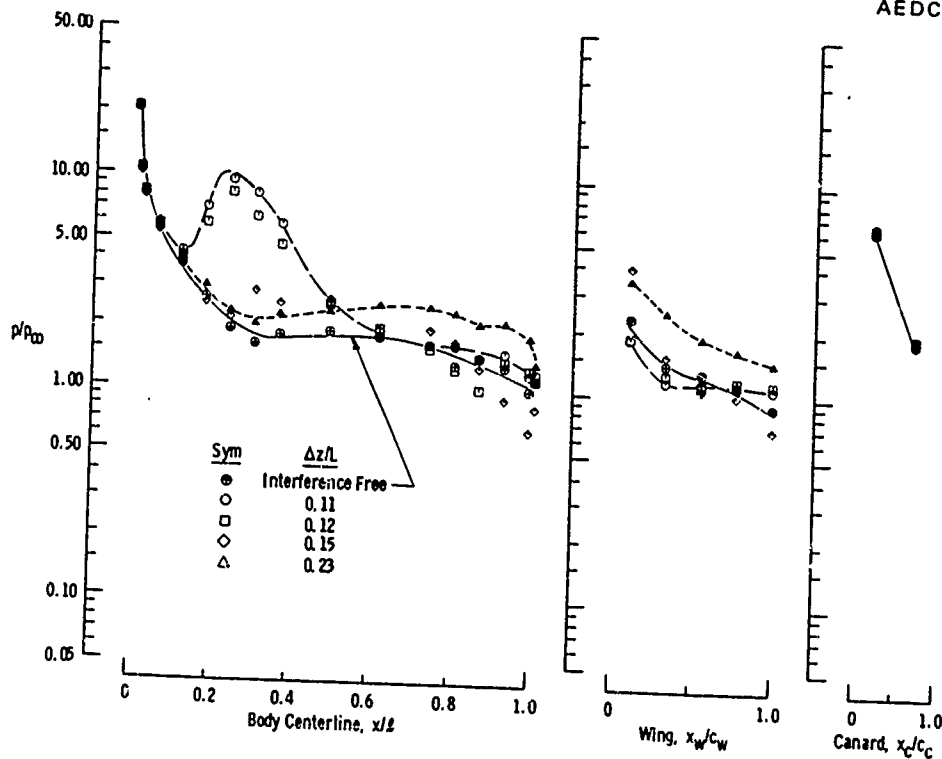
k. Booster, $\Delta x/L = 0.103$
Fig. II-1 Continued

l. Orbiter, $\Delta x/L = 0.103$
Fig. II-1 Continued

81
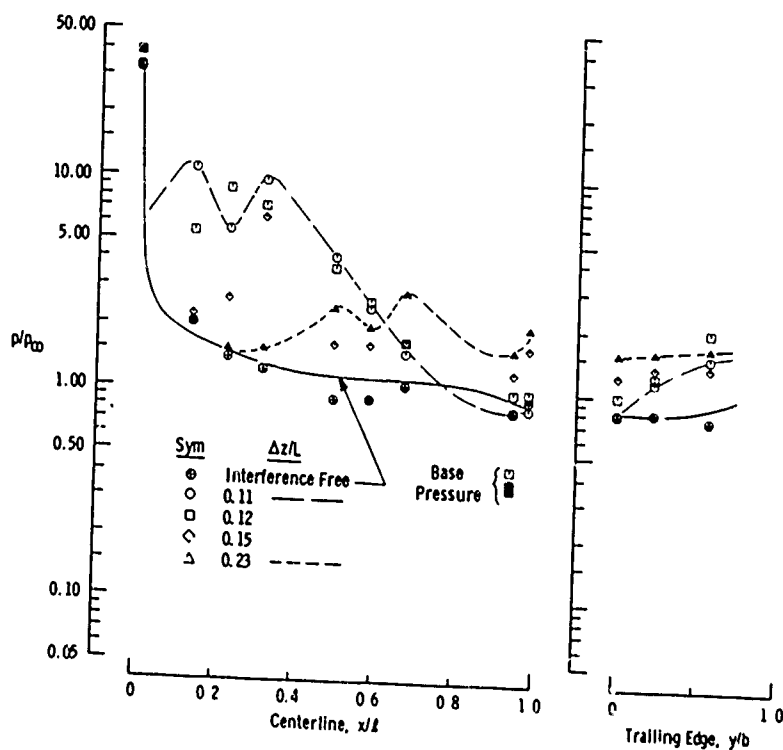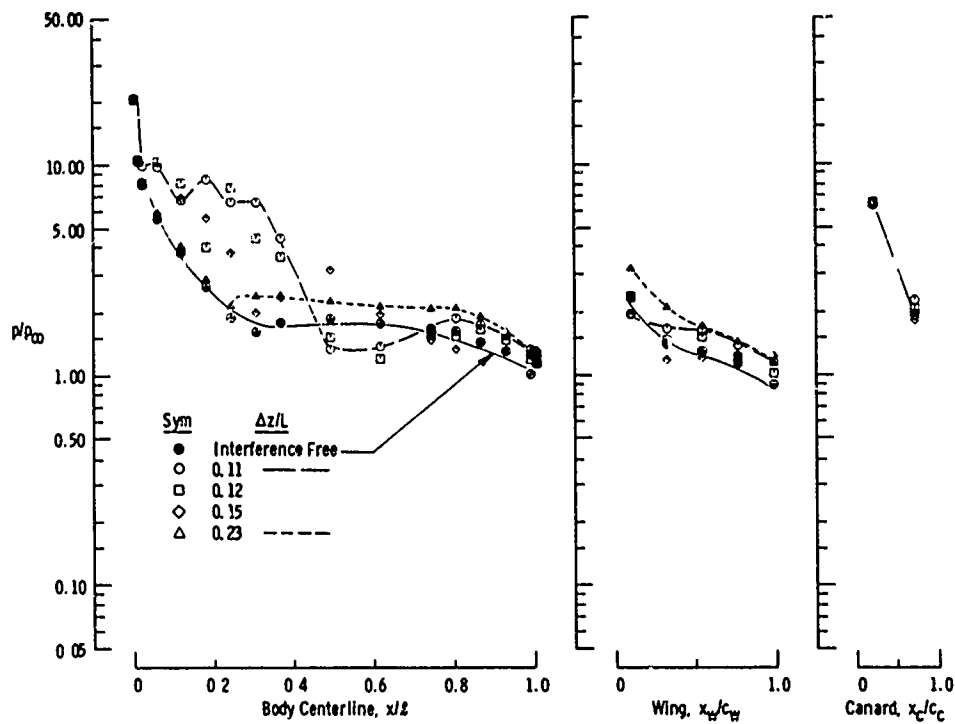
m. Booster, $\Delta x/L = 0.350$
Fig. II-1 Continued
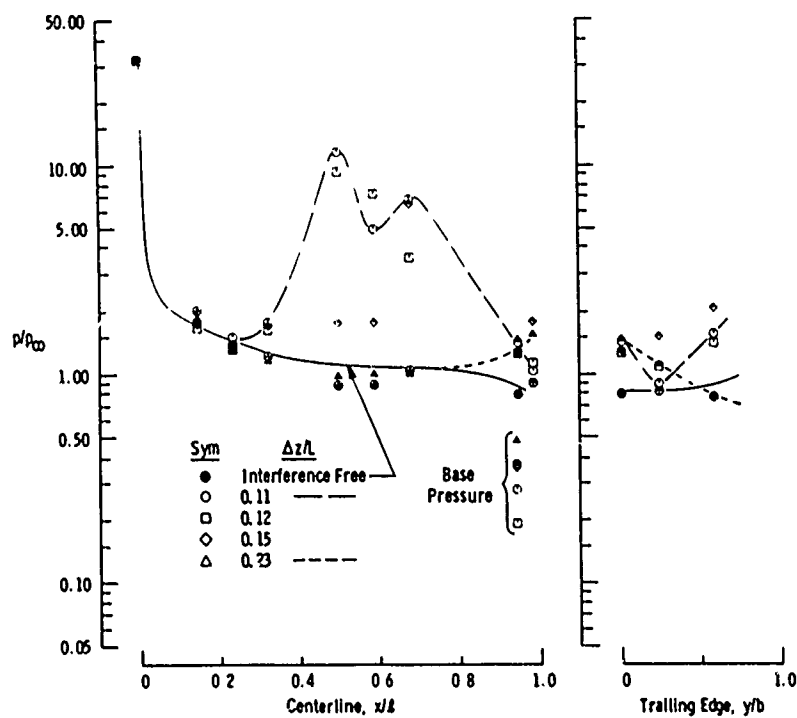
n. Orbiter, $\Delta x/L = 0.350$
Fig. II-1 Concluded
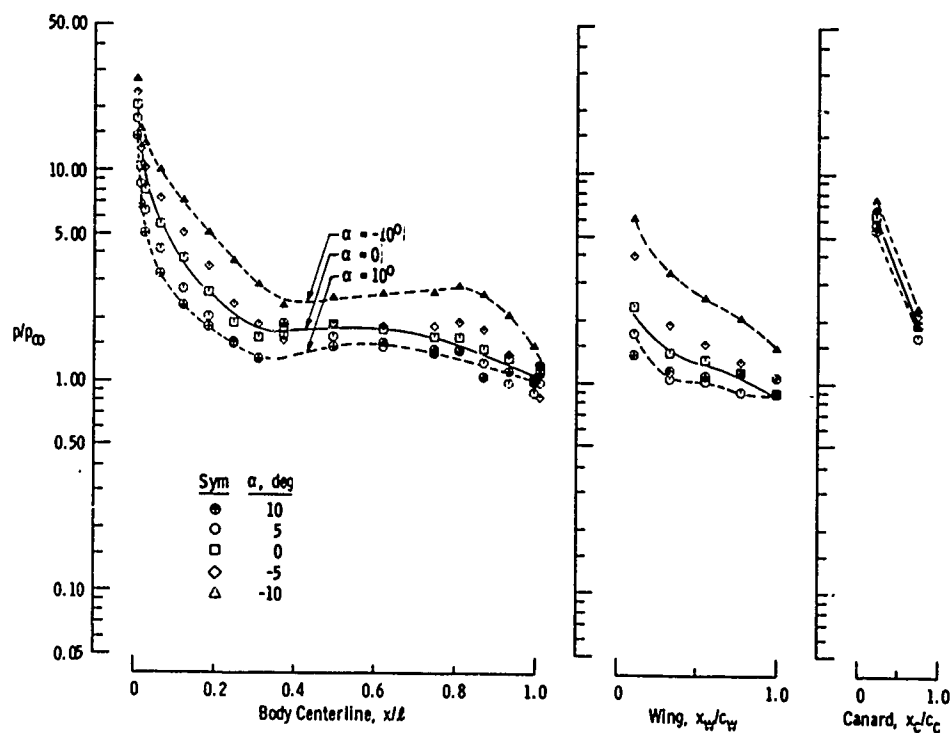
a. Booster, Interference Free
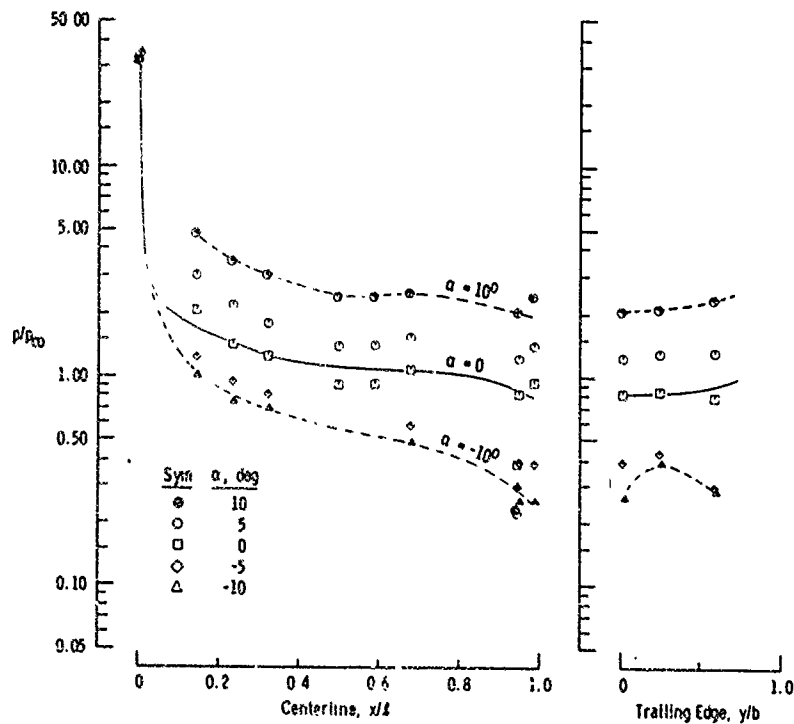
b. Orbiter, Interference Free

Fig. II-2 Angle-of-Attack Effects on the Booster and Orbiter Pressure Distributions
without Plume Simulation at $M_\infty = 4.97$, and $Re_\varrho = 1.5 \times 10^6$
(Variables $\Delta x/L$ and $\Delta z/L$)
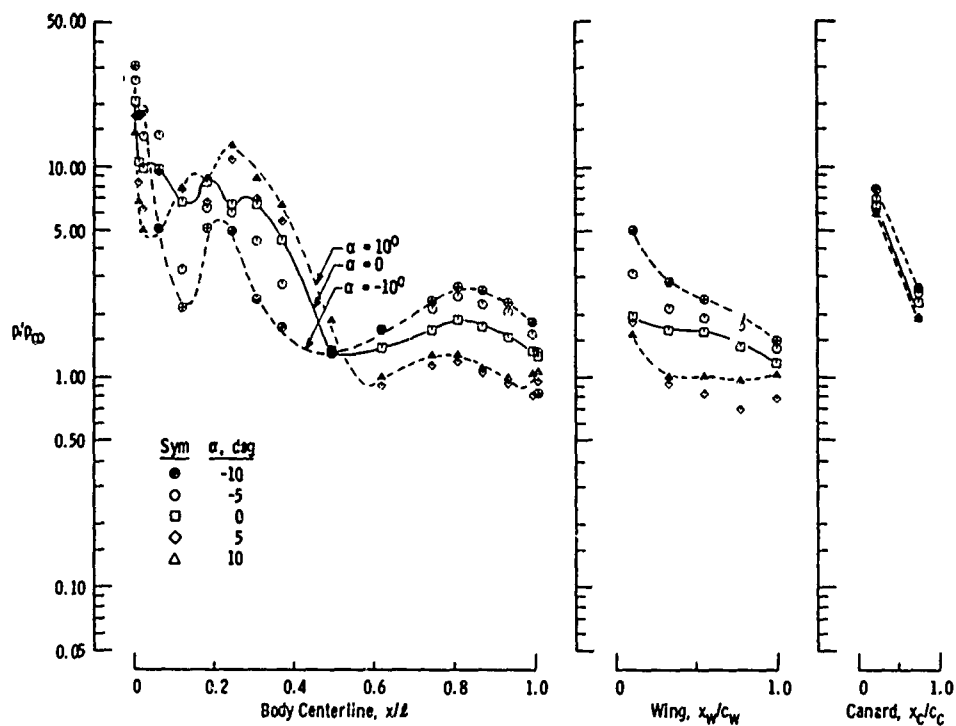
c. Booster, $\Delta x/L = 0.350$ and $\Delta z/L = 0.11$
Fig. II-2 Continued
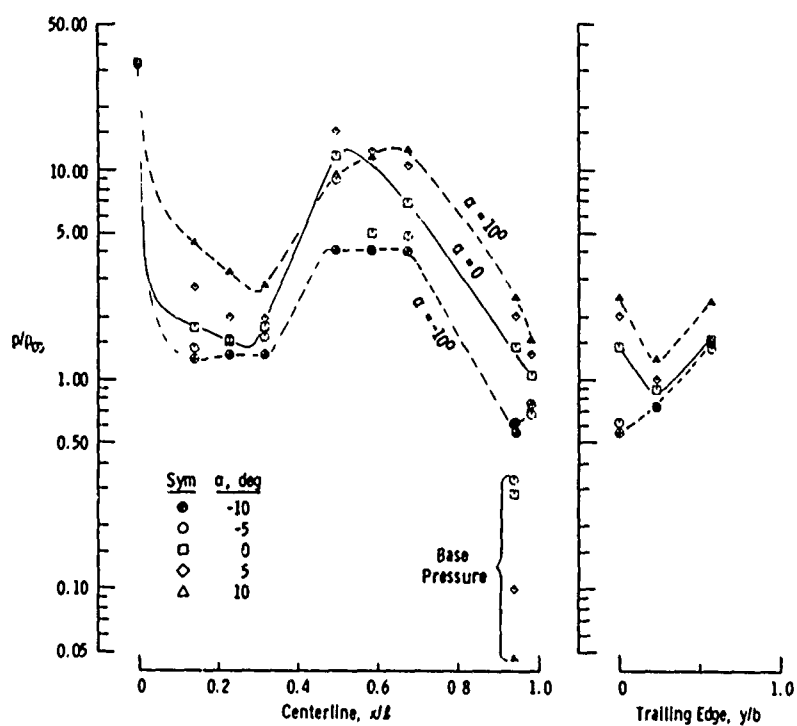
d. Orbiter, $\Delta x/L = 0.350$ and $\Delta z/L = 0.11$
Fig. II-2 Continued
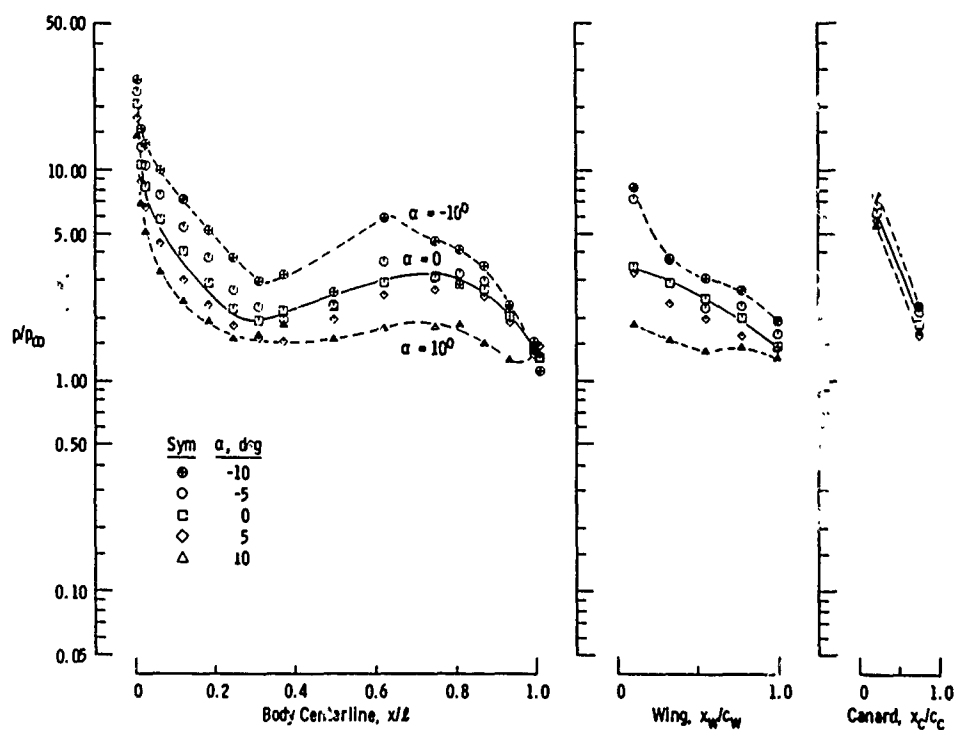
e. Booster, $\Delta x/L = -0.390$ and $\Delta z/L = 0.12$
Fig. II-2 Continued
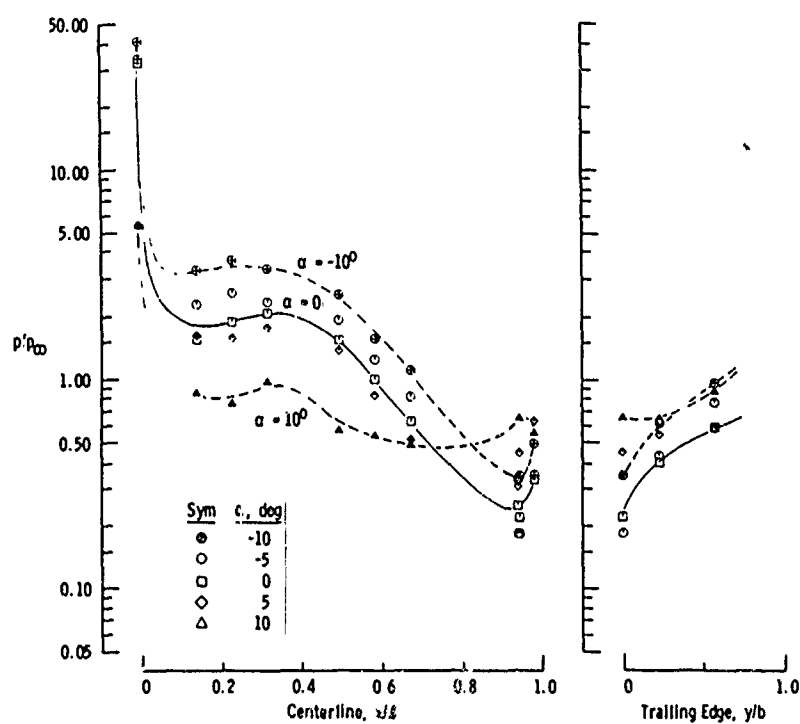
f. Orbiter, $\Delta x/L = -0.390$ and $\Delta z/L = 0.12$
Fig. II-2 Continued
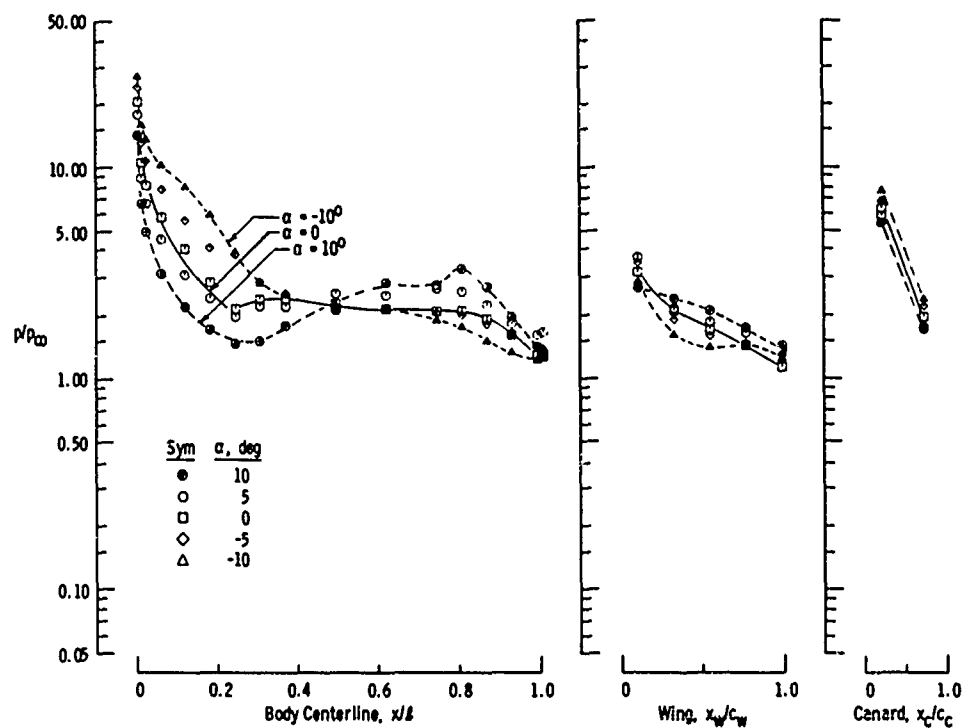
g. Booster, $\Delta x/L = 0.350$ and $\Delta z/L = 0.23$
Fig. II-2 Continued
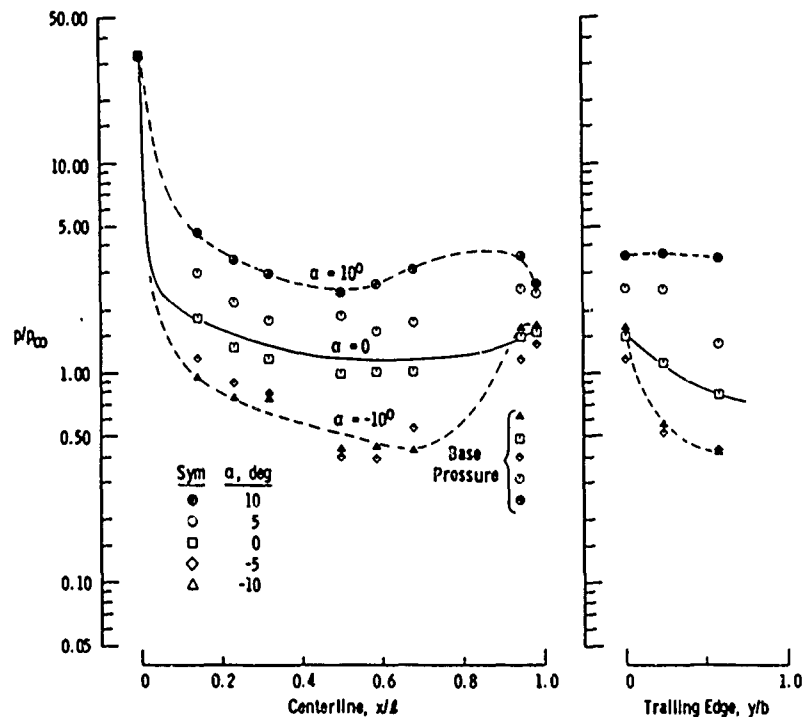
h. Orbiter, $\Delta x/L = 0.350$ and $\Delta z/L = 0.223$
Fig. I'-2 Continued
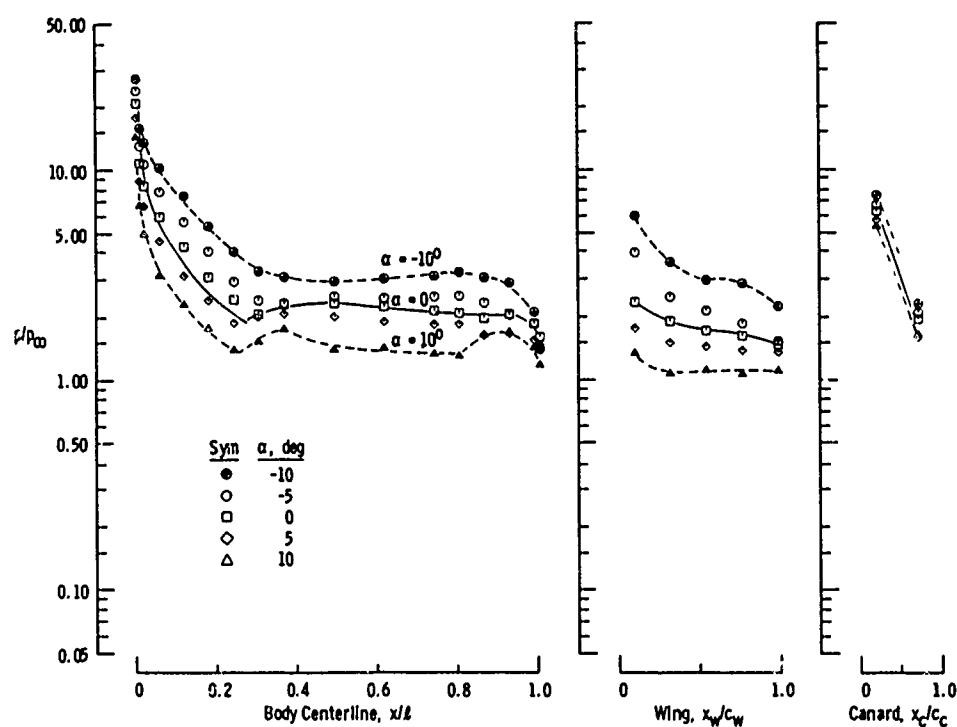
i. Booster, $\Delta x/L$ = -0.390 and $\Delta z/L$ = 0.23
Fig. II-2 Continued
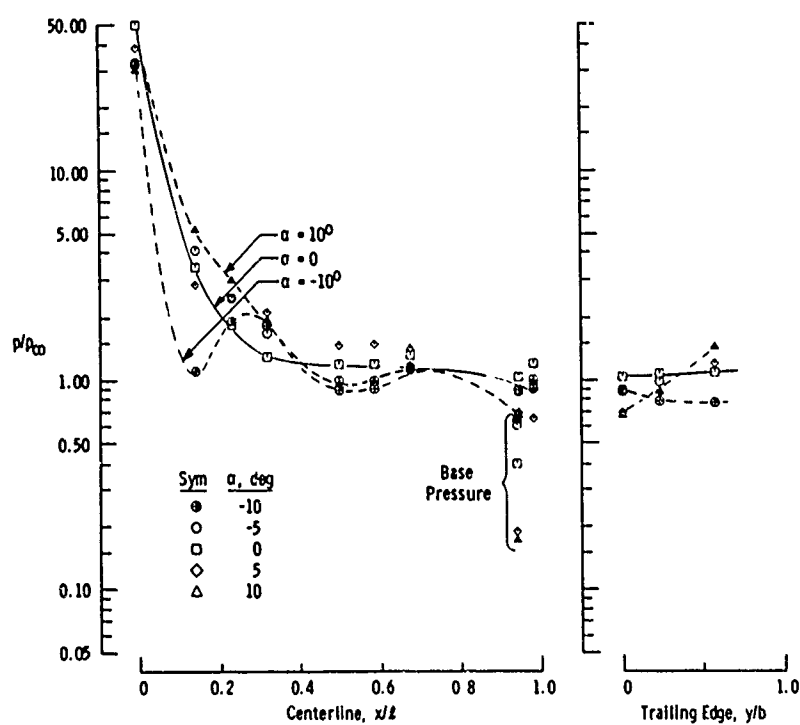
j. Orbiter, $\Delta x/L$ = -0.390 and $\Delta z/L$ = 0.23
Fig. II-2 Concluded

87
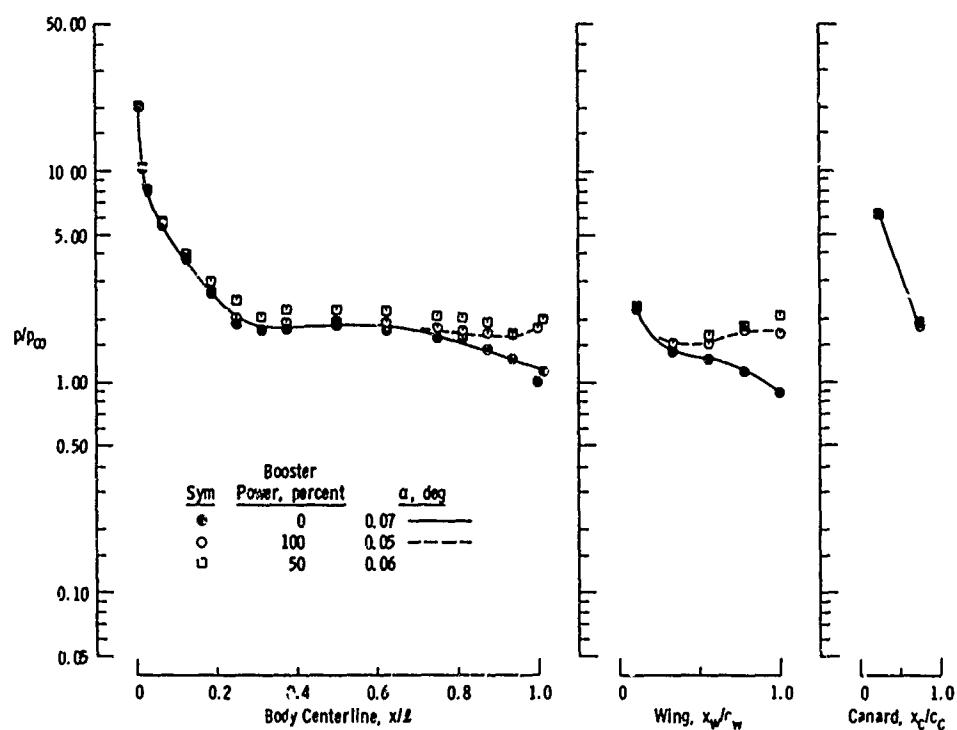
a. Booster, Interference Free
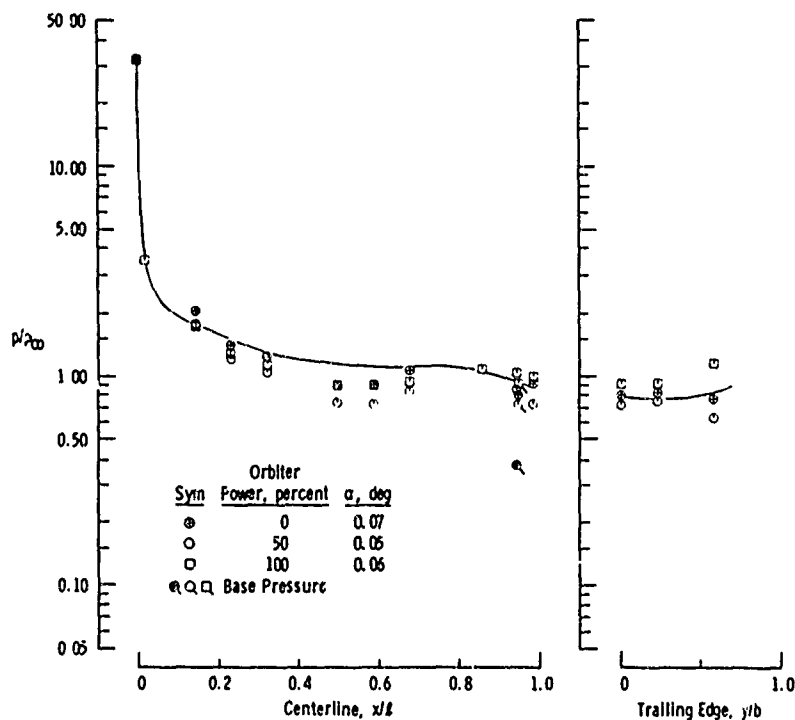
b. Orbiter, Interference Free

Fig. II-3 Plume Simulation (Power) Effects on the Orbiter and Booster Pressure
Distributions at $a = 0$, $M_\infty = 4.97$, and $Re\ell = 1.5 \times 10^6$

Power, percent		
Sym	Booster	Orbiter
◉	0	0 (Interference Free)
○	0	0
□	100	50
◇	50	100
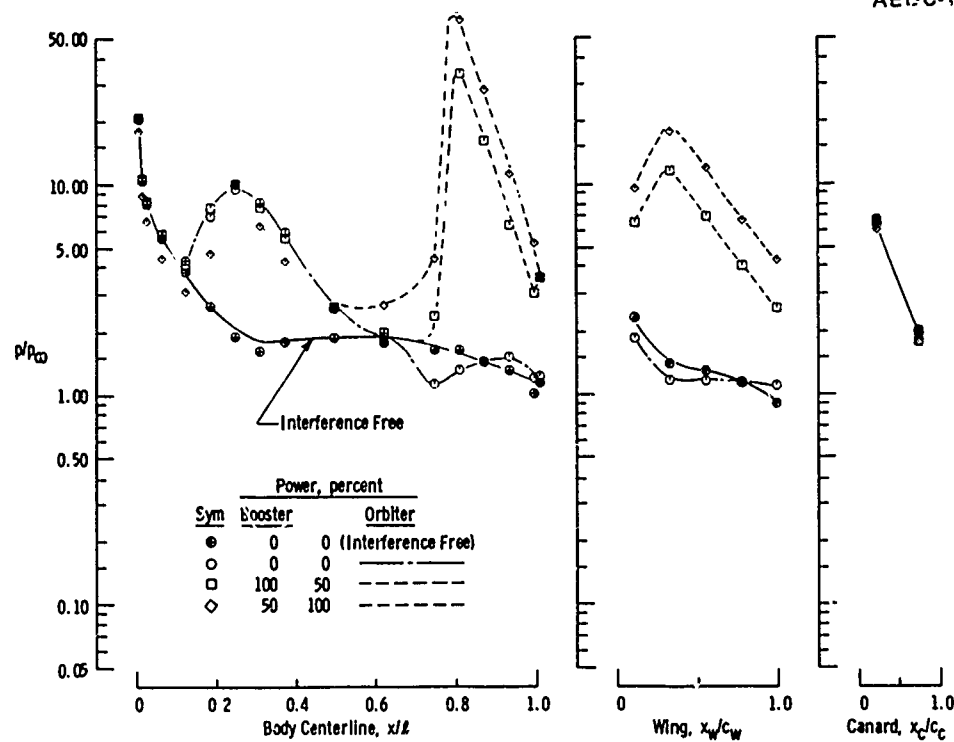
c. Booster, $\Delta x/L = 0.103$ and $\Delta z/L = 0.11$

Fig. II-3 Continued

Power, percent		
Sym	Booster	Orbiter
●	0	0 (Interference Free)
○	0	0
□	100	50
◇	50	100
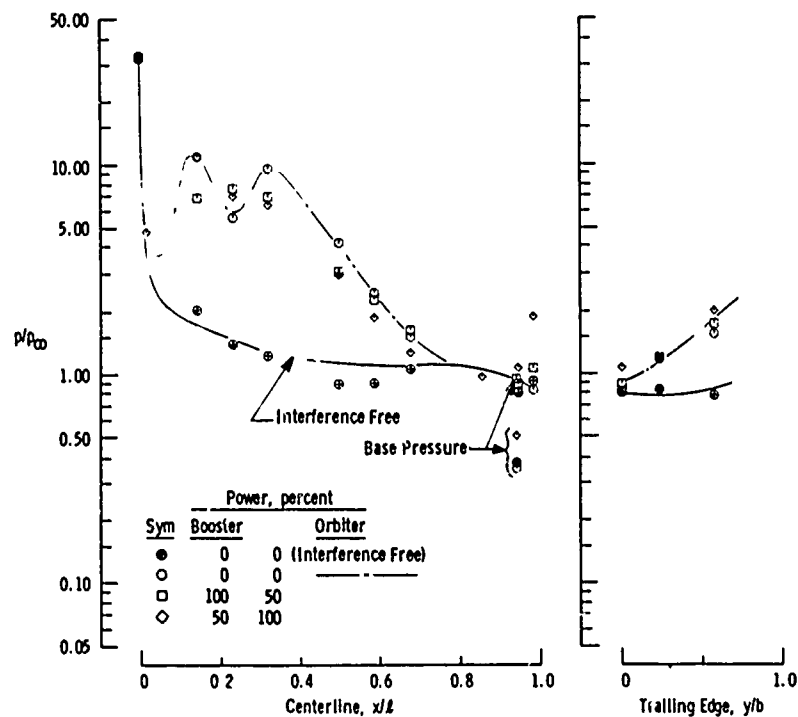
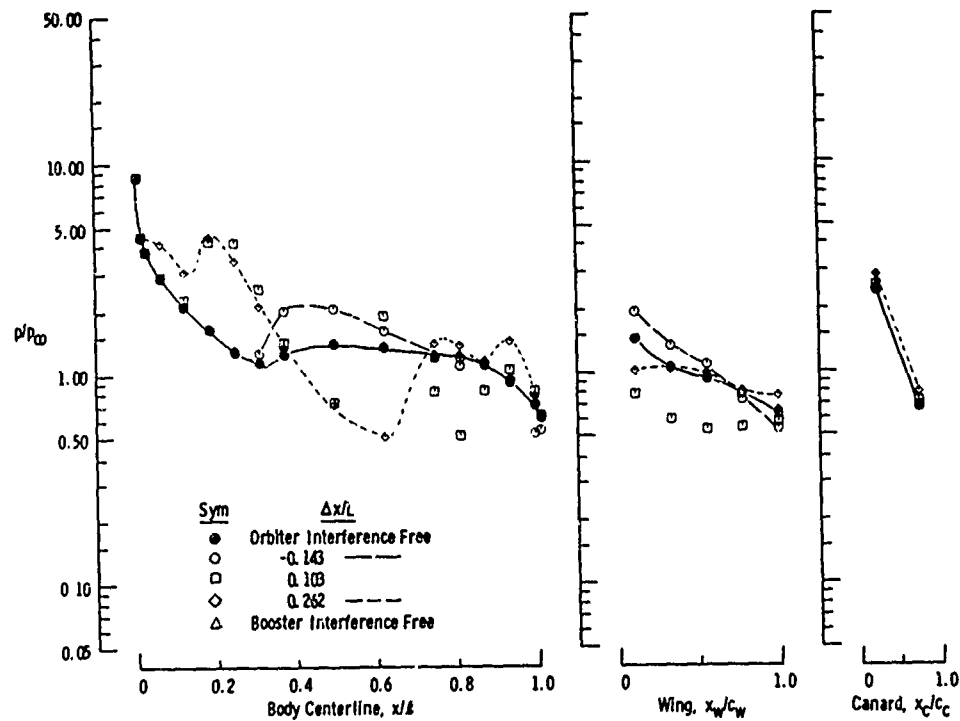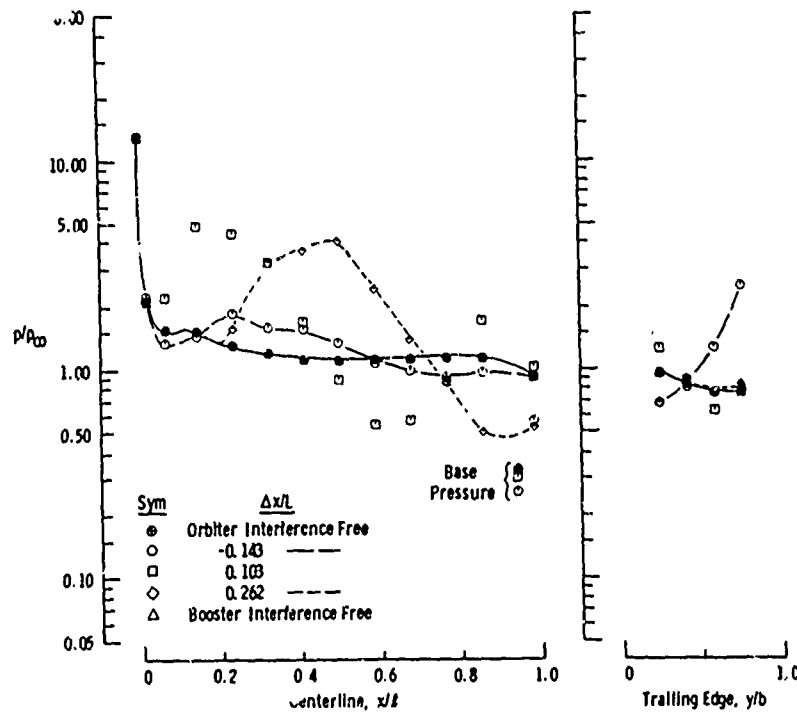d. Orbiter, $\Delta x/L = 0.103$ and $\Delta z/L = 0.11$

Fig. II-3 Concluded

89
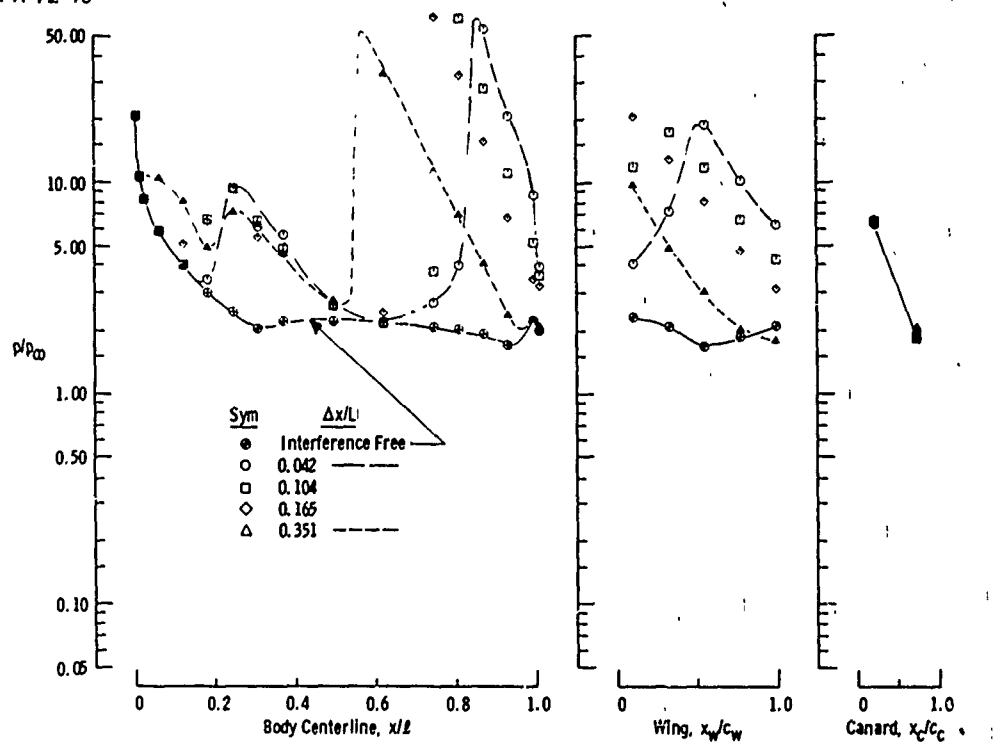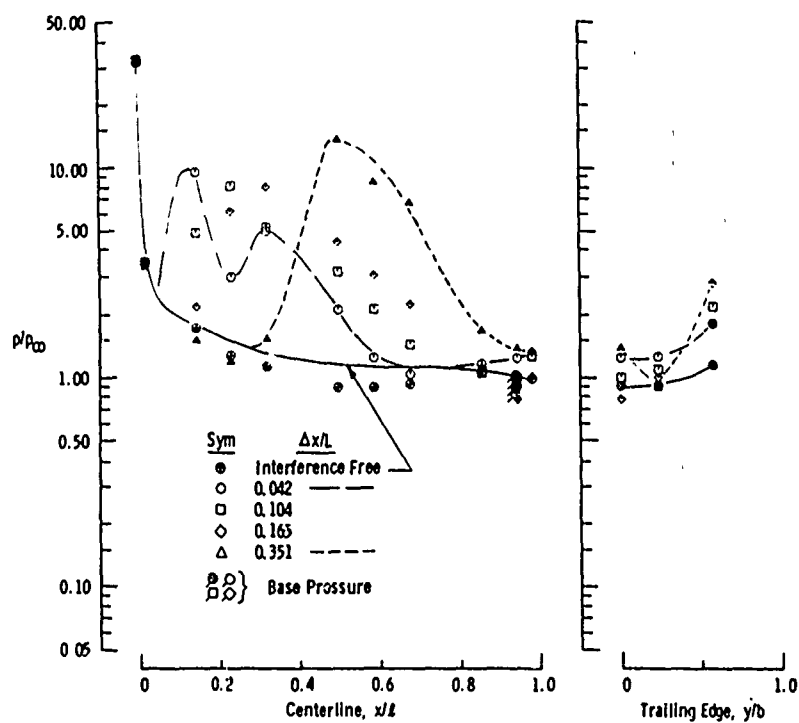
a. Booster, $\Delta z/L = 0.11$

b. Orbiter, $\Delta z/L = 0.11$

Fig. II-4 Booster and Orbiter Pressure Distributions at Various Staging Positions with Plume Simulation (50-percent Booster Power and 100-percent Orbiter Power) at $a = 0$, $M_\infty = 4.97$, and $Re_\ell = 1.5 \times 10^6$ (Variables $\Delta x/L$ and $\Delta z/L$)
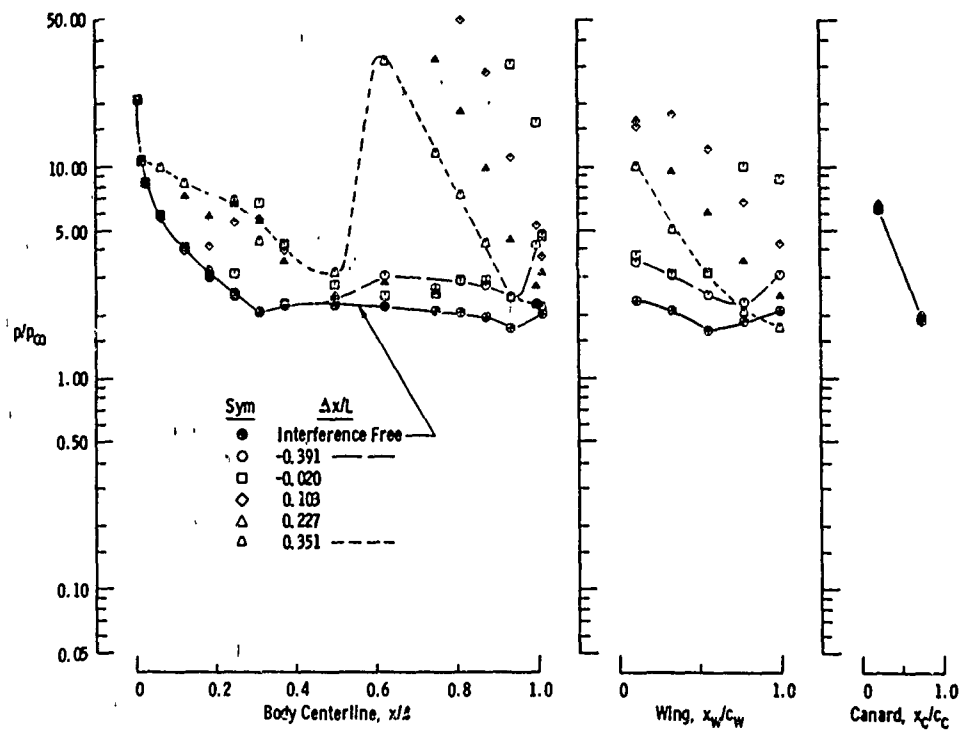
c. Booster, $\Delta z/L = 0.12$
Fig. II-4 Continued

d. Orbiter, $\Delta z/L = 0.12$
Fig. II-4 Continued

91
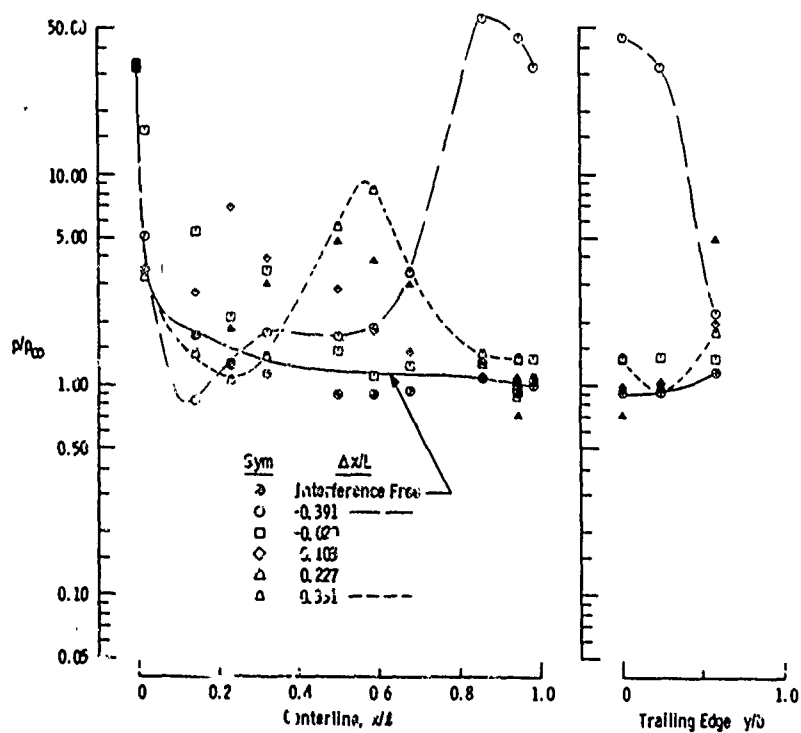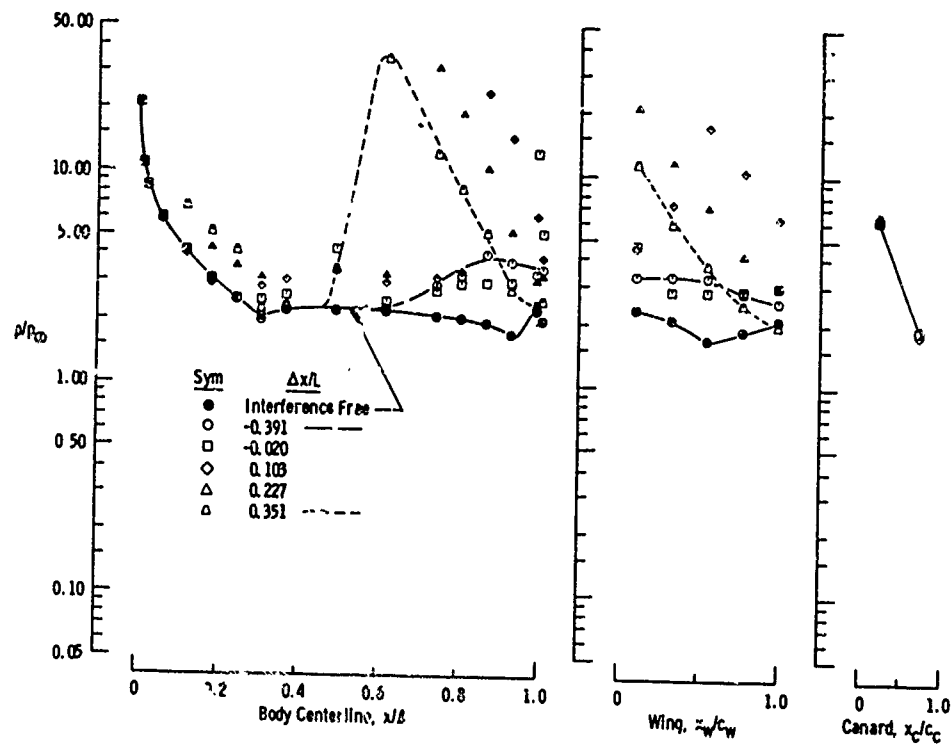
e. Booster, $\Delta z/L = 0.15$
Fig. II-4 Continued

f. Orbiter, $\Delta z/L = 0.15$
Fig. II-4 Continued

92
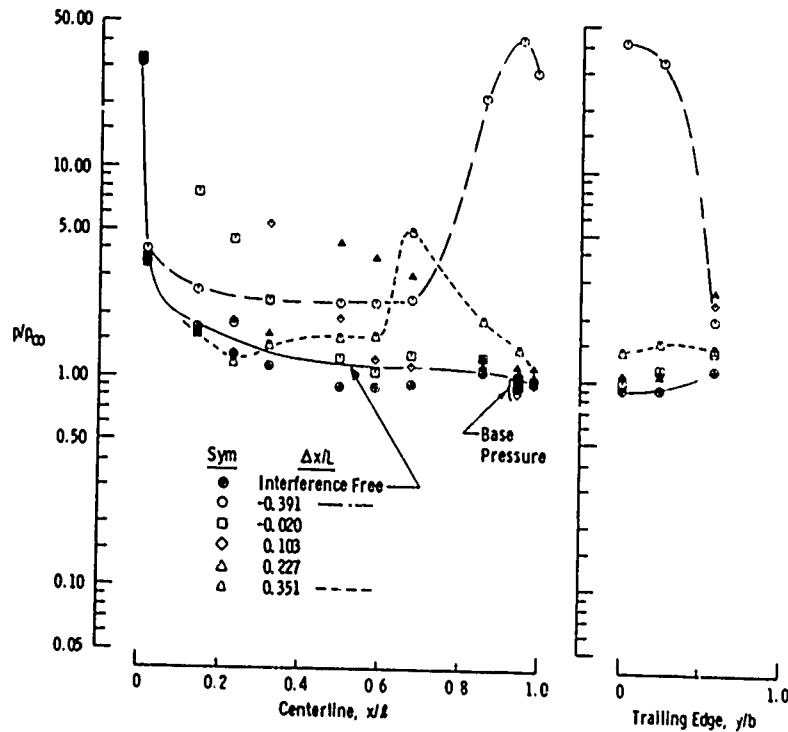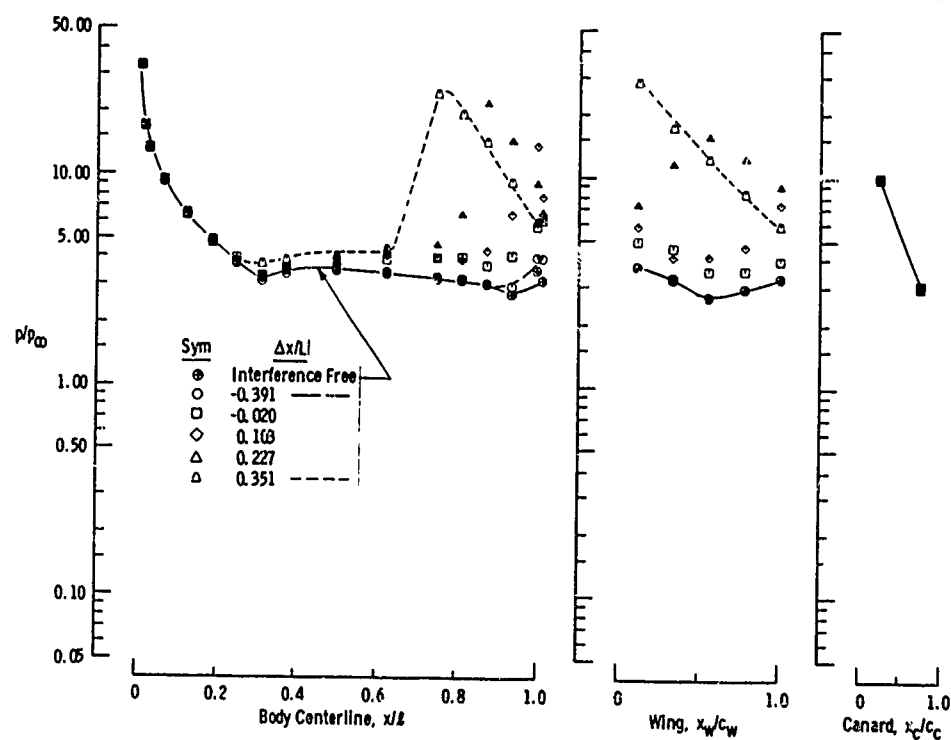
g. Booster, $\Delta z/L = 0.23$
Fig. II-4 Continued
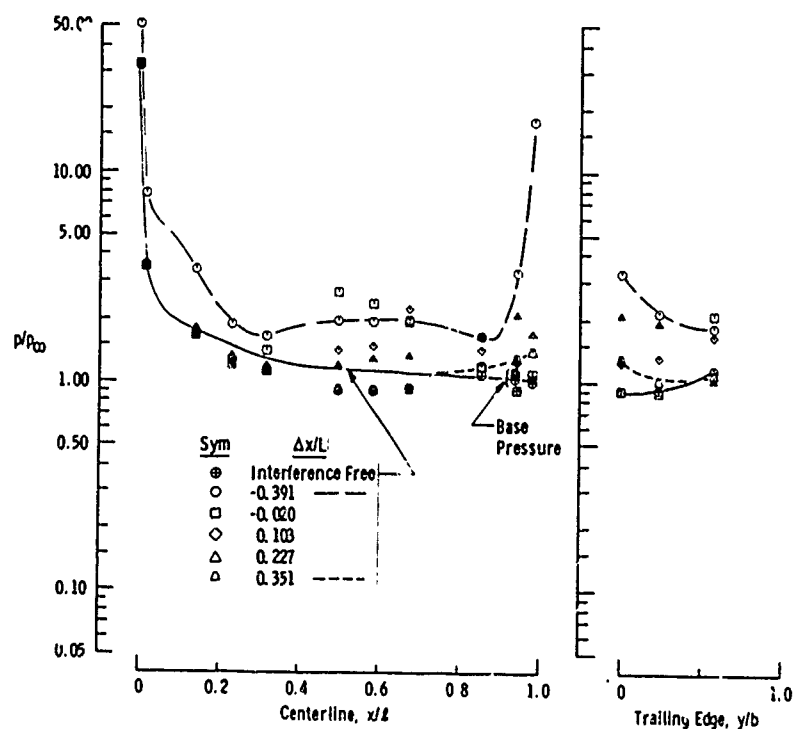
h. Orbiter, $\Delta z/L = 0.23$
Fig. II-4 Continued

93
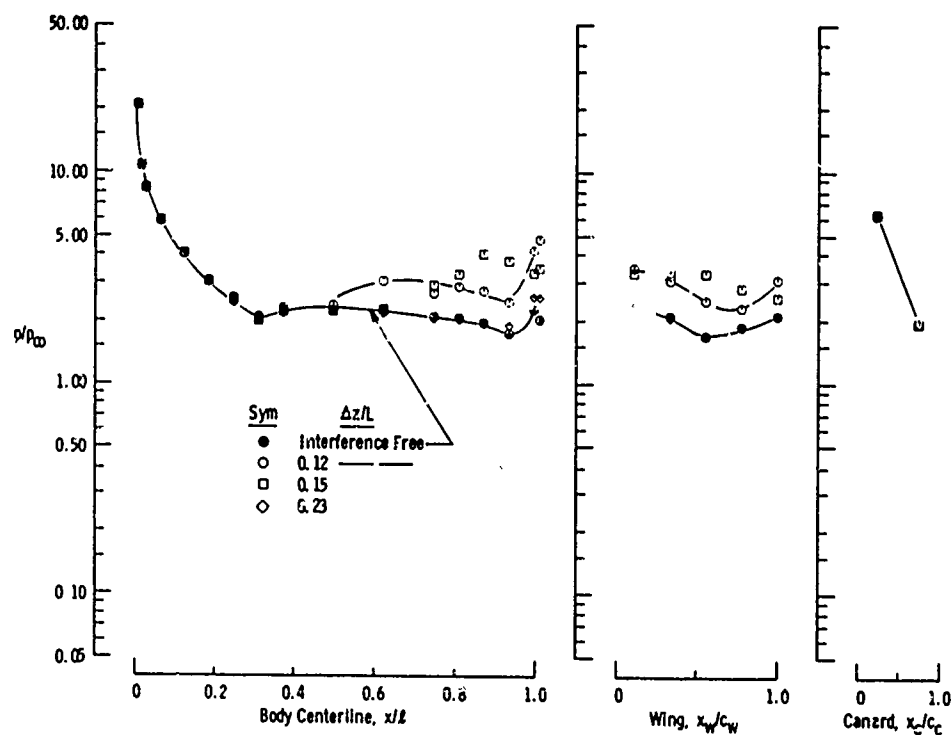
i. Booster, $\Delta x/L = -0.391$
Fig. II-4 Continued

j. Orbiter, $\Delta x/L = -0.391$
Fig. II-4 Continued

94
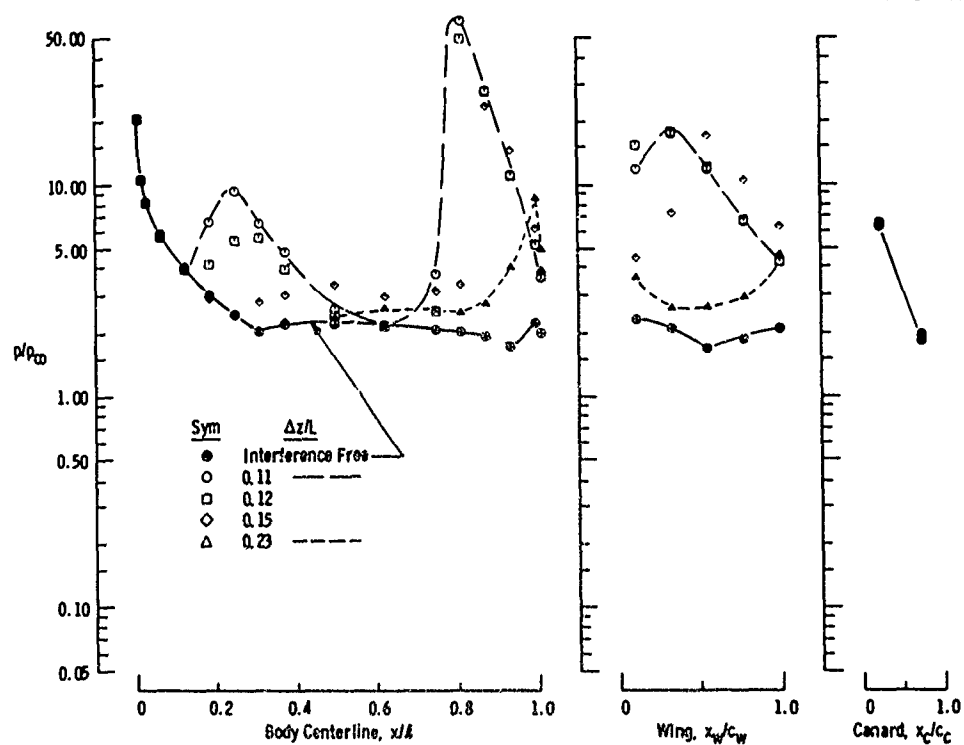
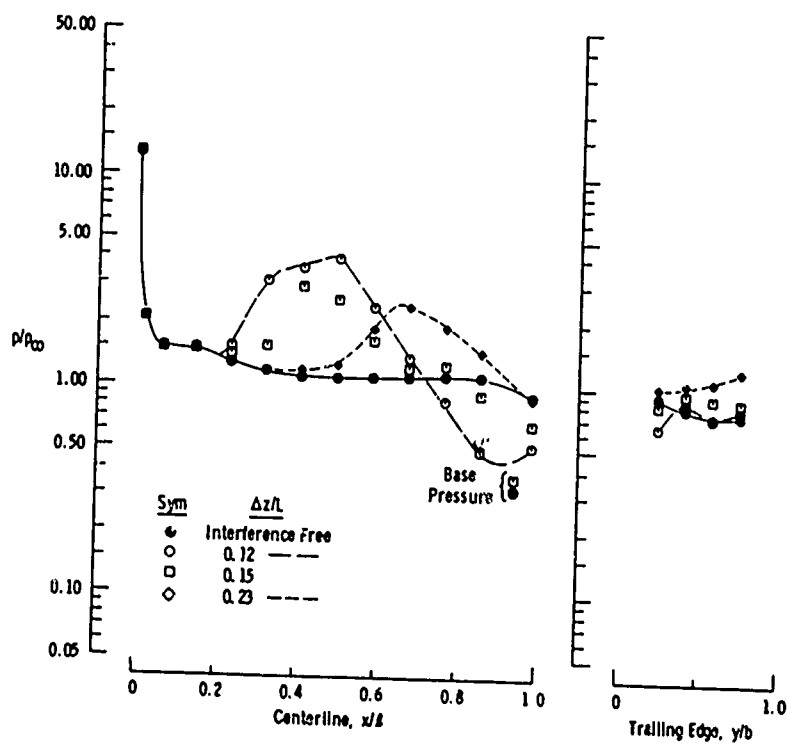k. Booster, $\Delta x/L = 0.103$
Fig. II-4 Continued
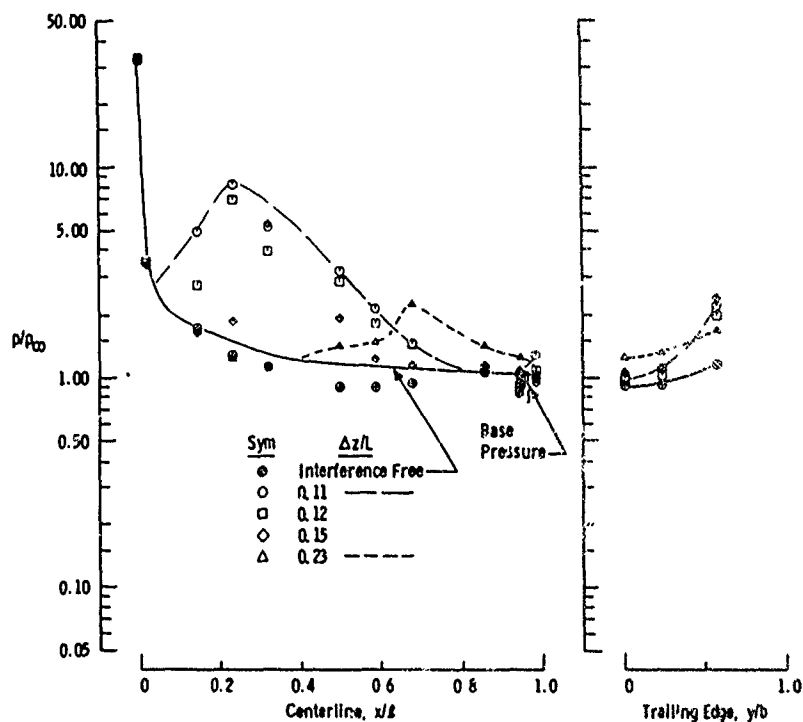
l. Orbiter, $\Delta x/L = 0.103$
Fig. II-4 Continued
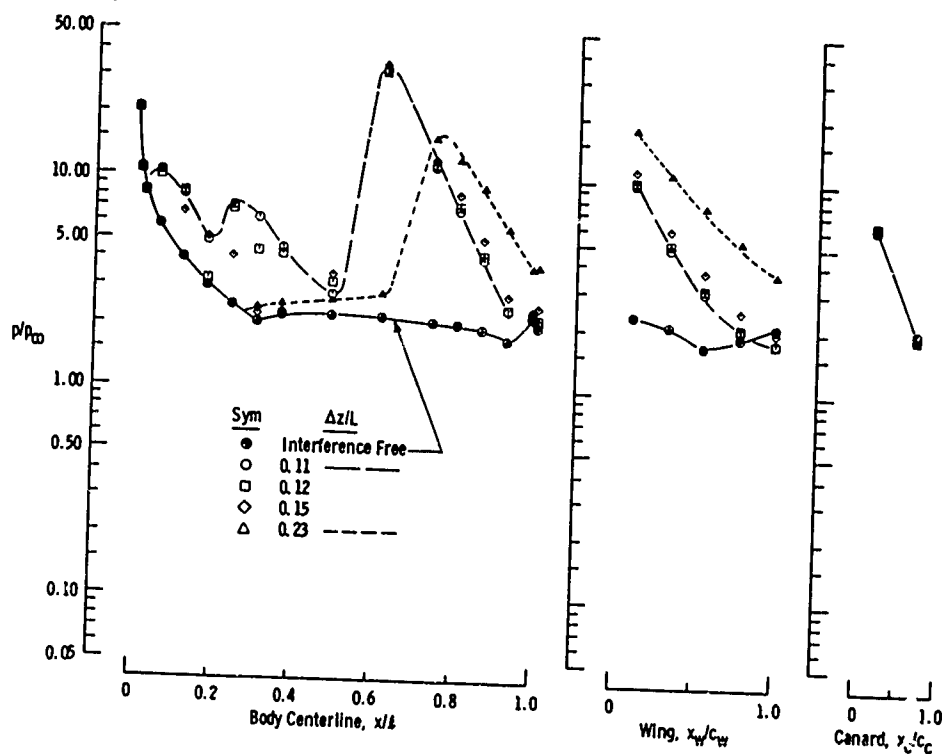
m. Booster, $\Delta x/L = 0.350$
Fig. II-4 Continued
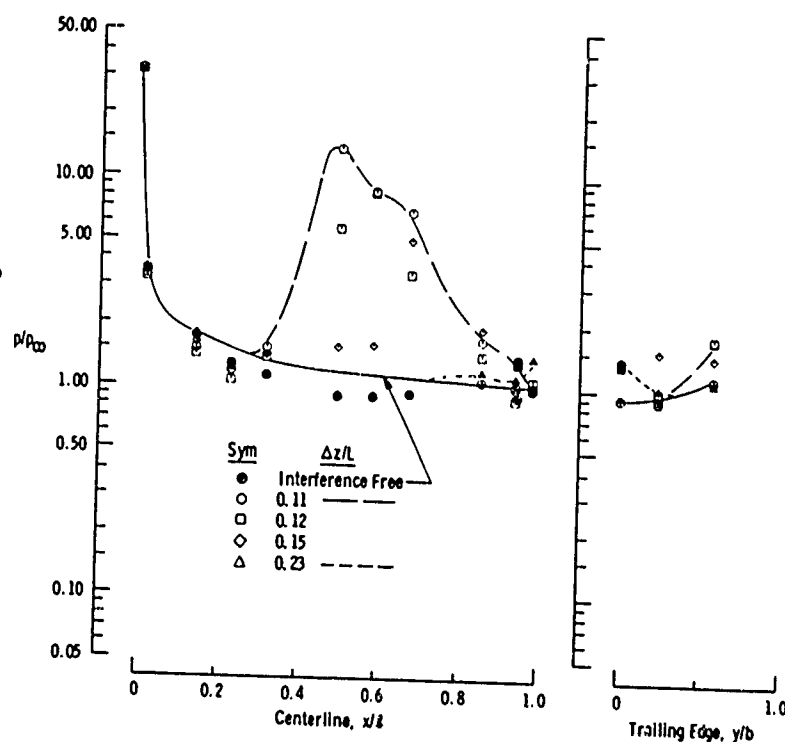
n. Orbiter, $\Delta x/L = 0.350$
Fig. II-4 Concluded
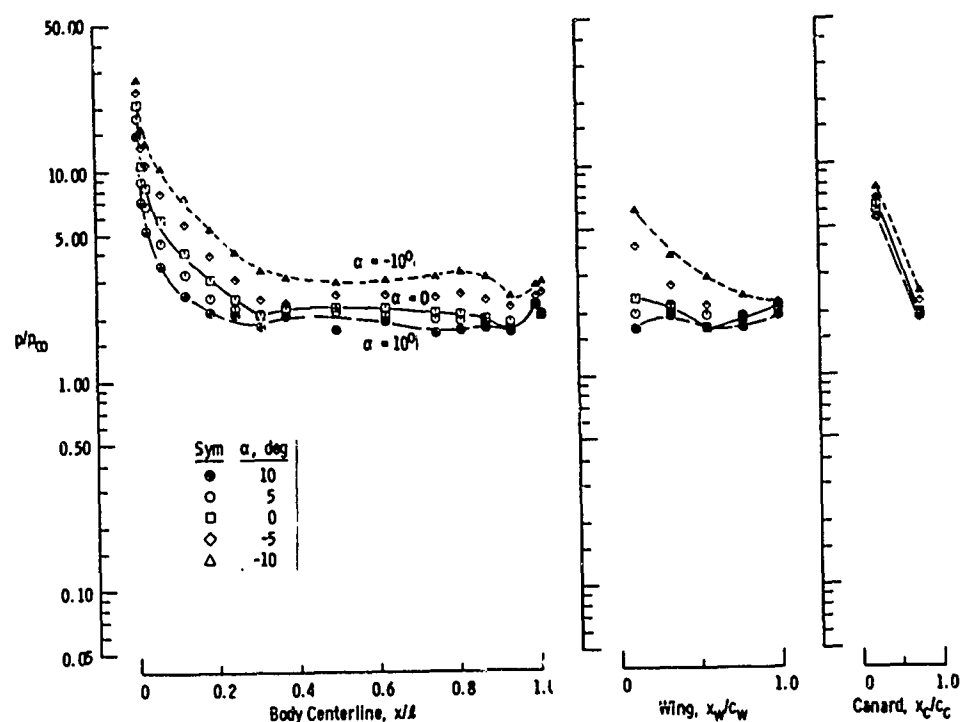
a. Booster, Interference Free
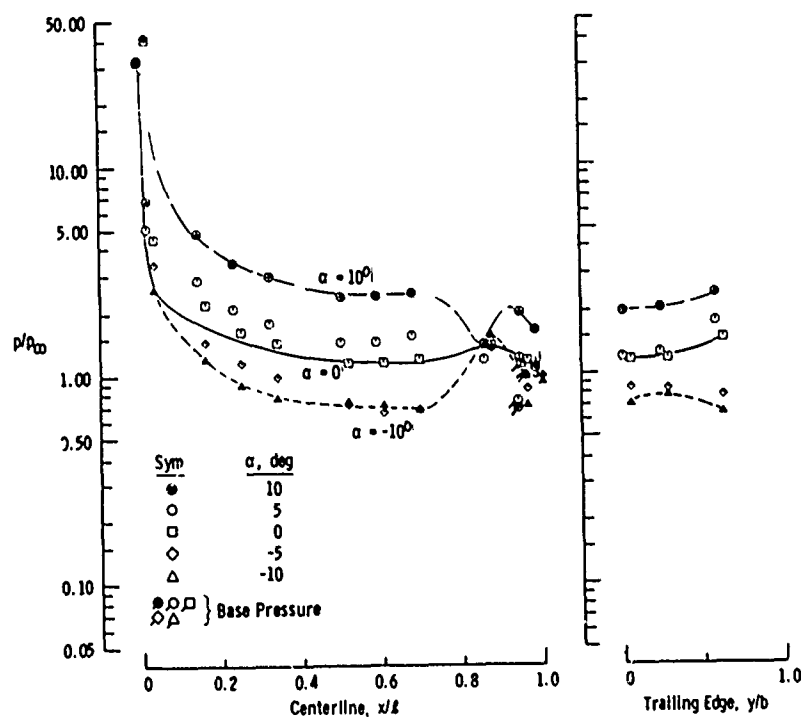
b. Orbiter, Interference Free

Fig. II-5 Angle-of-Attack Effects on the Booster and Orbiter Pressure Distributions with Plume Simulation (50-percent Booster Power and 100-percent Orbiter Power) at $M_\infty = 4.97$ and $Re_\ell = 1.5 \times 10^6$ (Variables a, $\Delta x/L$, and $\Delta z/L$)
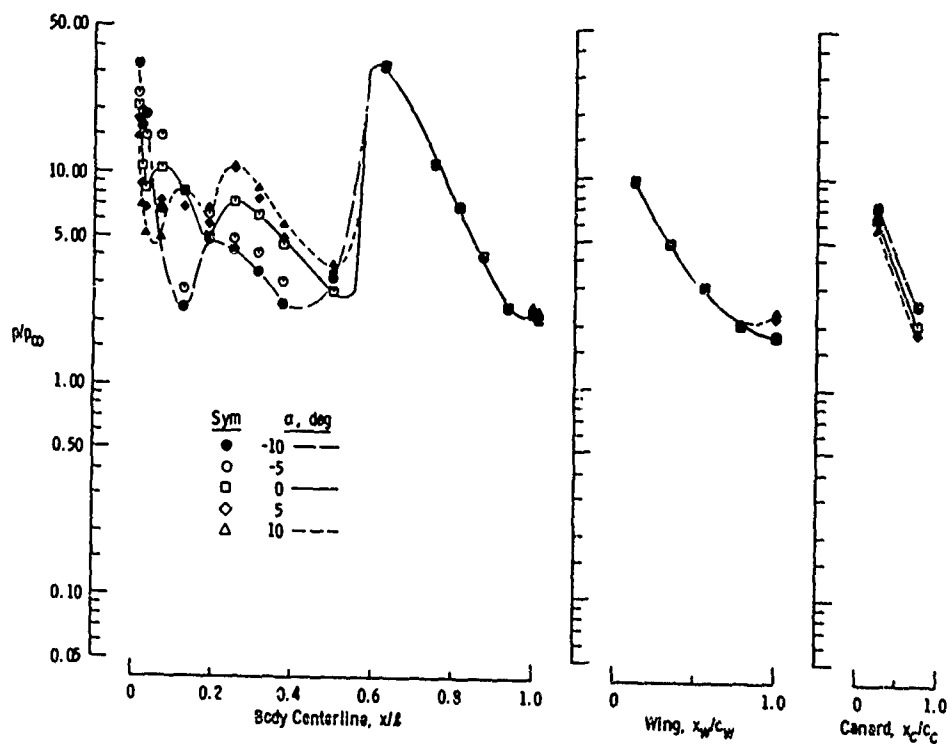
c. Booster, $\Delta x/L = 0.350$ and $\Delta z/L = 0.11$
Fig. II-5 Continued
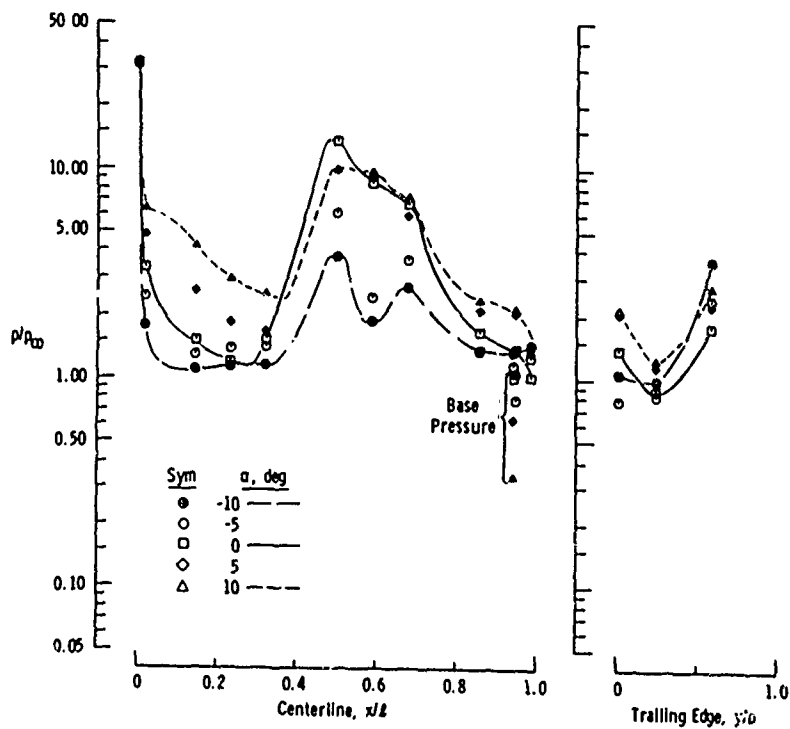
d. Orbiter, $\Delta x/L = 0.350$ and $\Delta z/L = 0.11$
Fig. II-5 Continued
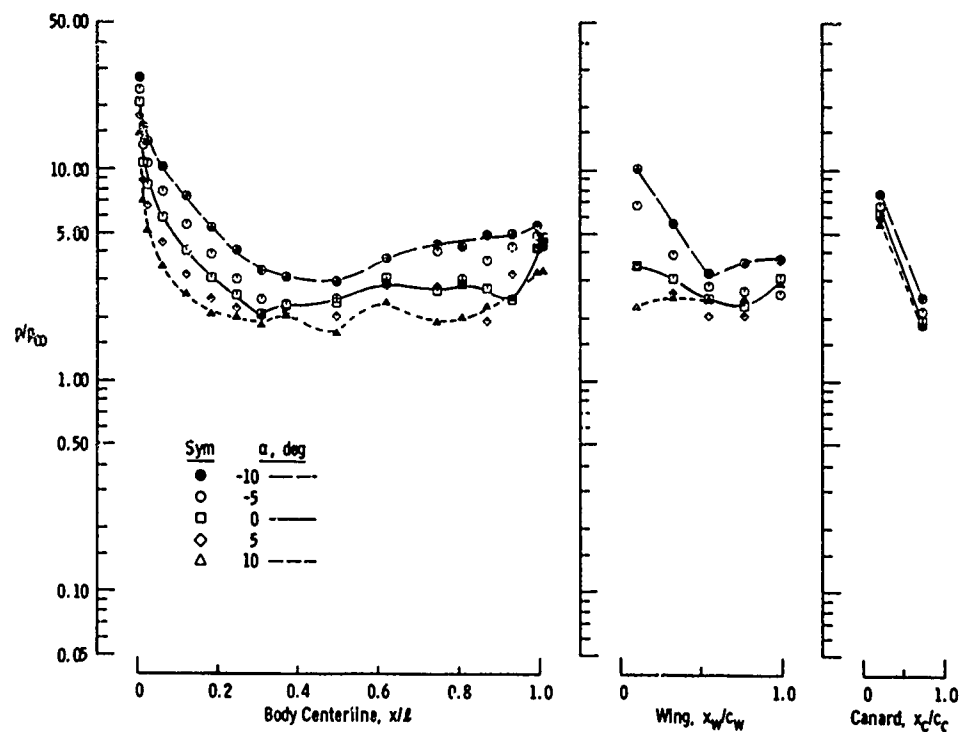
e. Booster, $\Delta x/L = -0.390$ and $\Delta x/L = 0.12$
Fig. II-5 Continued
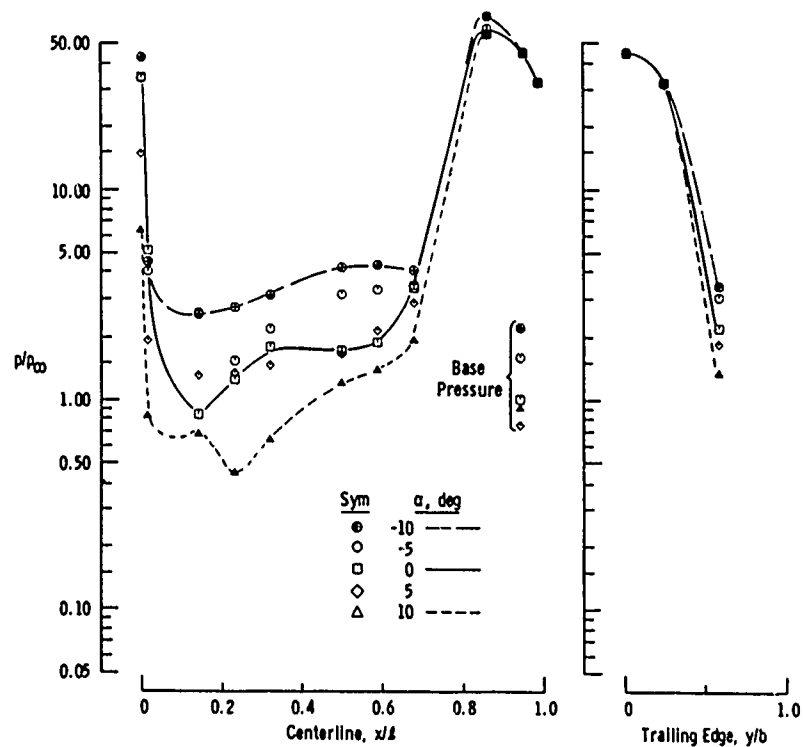
f. Orbiter, $\Delta x/L = -0.390$ and $\Delta z/L = 0.12$
Fig. II-5 Continued
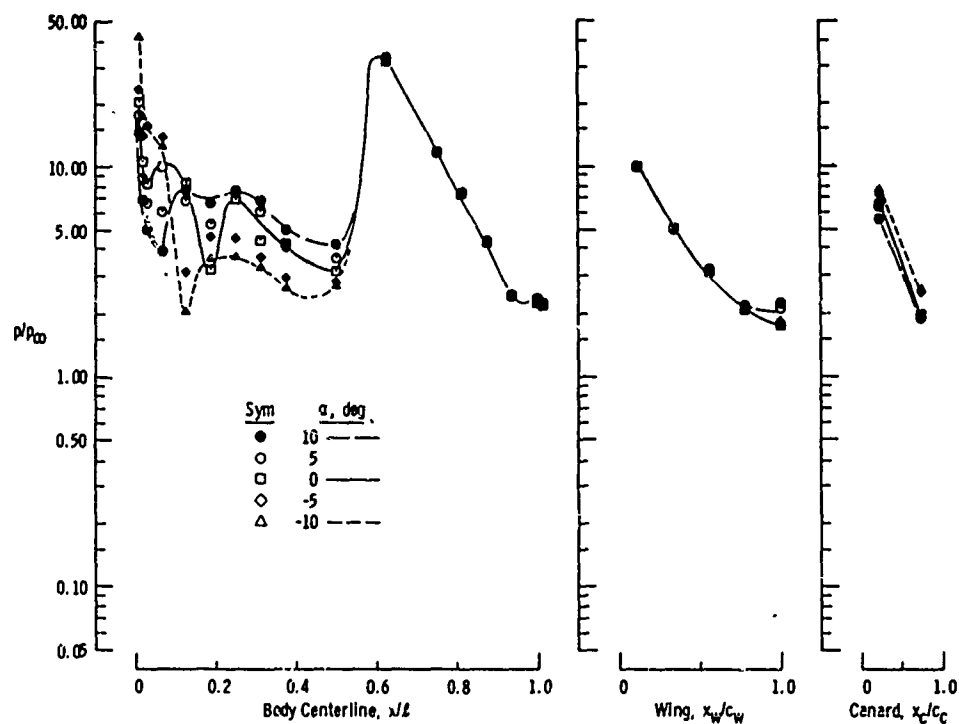
g. Booster, $\Delta x/L = 0.351$ and $\Delta z/L = 0.12$
Fig. II-5 Continued
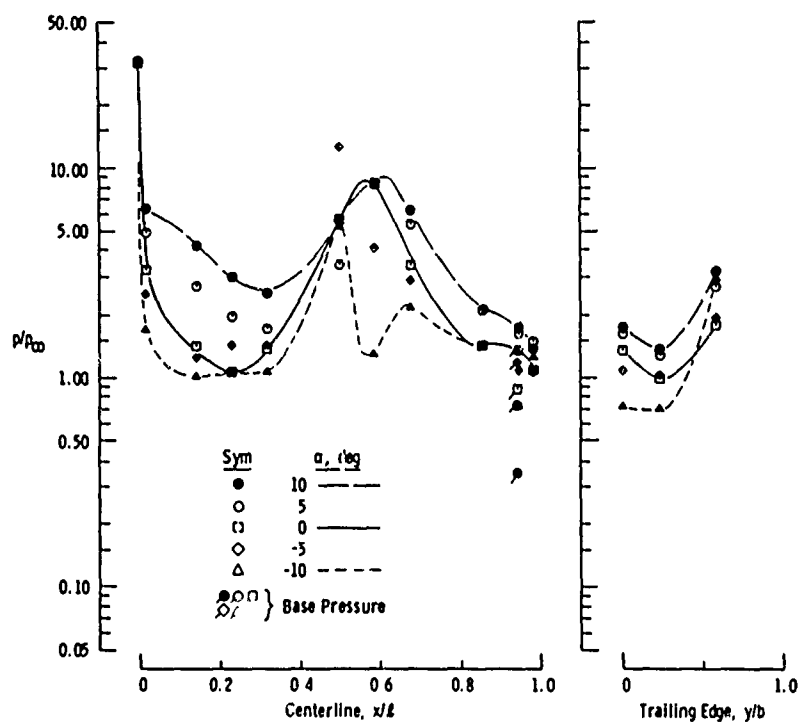
h. Orbiter, $\Delta x/L = 0.351$ and $\Delta z/L = 0.12$
Fig. II-5 Continued
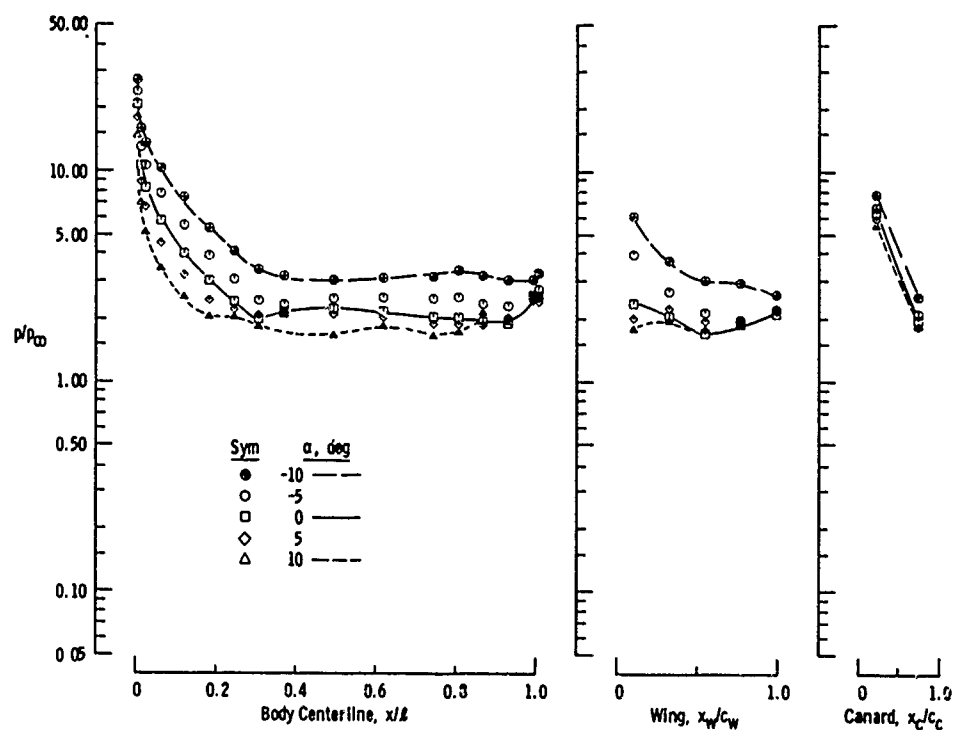
i. Booster, $\Delta x/L = -0.391$ and $\Delta z/L = 0.23$
Fig. II-5 Continued
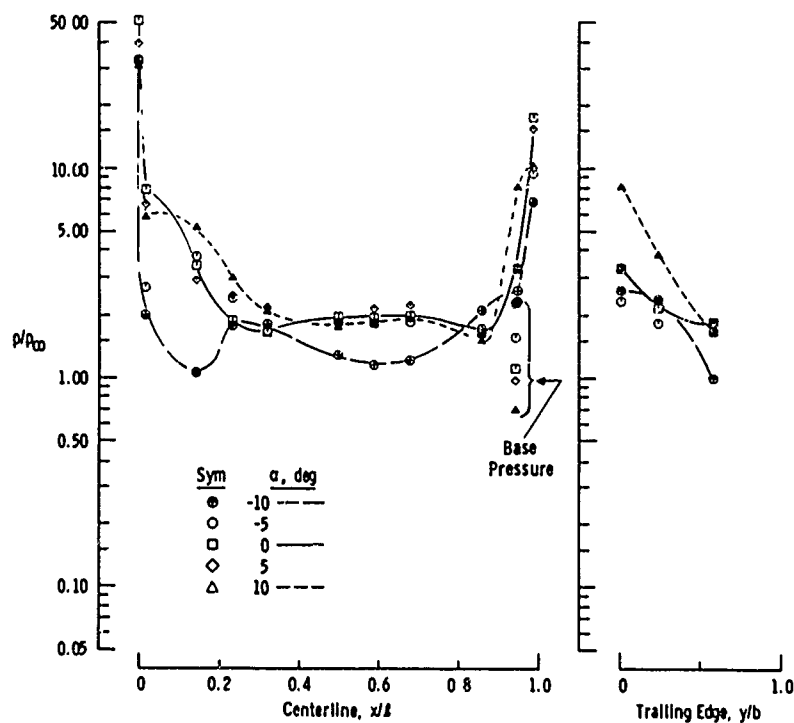
j. Orbiter, $\Delta x/L = 0.391$ and $\Delta z/L = 0.23$
Fig. II-5 Continued

101
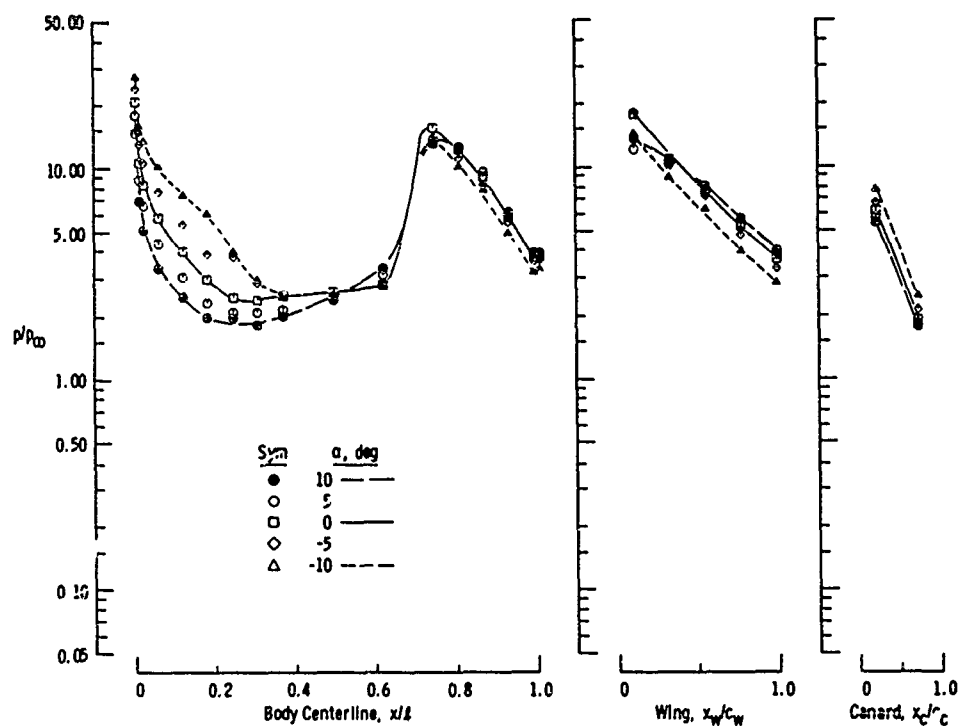
k. Booster, $\Delta x/L = 0.351$ and $\Delta z/L = 0.23$
Fig. II-5 Continued
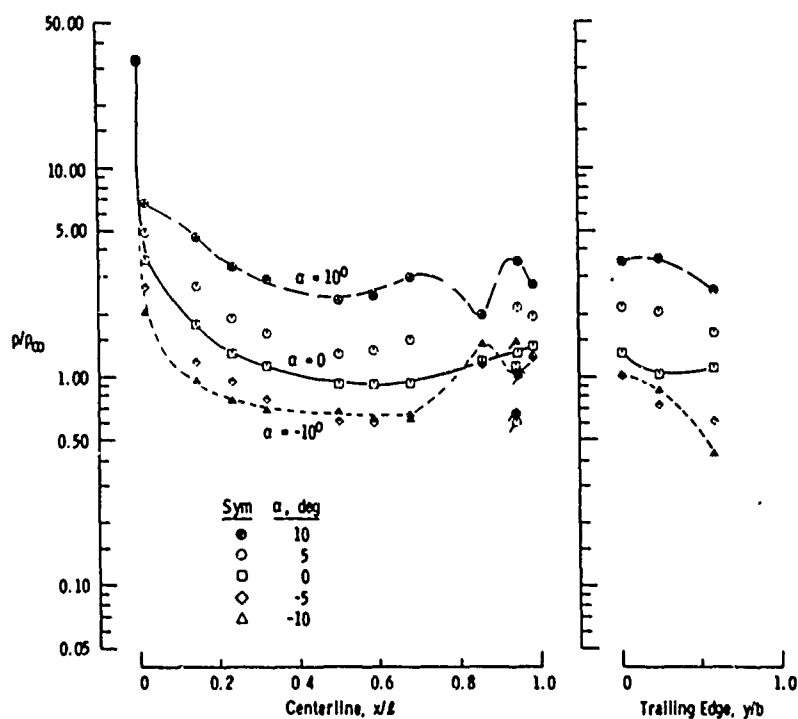
l. Orbiter, $\Delta x/L = 0.351$ and $\Delta z/L = 0.23$
Fig. II-5 Concluded
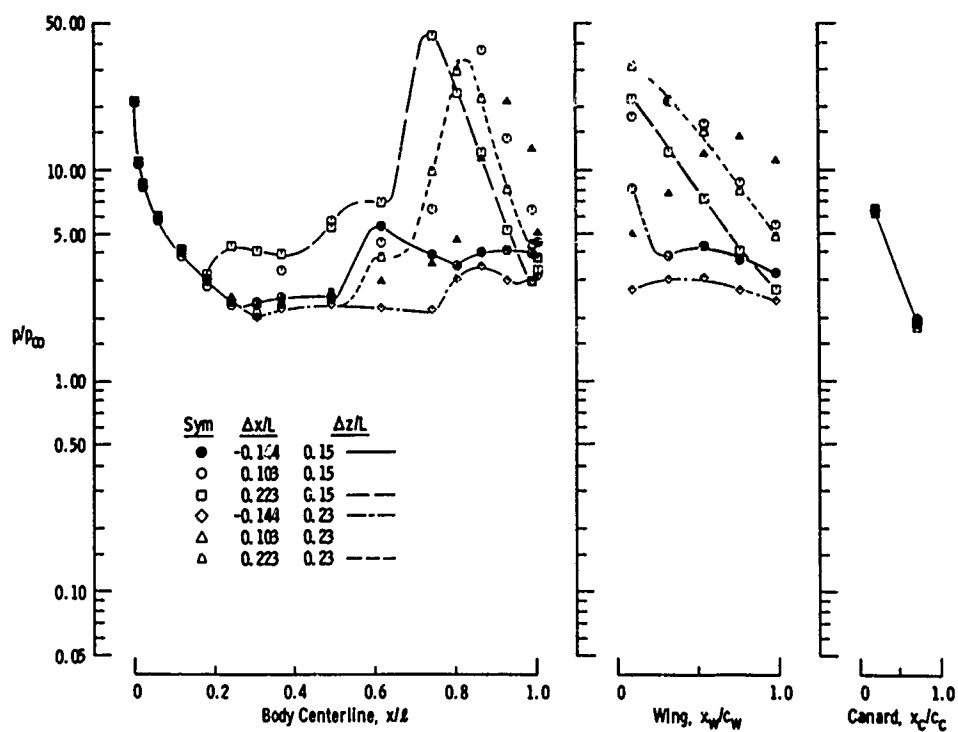
a. Booster, $a = 0$
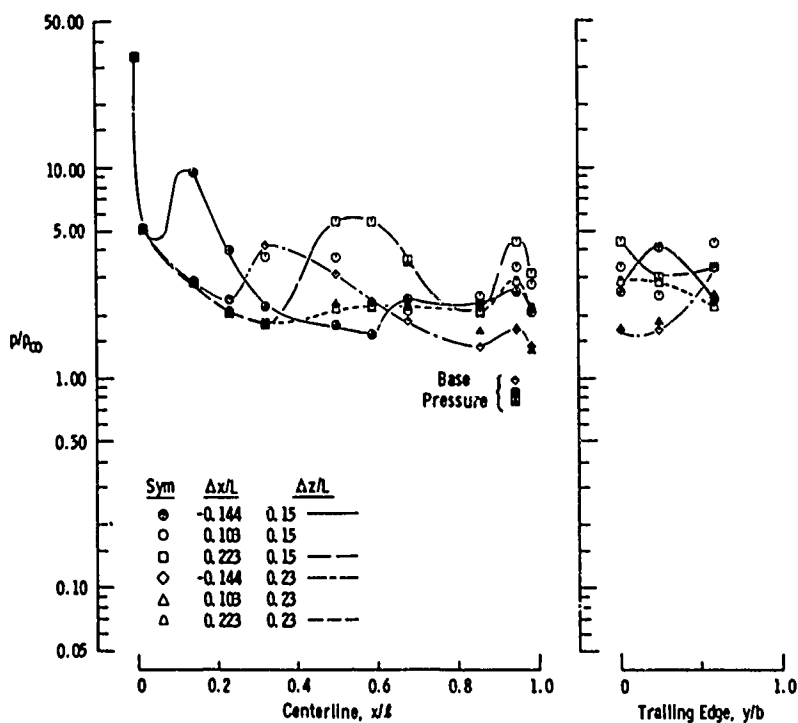
b. Orbiter, $a = 5$ deg

Fig. II-6 Booster and Orbiter Pressure Distributions at Various Staging Positions with
a Relative Orbiter Angle of Incidence of 5 deg, No Power Simulation,
$M_\infty = 4.97$, and $Re_\ell = 1.5 \times 10^6$ (Variables a, $\Delta x/L$, and $\Delta z/L$)
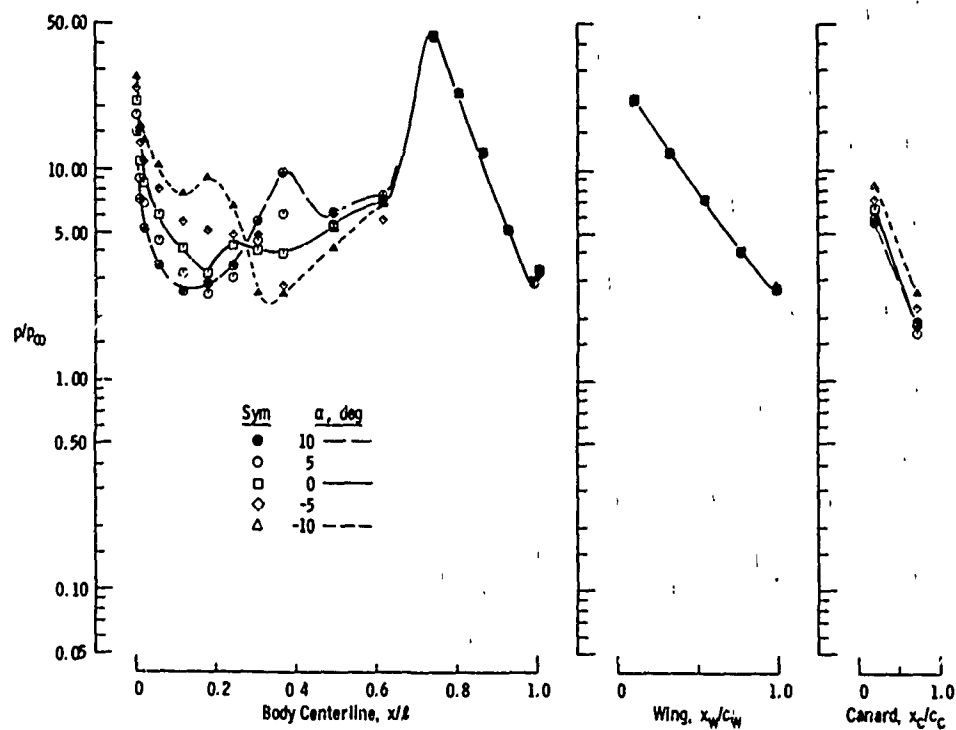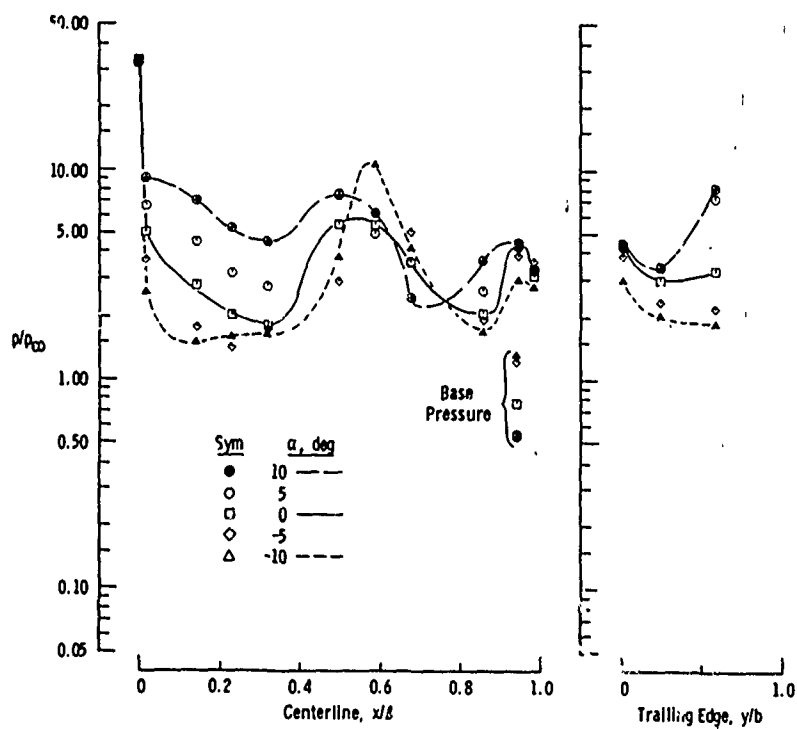
c. Booster, $\Delta x/L = 0.227$ and $\Delta z/L = 0.15$
Fig. II-6 Continued

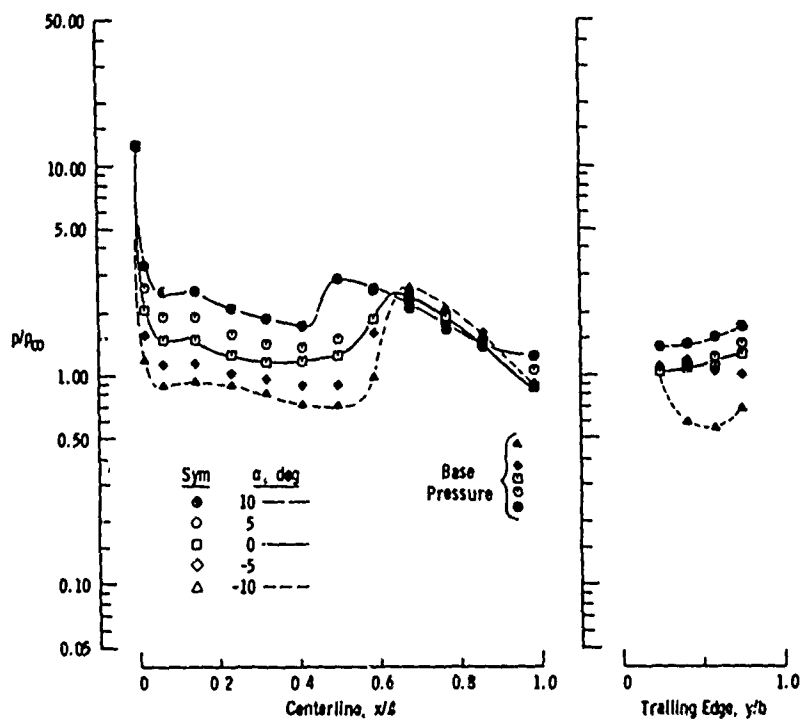d. Orbiter, $\Delta x/L = 0.227$ and $\Delta z/L = 0.15$
Fig. II-6 Continued

104
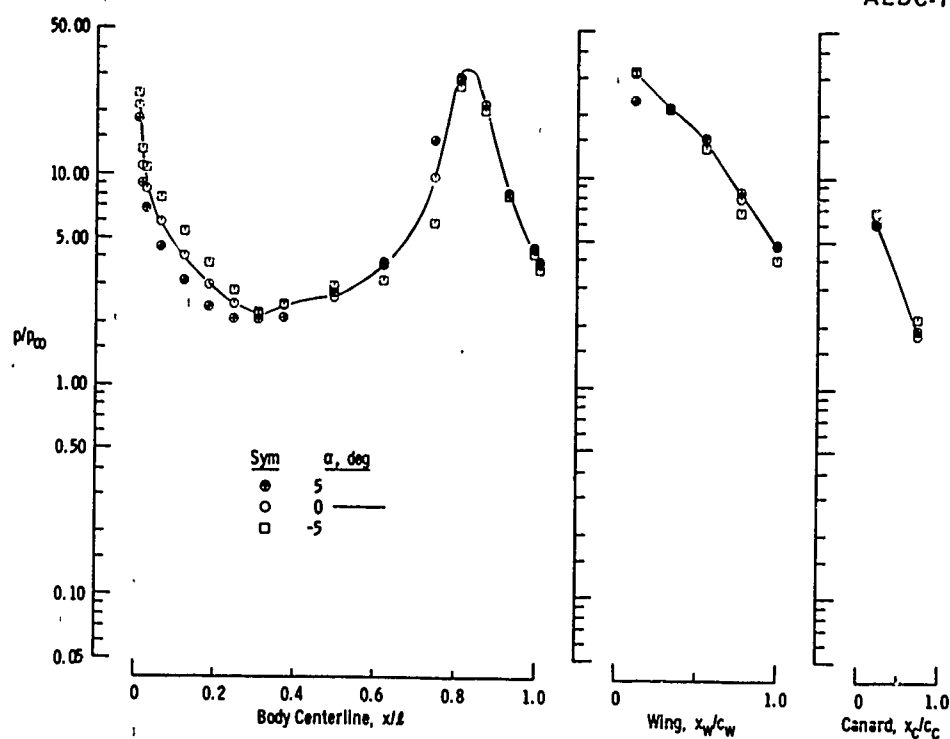
e. Booster, $\Delta x/L = 0.227$ and $\Delta z/L = 0.23$
Fig. II-6 Continued
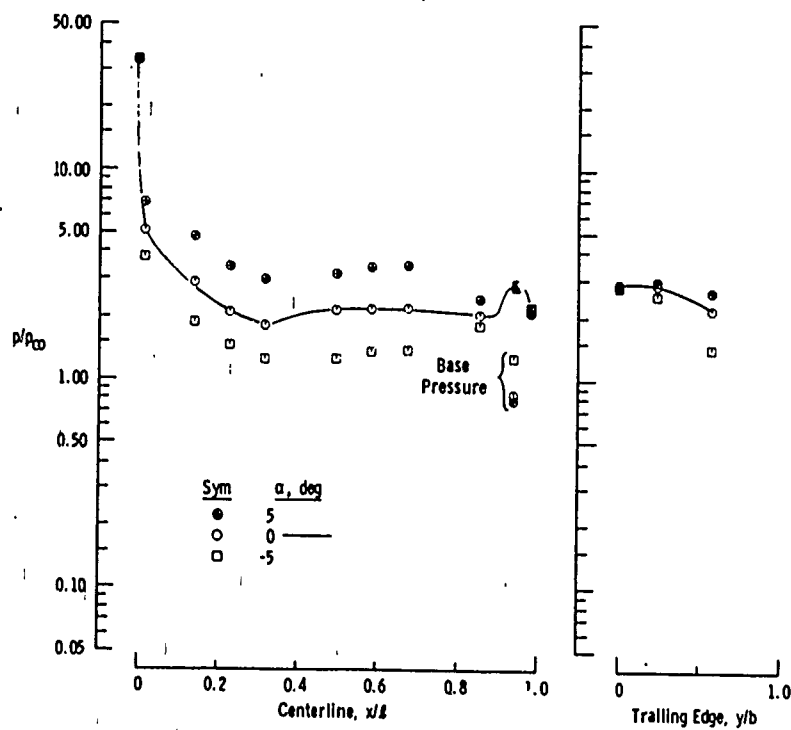
f. Orbiter, $\Delta x/L = 0.227$ and $\Delta z/L = 0.23$
Fig. II-6 Concluded
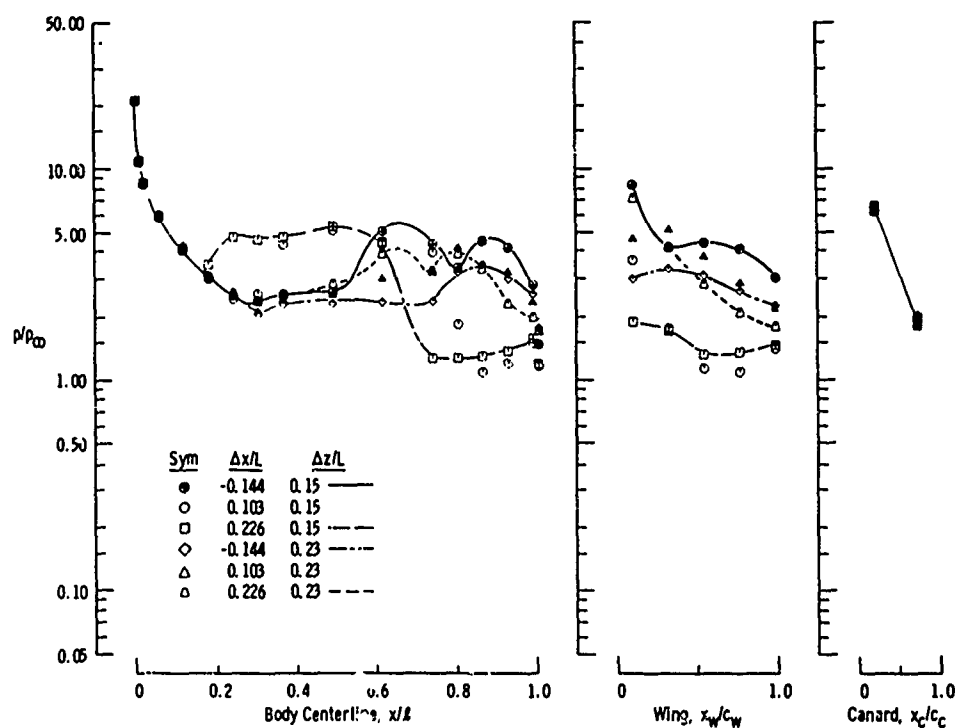
a. Booster, $a = 0$
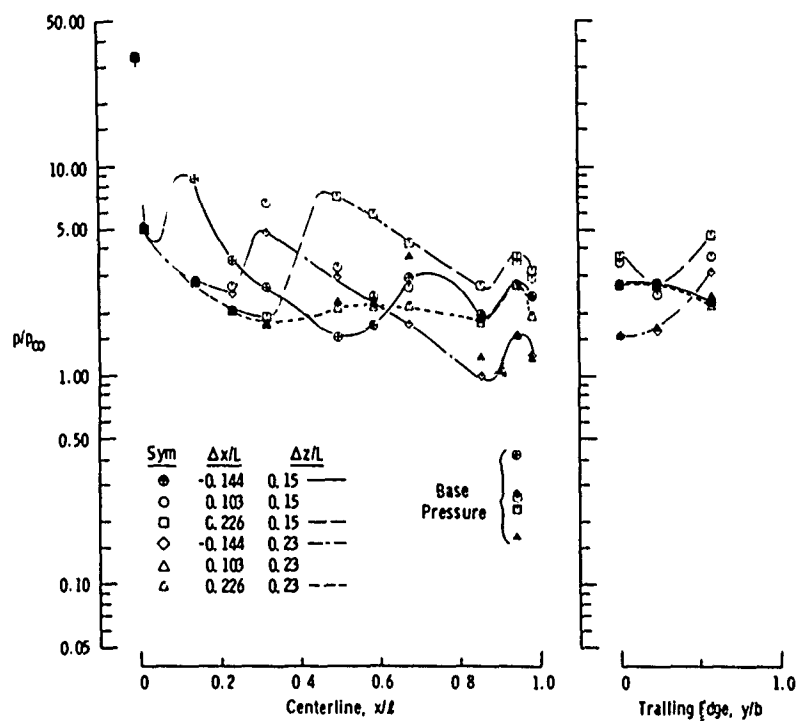
b. Orbiter, $a = 5$ deg

Fig. II-7 Booster and Orbiter Pressure Distributions at Various Staging Positions
with a Relative Orbiter Angle of Incidence of 5 deg, Power Simulation
of 50-percent on the Booster and 100-percent on the Orbiter, $M_\infty = 4.97$,
and $Re_\ell = 1.5 \times 10^6$ (Variables a, $\Delta x/L$, and $\Delta z/L$)
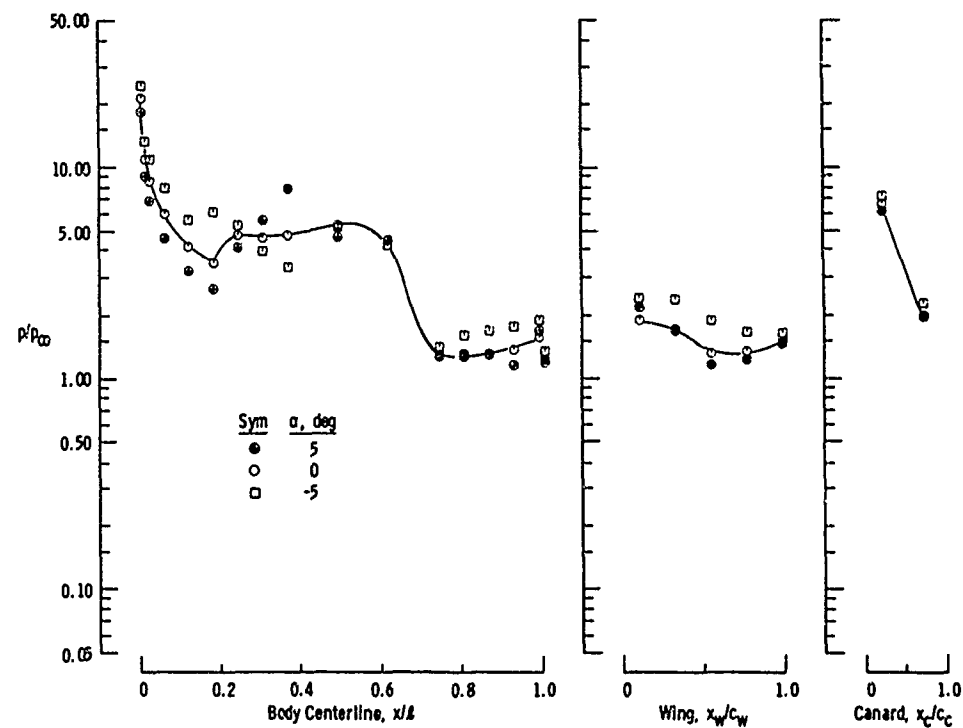
c. Booster, $\Delta x/L = 0.227$ and $\Delta z/L = 0.15$
Fig. II-7 Continued
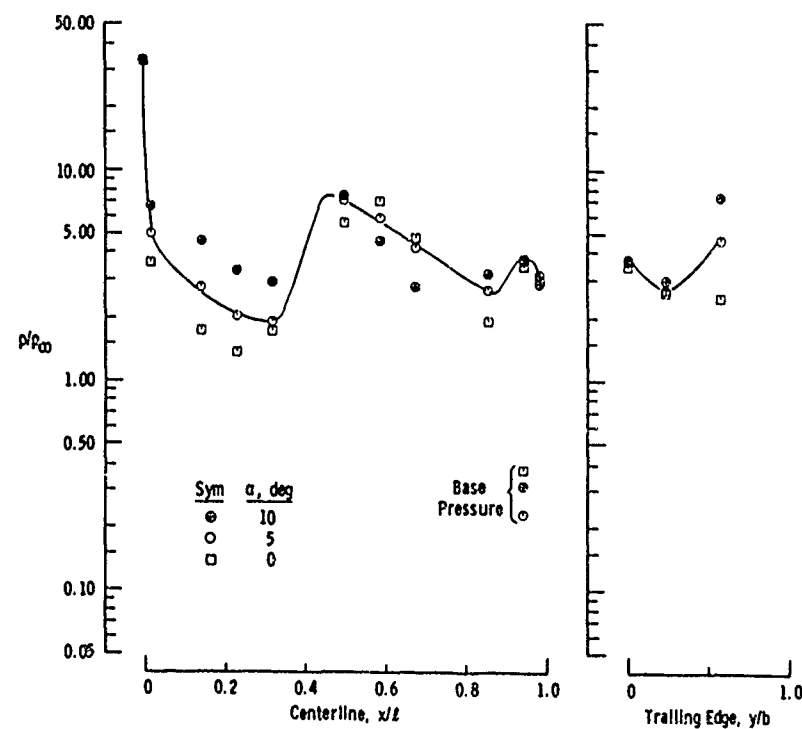
d. Orbiter, $\Delta x/L = 0.227$ and $\Delta z/L = 0.15$
Fig. II-7 Continued
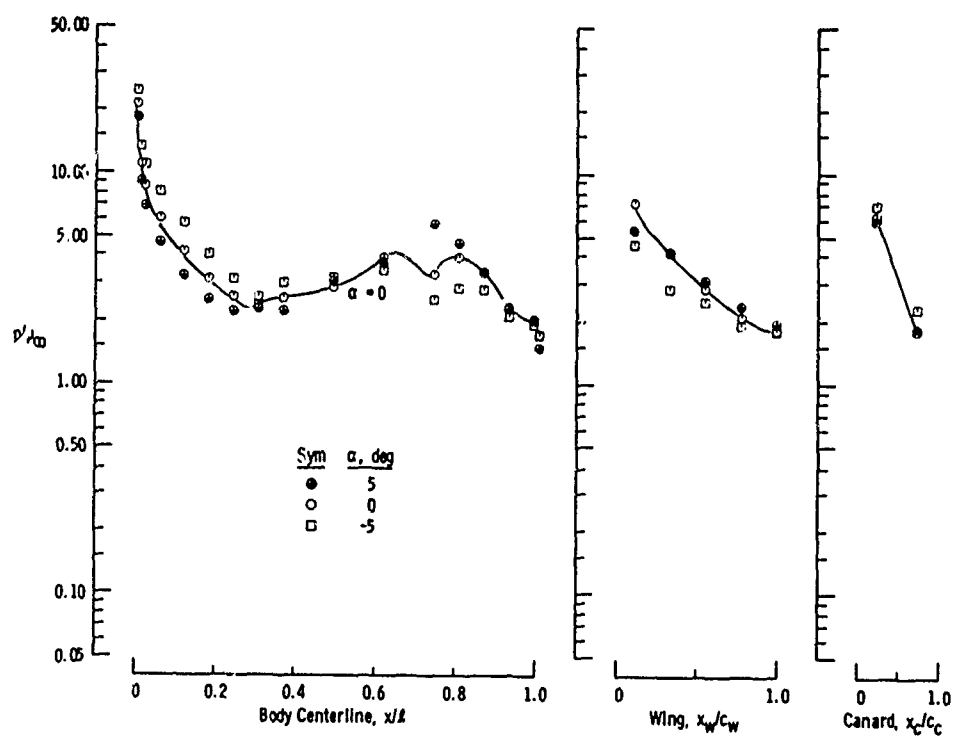
e. Booster, $\Delta x/L = 0.227$ and $\Delta z/L = 0.23$
Fig. II-7 Continued
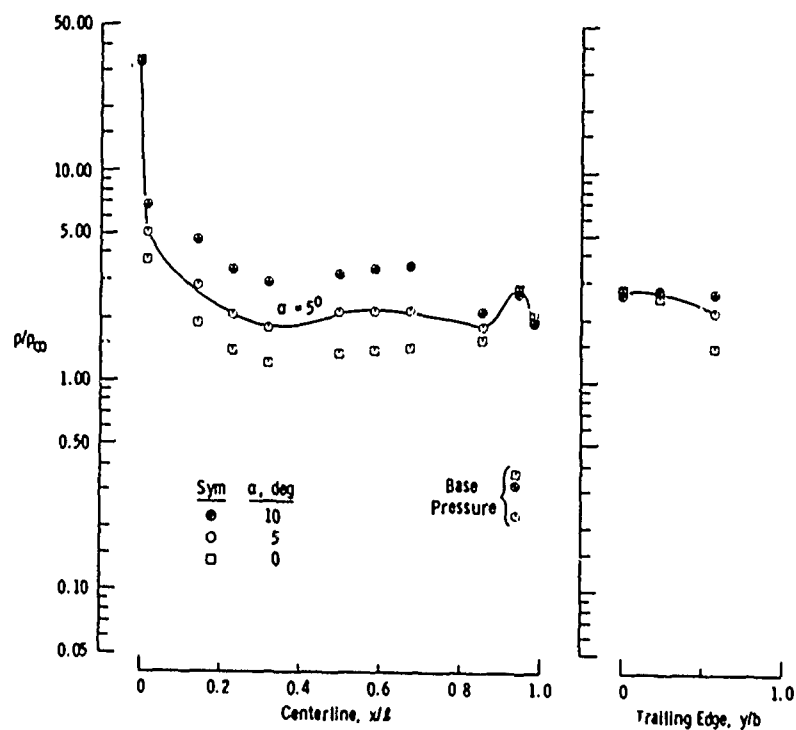
f. Orbiter, $\Delta x/L = 0.227$ and $\Delta z/L = 0.23$
Fig. II-7 Concluded

AEDC-TR-72-46
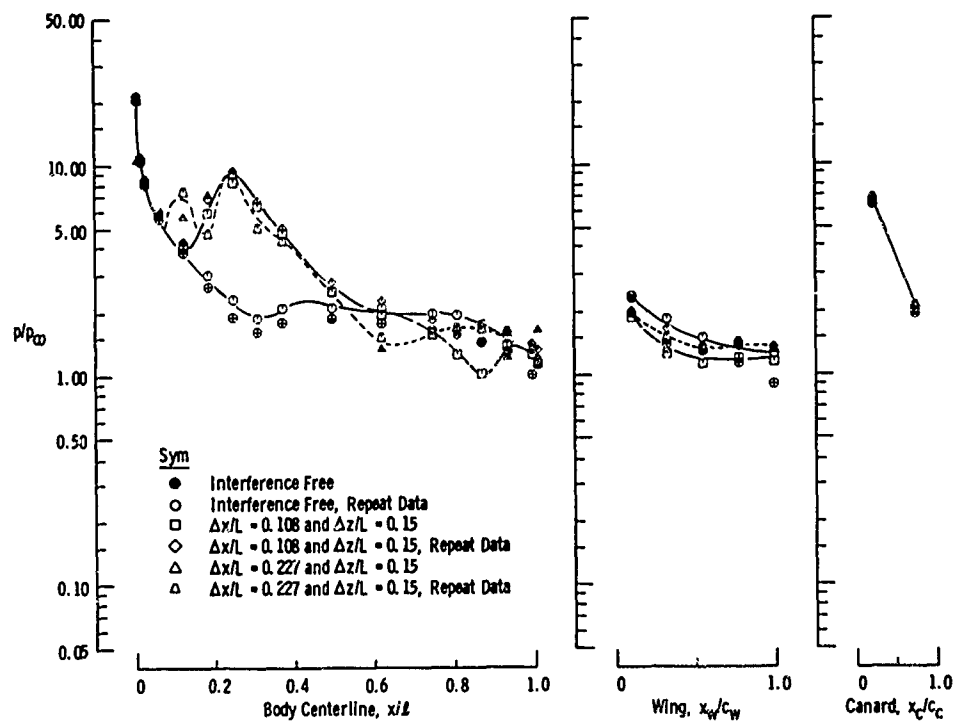
a. Booster without Power Simulation
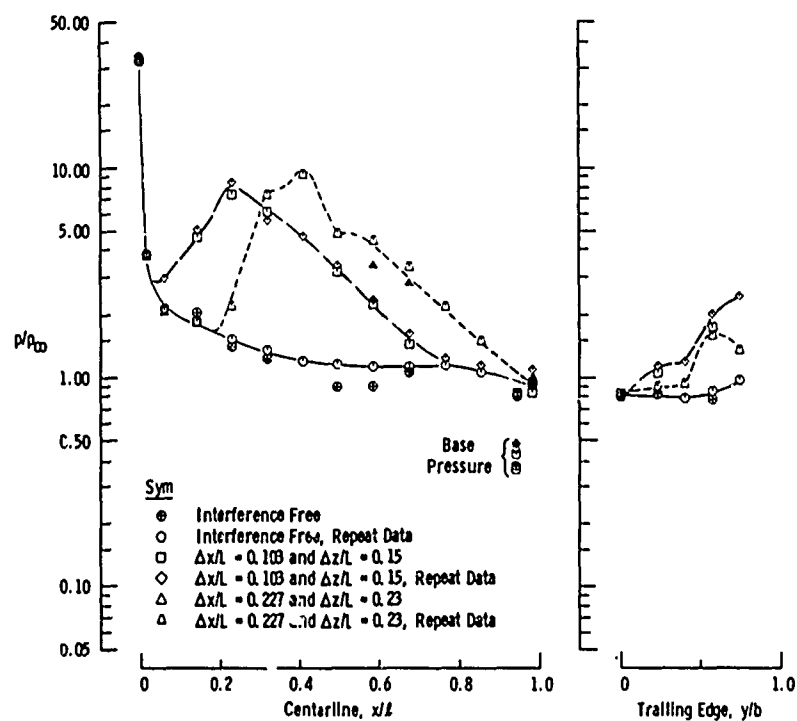
b. Orbiter without Power Simulation

Fig. II-8 Repeatability of the Booster and Orbiter Pressure Distributions Obtained at $a = 0$, $M_\infty = 4.97$, and $Re_\ell = 1.5 \times 10^6$

109
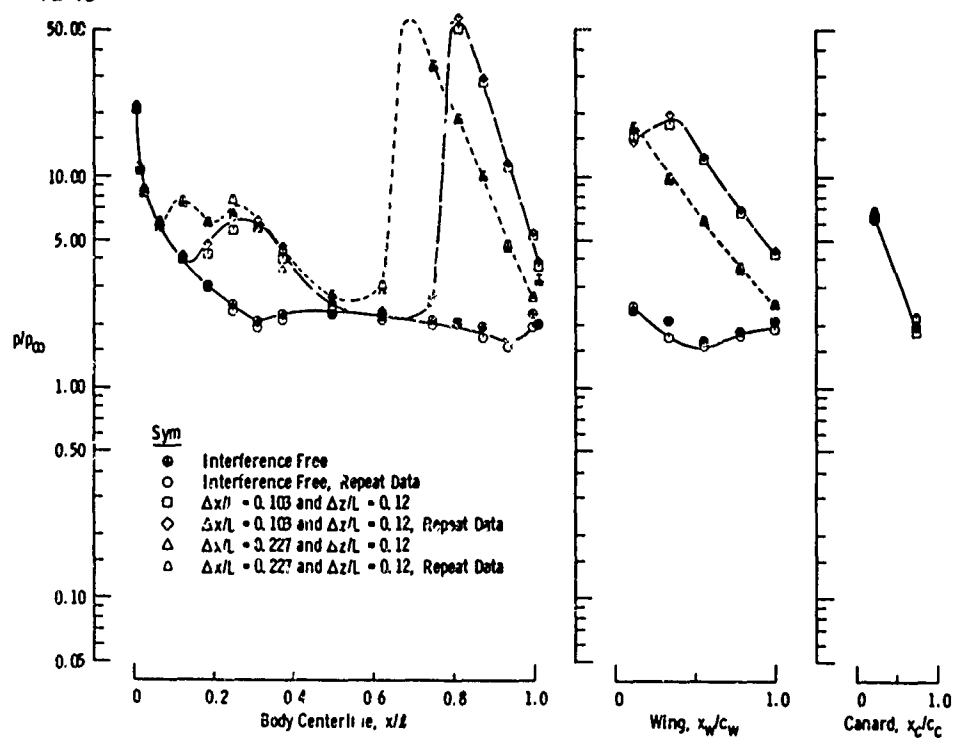
c. Booster with 50-percent Power Simulation
Fig. II-8 Continued
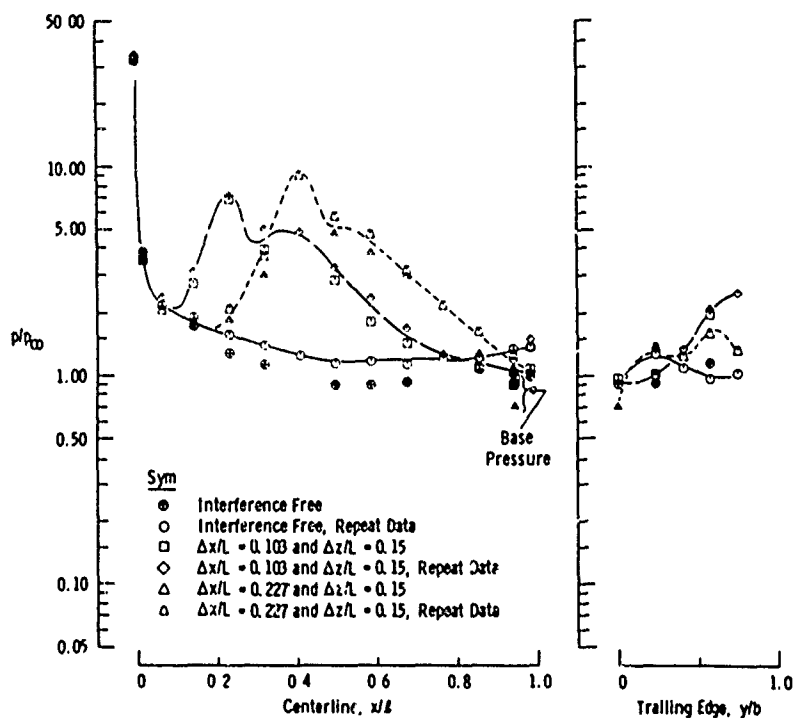
d. Orbiter with 100-percent Power Simulation
Fig. II-8 Concluded

110
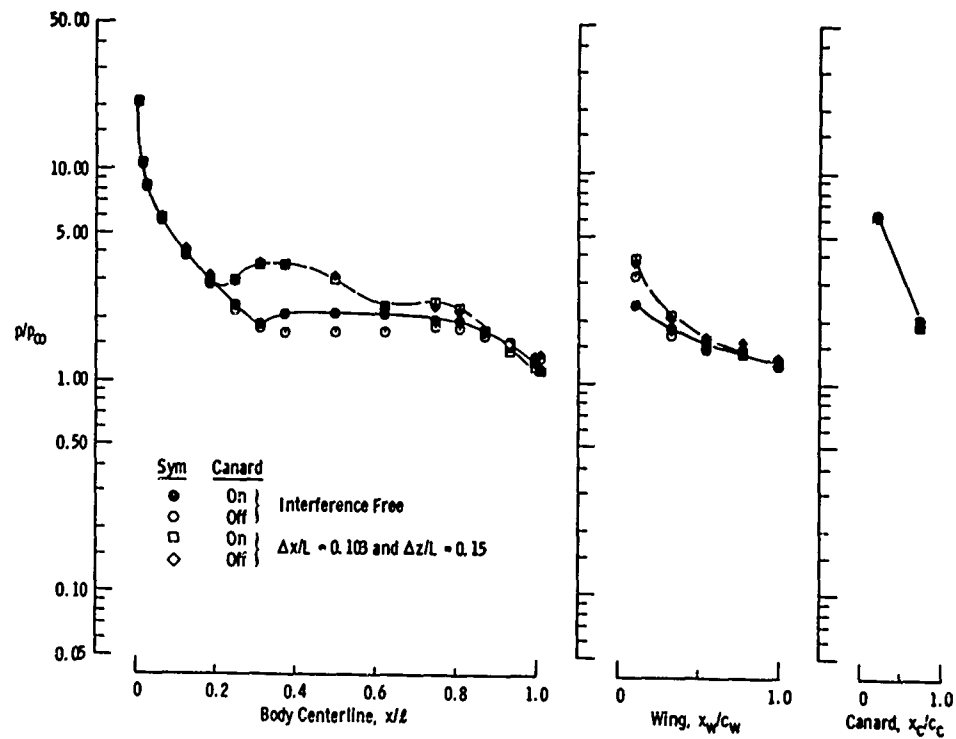
a. Booster and Canard Effects with and without an Interfering Flow Field
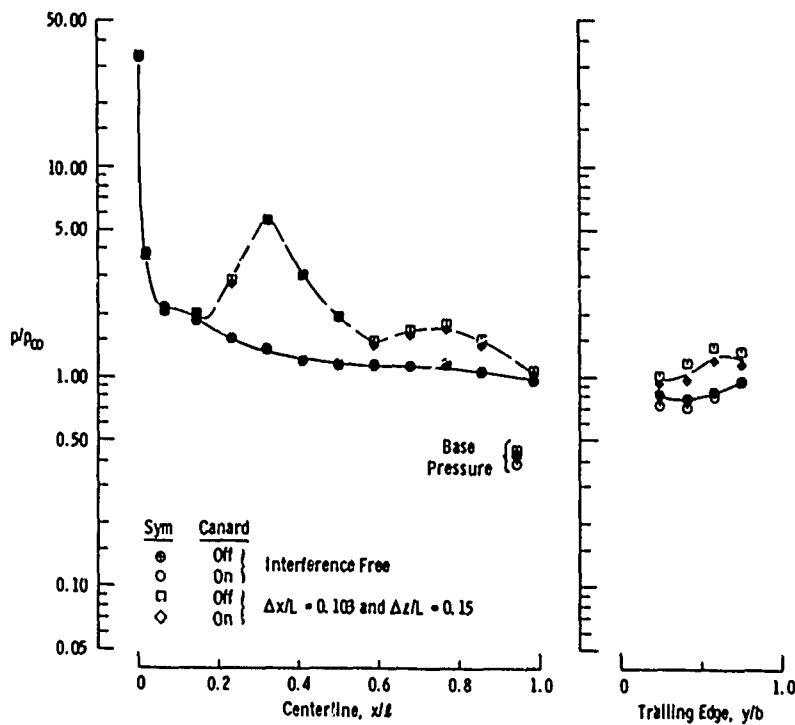
b. Orbiter and Canard Effects with and without an Interfering Flow Field
Fig. II-9 The Influence of the Booster Canard and the Booster and Orbiter
Boundary-Layer Trips on the Pressure Distributions at $\alpha = 0$, $M_\infty = 4.97$,
and $Re_\ell = 1.5 \times 10^6$

111
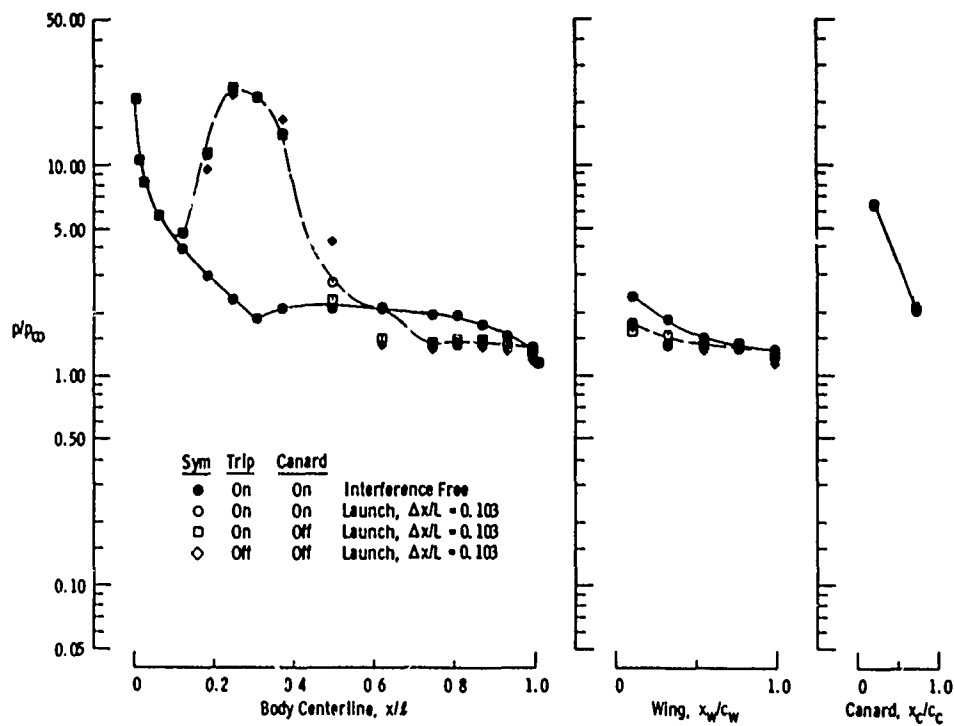
c. Booster, Boundary-Layer Trip, and Canard Effects on the Launch Configuration

Fig. II-9 Continued
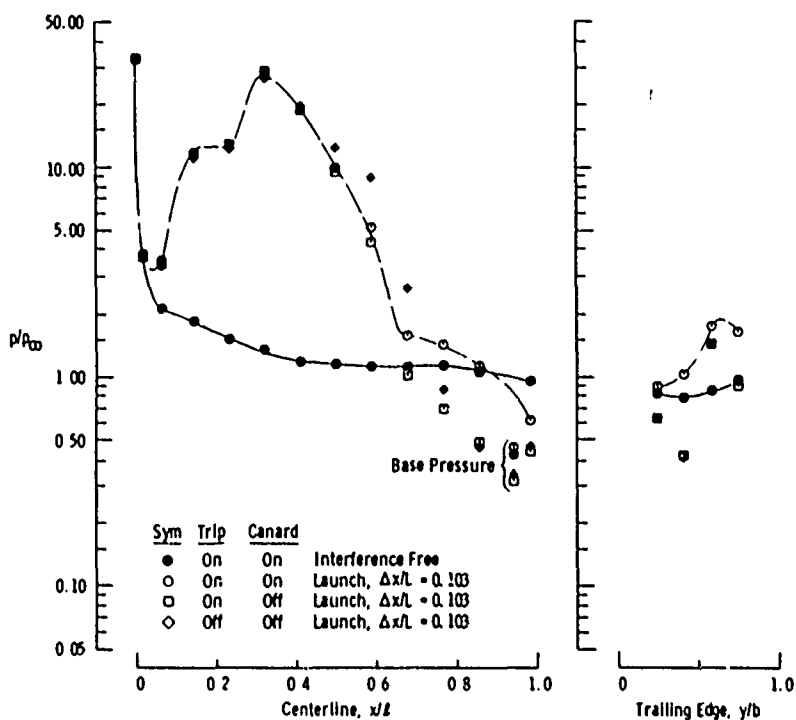
d. Orbiter, Boundary-Layer Trip, and Canard Effects on the Launch Configuration

Fig. II-9 Concluded
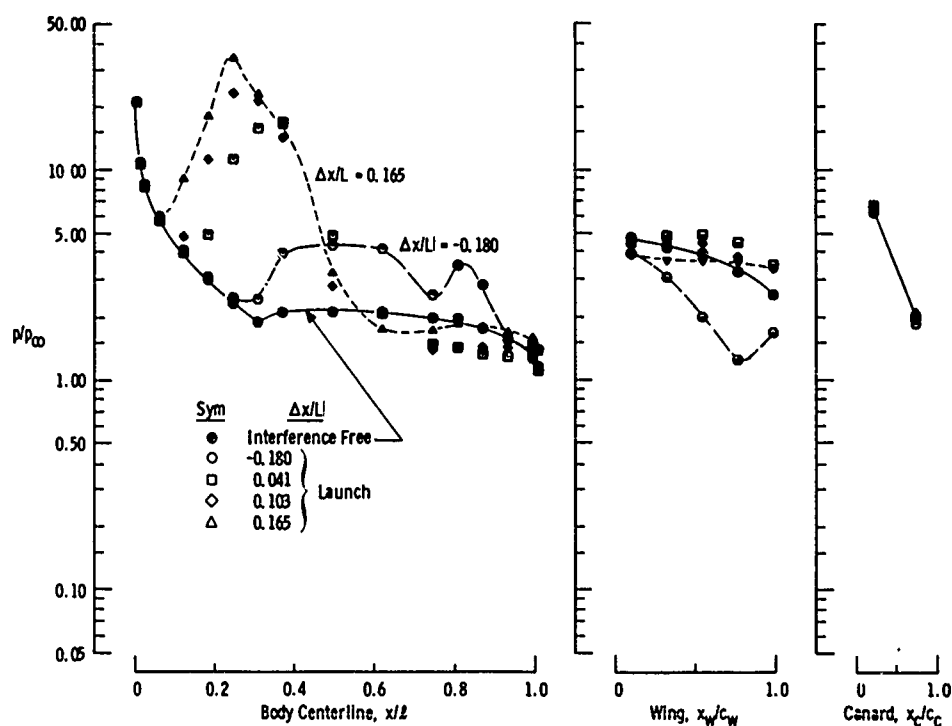
a. Booster, $a = 0$, No Power Simulation, $\Delta x/L$ Variable
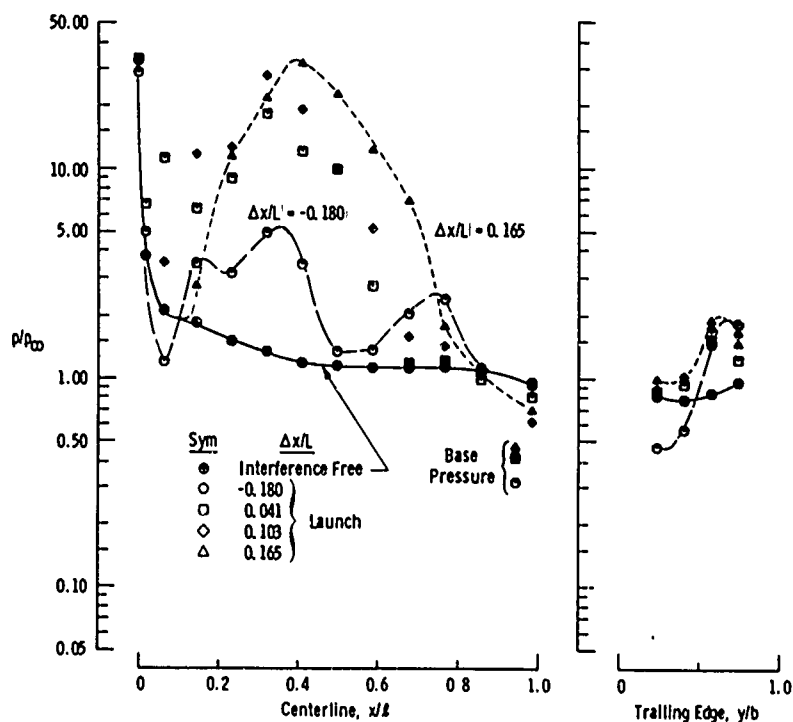
b. Orbiter, $a = 0$, No power Simulation, $\Delta x/L$ Variable

Fig. II-10 Booster and Orbiter Pressure Distributions during the Launch Configuration at $M_\infty = 4.97$ and $R_{\ell} = 1.5 \times 10^6$
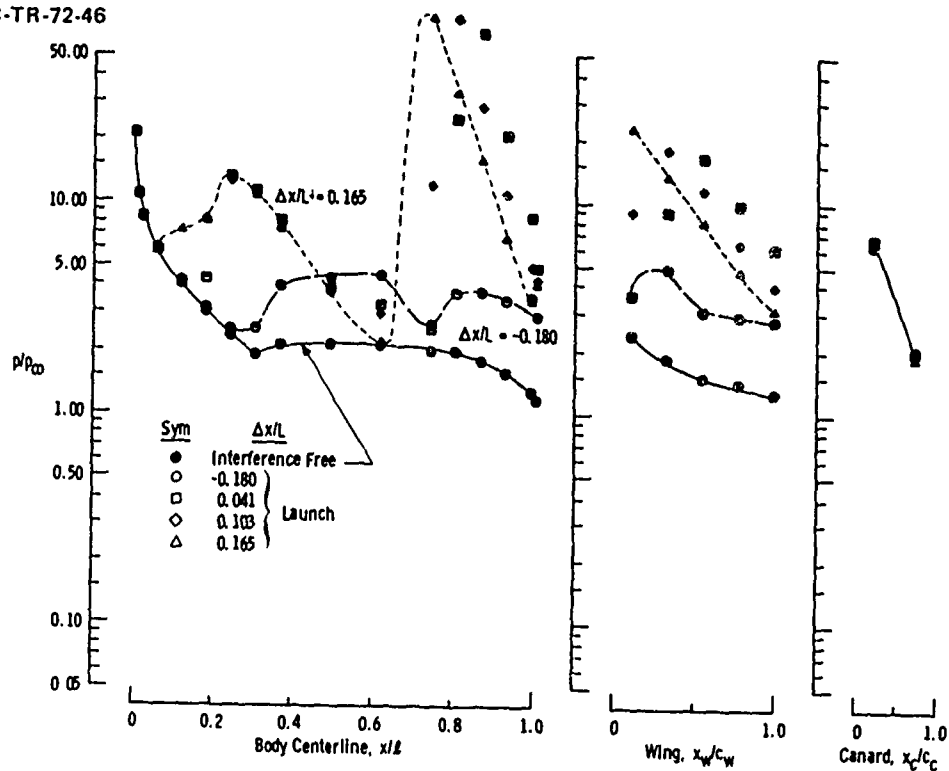
c. Booster, $a = 0$, 100-percent Power Simulation for Both Models, $\Delta x/L$ Variable
Fig. II-10 Continued
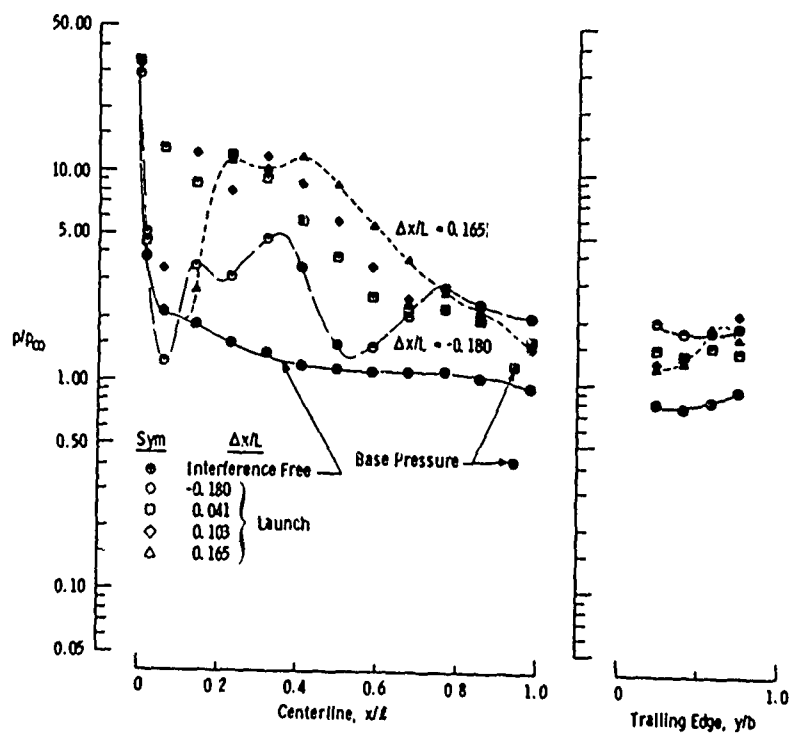
d. Orbiter, $a = 0$, 100-percent Power Simulation for Both Models, $\Delta x/L$ Variable
Fig. II-10 Continued
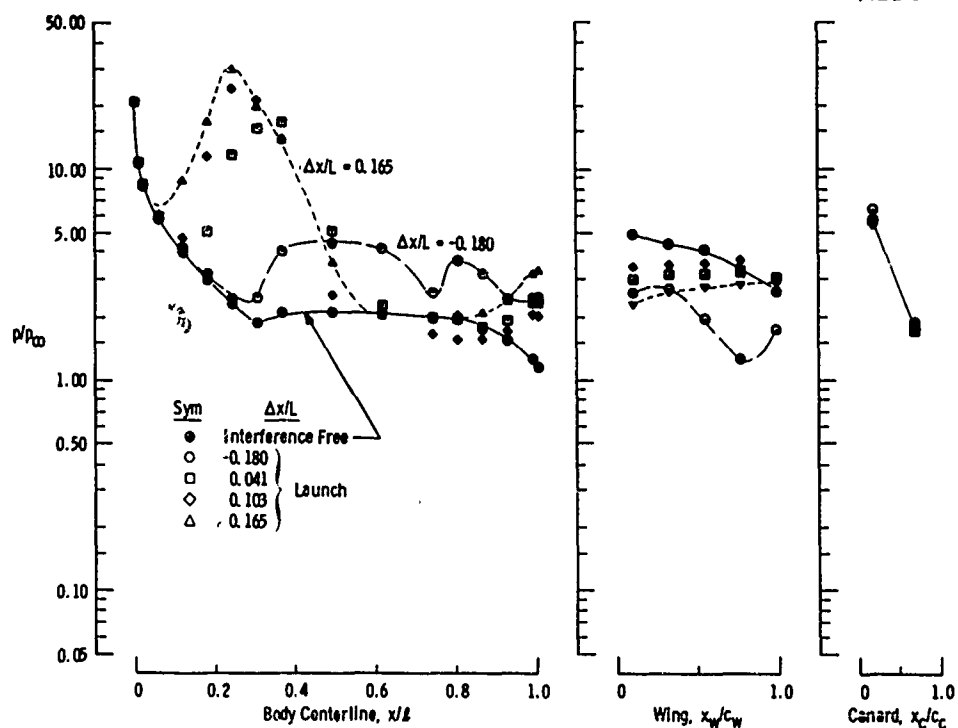
114

e. Booster, a = 0, 100-percent Booster Power Simulation, Zero Orbiter Power, $\Delta x/L$ Variable

Fig. II-10 Continued

f. Orbiter, a = 0, 100-percent Booster Power Simulation, Zero Orbiter Power, $\Delta x/L$ Variable

Fig. II-10 Continued

115
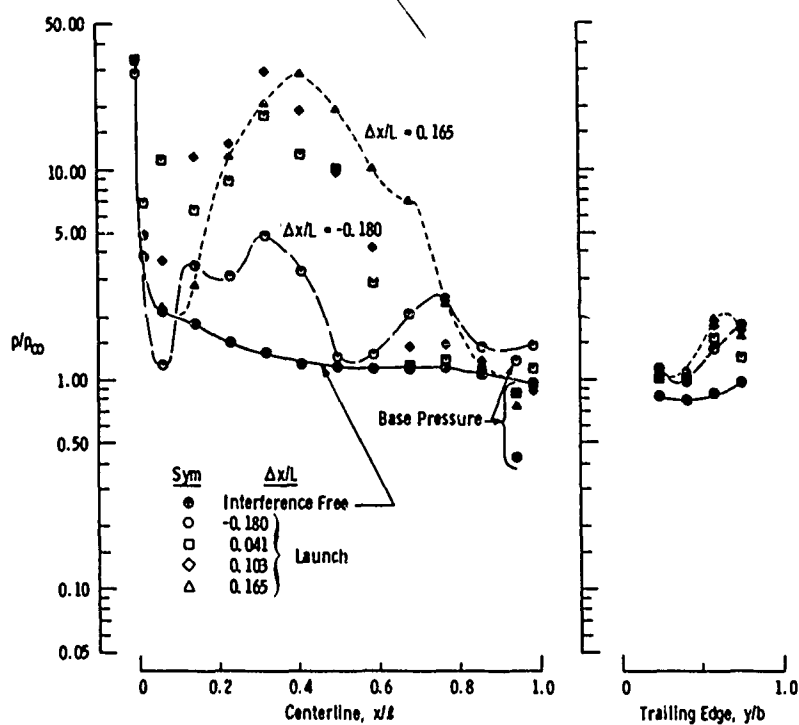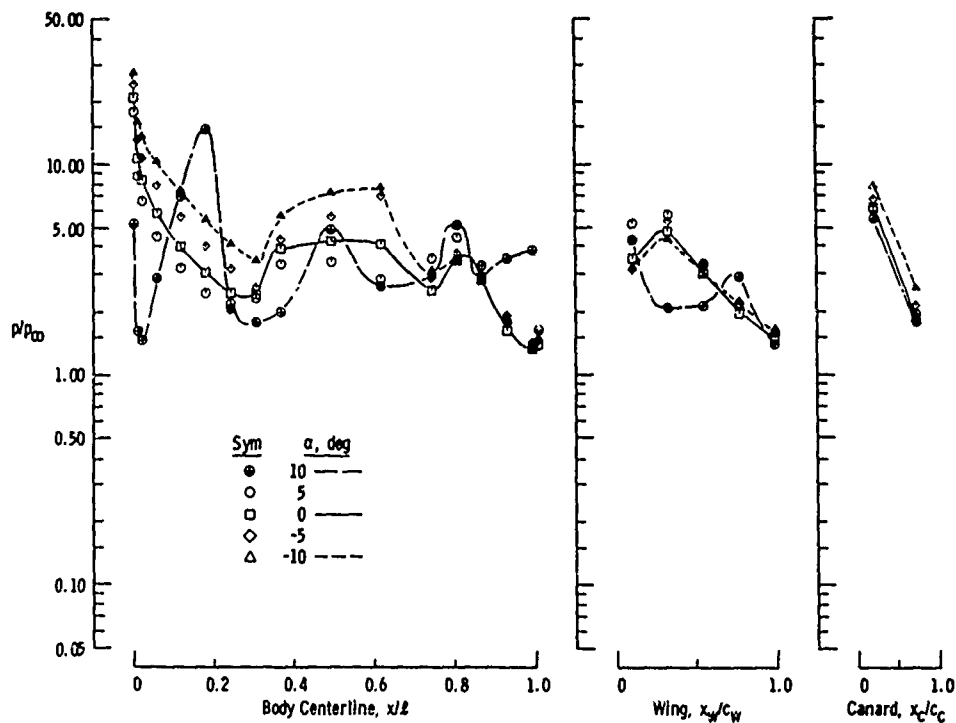
g. Booster, $\Delta x/L = -0.180$, No Power Simulation, a Variable
Fig. II-10 Continued
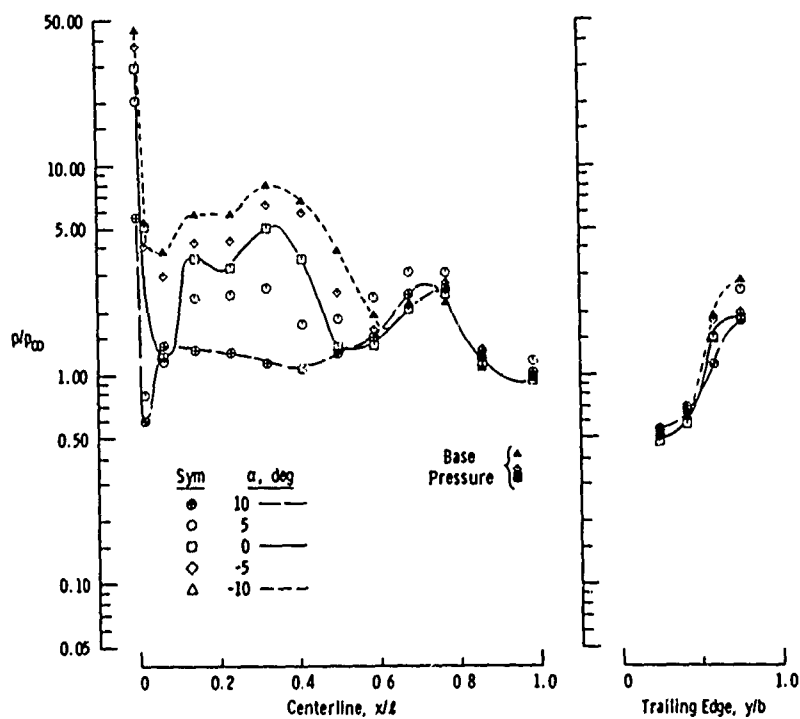
h. Orbiter, $\Delta x/L = -0.180$, No Power Simulation, a Variable
Fig. II-10 Continued
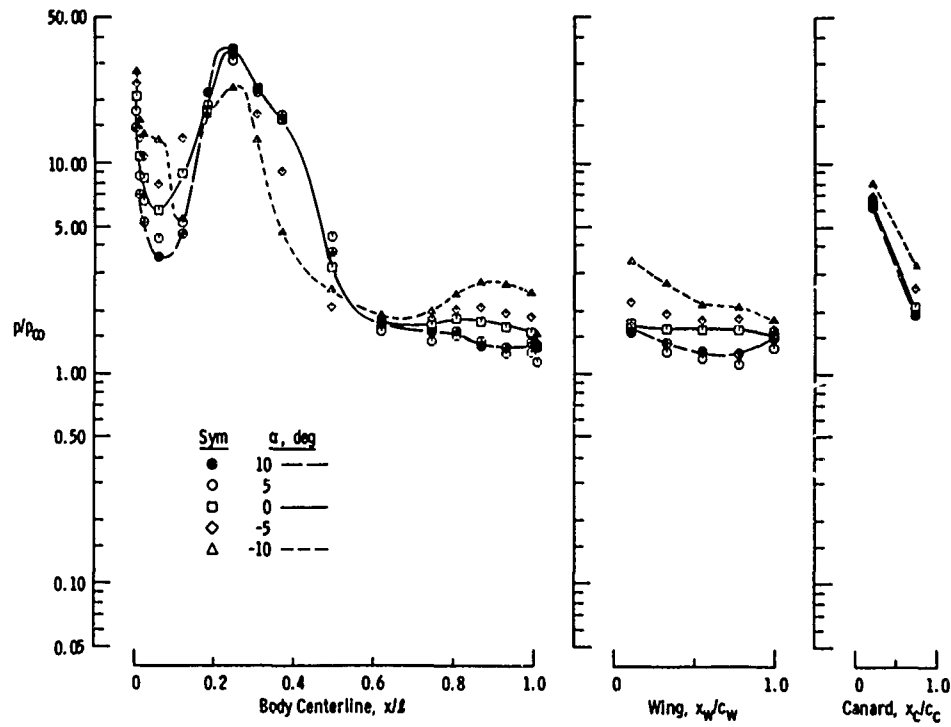
i. Booster, $\Delta x/L = 0.165$, No Power Simulation, a Variable
Fig. II-10 Continued
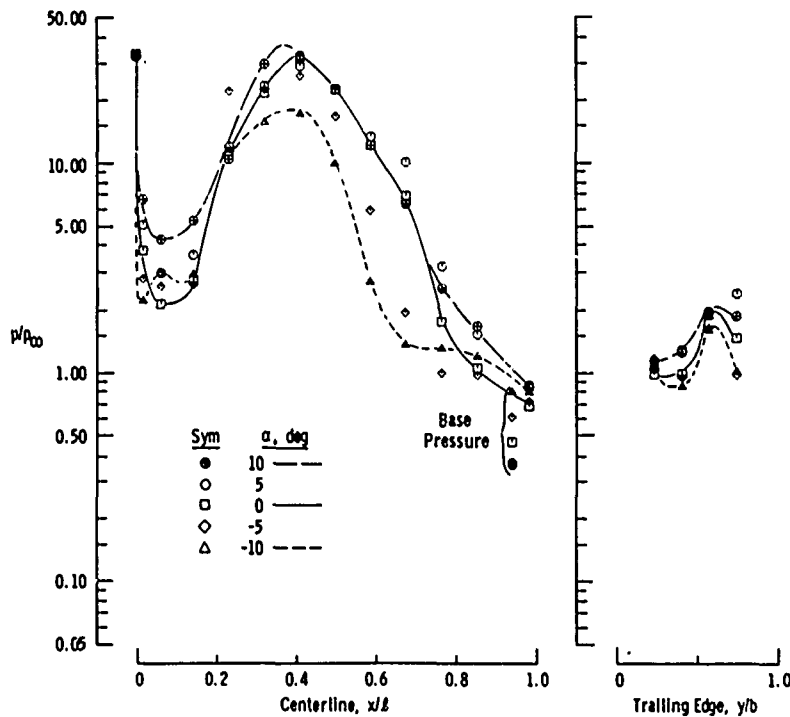
j. Orbiter, $\Delta x/L = 0.165$, No Power Simulation, a Variable
Fig. II-10 Continued

117
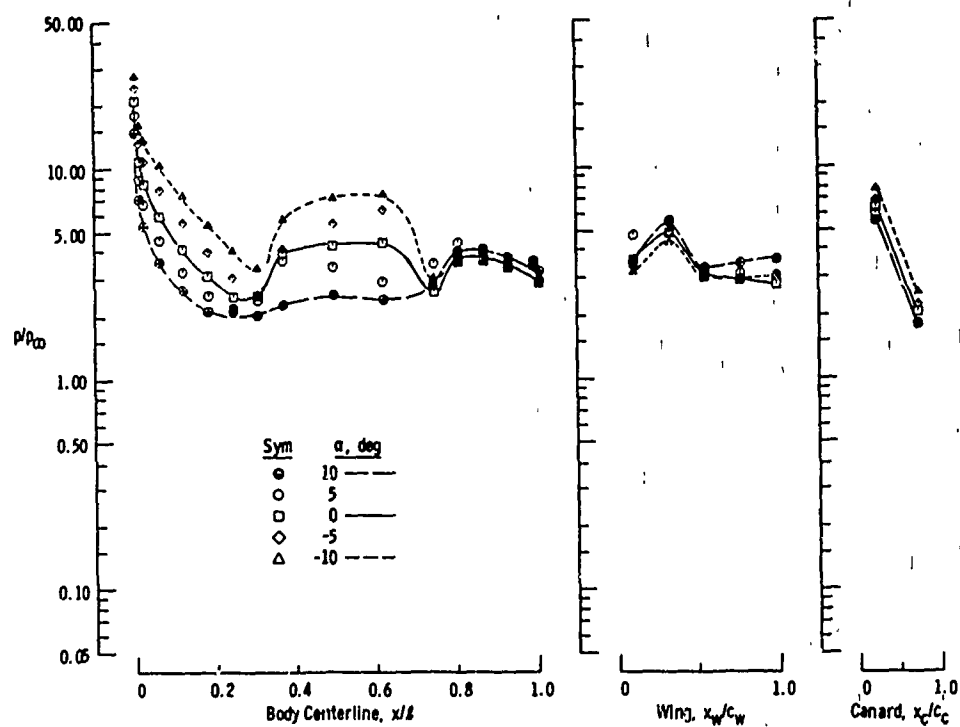
k. Booster, $\Delta x/L = -0.180$, 100-percent Power Simulation for Both Models, α Variable
Fig. II-10 Continued
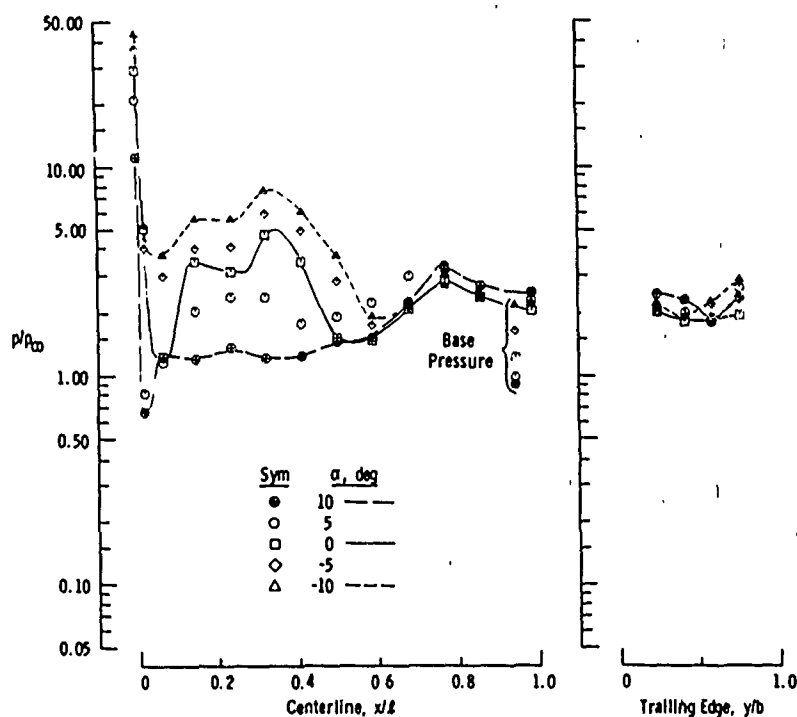
l. Orbiter, $\Delta x/L = -0.180$, 100-percent Power Simulation for Both Models, α Variable
Fig. II-10 Continued
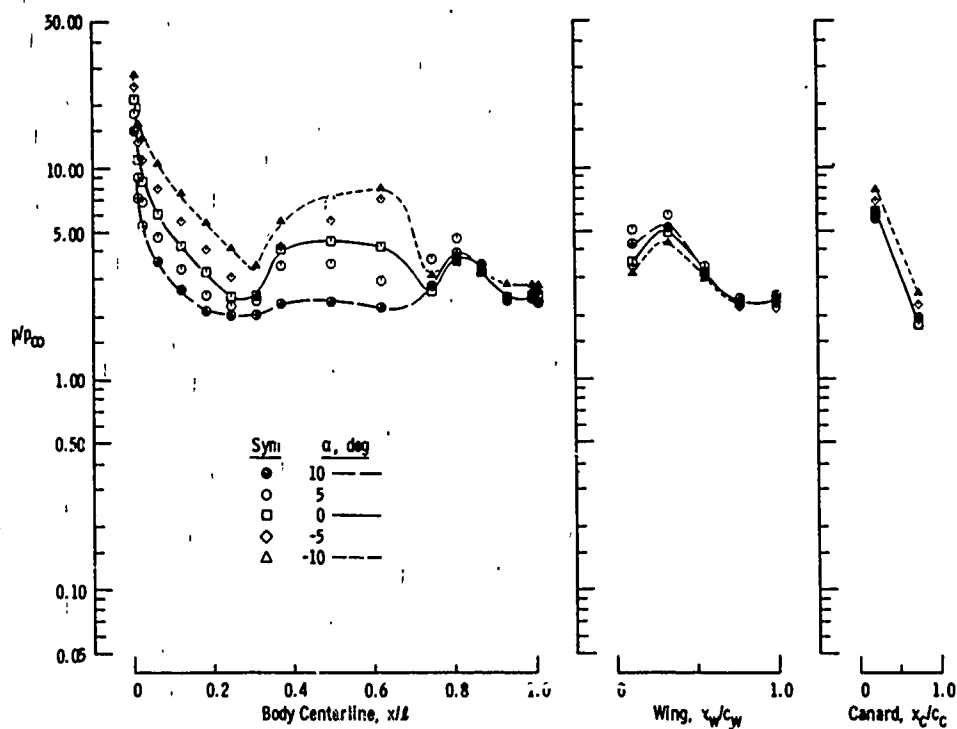
m. Booster, $\Delta x/L$ = -0.180, 100-percent Booster Power Simulation, Zero Orbiter Power, a Variable
Fig. II-10 Continued
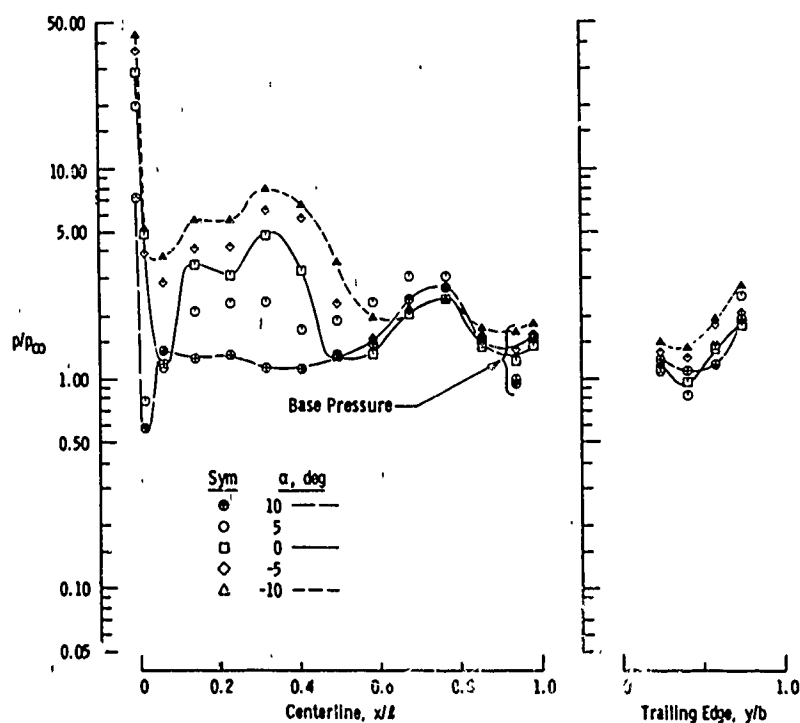
n. Orbiter, $\Delta x/L$ = -0.180, 100-percent Booster Power Simulation, Zero Orbiter Power, a Variable
Fig. II-10 Continued
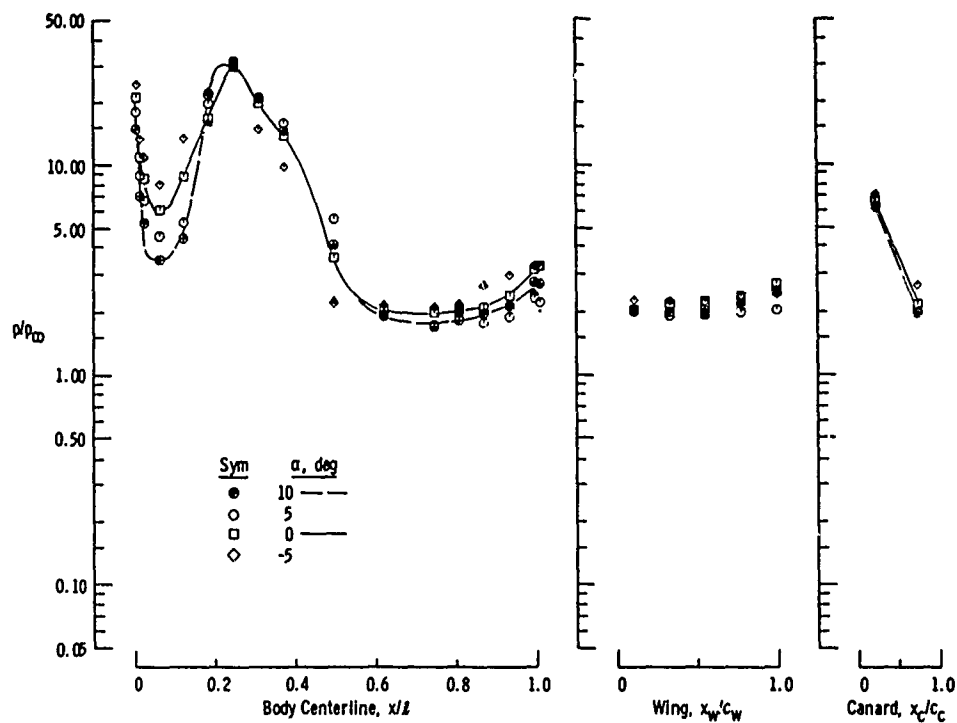
o. Booster, $\Delta x/L$ = 0.165, 100-percent Booster Power Simulation, Zero Orbiter Power, a Variable

Fig. II-10 Continued
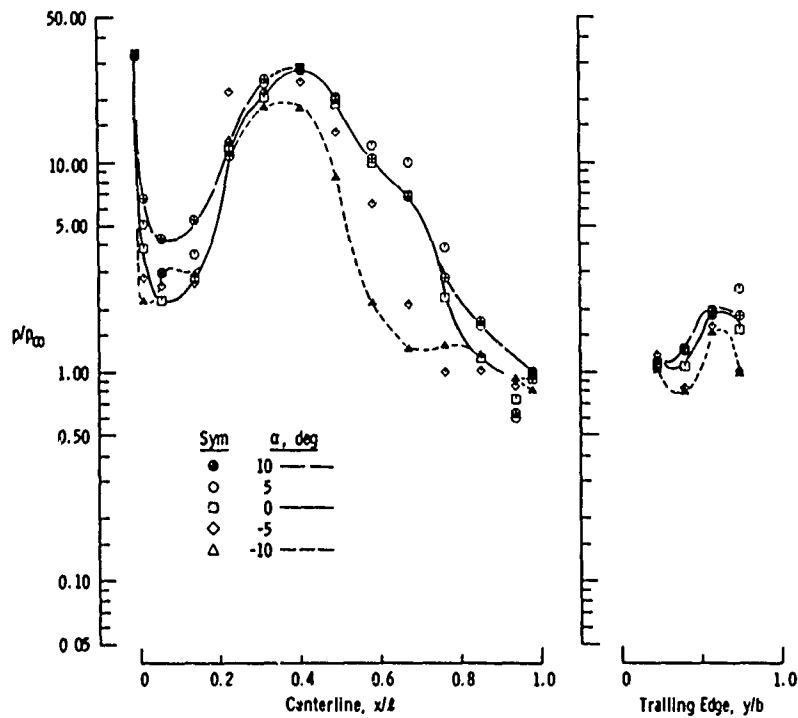
p. Orbiter, $\Delta x/L$ = 0.165, 100-percent Booster Power Simulation, Zero Orbiter Power, a Variable

Fig. II-10 Concluded

120
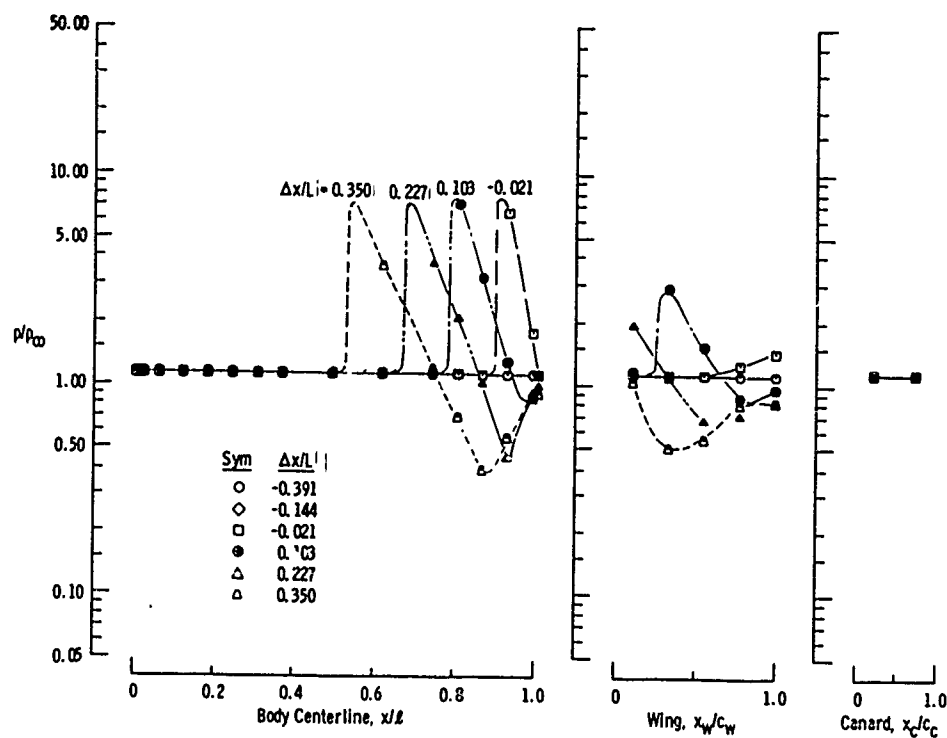
a. Booster, $\Delta z/L = 0.15$, Variable $\Delta x/L$
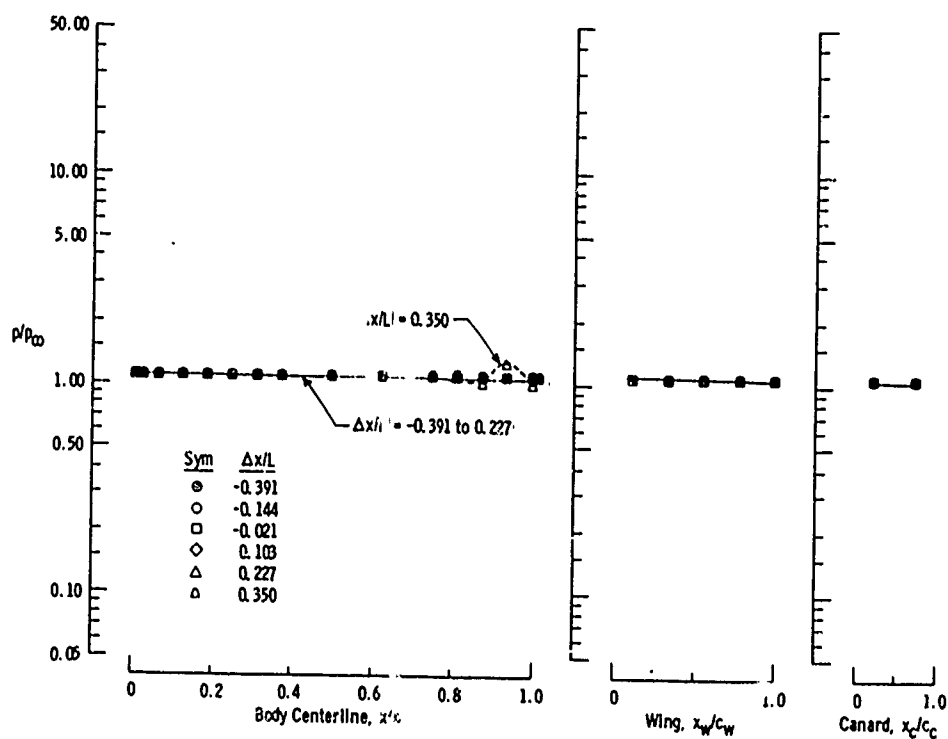
b. Booster, $\Delta z/L = 0.23$, Variable $\Delta x/L$

Fig. II-11 Plume Impingement Pressure Distribution on the Booster without External Flow ($M_\infty = 0$), 100-percent Orbiter Power Simulation with Orbiter at Incidence Angle or 5 deg
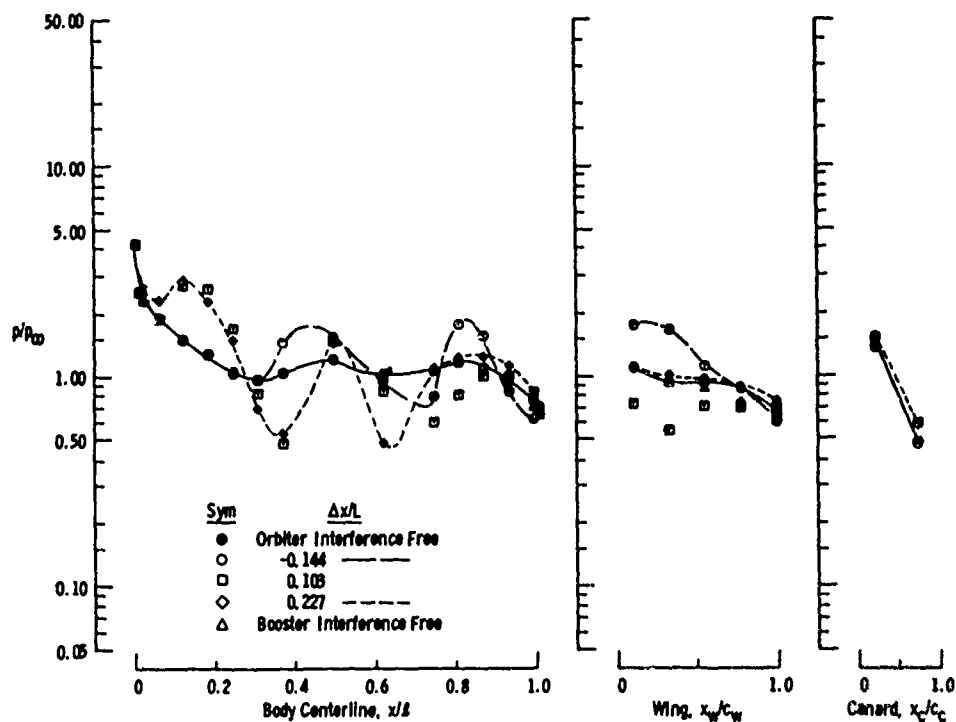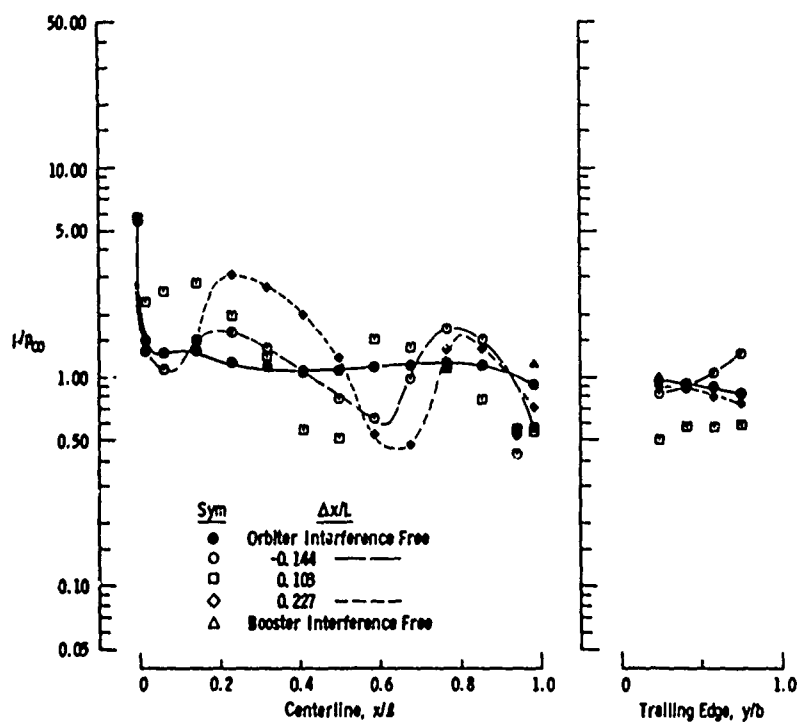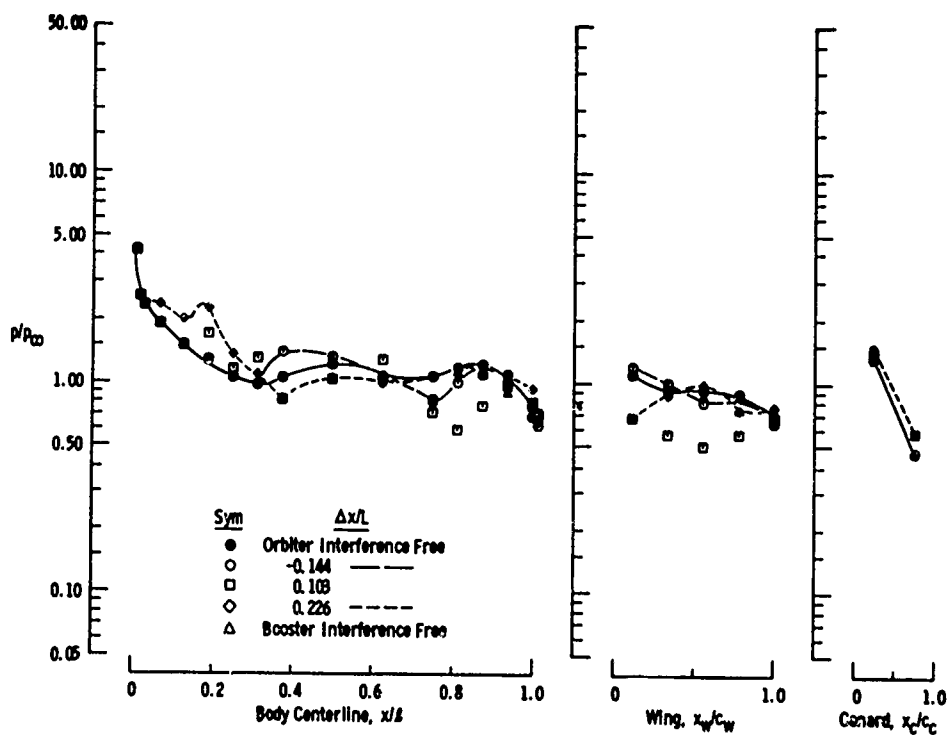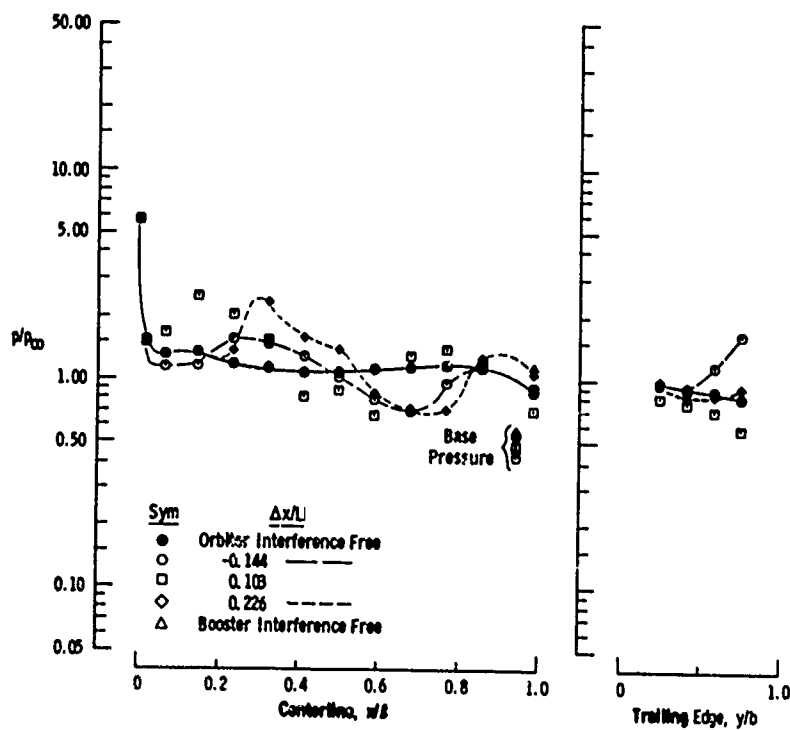
a. Booster, $\Delta z/L = 0.12$

b. Orbiter, $\Delta x/L = 0.12$

Fig. II-12 Booster and Orbiter Pressure Distributions at Various Staging Positions without Power Simulation at $a = 0$, $M_\infty = 3.00$, $Re_\ell = 2.2 \times 10^6$ (Variable $\Delta x/L$ and $\Delta z/L$)

122
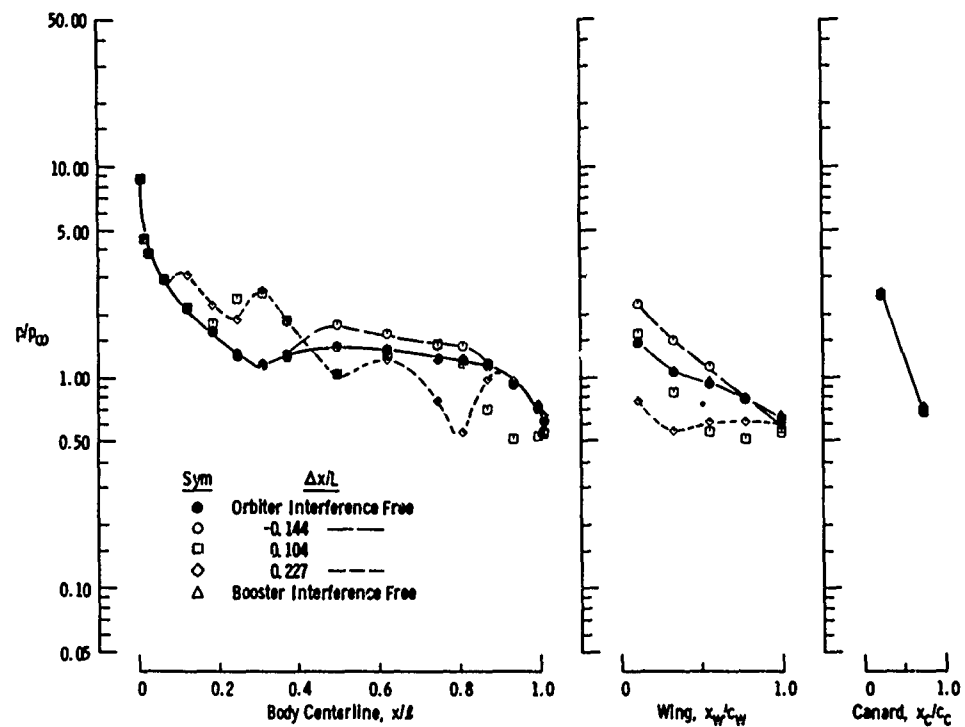
c. Booster, $\Delta z/L = 0.15$
Fig. II-12 Continued
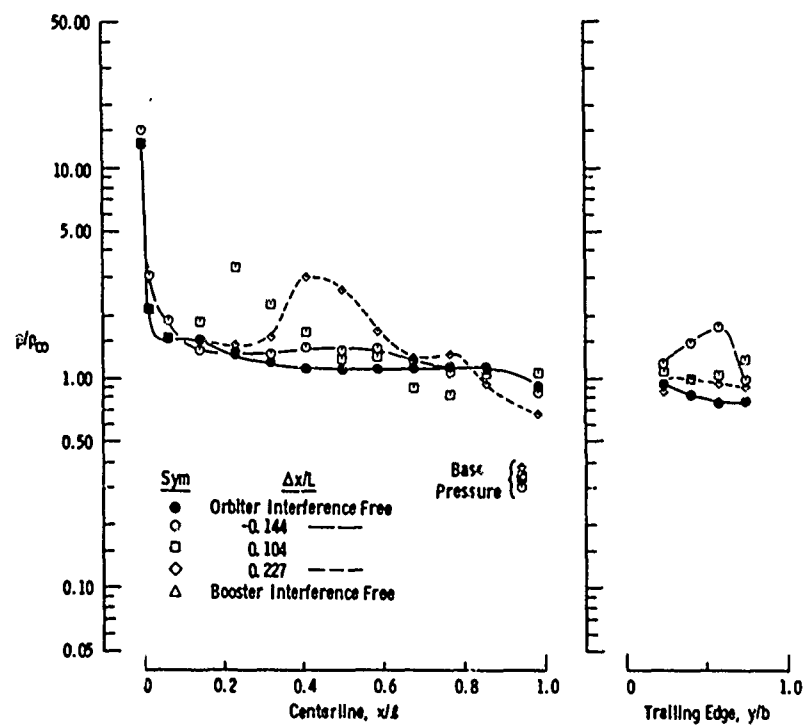
d. Orbiter, $\Delta z/L = 0.15$
Fig. II-12 Continued
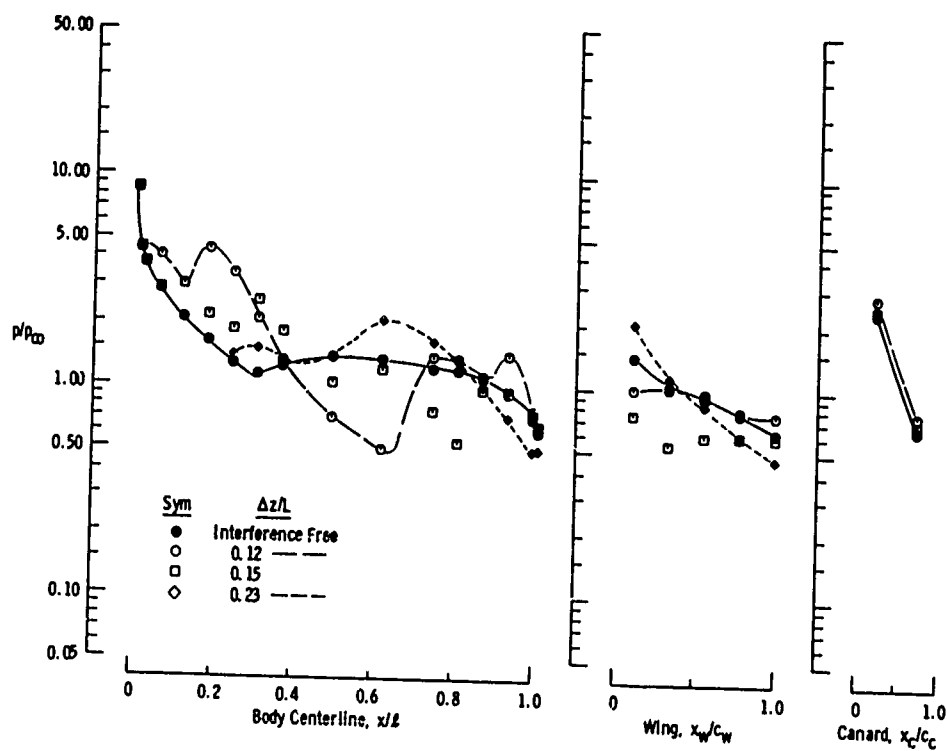
e. Booster, $\Delta x/L = 0.228$
Fig. II-12 Continued

f. Orbiter, $\Delta x/L = 0.228$
Fig. II-12 Concluded

124
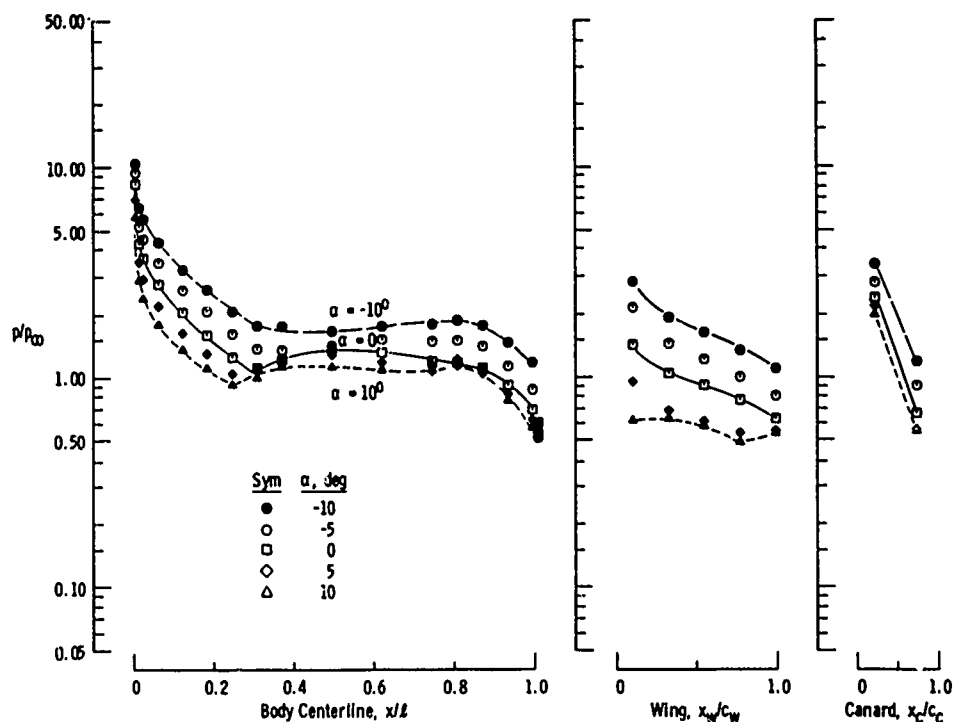
a. Booster, Orbiter Interference Free ($\Delta x/L = 0.517$ and $\Delta z/L = 0.91$)
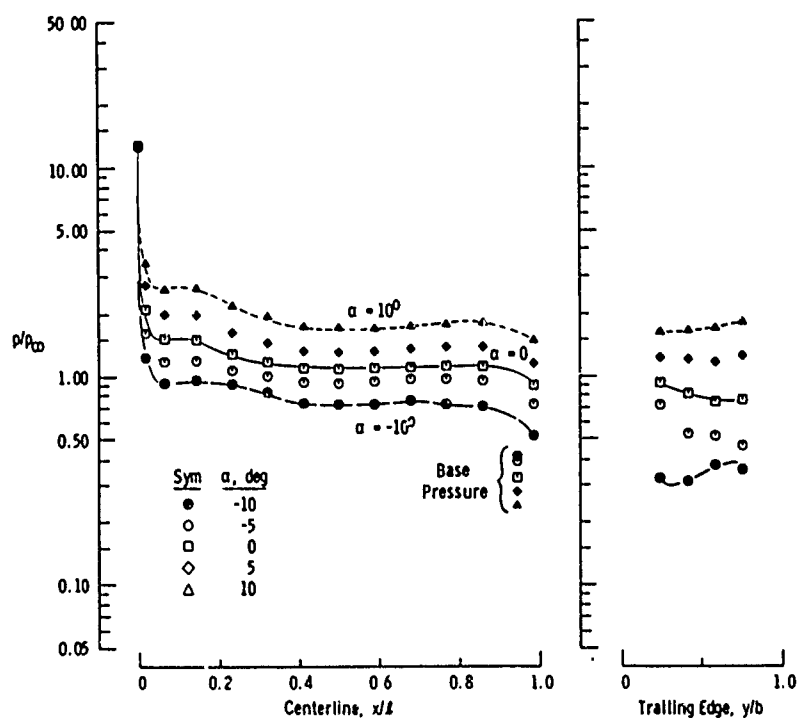
b. Orbiter, Orbiter Interference Free ($\Delta x/L = 0.517$ and $\Delta z/L = 0.91$)

Fig. II-13 Angle-of-Attack Effects on the Booster and Orbiter Pressure Distributions
without Power Simulation at $M_\infty = 3.00$ and $Re_\ell = 2.2 \times 10^6$
(Variable α, $\Delta x/L$, and $\Delta z/L$)

125
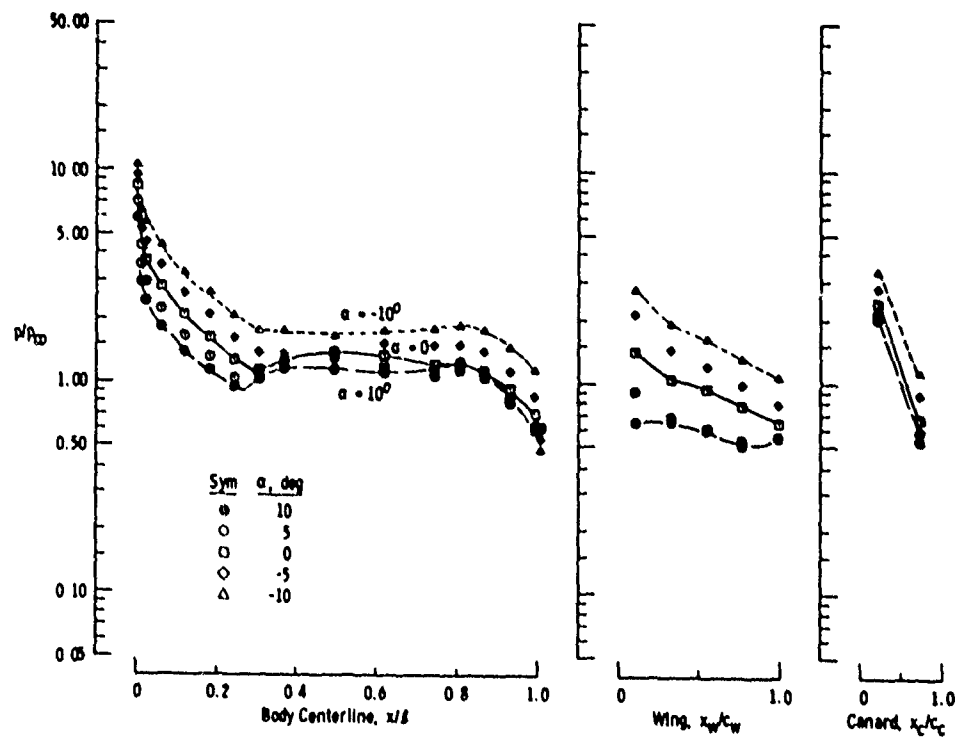
c. Booster, Booster Interference Free ($\Delta x/L = -0.391$ and $\Delta z/L = 0.91$)
Fig. II-13 Continued
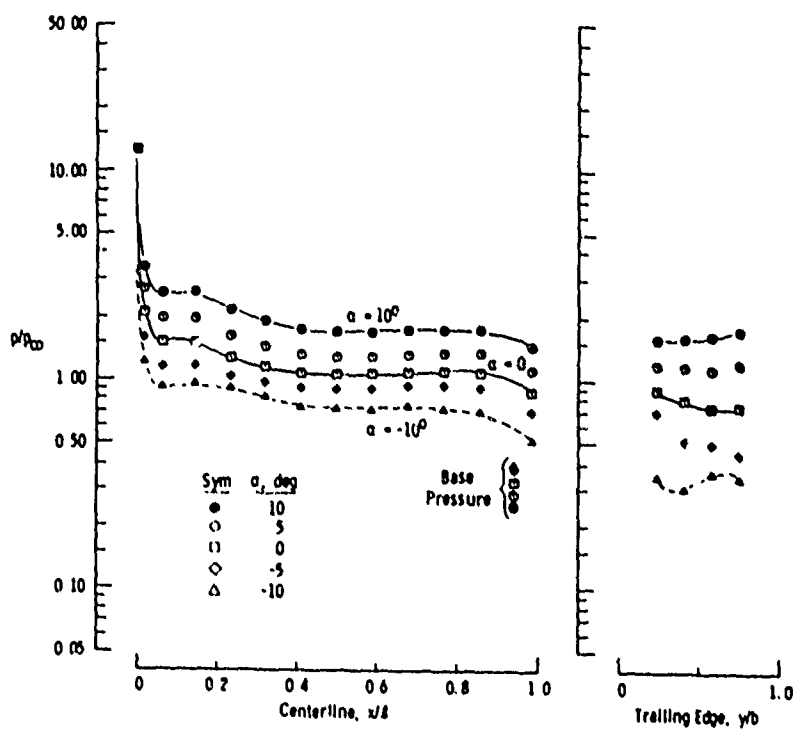
d. Orbiter, Booster Interference Free ($\Delta x/L = -0.391$ and $\Delta z/L = 0.91$)
Fig. II-13 Continued
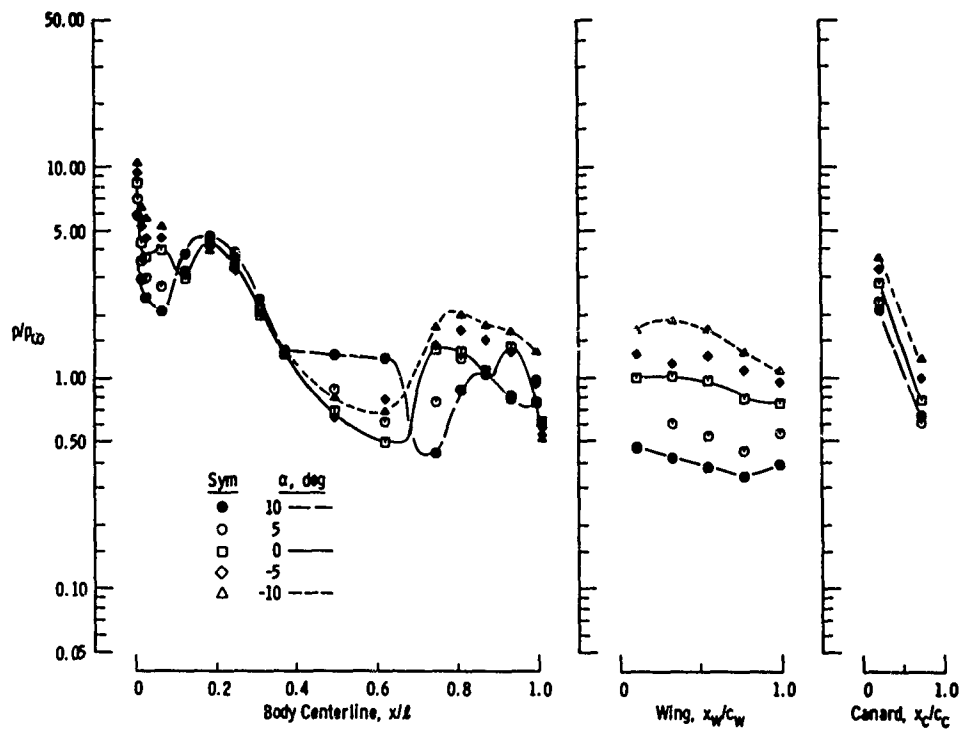
e. Booster, $\Delta x/L = 0.226$, and $\Delta z/L = 0.12$
Fig. II-13 Continued
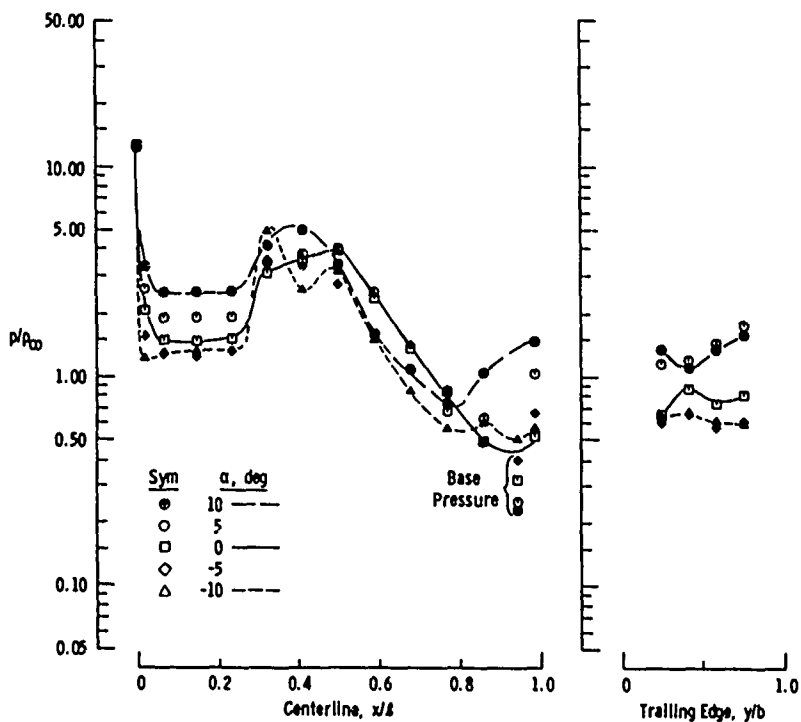
f. Orbiter, $\Delta x/L = 0.226$, and $\Delta z/L = 0.12$
Fig. II-13 Continued
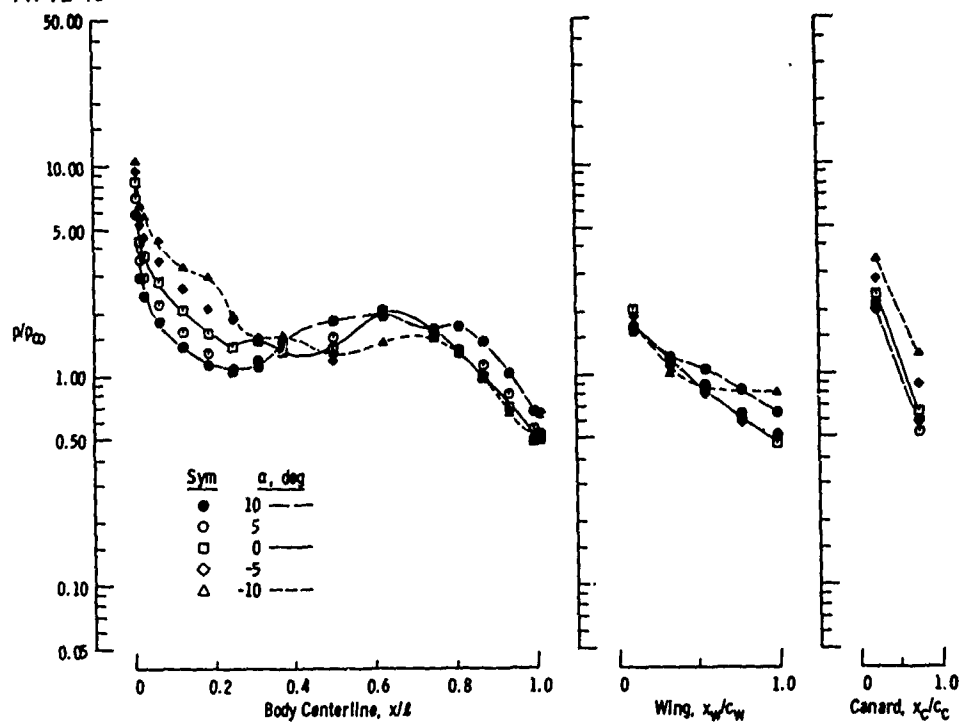
g. Booster, $\Delta x/L = 0.227$, and $\Delta x/L = 0.23$
Fig. II-13 Continued

h. Orbiter, $\Delta x/L = 0.227$, and $\Delta z/L = 0.23$
Fig. II-13 Concluded

128
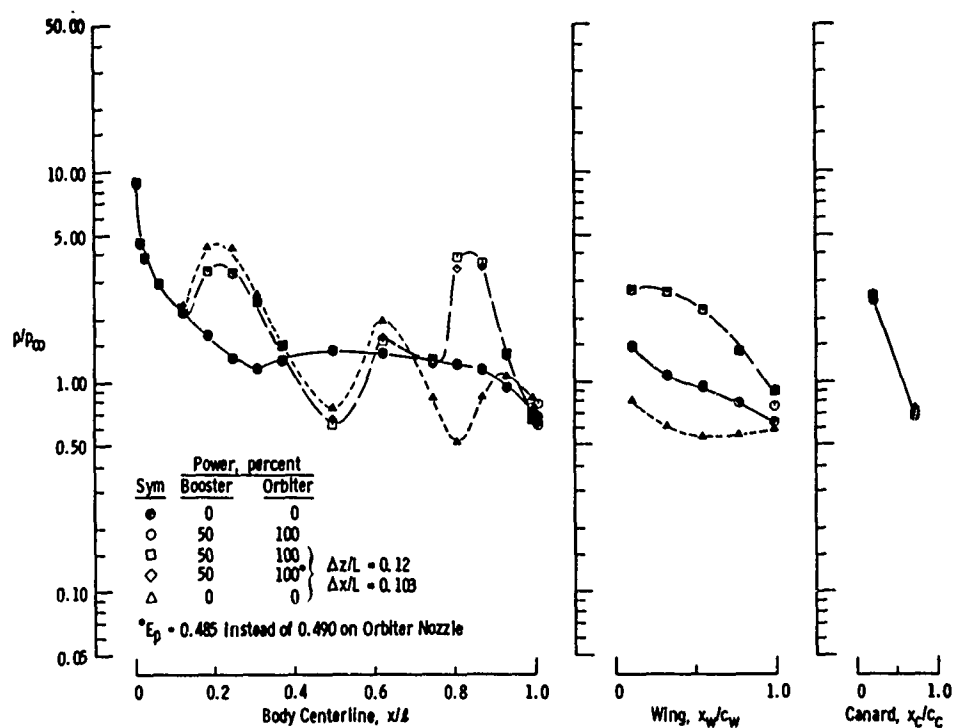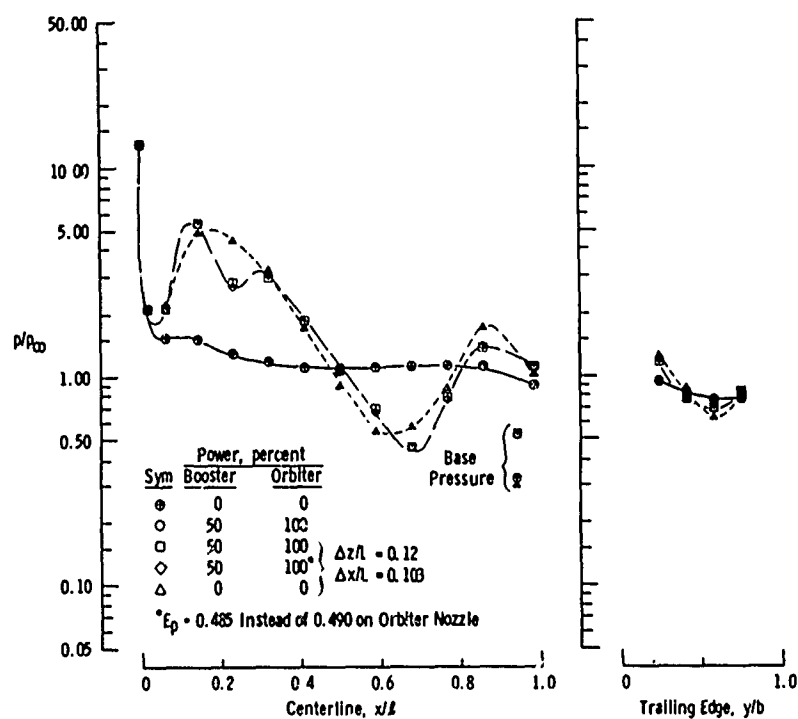
a. Booster

b. Orbiter

Fig. II-14 The Effect of Orbiter Nozzle Setting for the Power Simulation on the Orbiter and Booster Pressure Distributions at $a = 0$, $M_\infty = 3.00$, and $Re_\ell = 2.2 \times 10^6$
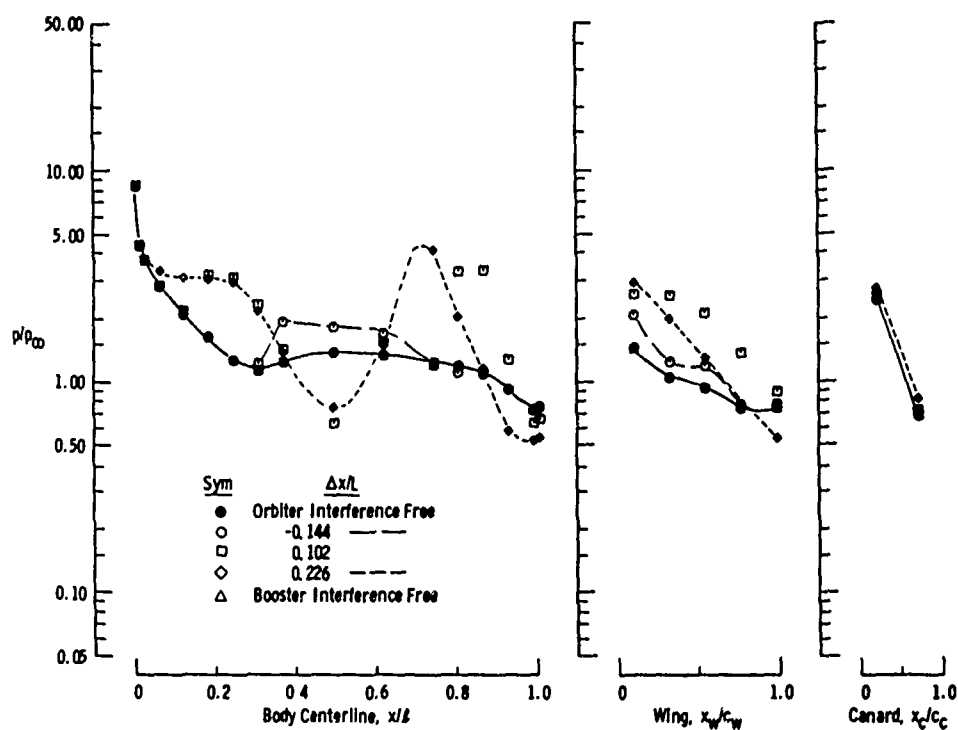
a. Booster, $\Delta z/L = 0.12$
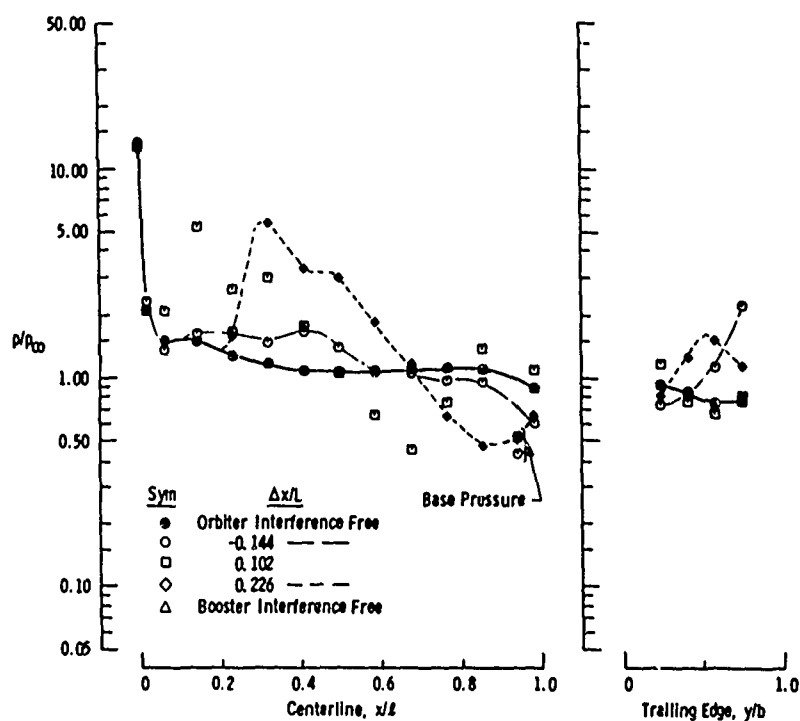
b. Orbiter, $\Delta z/L = 0.12$

Fig. II-15 Booster and Orbiter Pressure Distributions at Various Staging Positions with Power Simulation (50-percent Booster Power, 100-percent Orbiter Power) at $a = 0$, $M_\infty = 3.00$, $Re_\ell = 2.2 \times 10^6$
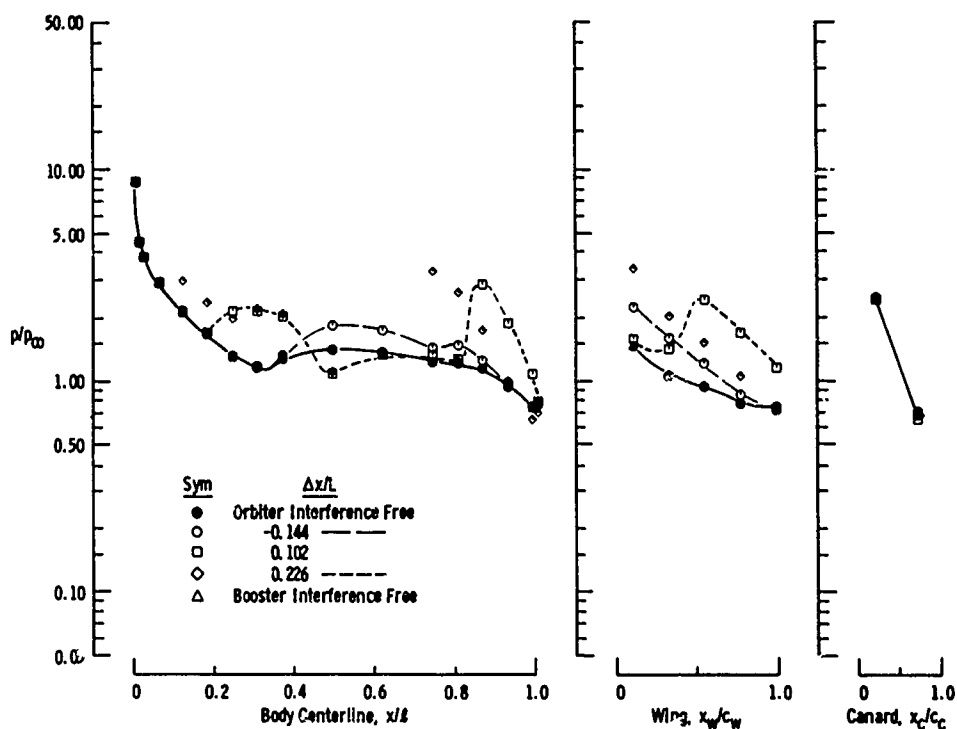
c. Booster, $\Delta z/L = 0.15$
Fig. II-15 Continued
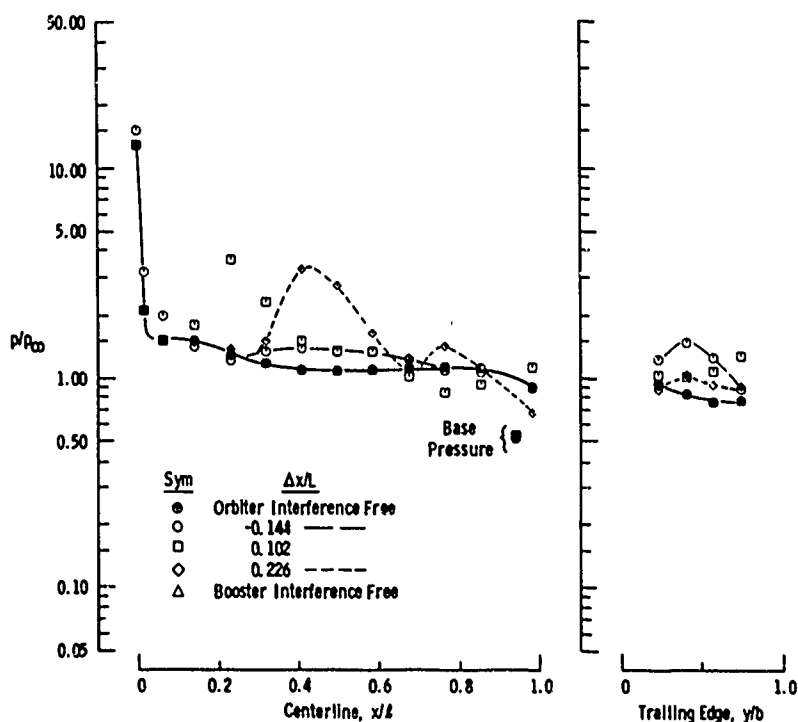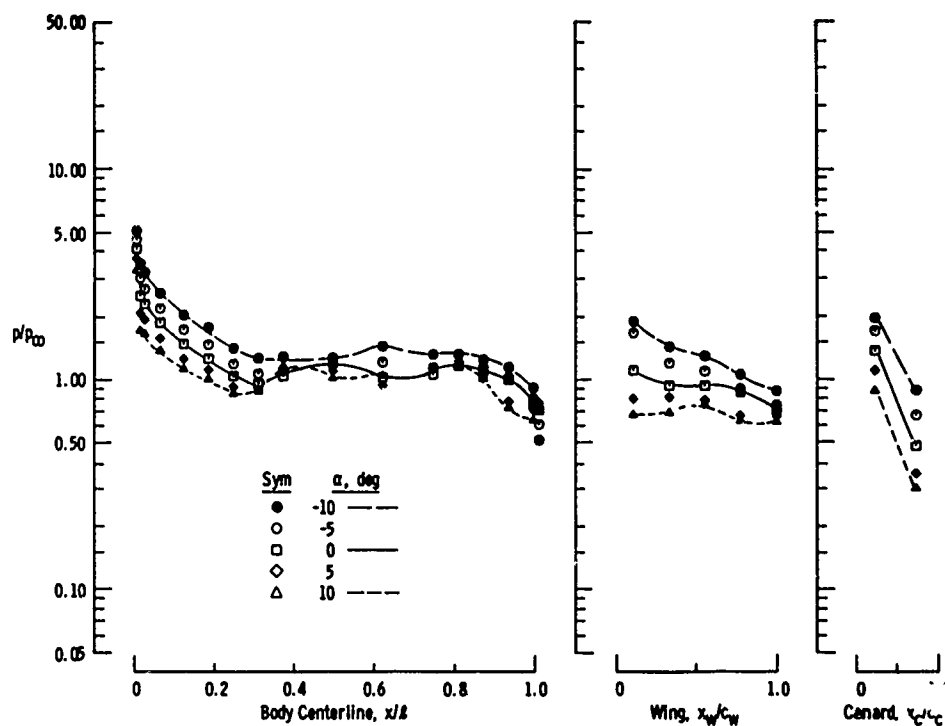

d. Orbiter, $\Delta z/L = 0.15$
Fig. II-15 Continued
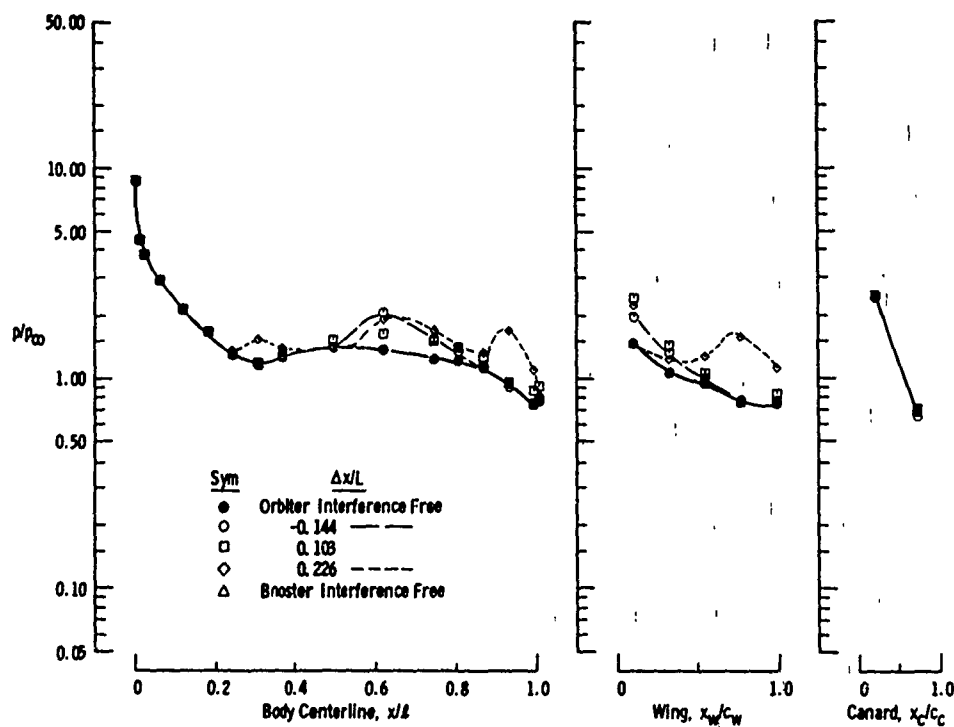
e. Booster, $\Delta z/L = 0.23$
Fig. II-15 Continued
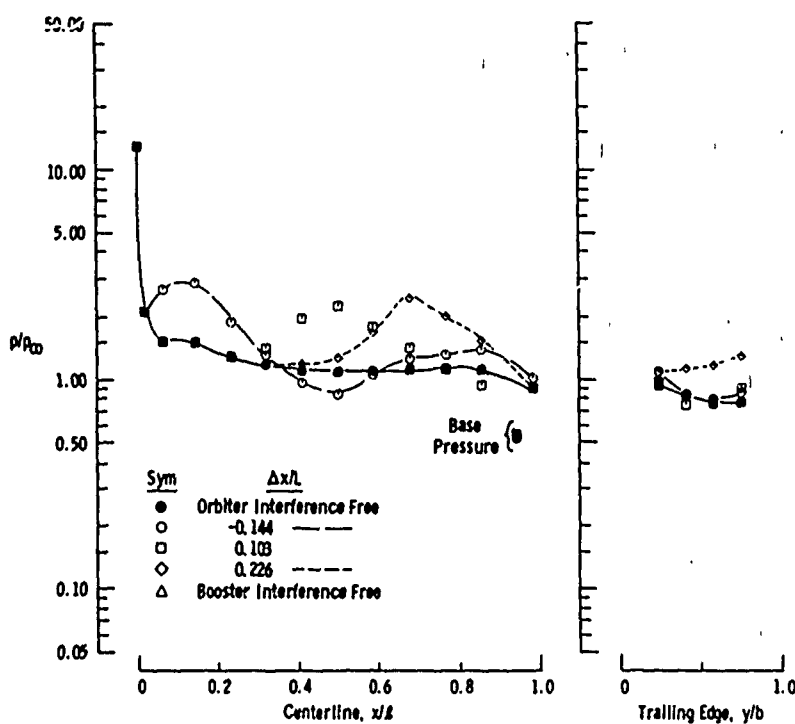
f. Orbiter, $\Delta z/L = 0.23$
Fig. II-15 Continued

132
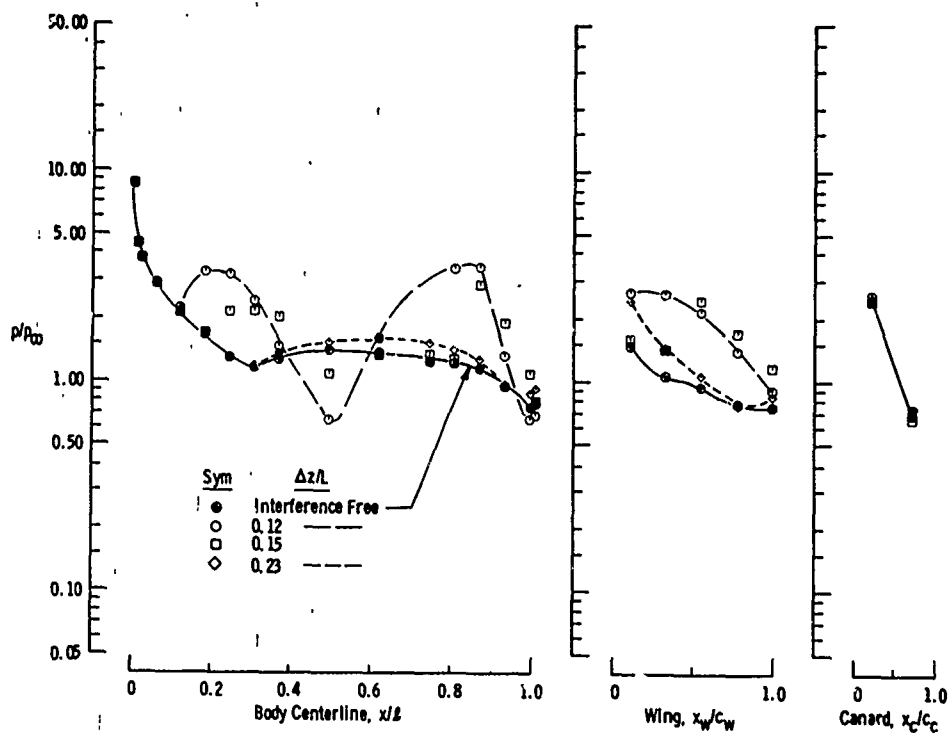
g. Booster, $\Delta x/L = 0.103$
Fig. II-15 Continued
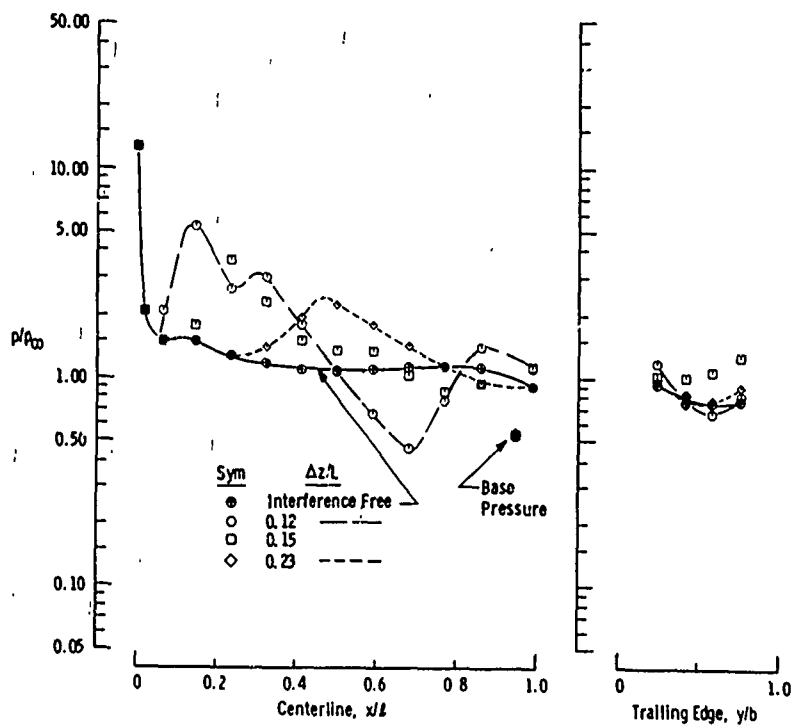
h. Orbiter, $\Delta x/L = 0.103$
Fig. II-15 Continued

133
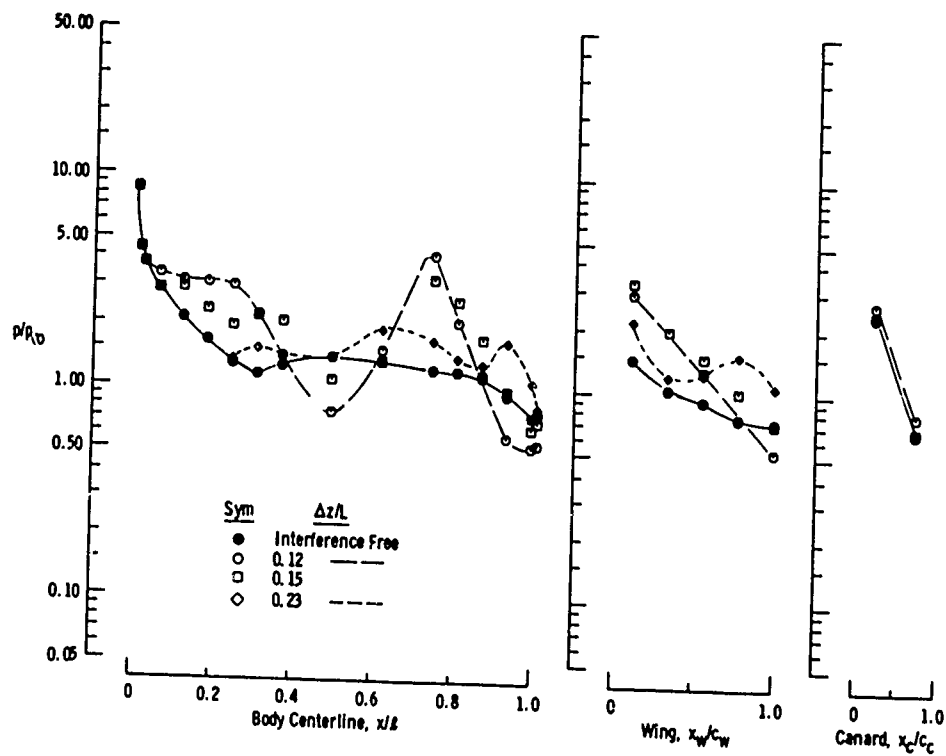
i. Booster, $\Delta x/L = 0.228$
Fig. II-15 Continued
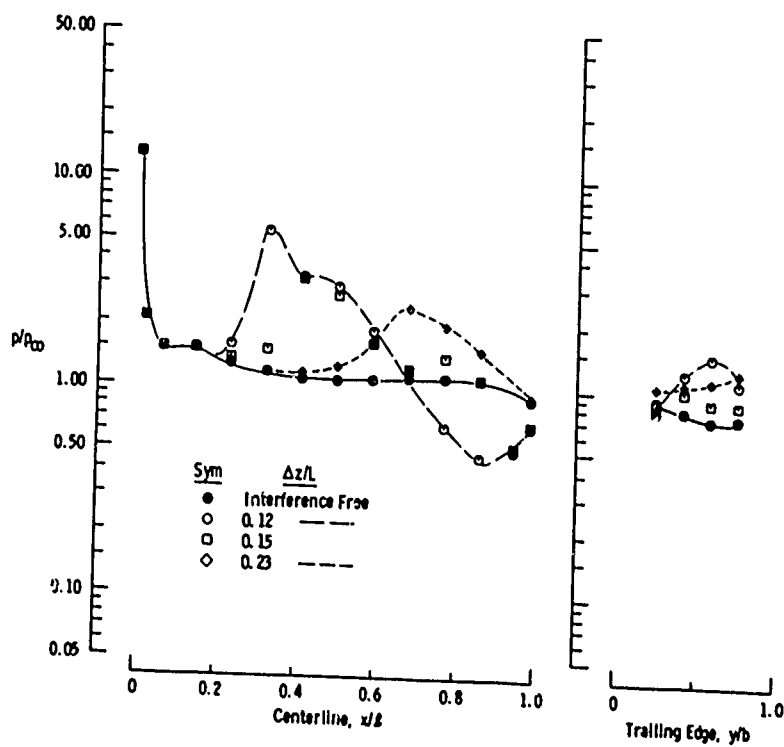
j. Orbiter, $\Delta x/L = 0.228$
Fig. II-15 Concluded

134
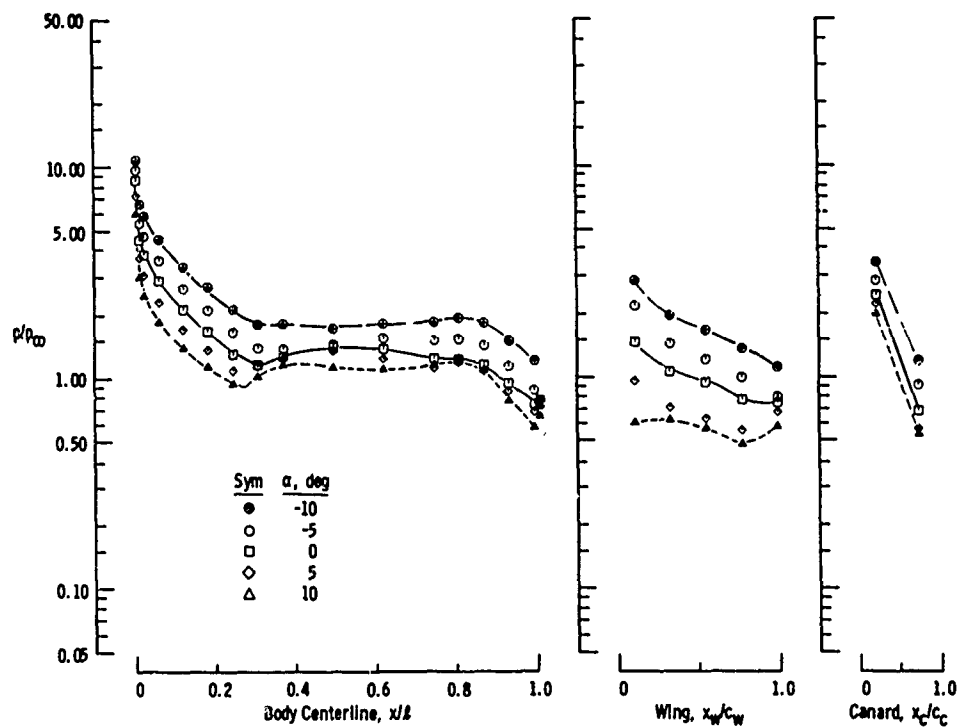
a. Booster, Interference Free
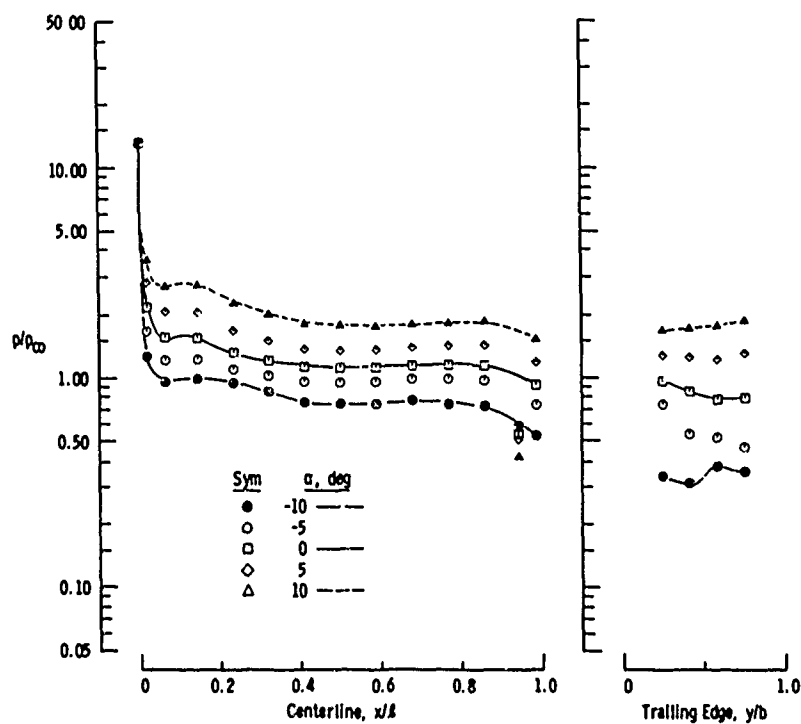
b. Orbiter, Interference Free

Fig. II-16 Angle-of-Attack Effects on the Booster and Orbiter Pressure Distributions with Power Simulation (50-percent Booster Power, 100-percent Orbiter Power) at $M_\infty = 3.00$ and $Re_\ell = 2.2 \times 10^6$
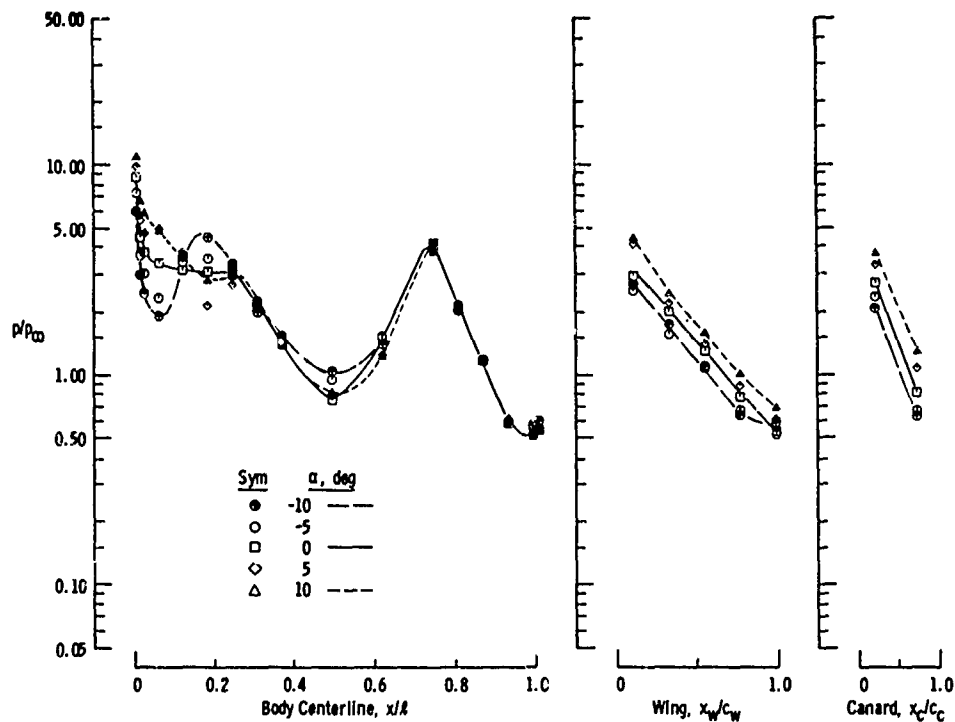
c. Booster, $\Delta x/L = 0.227$, and $\Delta z/L = 0.12$
Fig. II-16 Continued
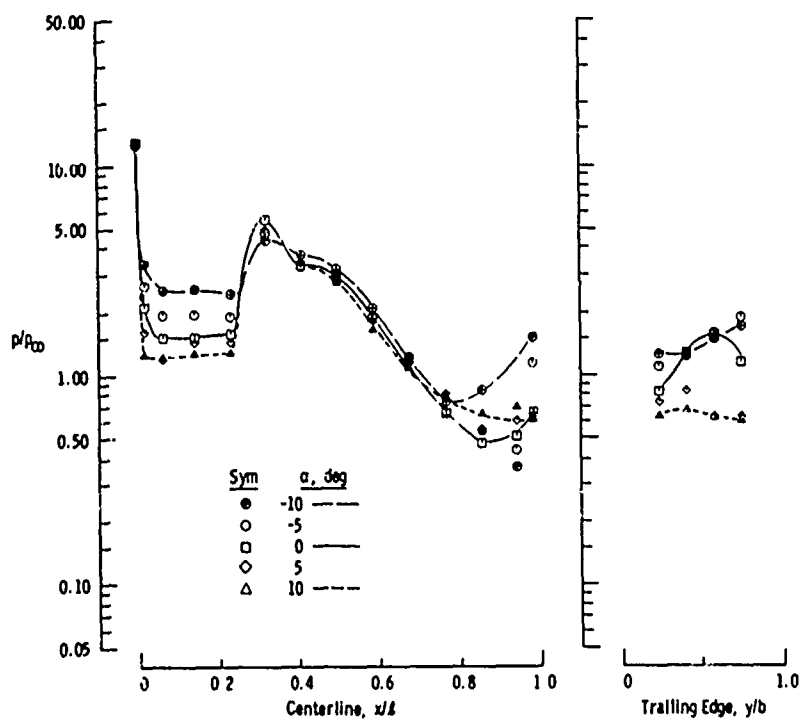
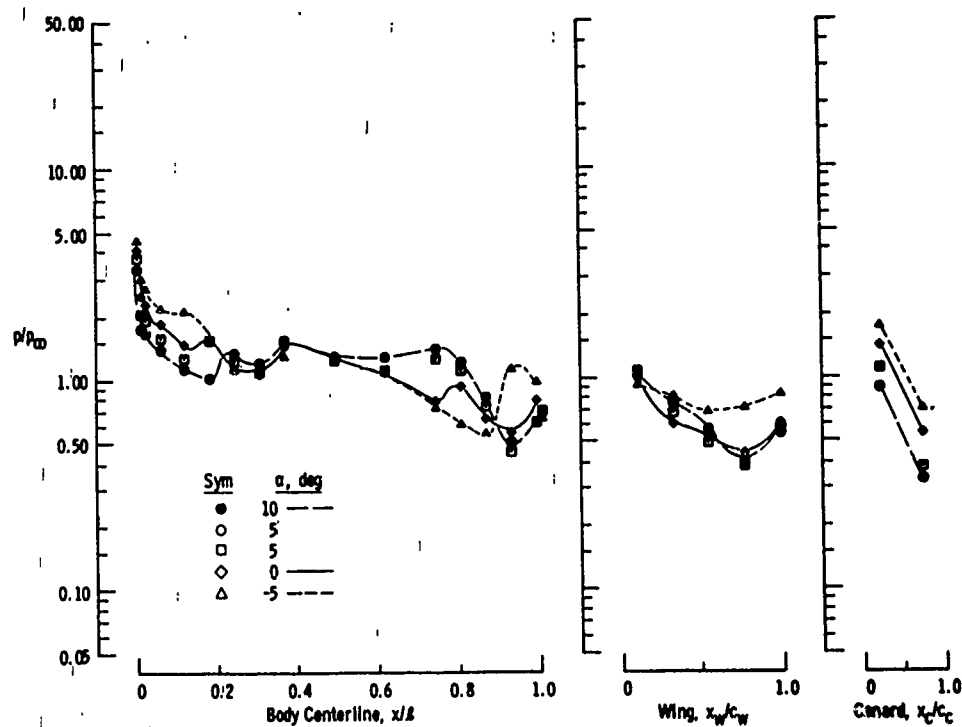d. Orbiter, $\Delta x/L = 0.227$ and $\Delta z/L = 0.12$
Fig. II-16 Continued
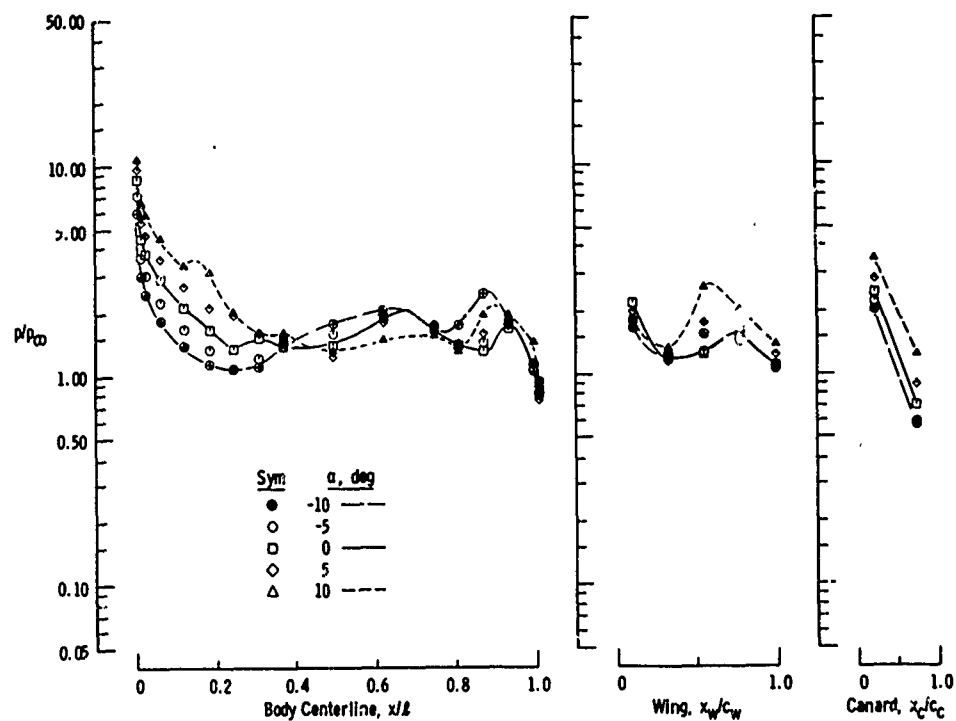
e. Booster, $\Delta x/L = 0.226$ and $\Delta z/L = 0.23$
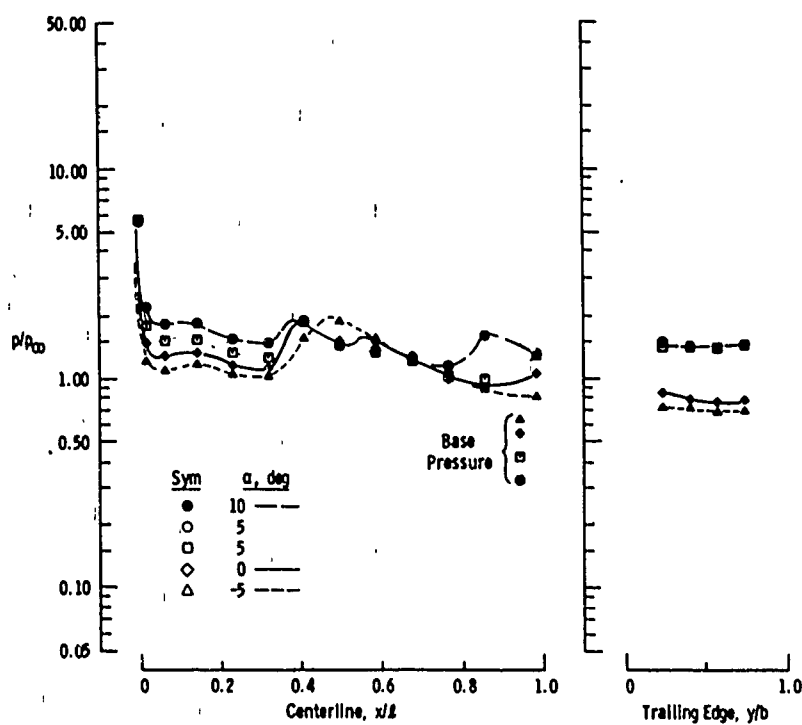Fig. II-16 Continued
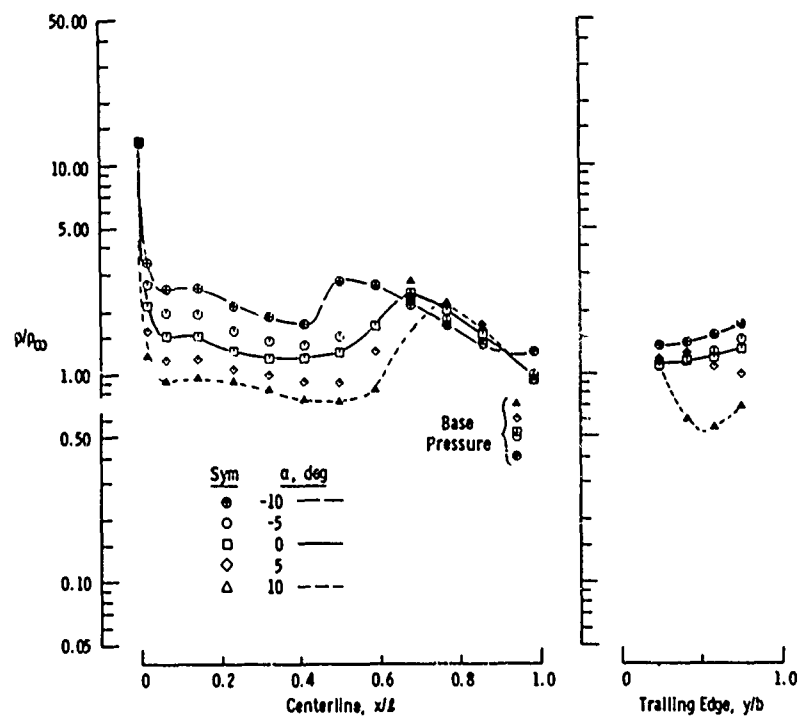
f. Orbiter, $\Delta x/L = 0.226$ and $\Delta z/L = 0.23$
Fig. II-16 Concluded

137
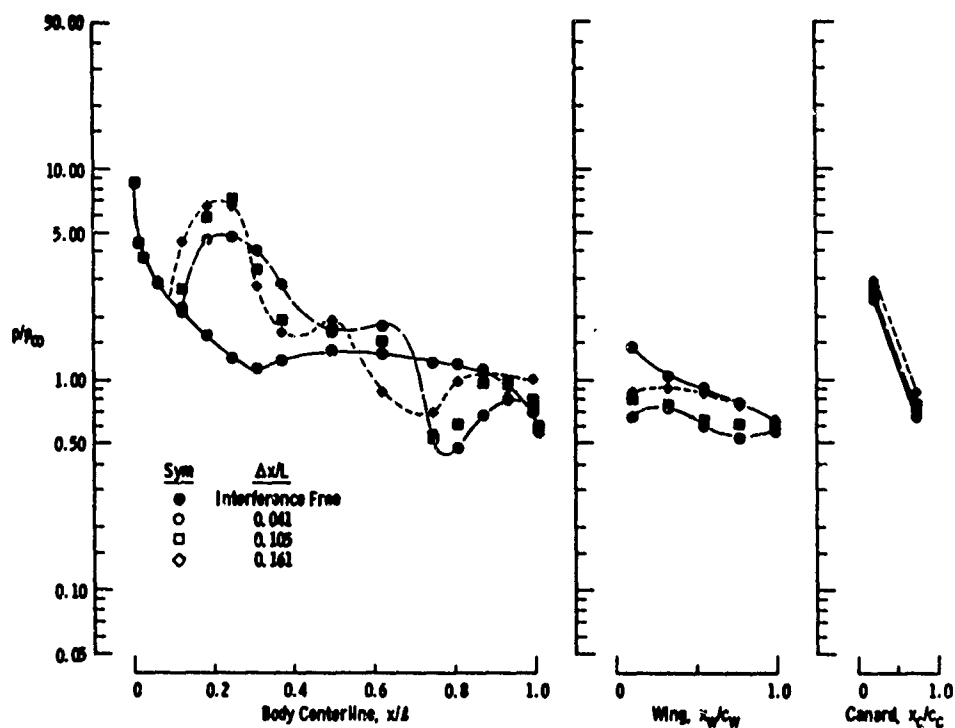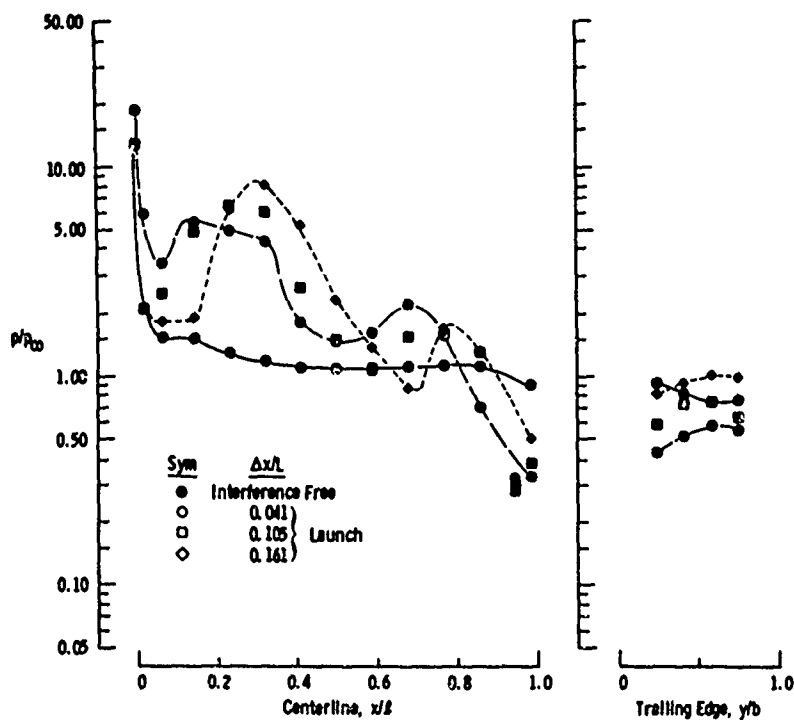
a. Booster, $a = 0$

b. Orbiter, $a = 0$

Fig. II-17 Booster and Orbiter Pressure Distributions during the Launch Configuration,
No Power Simulation, at $M_\infty = 3.00$ and $Re_\ell = 2.2 \times 10^6$
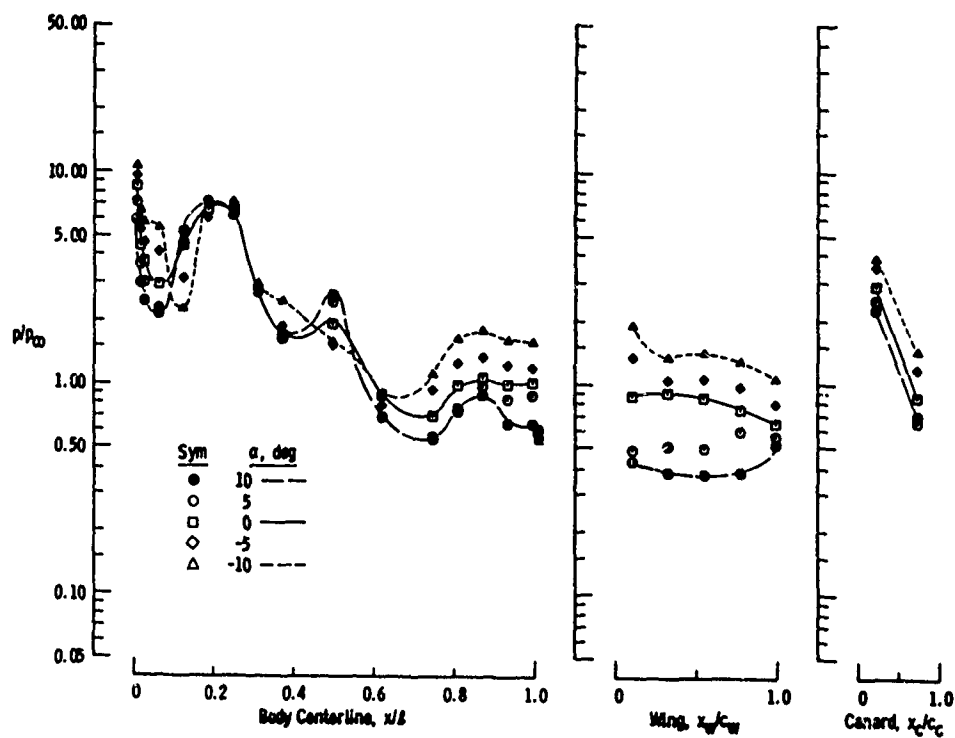
c. Booster, $\Delta x/L = 0.166$
Fig. II-17 Continued
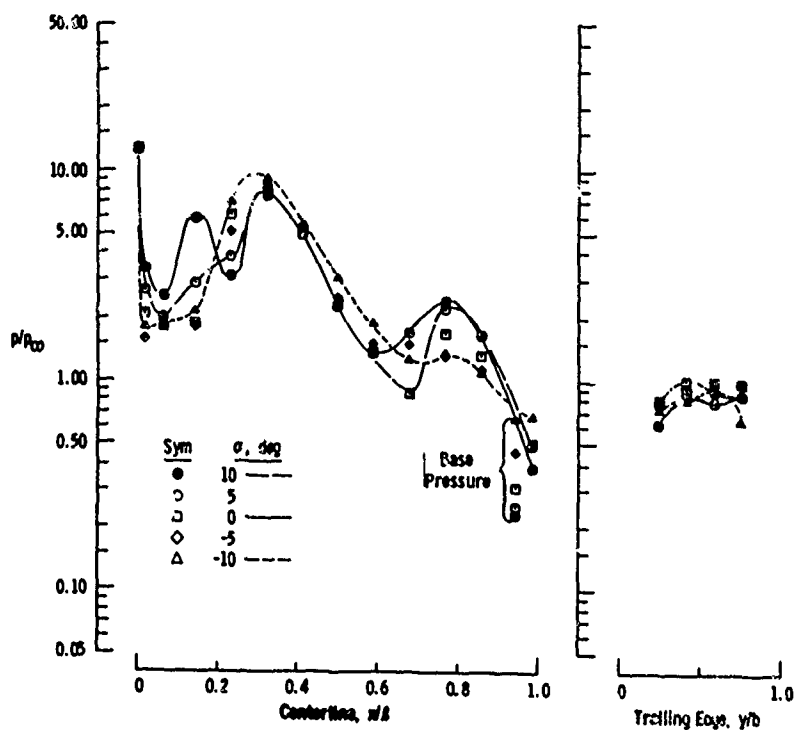
d. Orbiter, $\Delta x/L = 0.166$
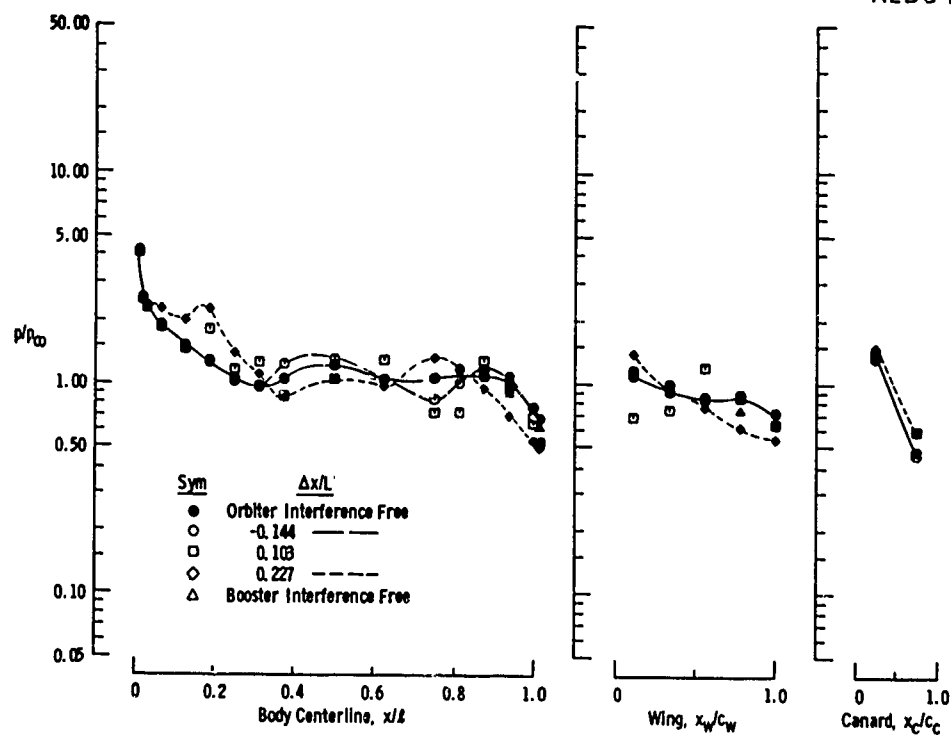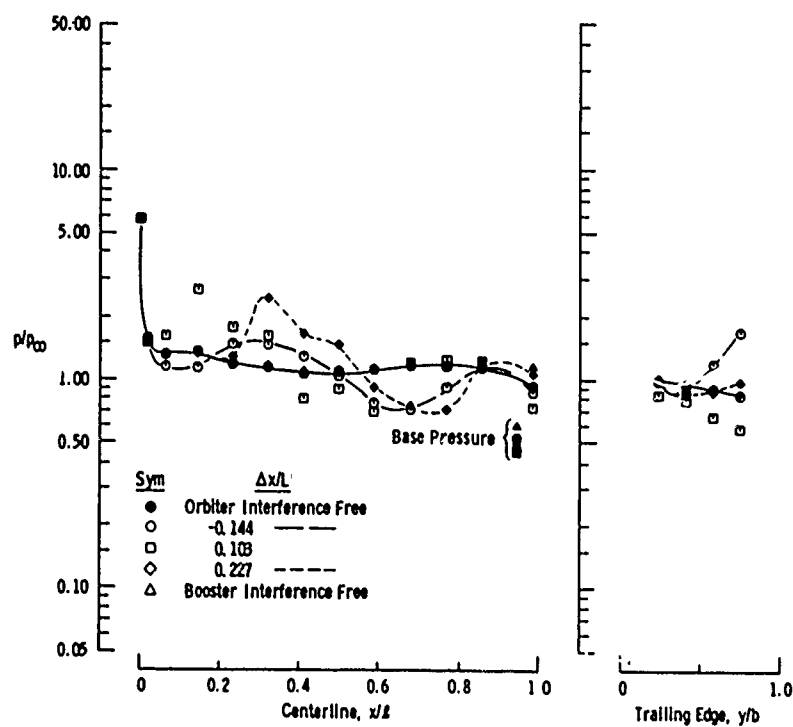Fig. II-17 Concluded

139

a. Booster, $\Delta z/L = 0.12$

b. Orbiter, $\Delta z/L = 0.12$

Fig. II-18 Booster and Orbiter Pressure Distributions at Various Staging Positions without Power Simulation at $\alpha = 0$, $M_\infty = 2.00$, and $Re_\ell = 2.3 \times 10^6$

140

c. Booster, $\Delta z/L = 0.15$
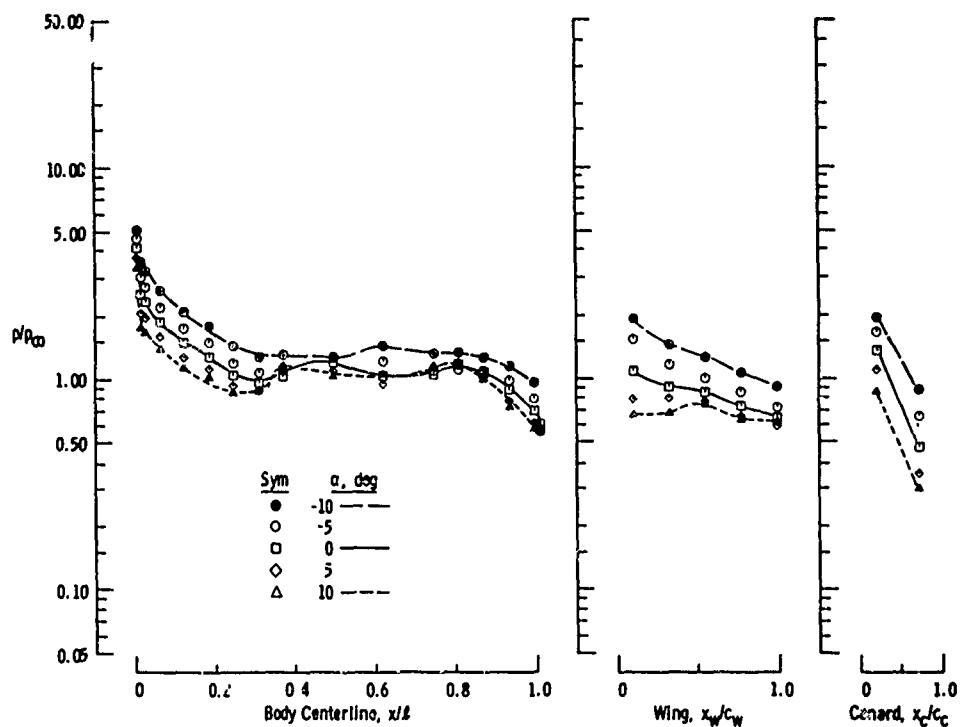Fig. II-18 Continued

d. Orbiter, $\Delta z/L = 0.15$
Fig. II-18 Continued

141
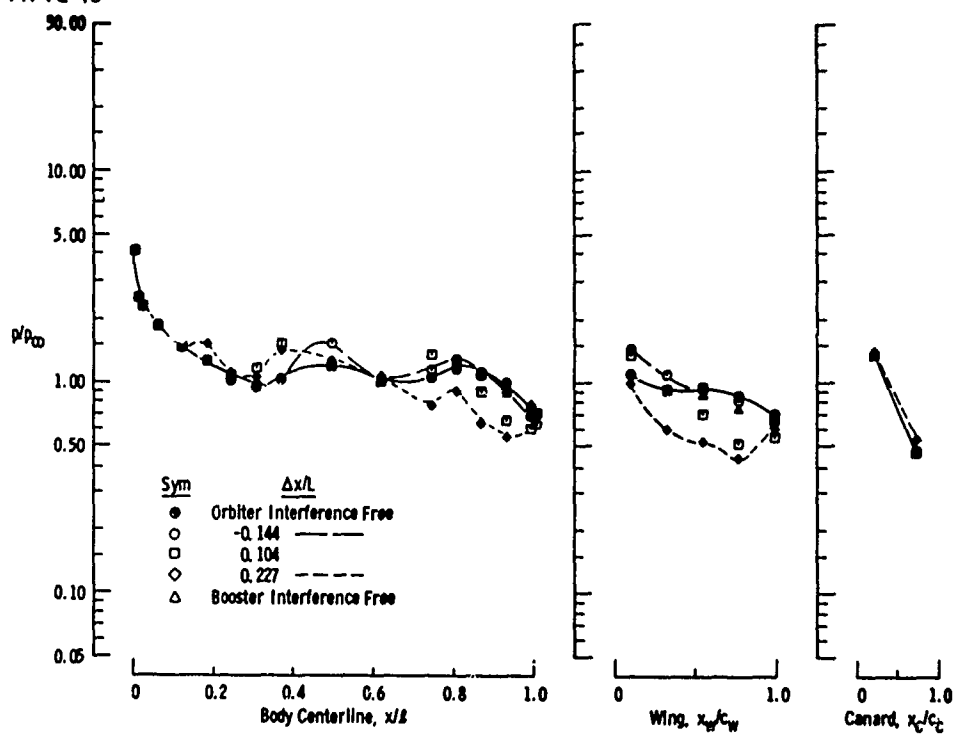
e. Booster, $\Delta z/L = 0.23$
Fig. II-18 Continued
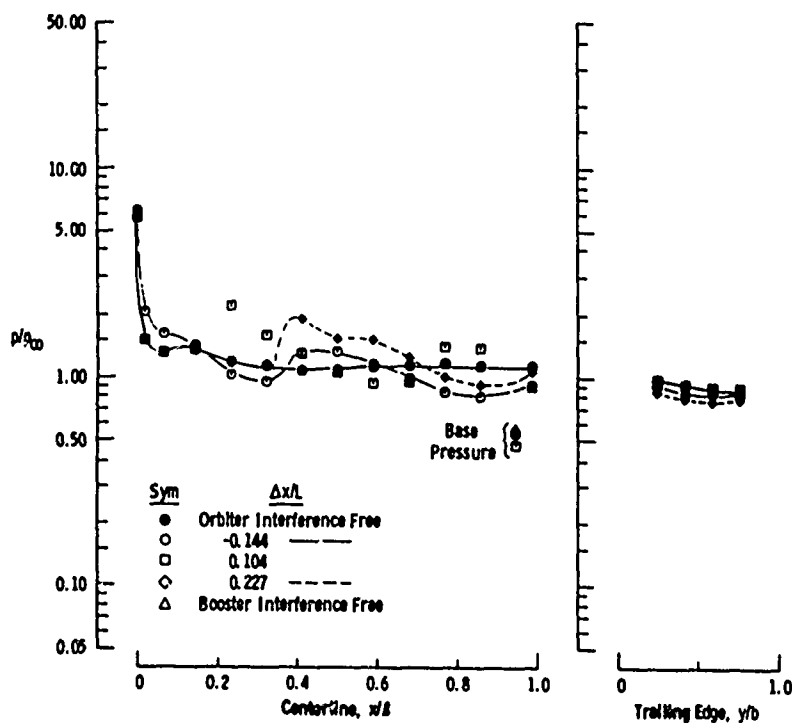
f. Orbiter, $\Delta z/L = 0.23$
Fig. II-18 Continued

142
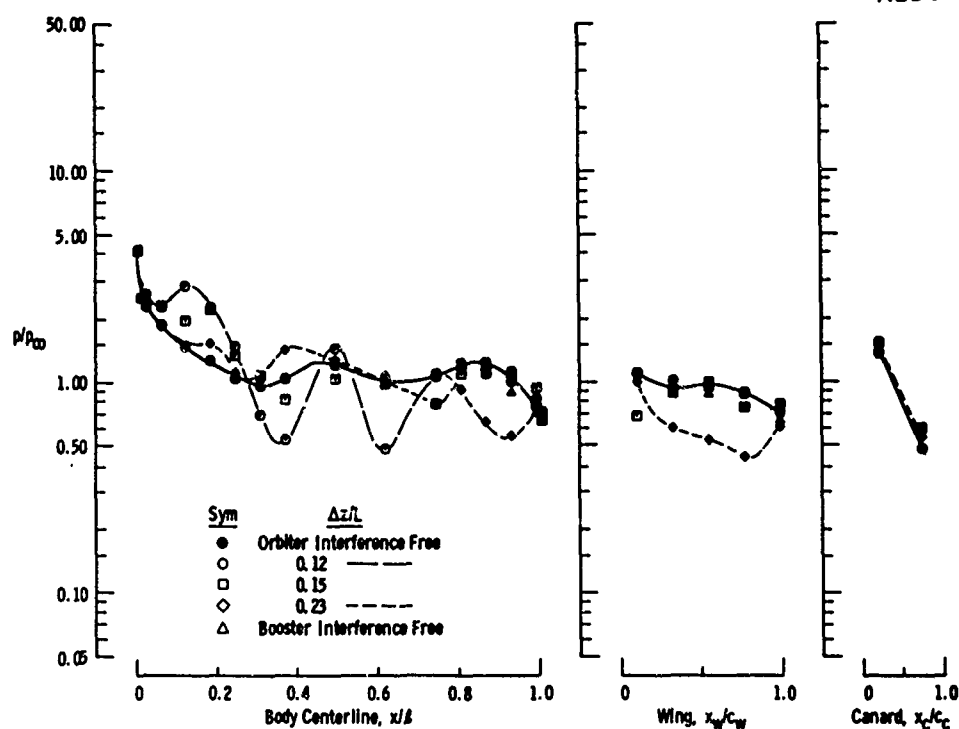
g. Booster, $\Delta x/L = 0.226$
Fig. II-18 Continued
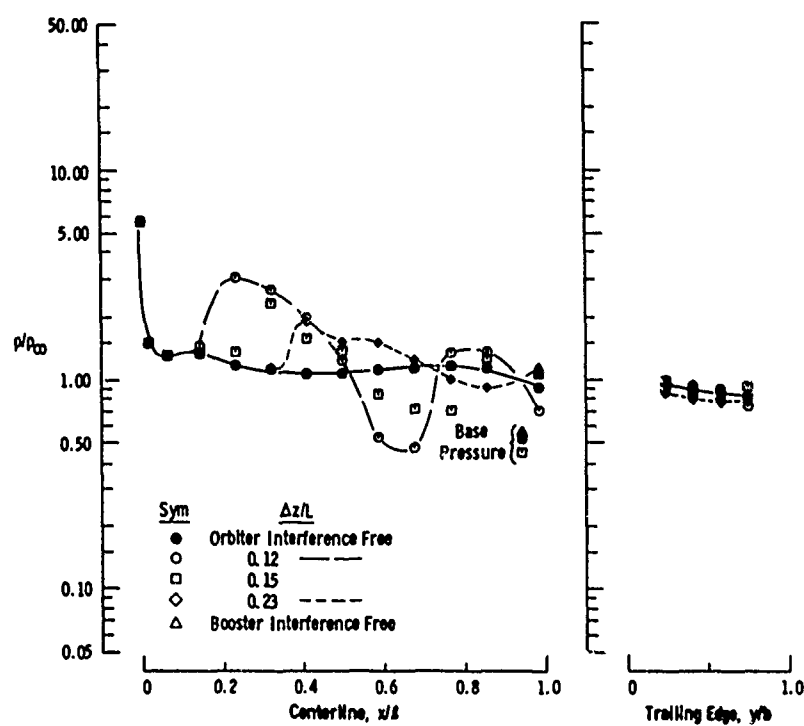
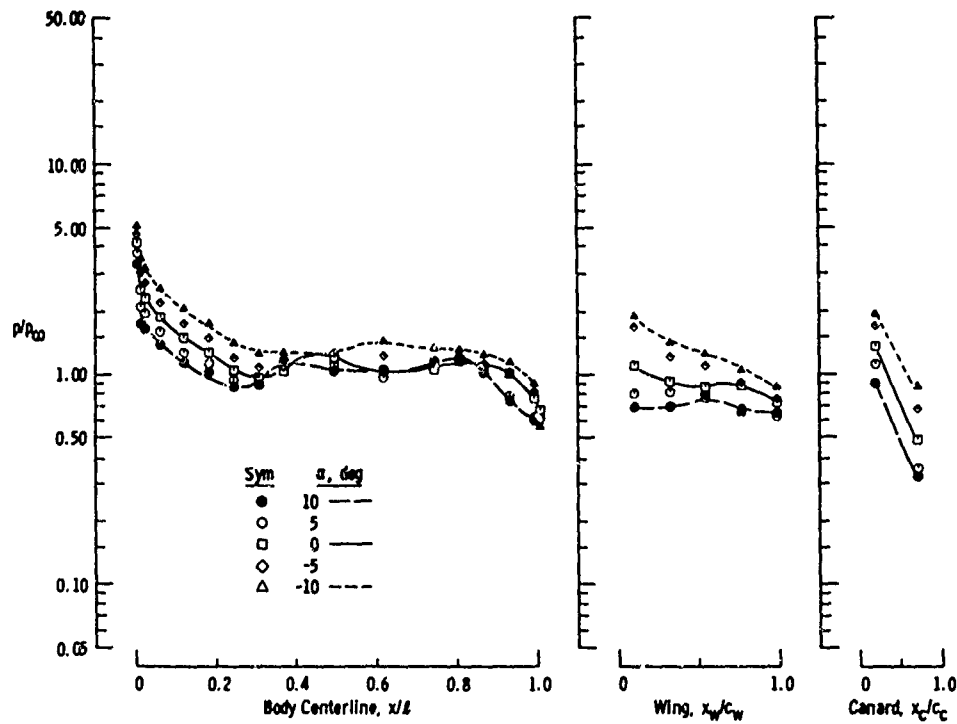h. Orbiter, $\Delta x/L = 0.226$
Fig. II-18 Concluded
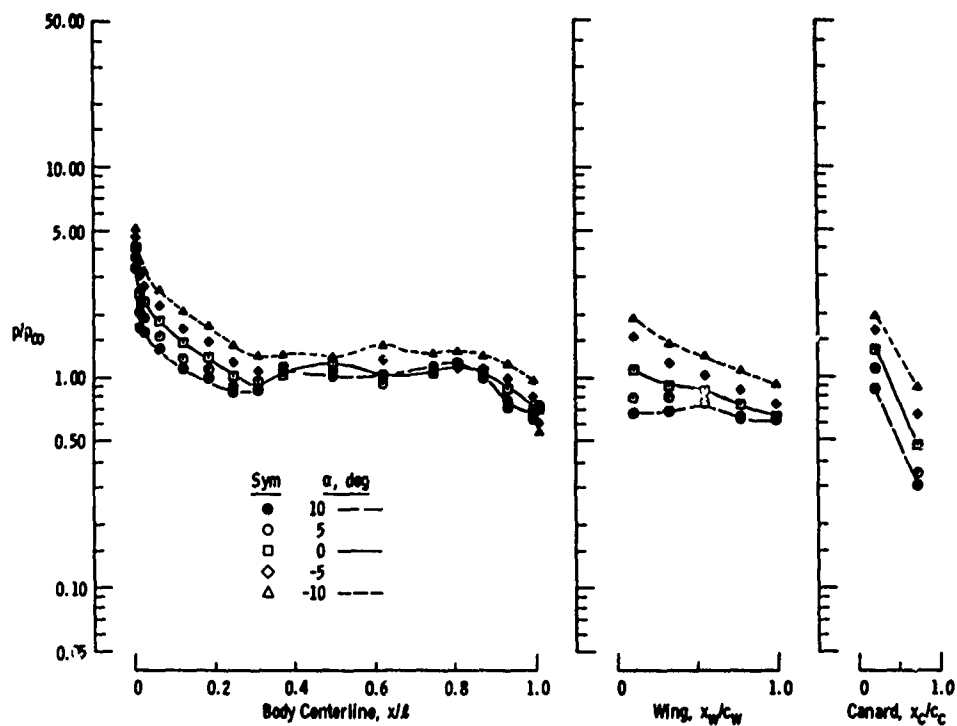
a. Booster, Booster Interference Free ($\Delta x/L$ = -0.391 and $\Delta z/L$ = 0.91)
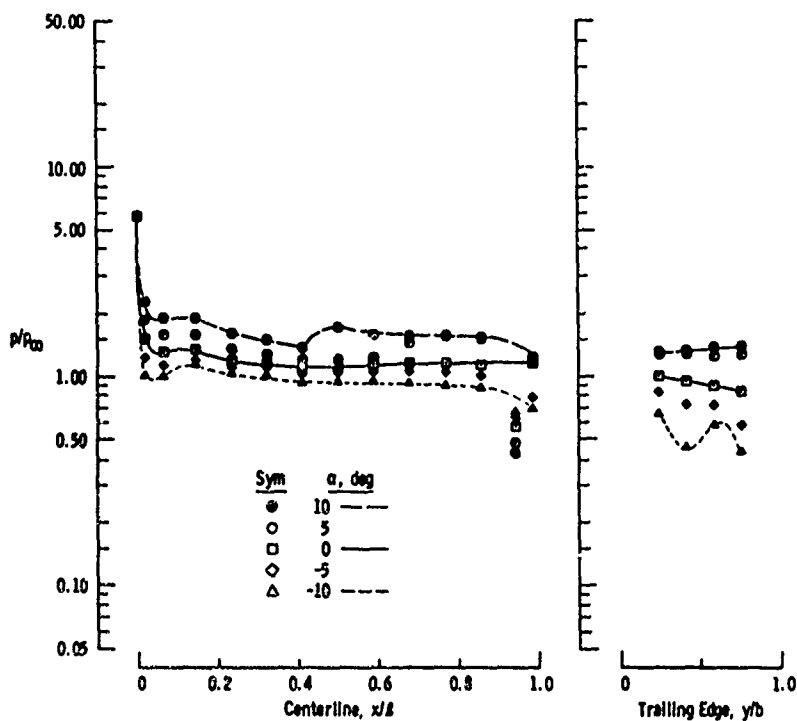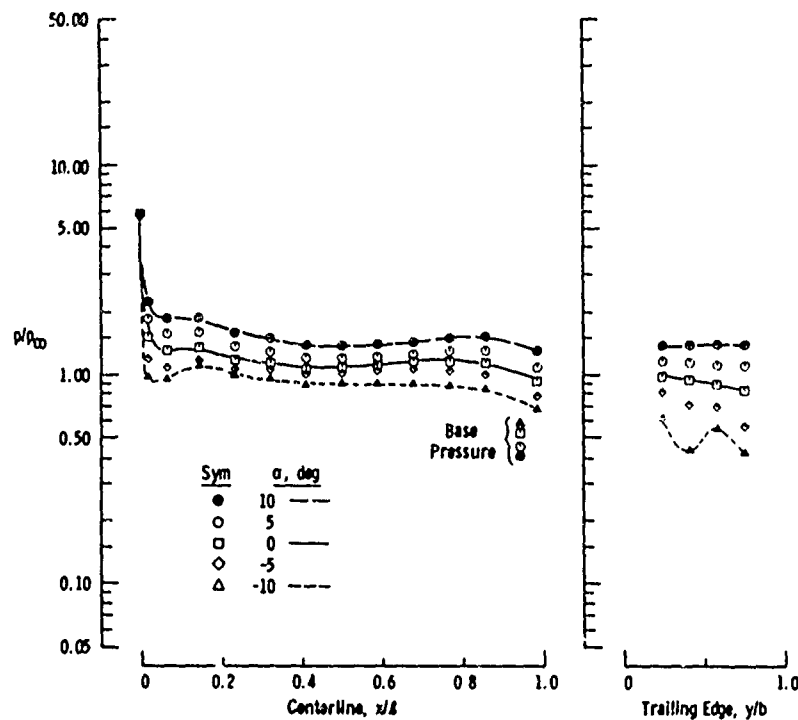

b. Orbiter, Booster Interference Free ($\Delta x/L$ = -0.391 and $\Delta z/L$ = 0.91)

Fig. II-19 Angle-of-Attack Effects on the Booster and Orbiter Pressure
Distributions without Power Simulation at M_∞ = 2.00 and
Re_ℓ = 2.3 x 10^6

144

c. Booster, Orbiter Interference Free ($\Delta x/L = 0.521$ and $\Delta z/L = 0.91$)

Fig. II-19 Continued

d. Orbiter, Orbiter Interference Free ($\Delta x/L = 0.521$ and $\Delta z/L = 0.91$)

Fig. II-19 Continued

145
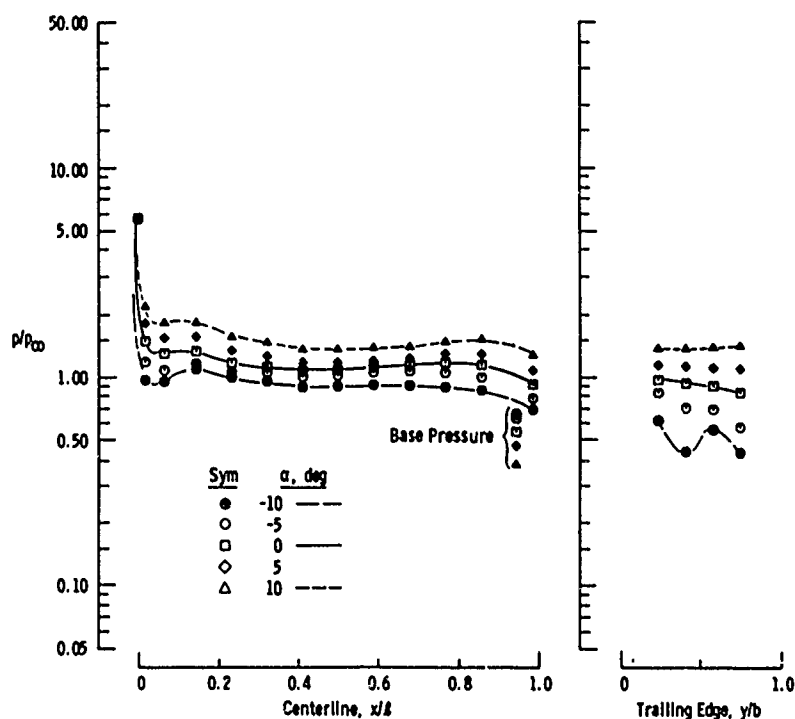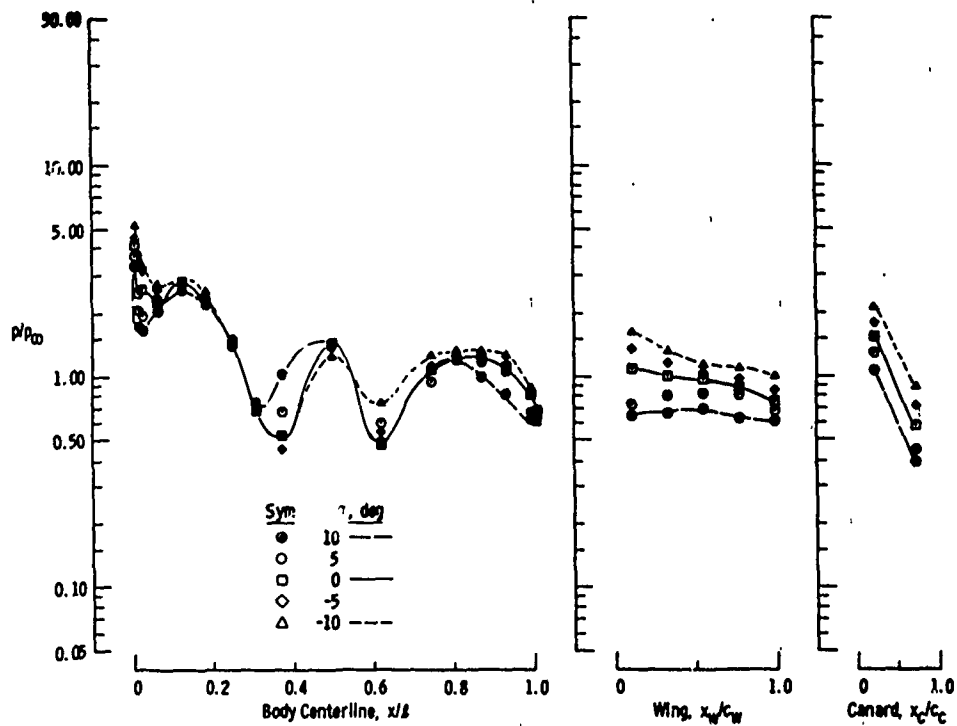
e. Booster, $\Delta x/L = 0.227$ and $\Delta z/L = 0.12$
Fig. II-19 Continued
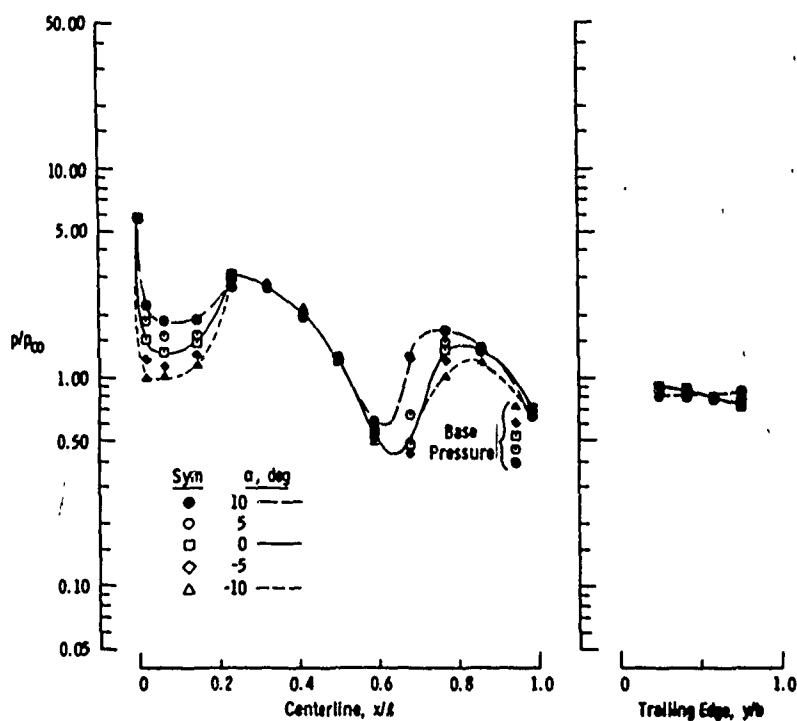
f. Orbiter, $\Delta x/L = 0.227$ and $\Delta z/L = 0.12$
Fig. II-19 Continued

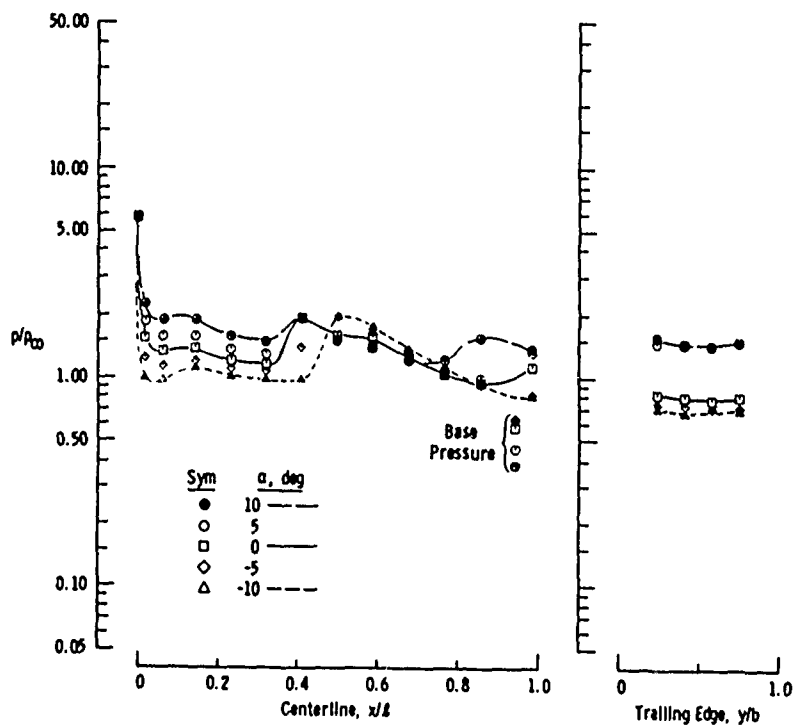g. Booster, $\Delta x/L = 0.227$ and $\Delta z/L = 0.23$
Fig. II-19 Continued

h. Orbiter, $\Delta x/L = 0.227$ and $\Delta z/L = 0.23$
Fig. II-19 Concluded
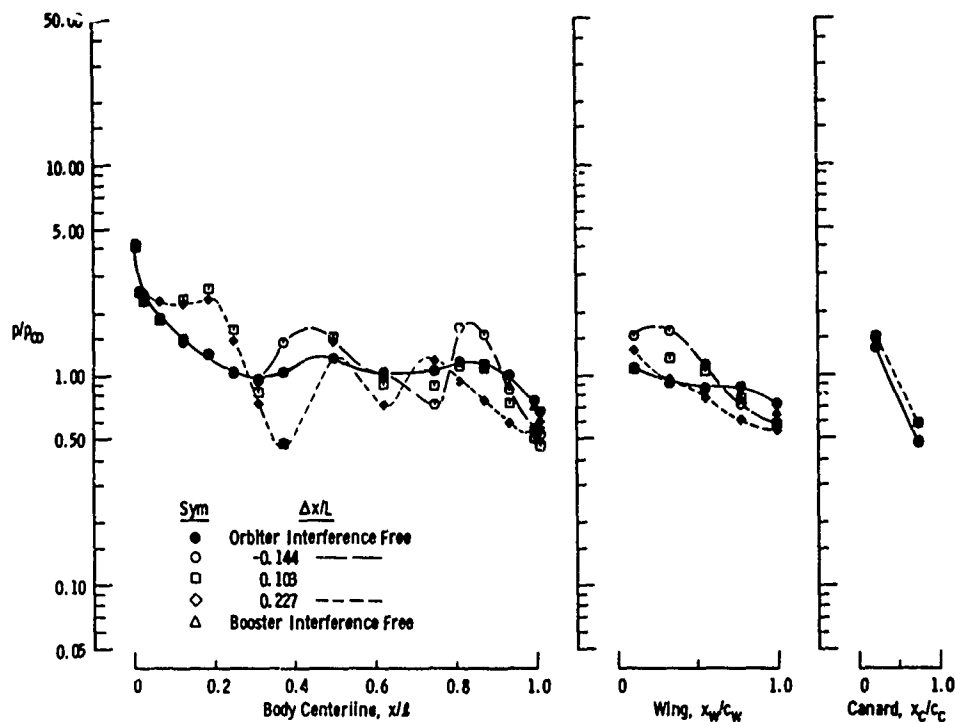
a. Booster, $\Delta z/L = 0.12$
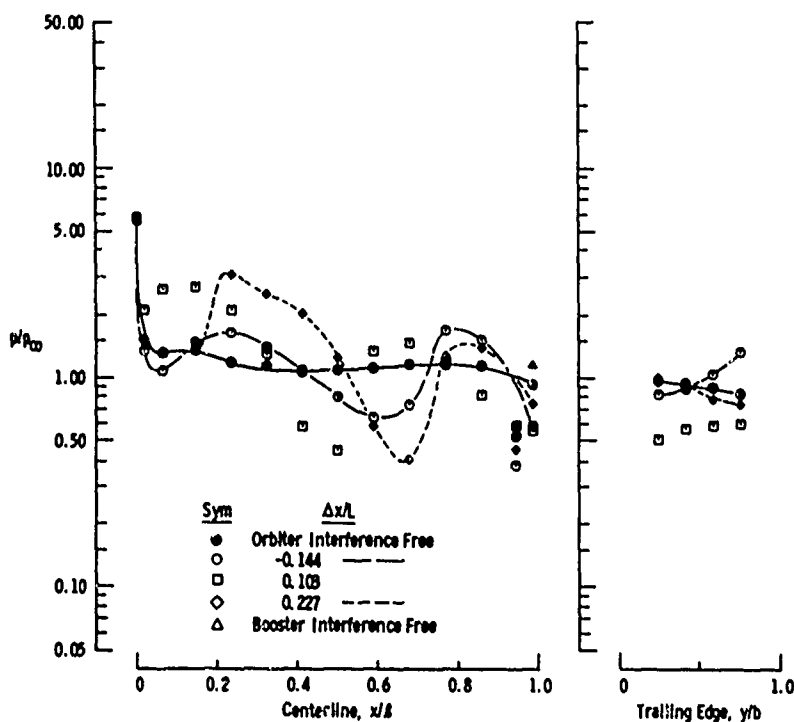
b. Orbiter, $\Delta z/L = 0.12$

Fig. II-20 Booster and Orbiter Pressure Distributions at Various Staging Positions with
Power Simulation (50-percent Booster Power, 100-percent Orbiter Power)
at $a = 0$, $M_\infty = 2.00$ and $Re_\ell = 2.3 \times 10^6$

c. Booster, $\Delta z/L = 0.15$
Fig. II-20 Continued

d. Orbiter, $\Delta z/L = 0.15$
Fig. II-20 Continued

149
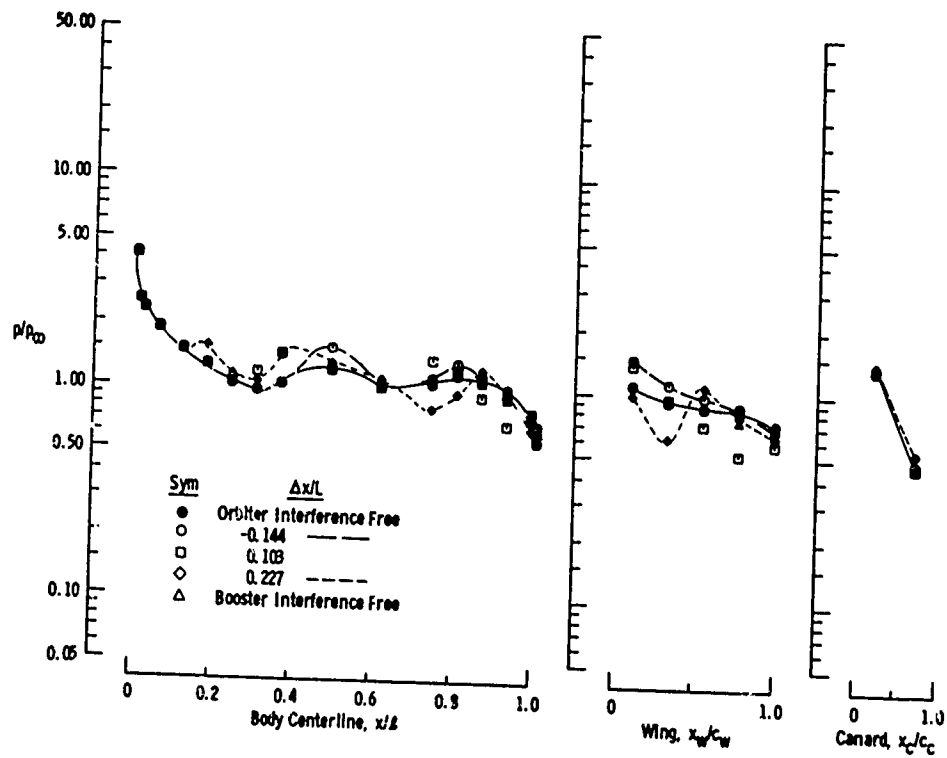
e. Booster, $\Delta z/L = 0.23$
Fig. II-20 Continued
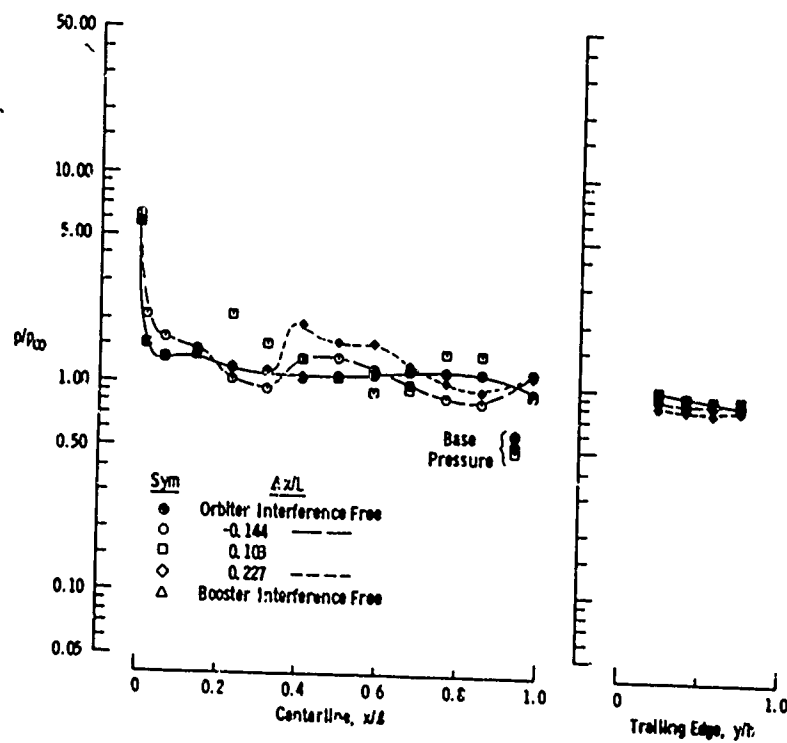
f. Orbiter, $\Delta z/L = 0.23$
Fig. II-20 Concluded

a. Booster, Booster Interference Free ($\Delta x/L = -0.391$ and $\Delta z/L = 0.91$)
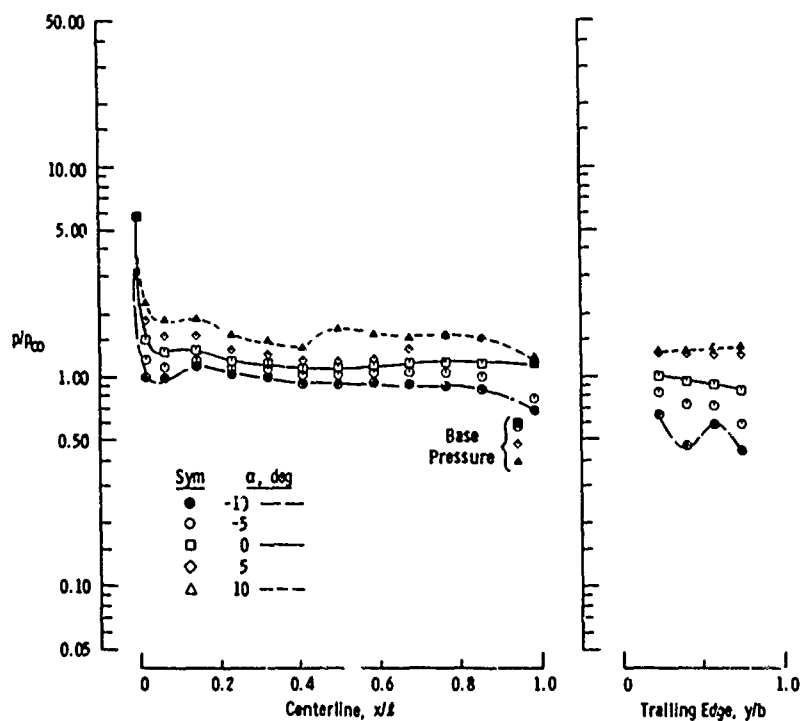
b. Orbiter, Booster Interference Free ($\Delta x/L = -0.391$ and $\Delta z/L = 0.91$)

Fig. II-21 Angle-of-Attack Effects on the Booster and Orbiter Pressure Distributions with Power Simulation (50-percent Booster Power, 100-percent Orbiter Power) at $a = 0$, $M_\infty = 2.00$, and $Re_\ell = 2.3 \times 10^6$

151

c. Booster, Orbiter Interference Free ($\Delta x/L = 0.521$ and $\Delta z/L = 0.91$)
Fig. II-21 Continued

d. Orbiter, Orbiter Interference Free ($\Delta x/L = 0.521$ and $\Delta z/L = 0.91$)
Fig. II-21 Continued
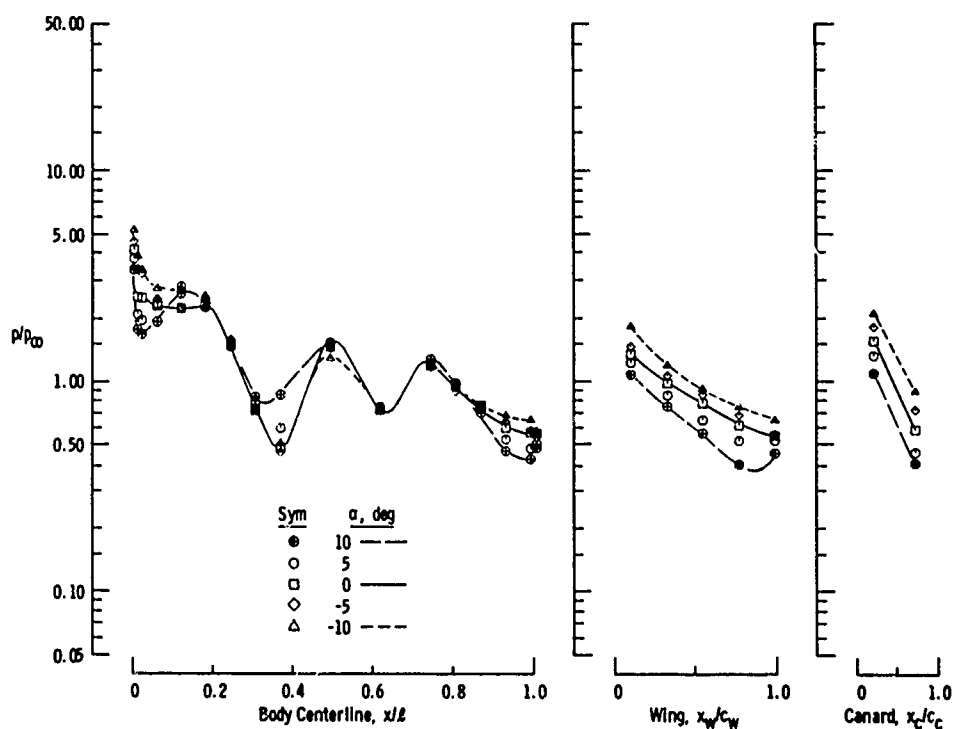
e. Booster, $\Delta x/L = 0.227$ and $\Delta x/L = 0.12$
Fig. II-21 Continued
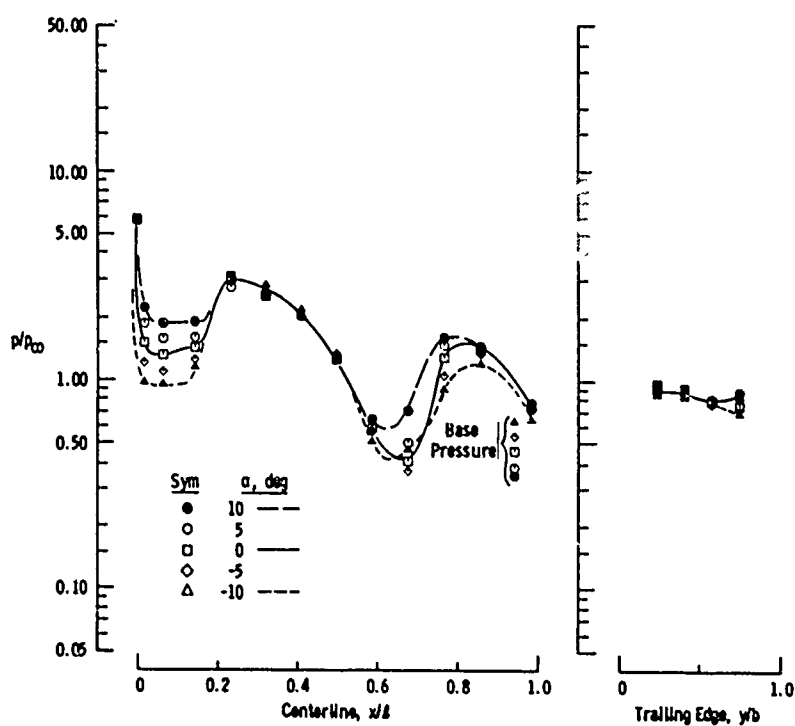
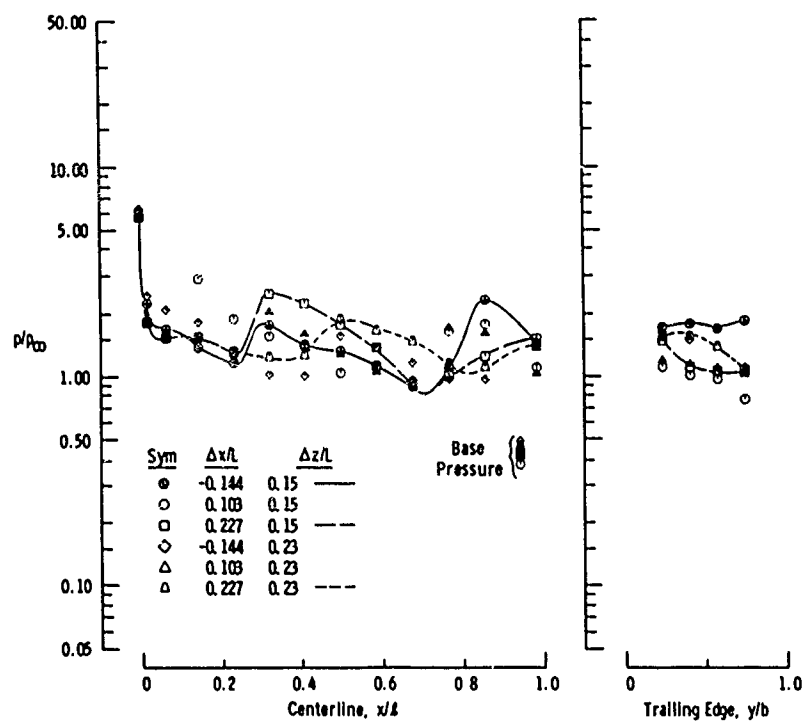**f. Orbiter, $\Delta x/L = 0.227$ and $\Delta z/L = 0.12$**
Fig. II-21 Continued
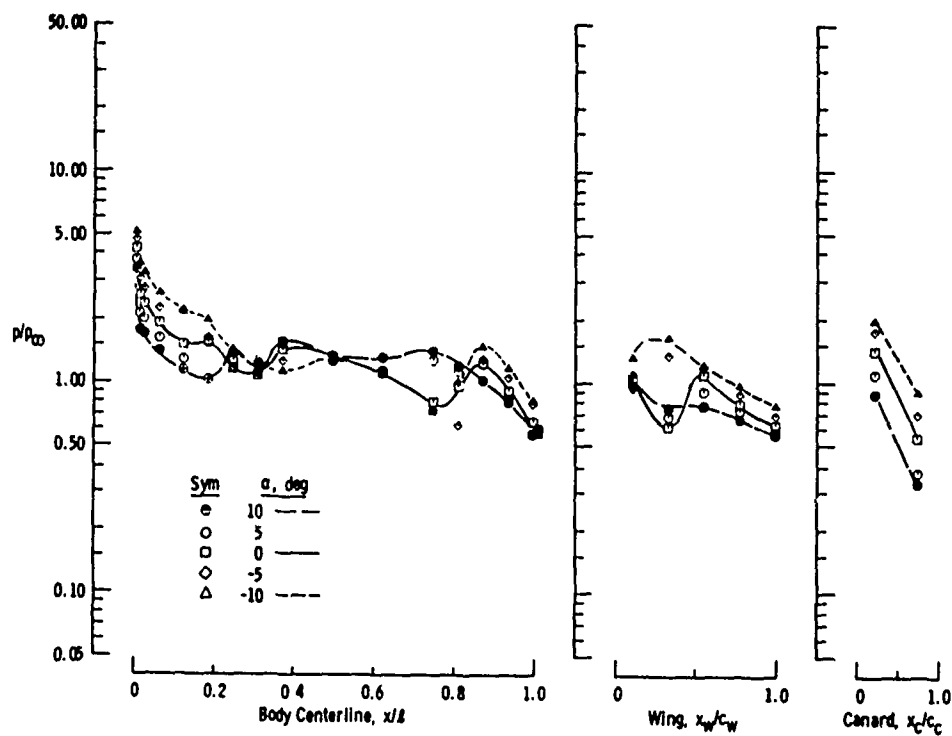
g. Booster, $\Delta x/L = 0.227$ and $\Delta z/L = 0.23$
Fig. II-21 Continued

h. Orbiter, $\Delta x/L = 0.227$ and $\Delta z/L = 0.23$
Fig. II-21 Concluded
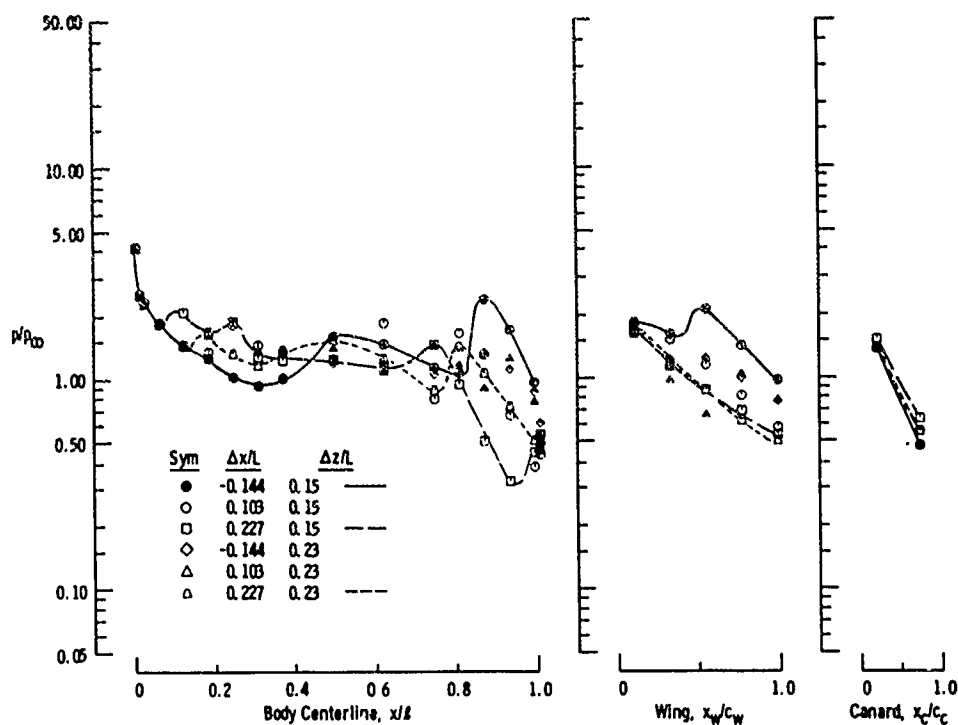
a. Booster, 50-percent Booster Power Simulation, 100-percent Orbiter Power
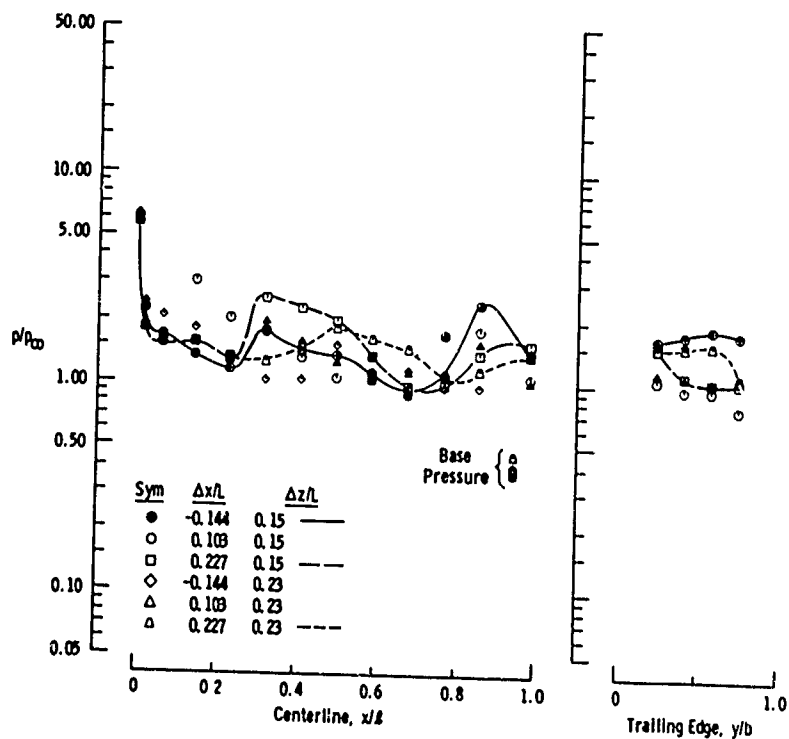

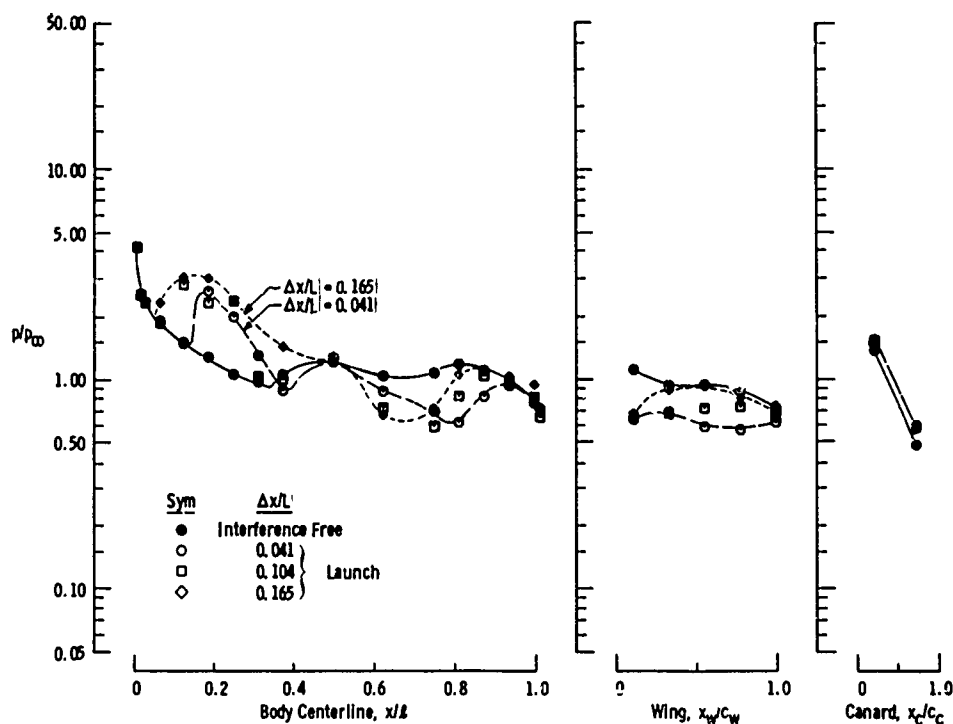b. Orbiter, 50-percent Booster Power Simulation, 100-percent Orbiter Power
Fig. II 22 Booster and Orbiter Pressure Distributions at Various Staging Positions with a
Relative Orbiter Angle of Incidence of 5 deg, $M_\infty = 2.00$, and
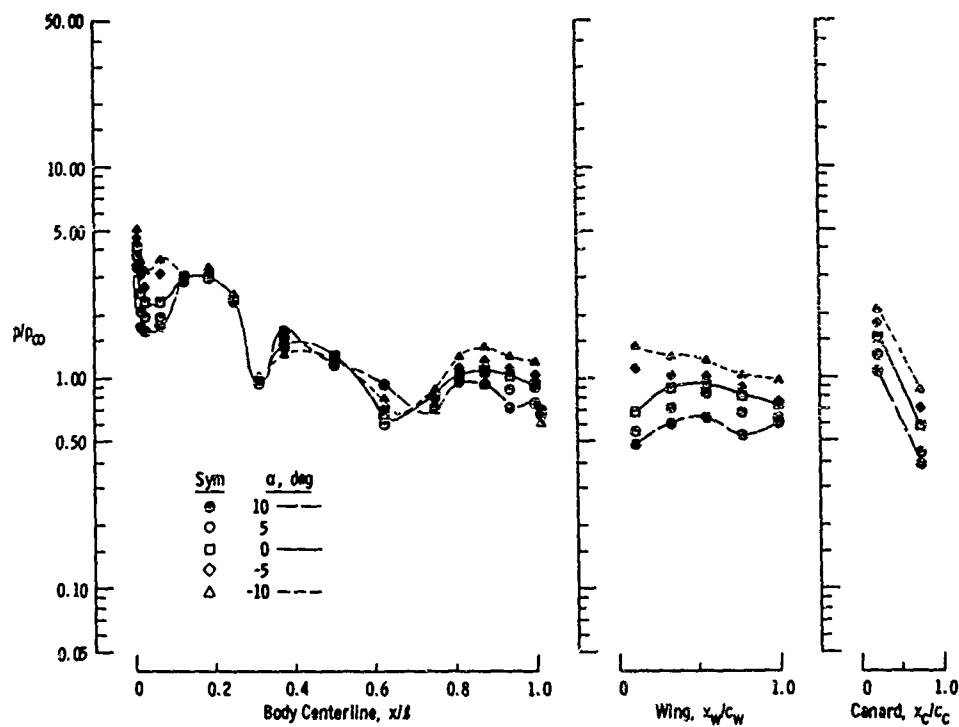$Re_\ell = 2.3 \times 10^6$

155
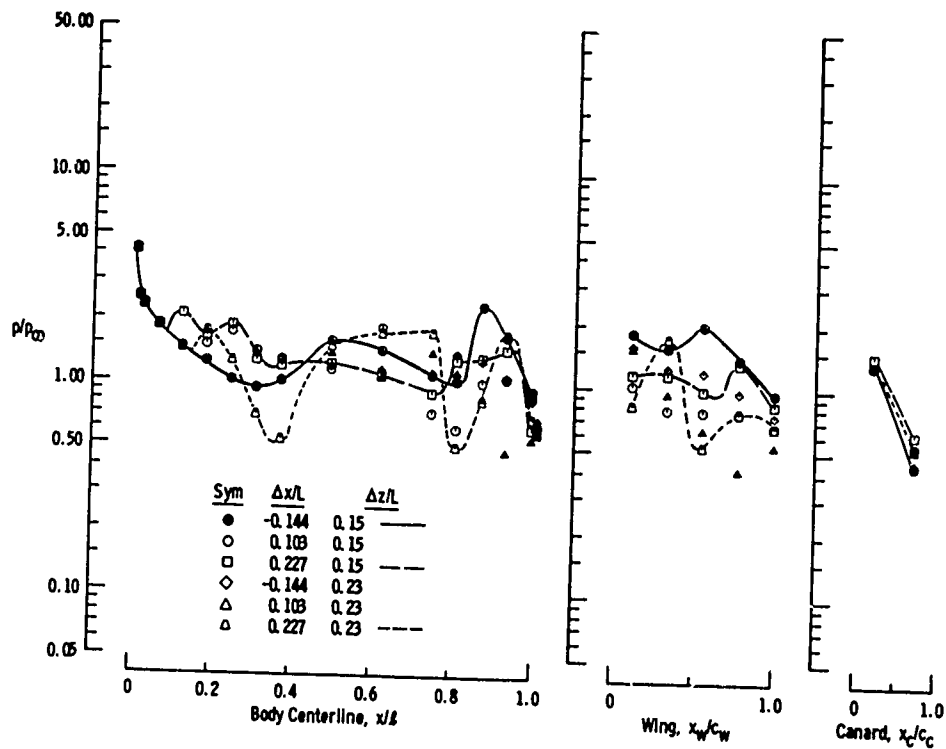
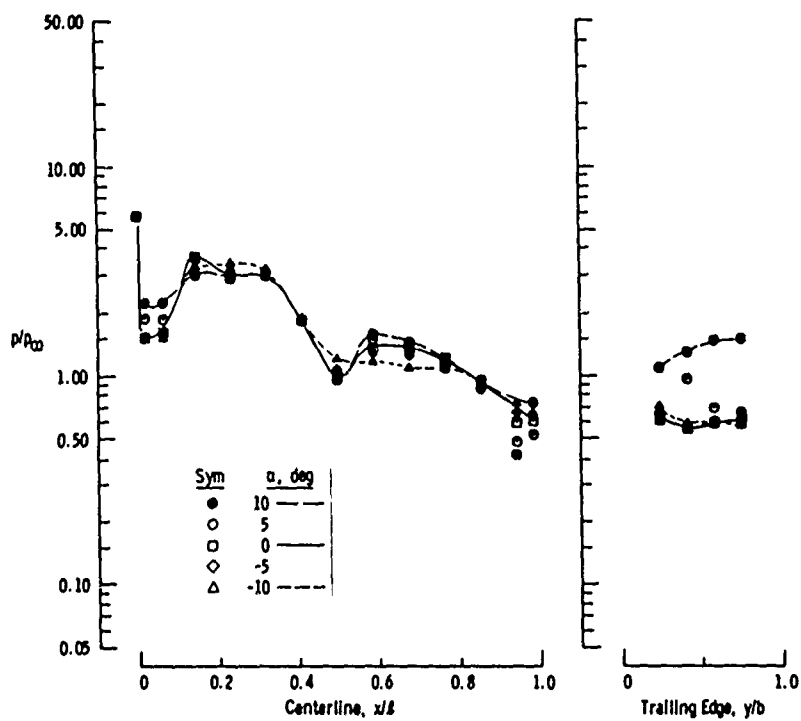c. Booster, No Power Simulation
Fig. II-22 Continued

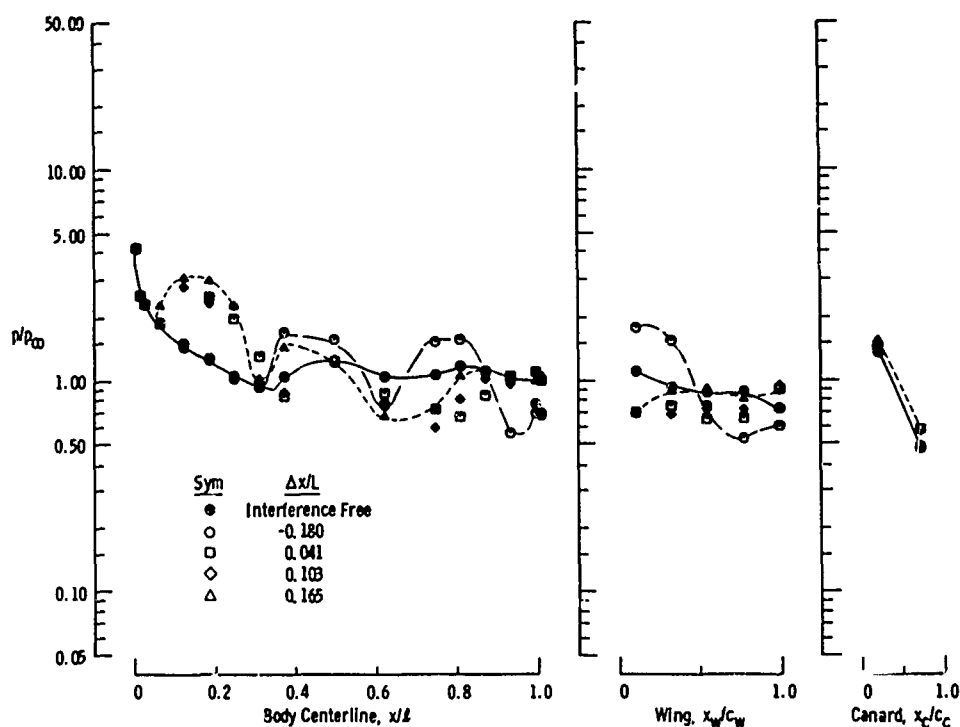d. Orbiter, No Power Simulation
Fig. II-22 Concluded

156

a. Booster, $a = 0$, No Power Simulation, $\Delta x/L$ Variable
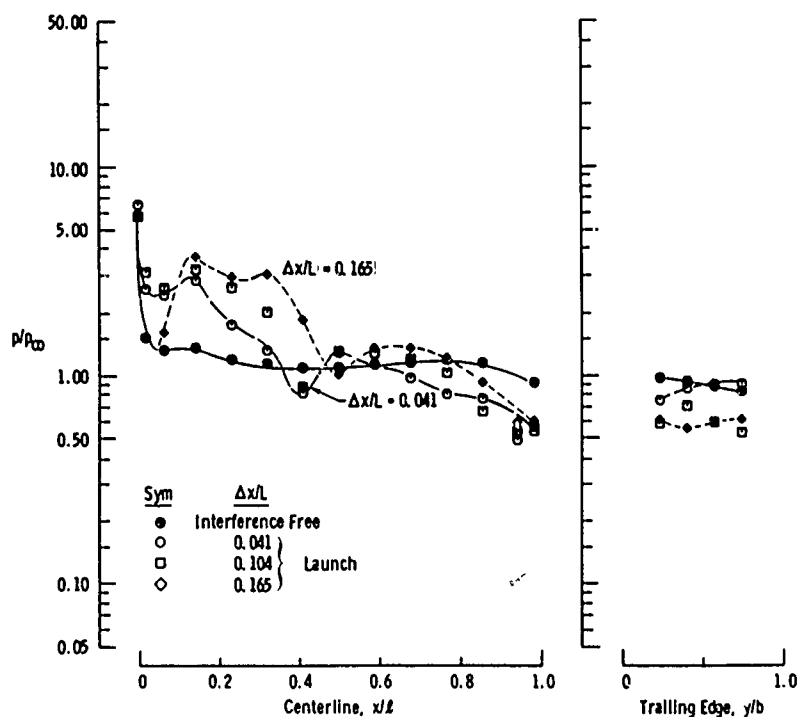
b. Orbiter, $a = 0$, No Power Simulation, $\Delta x/L$ Variable

Fig. II-23 Booster and Orbiter Pressure Distributions Obtained during the Launch Configuration at $M_\infty = 2.00$ and $Re_\ell = 2.3 \times 10^6$
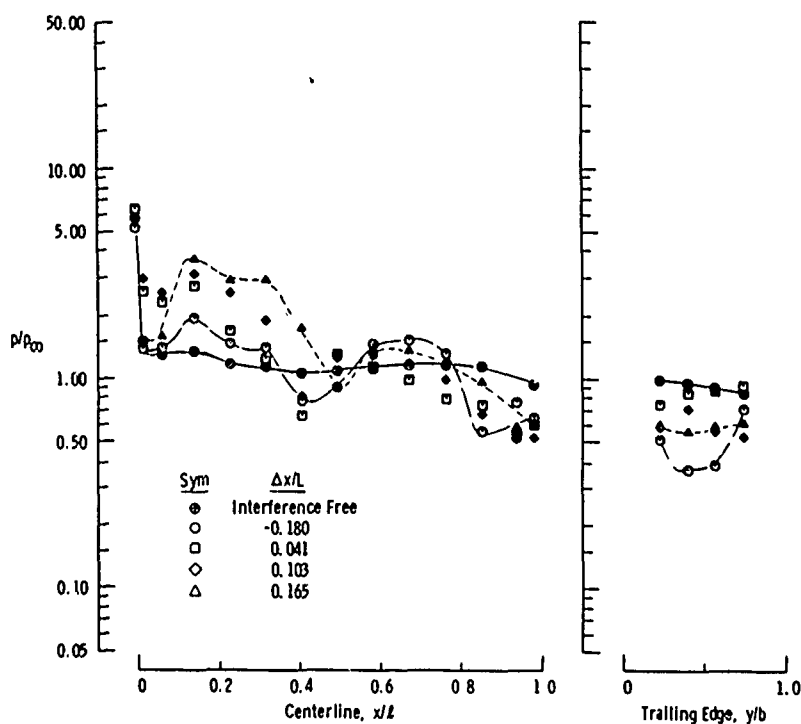
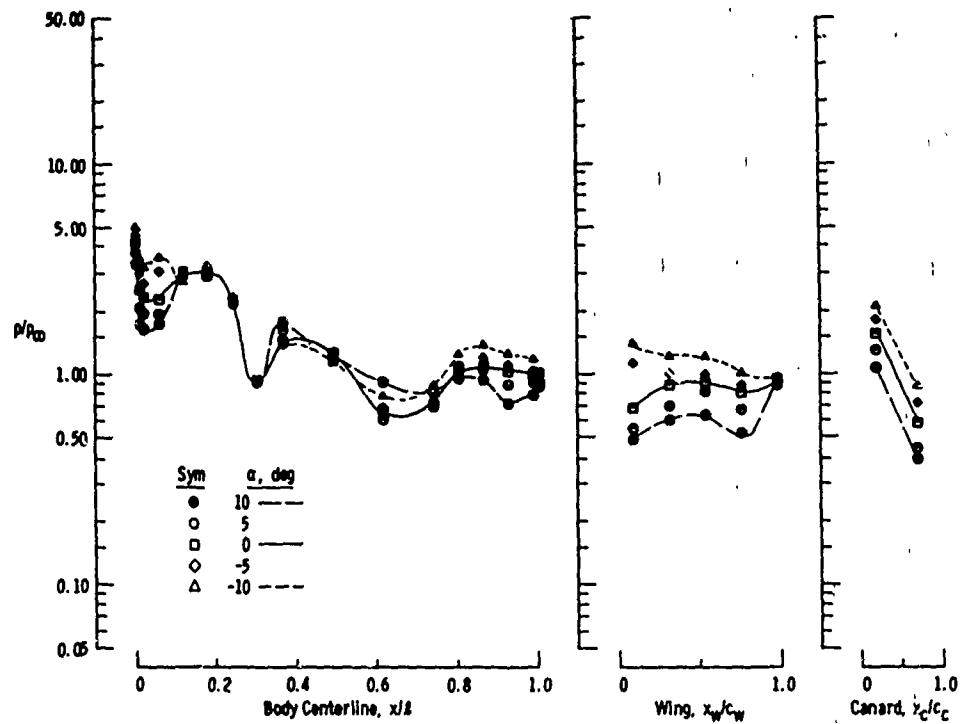c. Booster, $\Delta x/L = 0.165$, No Power Simulation, a Variable
Fig. II-23 Continued

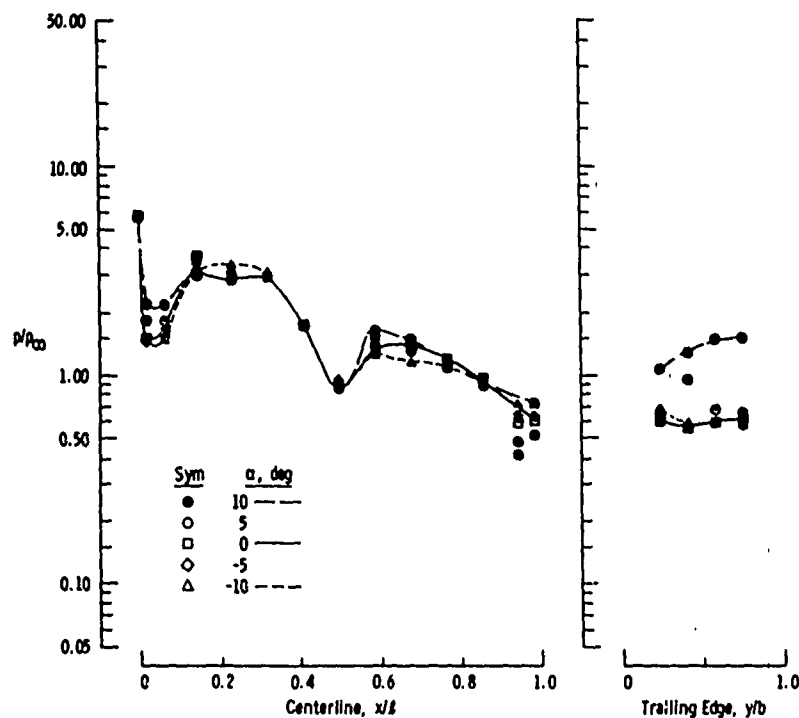d. Orbiter, $\Delta x/L = 0.165$, No Power Simulation, a Variable
Fig. II-23 Continued

e. Booster, $a = 0$, 50-percent Power Simulation, 100-percent Orbiter Power, $\Delta x/L$ Variable

Fig. II-23 Continued

f. Orbiter, $a = 0$, 50-percent Booster Power Simulation, 100-percent Orbiter Power, $\Delta x/L$ Variable

Fig. II-23 Continued

159

g. Booster, $\Delta x/L$ = 0.165, 50-percent Booster Power Simulation, 100-percent Orbiter Power, a Variable
Fig. II-23 Continued

h. Orbiter, $\Delta x/L$ = 0.165, 50-percent Booster Power Simulation, 100-percent Orbiter Power, a Variable
Fig. II-23 Concluded

160